



Dept. of Civil, Environmental & Architectural Engineering
 College of Engineering and Applied Science
 428 UCB
 Boulder, Colorado 80309-0428

t 303 492 8991
 f 303 492 7317
yunping.xi@colorado.edu

MEMORANDUM

To: Performance Improvement International
 2111 S El Camino Real
 Suite 200
 Oceanside, CA 92054
 Attention: Dr. Chong Chiu

From: Prof. Yunping Xi

Subject: Concrete Property Testing Results on Submitted Concrete Core Specimens

1. Introduction

Concrete core samples were delivered to the University of Colorado at Boulder in Nov. 2011. The concrete cores were cut into 13 samples for testing internal relative humidity, compressive strength, splitting tensile strength, coefficient of thermal expansion, accelerated creep, and freeze-thaw resistance. The identifications and dimensions of the samples will be described in the following sections together with testing result.

2. Internal Relative Humidity

The level of internal moisture and the distribution of internal moisture in a concrete structure are important for evaluating shrinkage and freeze-thaw damage of the concrete. Internal relative humidity (RH) distribution of the concrete was measured by using thermal and moisture sensors SHT75 from Sensirion. The concrete core used for this test is identified as S6 11/8/11. Eight sensors were embedded in the concrete cylinder at different depths from the surface to measure continuously both internal temperature and RH. The distances of the sensors from the surface are 1.0 in, 1.5 in, 2.0 in, 2.5 in, 3.0 in, 5.0 in, 7.0 in, and 8.5 in. Distributions of RH in the concrete sample were obtained. Test results are shown in Table 1 and in Fig. 1.

Table 1 RH test data at different times (Specimen S6 11/8/11)

Time	Depths from the surface (in)							
	1	1.5	2	2.5	3	5	7	8.5
11/18/2011 01:53 PM	60.07	63.57	64.26	59.07	60.44	67.01	67.92	69.41
11/19/2011 01:53 PM	59.7	63.08	63.07	58.32	59.5	67.07	68.01	69.14
11/20/2011 01:53 PM	58.63	61.94	61.42	56.82	57.91	66.55	67.55	68.42
11/21/2011 01:53 PM	58.14	61.32	60.44	56.02	57.26	66.52	67.48	68.24

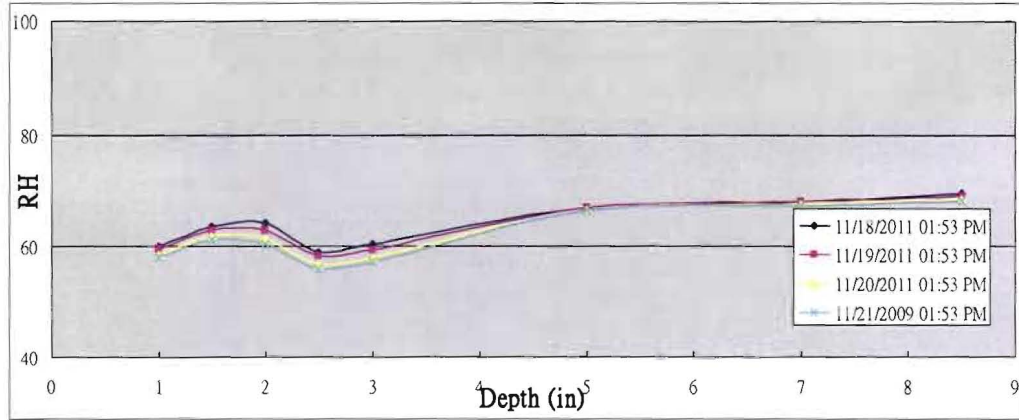


Fig. 2 RH distributions at different times

The RH values near the surface (from 1 in. to the range of 1.5 in. or 2 in.) are about 60%. The RH values at deeper locations approach to 70%, which is higher than the surface value. The values of RH reflect the annual average RH value of the environment. The gradient of RH is not large in the time period of Oct. and Nov., 2011.

After the test for internal relative humidity, a ponding test was performed using the same cylinder. The concrete cylinder was placed upright with the outer surface facing up. A water column of 13 cm was placed on top of the cylinder. The purpose of the test was to examine the resistance of the concrete to water and moisture penetration. The sensor at 3.0 in was damaged during the first test. So, seven sensors were used in the ponding test with the distances to the top surface 1.0 in, 1.5 in, 2.0 in, 2.5 in, 5.0 in, 7.0 in, and 8.5 in.

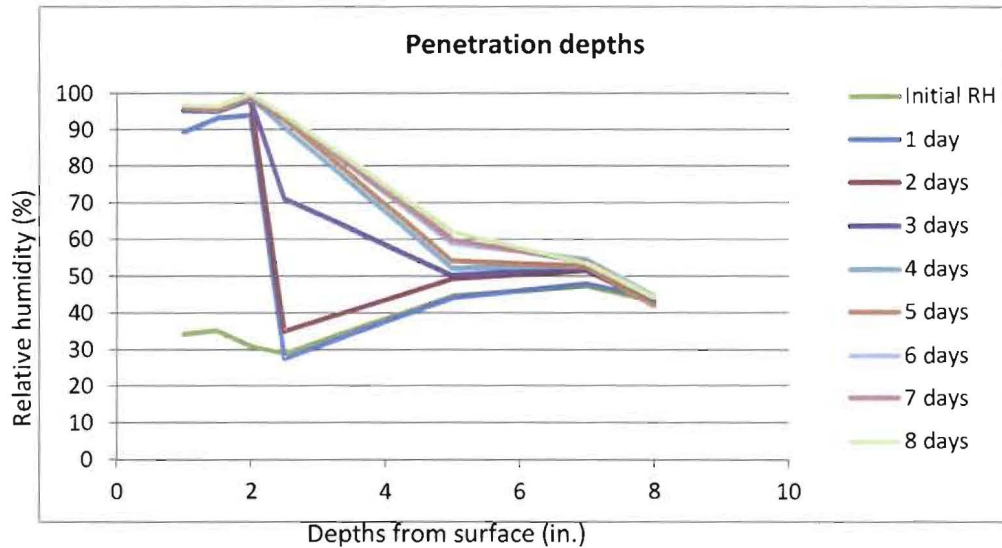


Fig. 3 RH distributions at different times during the ponding test

Fig. 3 shows the test data. The initial RH distribution is between 30% to 45%. This is because the test started on Feb. 7, 2012, more than two months after the first test. Within two days, the water penetrated to the depth of 2 inches, which indicated that the resistance of the surface layer concrete to water penetration is quite low. The concrete at 2.5 in. and deeper portion shows much higher resistance. The high moisture region with RH > 90% reached about 2.5 inches after four days of ponding.

These results showed that the rate of moisture penetration into the concrete depends strongly on the quality of surface layer concrete, where microcracks may form due to various deterioration mechanisms such as drying shrinkage. In order to determine moisture resistance of the concrete at different locations of the structure, more samples need to be taken from the structure and tested.

3. Compressive Strength

The compressive strength of concrete was tested according to ASTM C39. It is for the unconfined compressive strength of cylindrical concrete specimens. Four samples were used for the test. The identifications of the samples are shown in Table 2 and Fig. 4. Dimensions of the specimens and the test data are listed in Table 2.

Table 2 Compressive strength of the four specimens

No	Diameter (in.)	Length (in.)	fc' (psi)	Specimen description
1	2.65	5.76	5444	Hallway #1
2	2.65	5.76	6342	S9 680-3
3	3.39	5.88	7990	S4 11/8/11
4	3.39	6.38	10508	S4 11/8/11



Fig. 4 Specimen #1 (right) and #2 (left) after the compressive strength test

4. Splitting Tensile Strength

The splitting tensile strength of cylindrical concrete specimens was tested according to ASTM C496. The maximum load recorded, P , was used to calculate the splitting tensile strength of concrete samples based on Eq. 1.

$$f_{st} = \frac{2P}{\pi ld} \tag{Eq. 1}$$

in which f_{st} = splitting tensile strength; l and d are the length and diameter of specimen, respectively. Test results are shown in Table 3.

Table 3 Splitting tensile strength test data

Specimen	Length (in)	Diameter (in)	Area (in ²)	Force (kips)	f_{st} (psi)	Specimen description
No. 1	4.2	3.68	10.63	67.110	957.43	S8 11/8/11
No. 2	5.1	3.68	10.63	67.447	962.23	S8 11/3/11
No. 3	5.4	3.68	10.63	58.585	835.8	S3 11/8/11

5. Coefficient of Thermal Expansion (CTE)

Two cylindrical specimens (#S2 11/8/11, #S4 11/8/11) were used for the test. The diameters of the two samples are the same, 3.39 in. Thermal expansions of the two specimens were measured between two temperature ranges from 22°C to 40°C and then from 40°C to 60°C, then linear coefficients of thermal expansion were calculated based on the test data. The tests were conducted in an environmental chamber with temperature control. So, it is different from USBR 4910-92 conducted in U.S. Bureau of Reclamation, in which the specimens were submerged in water and the water temperature is varied to create the thermal expansion. The purpose of this test is to obtain CTE of concrete used in above ground structures.

Thermal sensors were installed inside of concrete samples to double check the internal temperature in concrete samples. When the internal temperature reaches the target temperature, deformation of concrete sample was measured after two hours of holding of the target temperature. This was to make sure that the internal temperature distribution in the cylinder reaches equilibrium (uniform distribution). The test data of the two specimens are shown in Table 4 and Table 5.

Table 4 CTE of Specimen #S2

ΔT (°C)	Length (in)	ΔL (in)	CTE (1/°C)	Average CTE (1/°C)
18 (from 22 to 40°C)	10.157	0.0013	0.00000711	0.00000875
20 (from 40 to 60°C)	10.157	0.0021	0.00001034	
38 (from 22 to 60°C)	10.157	0.0034	0.00000881	

Table 5 CTE of Specimen #S4

ΔT (°C)	Length (in)	ΔL (in)	CTE (1/°C)	Average CTE (1/°C)
18 (from 22 to 40°C)	10.284	0.0011	0.00000594	0.00000886
20 (from 40 to 60°C)	10.284	0.0024	0.00001167	
38 (from 22 to 60°C)	10.284	0.0035	0.00000896	

The average value of CTE of the two specimens = $8.8 \times 10^{-6} / ^\circ\text{C}$. The CTE measured by USBR = $5.2 \times 10^{-6} / ^\circ\text{F} = 9.4 \times 10^{-6} / ^\circ\text{C}$. Our CTE value is slightly smaller than the CTE measured by USBR because when the concrete was heated in air, the measured thermal expansion is actually a combination of pure thermal expansion and drying shrinkage.

In addition to the test of CTE in the temperature range above 0°C , another series of tests was performed for the thermal strains in the temperature range below 0°C . The purpose of this test was to examine the effect of ice formation on thermal expansion of the concrete. The testing sample was S2 11/8/11. The diameter of the specimen is 3.46 in. and 11.5 in. long.

Two tests were performed. One is called dry test. The specimen was placed in a high temperature chamber for 14 days under 80°C to dry out the internal moisture, and then placed in a freezing chamber with programmable temperature control. The test started at 20°C , the temperature was reduced to 15°C in 30 minutes, stayed at 15°C for 3 hours, and the strain was measured. The process was repeated until the target temperature of -25°C . The test data are shown as the blue curve in Fig. 5.

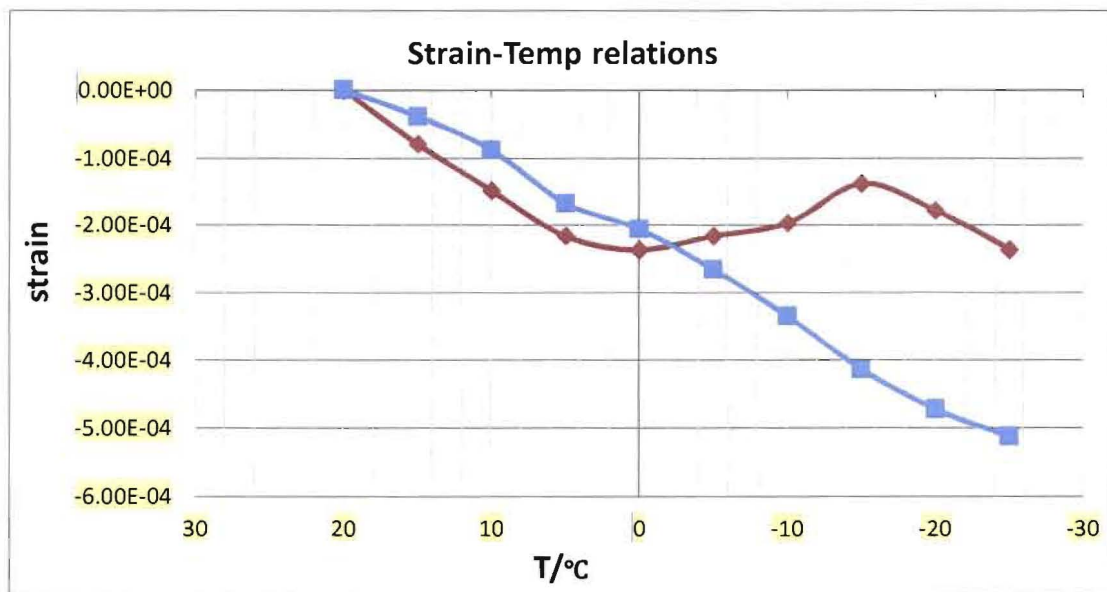


Fig. 5 Thermal strains under low temperatures for the effect of ice formation in the concrete (Blue curve: Dry sample Red curve: Wet sample)

After the test for the dry sample, the specimen was placed in a water tank for 68 hours for saturation. The same testing procedure was used to obtain the thermal strain under low temperatures. The test was called wet test. The test data are shown as the red curve in Fig. 5. It is important to see from Fig. 5 that the concrete contracts upon cooling from 20°C to 0°C , starts to expand from 0°C to -15°C , and then starts to contract again. The first reversal from contraction to expansion is due to the ice formation in the concrete, because the CTE of ice is about five times higher than the CTE of concrete. The second reversal is an indication of the completion of ice formation. Both ice and concrete contract upon a further cooling.

The test results indicated that with a high moisture content, the effect of ice formation on thermal strain of the concrete sample is significant, resulting in an expansion under the low temperature from 0°C to -15°C. Because of limited time, the internal moisture distribution in the sample may not be uniform, so the measured strains represent average values of the thermal strains. In order to determine the coupling effects among moisture content, low temperature, and ice formation, a more systematic experimental study with more samples is needed.

6. Accelerated Creep

The accelerated creep tests were performed to obtain creep strain of the concrete used in Davis-Besse Nuclear Power Station. The creep tests generally follow the procedure described in ASTM C-512 “Standard Test Method for Creep in Compression”. Three accelerated creep tests were performed under 40 °C (with and without humidity control) and 80 °C (with humidity control), respectively. Different relative humidity controls were used in the tests to find the effect of moisture level on the creep of concrete. Some of the basic terminologies used in this section are

- Basic creep – The long-term strain of concrete due to loading without drying and heating.
- Drying shrinkage – The long-term strain of concrete due to drying without loading and heating.
- Drying creep – The long-term strain of concrete due to loading and drying without heating.



Fig. 6 The MTS machine provides a stable compressive force at 16 kips

6.1 Testing method

- One cylindrical specimens (#S2 11/8/11) was cut into a cylinder of 11.5 in. long. The diameter of the specimen is 3.46 in.
- Two contact points were installed on the top and bottom portion of the specimen. The distance between the two contact points equals the gage length of the dial gauge to be used to measure the length change of the specimen.
- The specimen was capped on top and bottom surfaces.
- The specimen was loaded by a MTS machine mounded in an environmental chamber. The

loading level was kept as a constant 16 kips, which resulted in a compressive stress of 1702 psi. This stress level is less than 40% of the average compressive strength of the concrete (7,600 psi). Fig. 6 shows the loading setup.

- The chamber was maintained at a constant temperature of 40°C or 80°C.
- For the first specimen, the temperature was kept at 40°C without humidity control. For the second specimen, the temperature was kept at 80°C, and the humidity was controlled in the range of 70% to 80%. For the third specimen, the temperature was kept at 40°C, and the humidity was controlled in the range of 70% to 80%.

6.2 Test results

The test results of the three accelerated creep tests are plotted in Figs. 7, 8, and 9. Fig. 7 shows the test results under 40°C without humidity control; Fig. 8 is for the test results under 80°C with humidity control; and Fig. 9 is for the test results under 40°C with humidity control.

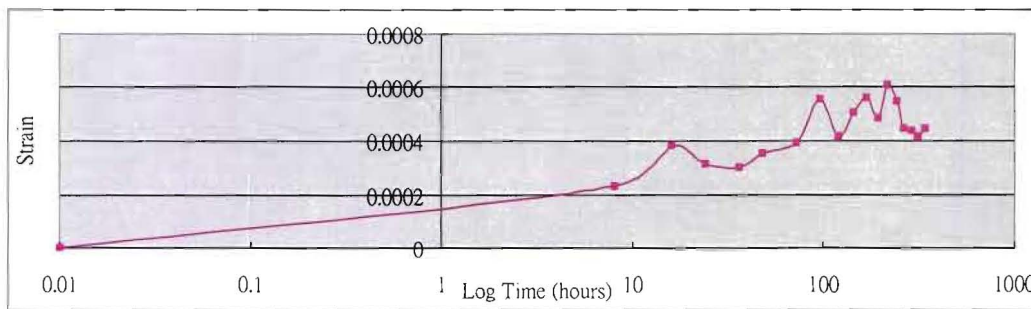


Fig. 7 Test results obtained under 40°C without humidity control

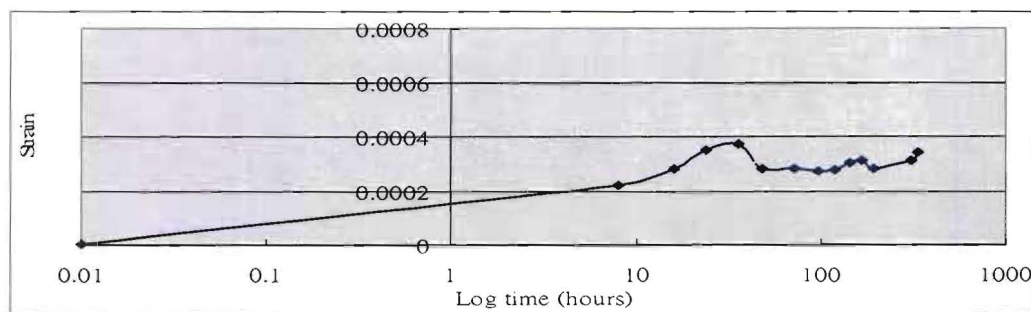


Fig. 8 Test results obtained under 80°C with humidity control

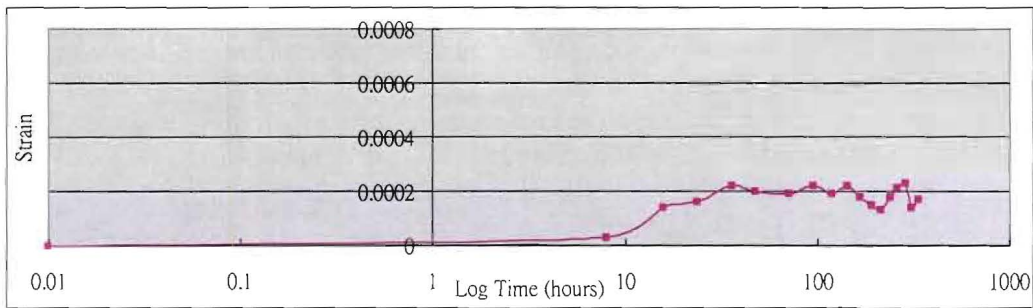


Fig. 9 Test results obtained under 40°C with humidity control

6.3 Comparisons and discussions

Comparison of Fig. 7 and Fig. 9 shows the effect of drying on concrete creep. The creep reading in Fig. 7 is about 0.0005 (500 microstrain) after 100 hours, which is about 2.5 times the value in Fig. 9, which is about 0.0002 (200 microstrain). The difference between the two tests was the relative humidity in the chamber. In Fig 9, the relative humidity was controlled at the range of 70%-80%, so the test data represent basic creep of the concrete. In Fig. 7, there was no humidity control, so the test data represent a combination of basic creep and drying shrinkage, and that is why the measured strains are much higher. Basically, the effect of drying shrinkage is quite significant, and the creep of concrete under an arid environment (low humidity) is much higher than that in a humid environment.

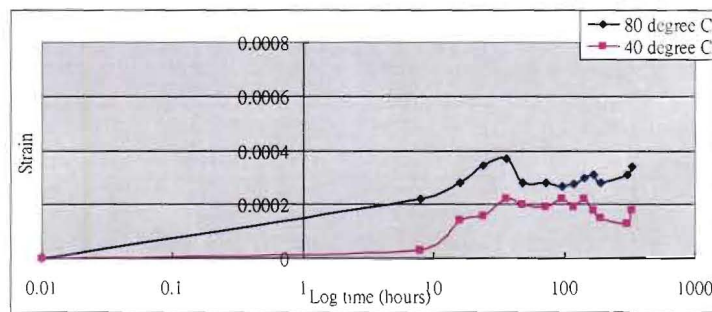


Fig. 10 Comparison of creep strains under 40°C and 80°C (log time scale)

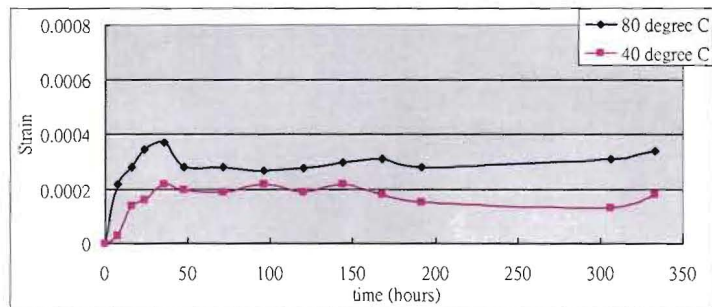


Fig. 11 Comparison of creep strains under 40°C and 80°C (regular time scale)

Comparison of Fig. 8 and Fig. 9 shows the effect of temperature on concrete creep. The same humidity controls were used for the two tests, and thus there is no effect of drying shrinkage. Combining Fig. 8 and Fig. 9 gives Fig. 10 in log time scale and Fig. 11 in regular time scale. Fig. 11 can be used to obtain creep compliance functions under two different temperatures, which can be used further to obtain the creep coefficient of concrete.

7. Freeze-thaw resistance

The accelerated freeze-thaw tests were planned to obtain freeze-thaw of the concrete used in Davis-Besse Nuclear Power Station. The freeze-thaw tests generally follow the procedure described in ASTM C-666. The testing chest is shown in Fig.12. Each freeze-thaw cycle is approximately 2-3 hours. There will be 300 cycles. Two samples were used for the test: S9 680-3 and In Steam Room 602 #1



Fig. 12. The rapid freeze-thaw test chest

After one day of testing, the temperature controller of the testing machine was broken. The test was stopped. After a new controller was installed, we did not re-start the test, because this is a long-term test and it cannot be done before the completion of the project.

A summary table is shown in the next page for identifications of all sample tested at University of Colorado.

Tests at Univ. of Colorado

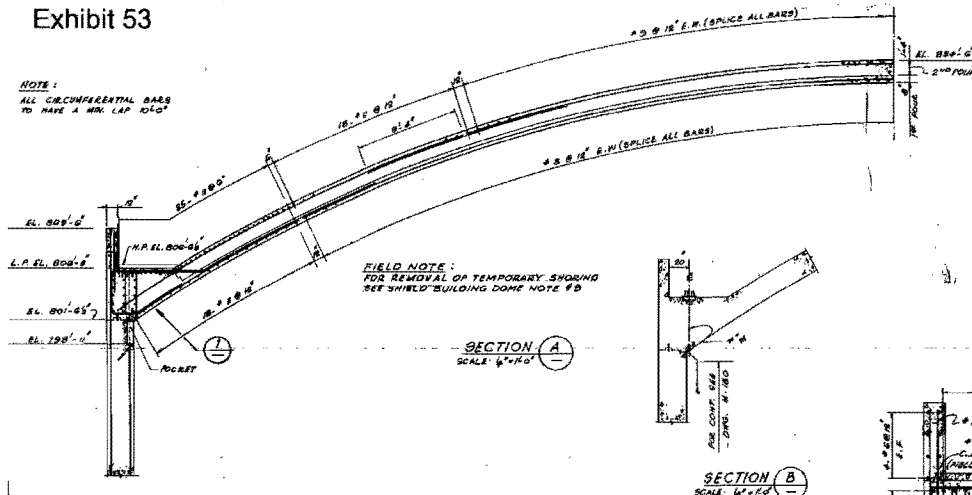
Test	Core identification
Internal moisture and ponding test	S6 11/8/11
Compression	Hallway #1
	S9 680-3
	S4 11/8/11
	S4 11/8/11
Splitting tension	S8 11/8/11
	S8 11/8/11
	S3 11/8/11
Coefficient of thermal expansion	S2
	S4
Creep and CTE at low temperatures	S2 11/8/11
Freeze-thaw	S9 680-3
	In Steam Room 602 #1



Exhibit 53: C-0109 Roof Plans and Details

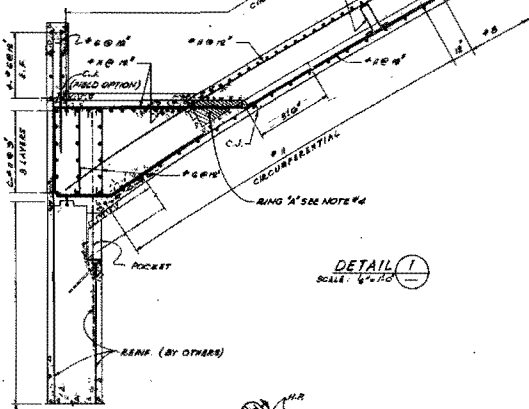
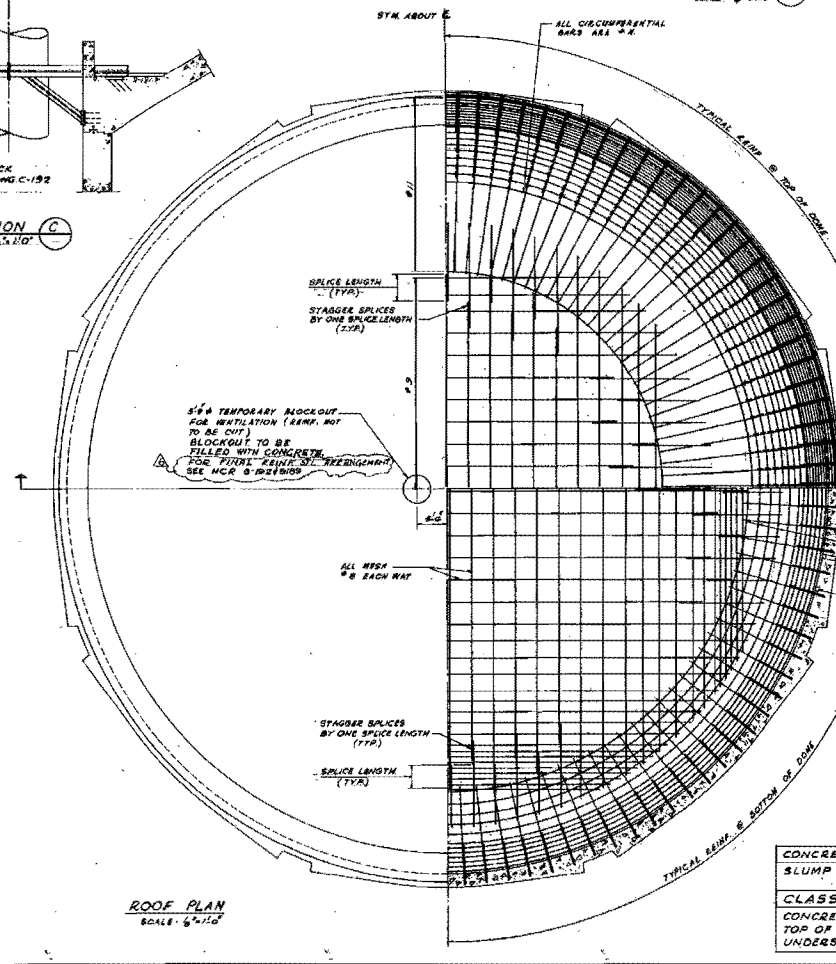
Exhibit 53

NOTE:
ALL CIRCUMFERENTIAL BARS TO HAVE A MIN. LAP 60"



GENERAL NOTES

1. MATERIALS, MANUFACTURE AND WORKMANSHIP SHALL BE IN ACCORDANCE WITH SPECIFICATION NO. 215 AND BUILDING CODE REQUIREMENTS FOR REINFORCED CONCRETE AND THE SHIELD BUILDING CODE.
2. ALL CONCRETE EXCEPT FOR THE SHIELD BUILDING DOME SHALL BE CLASS D-1 AND 9-2 WITH 3000 PSI MINIMUM COMPRESSIVE STRENGTH @ 28 DAYS AS SPECIFIED IN SPECIFICATION NO. 214B-C-26. CLASS D-1 WILL BE USED FOR WALLS AND CLASS D-2 SHALL BE USED FOR SLABS. ALL CONCRETE SHALL BE ASTM TYPE 11. CONCRETE SHALL BE PLACED IN ACCORDANCE WITH THE DRAWINGS AND WITHIN THE REQUIRED TOLERANCES UNLESS OTHERWISE NOTED.
3. ALL REINFORCING STEEL SHALL BE ASTM A 615, GRADE 60, REBARS. ALL REINFORCING STEEL SHALL BE PLACED IN ACCORDANCE WITH THE DRAWINGS. STEEL SHALL BE PLACED IN LOCATION AND AT SPACING SHOWN AND ACCURATELY TIED IN PLACE IN SUCH A MANNER THAT IT WILL NOT BE DISPLACED DURING THE CONCRETE POURING OPERATION. ALL BARS, TIES AND CLEARANCES SHALL BE AS SHOWN IN ACCORDANCE WITH THE DRAWINGS.
4. ALL SLICES OF REINFORCEMENT SHALL BE IN ACCORDANCE WITH THE TIME ON DAM-C-202 EXCEPT AS NOTED.
5. ALL REINFORCING STEEL SHALL BE PLACED IN ACCORDANCE WITH THE DRAWINGS.
6. WITHIN CONCRETE PROTECTION FOR REINFORCEMENT SHALL CONFORM TO ACI 318-89 EXCEPT WHERE NOTED OTHERWISE ON THE DRAWINGS.
7. NO CONCRETE SHALL BE Poured WITH ALL METAL TIES INCLUDING REINFORCING STEEL TIES, TIES, TIES AND ELECTRICAL GROUND ROD CIRCUIT AND BLOODWAYS HAVE BEEN ACCURATELY PLACED, PROPERLY FASTENED, AND INSPECTED AND APPROVED BY THE CONSTRUCTION SUPERVISOR. BLOODWAYS AT ALL CLOSED OBSTRUCTION POINTS (POINTS WHERE THERE IS AN OBSTRUCTION) SHALL BE 1/2" x 1/2" FLAT CHANNELS TYPE SIMILAR TO "GRADE SERVICES" CODE 90317-1.
8. ALL FLOORS SHALL BE SLOPED AT A MINIMUM OF 1/8" PER FOOT TOWARD FLOOR DRAINS UNLESS NOTED OTHERWISE. FLOOR ELEVATIONS WILL BE AT HIGH POINT OF FLOOR.
9. FOR LOCATION OF FLOOR DRAINS, EQUIPMENT CRAWLS AND UNDESIRED PIPING, SEE MECHANICAL ENG. W-182, W-194 AND W-195.
10. CONCRETE ON STAIRS SHALL BE AS SHOWN AND LOCATED ON THE DRAWINGS AND MADE IN ACCORDANCE WITH A.C.I. 318 AND SPEC. NO. 214B-C-26. ANY DEVIATION FROM THIS SHALL BE APPROVED BY ENGINEERING. ADDITIONAL CONSTRUCTION JOBS NOT SHOWN ON DRAWINGS WILL REQUIRE CONSTRUCTION MANAGEMENT APPROVAL.
11. CONCRETE IF REQUIRED SHALL BE IN ACCORDANCE WITH SPECIFICATION.
12. STEELLESS STEEL LINER PLATE (SUPPLIED AND INSTALLED BY OTHERS) SHALL BE USED IN THE REACTOR CAVITY AND THE CENTRAL PLATE LINER IN THE INSTRUMENTATION TOWER. THIS SHALL BE PROVIDED AND INSTALLED BY THE CONTRACTOR. THE LINER SHALL BE JOIST AS CONCRETE FORMWORK WITH INSULATION. CONCRETE SHALL BE PLACED ON STEEL DECKING SHALL CONFORM TO SPEC 214B-C-26.



NOTES FOR SHIELD BUILDING DOME

1. ALL CONSTRUCTION JOINTS IN THE DOME SHALL BE SANDBLASTED OR WATERBLASTED AT A MIN. PRESSURE OF 5000 PSI.
2. THE RING UNDER & THE BOTTOM OF SLAB SHALL BE POURED FIRST. THE SECOND RING SHALL NOT BE PLACED UNTIL THE PREVIOUS POUR HAS GAINED A STRENGTH OF 75% OF DESIGN STRENGTH. SEE NOTE #9.
3. CONCRETE SHALL NOT BE DEPOURED FEER FROM A HEIGHT OF MORE THAN 4 FEET.
4. DOME CONCRETE SHALL BE PLACED AT THE FOLLOWING RATE: RING 1" 40 YDS. PER HOUR REST OF CONCRETE 80 YDS. PER HOUR ABOVE QUANTITIES MAY VARY AS DIRECTED BY FIELD ENGINEER DEPENDING ON FIELD CONDITIONS, HOWEVER THE PLACEMENT SHALL BE MADE IN SUCH A MANNER THAT CONCRETE IS PRE-SATURATED PRIOR TO PLACING ADJACENT POUR BUT NOT SO LONG AS TO RESULT IN A FINAL SET OR A COLD JOINT.
5. DURING THE FIRST POUR & THE SECOND POUR OF DOME CONCRETE SHALL BE PLACED IN A MANNER OF MULTIPLE CONCRETE RINGS.
6. THE FIRST POUR SHALL BE NETTED DOWN FOR A PERIOD OF TWO (2) HOURS JUST PRIOR TO POURING THE BALANCE OF DOME CONCRETE AS PER SPECIFICATION 214B-C-20A.
7. WORK THIS DOME WITH DING C-100, C-101 & C-102.
8. FOR REBAR SPACING SEE DOME D-100.
9. AFTER FIRST POUR HAS ATTAINED STRENGTH AS STATED IN NOTE #9 PRIOR TO THE SECOND POUR ALL THE RING COLUMNS MUST BE CUT IN SUCH A WAY AS TO LEAVE THE FIRST POUR OF THE DOME FREE STANDING & NOT TRANSMITTING ANY LOAD TO THE STEEL DOME BELOW.
10. THE COLUMN CUTTING ROUGHNESS SHALL BE FROM THE CENTER OF THE DOME WORKING TOWARD THE OUTSIDE CIRCLE BY CIRCLE.

CONCRETE: 5000 PSI 10M RYASH (PCN 60)
SLUMP: 3" CLASS D-2
CLASS I STRUCTURE
CONCRETE FINISH:
TOP OF DOME STEEL TROWELED
UNDERSIDE OF DOME FORMED

STRUCTURAL STEEL

1. ALL STRUCTURAL STEEL AND WELDING SHALL CONFORM TO THE SHIELD BUILDING CODE AND SPEC. NO. 214B-C-26 EXCEPT AS NOTED OTHERWISE ON THE DRAWINGS.
2. ALL WELDS SHALL BE MADE IN ACCORDANCE WITH THE SHIELD BUILDING CODE AND SPEC. NO. 214B-C-26 EXCEPT AS NOTED OTHERWISE ON THE DRAWINGS.
3. ALL WELDS SHALL BE MADE BY THE SHIELD BUILDING DOME CONTRACTOR.
4. ALL WELDS SHALL BE MADE BY THE SHIELD BUILDING DOME CONTRACTOR.
5. ALL WELDS SHALL BE MADE BY THE SHIELD BUILDING DOME CONTRACTOR.
6. ALL WELDS SHALL BE MADE BY THE SHIELD BUILDING DOME CONTRACTOR.
7. ALL WELDS SHALL BE MADE BY THE SHIELD BUILDING DOME CONTRACTOR.
8. ALL WELDS SHALL BE MADE BY THE SHIELD BUILDING DOME CONTRACTOR.
9. ALL WELDS SHALL BE MADE BY THE SHIELD BUILDING DOME CONTRACTOR.
10. ALL WELDS SHALL BE MADE BY THE SHIELD BUILDING DOME CONTRACTOR.

NO. 1	NO. 2	NO. 3	NO. 4	NO. 5	NO. 6	NO. 7	NO. 8	NO. 9	NO. 10	NO. 11	NO. 12	NO. 13	NO. 14
✓	✓	✓	✓	✓	✓	✓	✓	✓	✓	✓	✓	✓	✓

BECKETT COMPANY
SUPERCONCRETE, PORTLAND

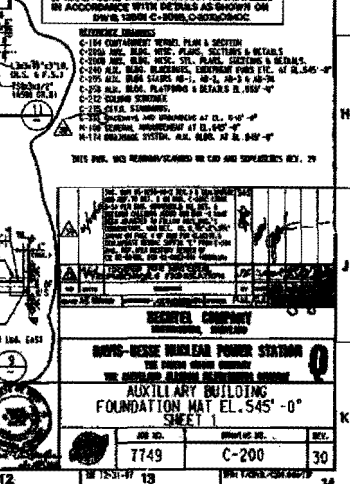
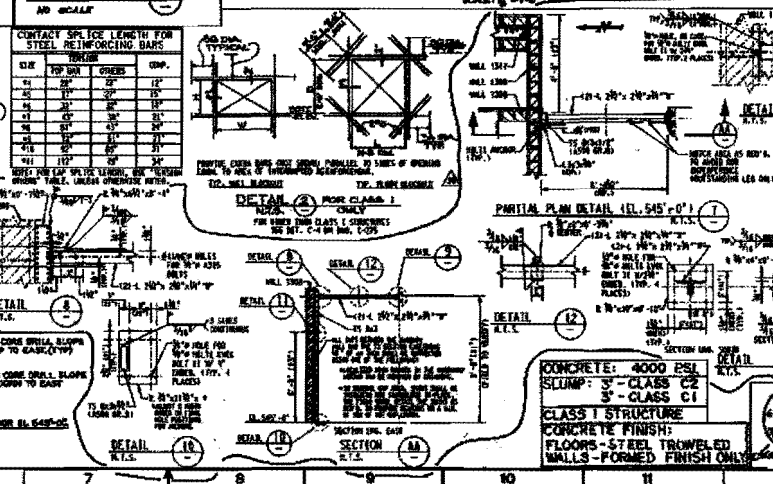
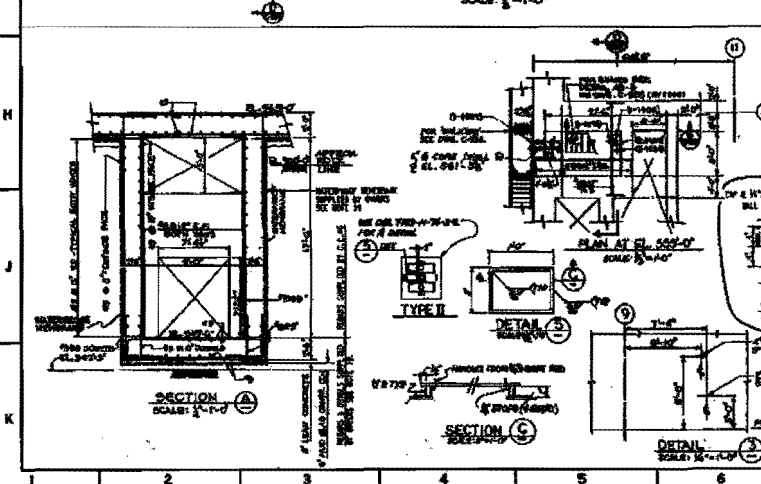
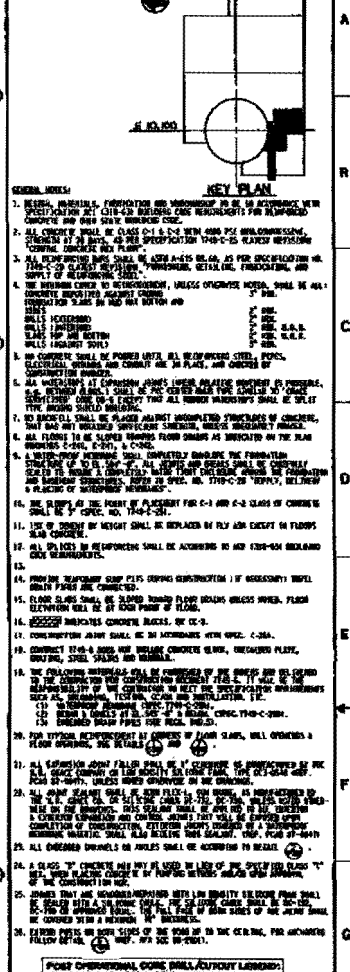
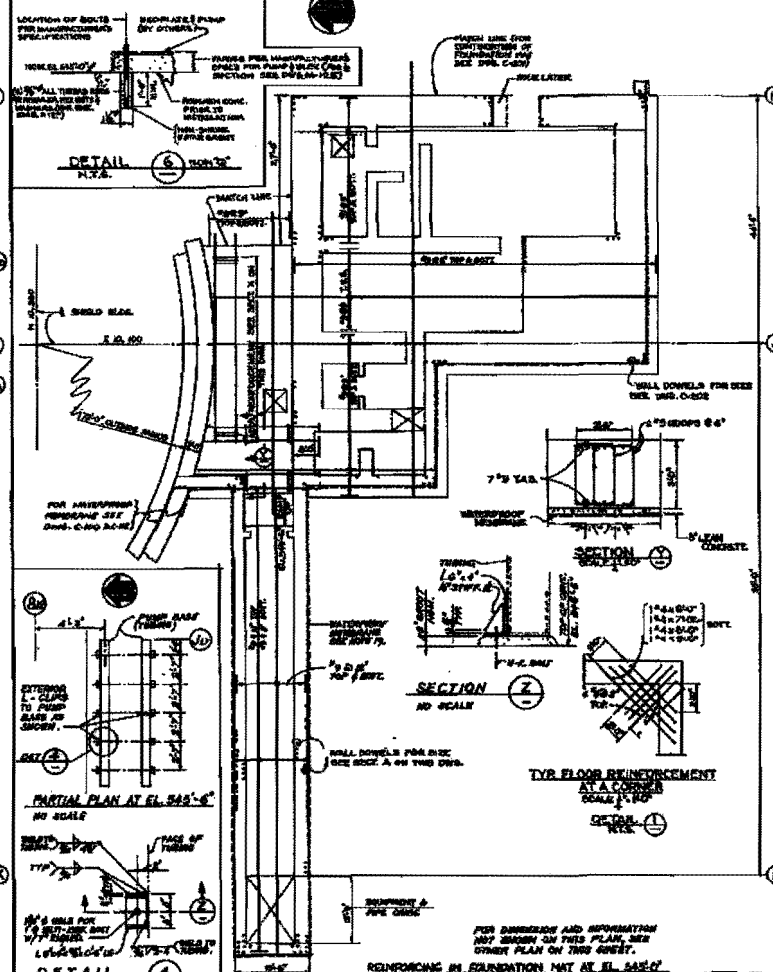
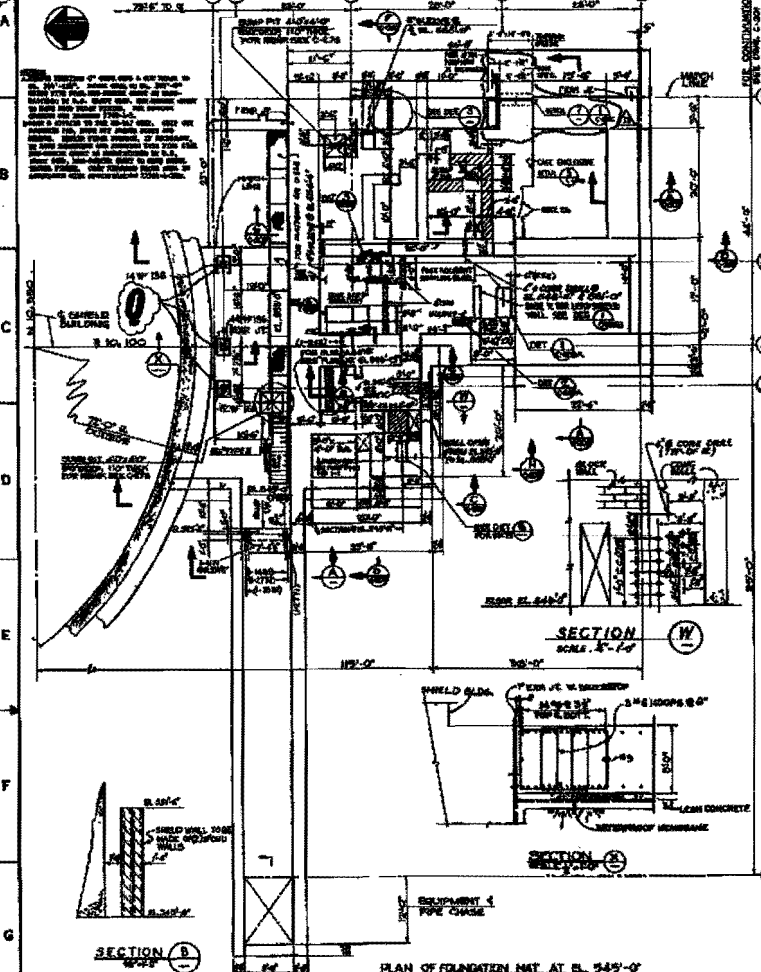
DAVIS-BESSE NUCLEAR POWER STATION
THE CLEVELAND ELECTRIC LIGHTING COMPANY

SHIELD BUILDING
ROOF PLAN AND DETAILS SH. 1

7748 C-109 6



Exhibit 54: C-200



CONTACT SPICE LENGTH FOR STEEL REINFORCING BARS

SIZE	TOP BAR	OTHERS	CONC.
#3	12"	12"	12"
#4	12"	12"	12"
#5	12"	12"	12"
#6	12"	12"	12"
#7	12"	12"	12"
#8	12"	12"	12"
#9	12"	12"	12"
#10	12"	12"	12"
#11	12"	12"	12"
#12	12"	12"	12"
#13	12"	12"	12"
#14	12"	12"	12"
#15	12"	12"	12"
#16	12"	12"	12"
#17	12"	12"	12"
#18	12"	12"	12"
#19	12"	12"	12"
#20	12"	12"	12"
#21	12"	12"	12"
#22	12"	12"	12"
#23	12"	12"	12"
#24	12"	12"	12"
#25	12"	12"	12"
#26	12"	12"	12"
#27	12"	12"	12"
#28	12"	12"	12"
#29	12"	12"	12"
#30	12"	12"	12"

- GENERAL NOTES:**
1. DESIGN, MATERIALS, CONSTRUCTION AND WORKMANSHIP TO BE IN ACCORDANCE WITH THE SPECIFICATIONS FOR STRUCTURAL STEEL AND REINFORCING BARS FOR PRECAST CONCRETE AND WITH THE SPECIFICATIONS FOR PRECAST CONCRETE AND WITH THE SPECIFICATIONS FOR REINFORCING BARS FOR PRECAST CONCRETE.
 2. ALL DIMENSIONS SHALL BE AS SHOWN UNLESS OTHERWISE SPECIFIED. DIMENSIONS SHALL BE TO THE FACE UNLESS OTHERWISE SPECIFIED.
 3. ALL REINFORCING BARS SHALL BE ASTM A-616 OR A-618, AS PER SPECIFICATION IN THE SPECIFICATIONS FOR REINFORCING BARS FOR PRECAST CONCRETE, UNLESS OTHERWISE SPECIFIED.
 4. THE REINFORCING BARS SHALL BE PLACED AS SHOWN UNLESS OTHERWISE SPECIFIED. THE REINFORCING BARS SHALL BE PLACED AS SHOWN UNLESS OTHERWISE SPECIFIED.
 5. ALL REINFORCING BARS SHALL BE PLACED AS SHOWN UNLESS OTHERWISE SPECIFIED. THE REINFORCING BARS SHALL BE PLACED AS SHOWN UNLESS OTHERWISE SPECIFIED.
 6. ALL REINFORCING BARS SHALL BE PLACED AS SHOWN UNLESS OTHERWISE SPECIFIED. THE REINFORCING BARS SHALL BE PLACED AS SHOWN UNLESS OTHERWISE SPECIFIED.
 7. ALL REINFORCING BARS SHALL BE PLACED AS SHOWN UNLESS OTHERWISE SPECIFIED. THE REINFORCING BARS SHALL BE PLACED AS SHOWN UNLESS OTHERWISE SPECIFIED.
 8. ALL REINFORCING BARS SHALL BE PLACED AS SHOWN UNLESS OTHERWISE SPECIFIED. THE REINFORCING BARS SHALL BE PLACED AS SHOWN UNLESS OTHERWISE SPECIFIED.
 9. ALL REINFORCING BARS SHALL BE PLACED AS SHOWN UNLESS OTHERWISE SPECIFIED. THE REINFORCING BARS SHALL BE PLACED AS SHOWN UNLESS OTHERWISE SPECIFIED.
 10. ALL REINFORCING BARS SHALL BE PLACED AS SHOWN UNLESS OTHERWISE SPECIFIED. THE REINFORCING BARS SHALL BE PLACED AS SHOWN UNLESS OTHERWISE SPECIFIED.
 11. ALL REINFORCING BARS SHALL BE PLACED AS SHOWN UNLESS OTHERWISE SPECIFIED. THE REINFORCING BARS SHALL BE PLACED AS SHOWN UNLESS OTHERWISE SPECIFIED.
 12. ALL REINFORCING BARS SHALL BE PLACED AS SHOWN UNLESS OTHERWISE SPECIFIED. THE REINFORCING BARS SHALL BE PLACED AS SHOWN UNLESS OTHERWISE SPECIFIED.
 13. ALL REINFORCING BARS SHALL BE PLACED AS SHOWN UNLESS OTHERWISE SPECIFIED. THE REINFORCING BARS SHALL BE PLACED AS SHOWN UNLESS OTHERWISE SPECIFIED.
 14. ALL REINFORCING BARS SHALL BE PLACED AS SHOWN UNLESS OTHERWISE SPECIFIED. THE REINFORCING BARS SHALL BE PLACED AS SHOWN UNLESS OTHERWISE SPECIFIED.
 15. ALL REINFORCING BARS SHALL BE PLACED AS SHOWN UNLESS OTHERWISE SPECIFIED. THE REINFORCING BARS SHALL BE PLACED AS SHOWN UNLESS OTHERWISE SPECIFIED.
 16. ALL REINFORCING BARS SHALL BE PLACED AS SHOWN UNLESS OTHERWISE SPECIFIED. THE REINFORCING BARS SHALL BE PLACED AS SHOWN UNLESS OTHERWISE SPECIFIED.
 17. ALL REINFORCING BARS SHALL BE PLACED AS SHOWN UNLESS OTHERWISE SPECIFIED. THE REINFORCING BARS SHALL BE PLACED AS SHOWN UNLESS OTHERWISE SPECIFIED.
 18. ALL REINFORCING BARS SHALL BE PLACED AS SHOWN UNLESS OTHERWISE SPECIFIED. THE REINFORCING BARS SHALL BE PLACED AS SHOWN UNLESS OTHERWISE SPECIFIED.
 19. ALL REINFORCING BARS SHALL BE PLACED AS SHOWN UNLESS OTHERWISE SPECIFIED. THE REINFORCING BARS SHALL BE PLACED AS SHOWN UNLESS OTHERWISE SPECIFIED.
 20. ALL REINFORCING BARS SHALL BE PLACED AS SHOWN UNLESS OTHERWISE SPECIFIED. THE REINFORCING BARS SHALL BE PLACED AS SHOWN UNLESS OTHERWISE SPECIFIED.
 21. ALL REINFORCING BARS SHALL BE PLACED AS SHOWN UNLESS OTHERWISE SPECIFIED. THE REINFORCING BARS SHALL BE PLACED AS SHOWN UNLESS OTHERWISE SPECIFIED.
 22. ALL REINFORCING BARS SHALL BE PLACED AS SHOWN UNLESS OTHERWISE SPECIFIED. THE REINFORCING BARS SHALL BE PLACED AS SHOWN UNLESS OTHERWISE SPECIFIED.
 23. ALL REINFORCING BARS SHALL BE PLACED AS SHOWN UNLESS OTHERWISE SPECIFIED. THE REINFORCING BARS SHALL BE PLACED AS SHOWN UNLESS OTHERWISE SPECIFIED.
 24. ALL REINFORCING BARS SHALL BE PLACED AS SHOWN UNLESS OTHERWISE SPECIFIED. THE REINFORCING BARS SHALL BE PLACED AS SHOWN UNLESS OTHERWISE SPECIFIED.
 25. ALL REINFORCING BARS SHALL BE PLACED AS SHOWN UNLESS OTHERWISE SPECIFIED. THE REINFORCING BARS SHALL BE PLACED AS SHOWN UNLESS OTHERWISE SPECIFIED.
 26. ALL REINFORCING BARS SHALL BE PLACED AS SHOWN UNLESS OTHERWISE SPECIFIED. THE REINFORCING BARS SHALL BE PLACED AS SHOWN UNLESS OTHERWISE SPECIFIED.
 27. ALL REINFORCING BARS SHALL BE PLACED AS SHOWN UNLESS OTHERWISE SPECIFIED. THE REINFORCING BARS SHALL BE PLACED AS SHOWN UNLESS OTHERWISE SPECIFIED.
 28. ALL REINFORCING BARS SHALL BE PLACED AS SHOWN UNLESS OTHERWISE SPECIFIED. THE REINFORCING BARS SHALL BE PLACED AS SHOWN UNLESS OTHERWISE SPECIFIED.
 29. ALL REINFORCING BARS SHALL BE PLACED AS SHOWN UNLESS OTHERWISE SPECIFIED. THE REINFORCING BARS SHALL BE PLACED AS SHOWN UNLESS OTHERWISE SPECIFIED.
 30. ALL REINFORCING BARS SHALL BE PLACED AS SHOWN UNLESS OTHERWISE SPECIFIED. THE REINFORCING BARS SHALL BE PLACED AS SHOWN UNLESS OTHERWISE SPECIFIED.

CONCRETE: 4000 PSI
SLUMP: 3" CLASS C2
3" CLASS C1
CLASS 1 STRUCTURE
CONCRETE FINISH:
FLOORS - 57 REEL TROWELED
WALLS - FORMED FINISH ONLY

REINER COMPANY
REINFORCING BARS
11111 11111
11111 11111

MOYD-BENNE WHEELER POWER STATION
THE POWER STATION OWNER
THE DESIGN AND CONSTRUCTION ENGINEER

AUXILIARY BUILDING
FOUNDATION MAT EL. 545'-0"

SHEET 1

NO. 7749	REV. C-200	DATE 10/20/57
1	2	3



Exhibit 55: ACI 201.2R-08, Table 6.3

Table 6.1—Effect of commonly used chemicals on concrete

Rate of attack at ambient temperature	Inorganic acids	Organic acids	Alkaline solutions	Salt solutions	Miscellaneous
Rapid	Hydrochloric Nitric Sulfuric	Acetic Formic Lactic	—	Aluminum chloride	—
Moderate	Phosphoric	Tannic	Sodium hydroxide* > 20%	Ammonium nitrate Ammonium sulfate Sodium sulfate Magnesium sulfate Calcium sulfate	Bromine (gas) Sulfite liquor
Slow	Carbonic	—	Sodium hydroxide* 10 to 20% Sodium hypochlorite	Ammonium chloride Magnesium chloride Sodium cyanide	Chlorine (gas) Seawater Soft water
Negligible	—	Oxalic Tartaric	Sodium hydroxide* < 10% Sodium hypochlorite Ammonium hydroxide	Calcium chloride Sodium chloride Zinc nitrate Sodium dichromate	Ammonia (liquid)

*The effect of potassium hydroxide is similar to that of sodium hydroxide.

DePuy (1994), Taylor (1997), Skalny et al. (1998), Thomas and Skalny (2006), and Naik et al. (2006). Publications with particular emphasis on permeability and the ability of concrete to resist ingress and movement of water include Reinhardt (1997), Hearn et al. (1994), Hearn and Young (1999), Diamond (1998), and Diamond and Lee (1999).

6.2.3 Recommendations—Protection against sulfate attack is obtained by using concrete that retards the ingress and movement of water and concrete-making ingredients appropriate for producing concrete having the needed sulfate resistance. The ingress and movement of water are reduced by lowering the *w/cm*. Care should be taken to ensure that the concrete is designed and constructed to minimize shrinkage cracking. Air entrainment is beneficial if it is accompanied by a reduction in the *w/cm* (Verbeck 1968). Proper placement, compaction, finishing, and curing of concrete are essential to minimize the ingress and movement of water that is the carrier of the aggressive salts. Recommended procedures for these are found in ACI 304R, 302.1R, 308R, 305R, and 306R.

The sulfate resistance of portland cement generally decreases with an increase in its calculated tricalcium-aluminate (C₃A) content (Mather 1968). ASTM C150 permits the use of Type V sulfate-resisting cement and C₃A with a maximum limit of 5%, and Type II moderately sulfate-resisting cement and C₃A limited to 8%. There is also some evidence that the alumina in the aluminoferrite phase of portland cement can participate in sulfate attack. Therefore, ASTM C150 states that the C₄AF + 2C₃A in Type V cement should not exceed 25% unless the alternate requirement based on the use of the performance test (ASTM C452) is invoked. In the case of Type V cement, the sulfate-expansion test (ASTM C452) can be used instead of the chemical requirements (Mather 1978). The use of ASTM C1012 is discussed by Patzias (1991).

Table 6.3 provides recommendations for various degrees of potential exposure. These recommendations are designed to protect against concrete distress from sulfate from sources external to the concrete, such as adjacent soil and groundwater.

Recommendations for the maximum *w/cm* and the type of cementitious material for concrete that will be exposed to sulfates in soil or groundwater are given in Table 6.3. Both

Table 6.2—Factors influencing chemical attack on concrete

Factors that accelerate or aggravate attack	Factors that mitigate or delay attack
1. High porosity due to: i. High water absorption ii. Permeability iii. Voids	1. Dense concrete achieved by: i. Proper mixture proportioning* ii. Reduced unit water content iii. Increased cementitious material content iv. Air entrainment v. Adequate consolidation vi. Effective curing†
2. Cracks and separations due to: i. Stress concentrations ii. Thermal shock	2. Reduced tensile stress in concrete by:‡ i. Using tensile reinforcement of adequate size, correctly located ii. Inclusion of pozzolan (to reduce temperature rise) iii. Provision of adequate contraction joints
3. Leaching and liquid penetration due to: i. Flowing liquid§ ii. Ponding iii. Hydraulic pressure	3. Structural design: i. To minimize areas of contact and turbulence ii. Provision of membranes and protective-barrier system(s)¶ to reduce penetration

*The mixture proportions and the initial mixing and processing of fresh concrete determine its homogeneity and density.

†Poor curing procedures result in flaws and cracks.

‡Resistance to cracking depends on strength and strain capacity.

§Movement of water-carrying deleterious substances increases reactions that depend on both the quantity and velocity of flow.

¶Concrete that will be frequently exposed to chemicals known to produce rapid deterioration should be protected with a chemically resistant protective-barrier system.

of these recommendations are important. Limiting only the type of cementitious material is not adequate for satisfactory resistance to sulfate attack (Kalousek et al. 1976).

The field conditions of concrete exposed to sulfate are numerous and variable. The aggressiveness of the conditions depends on soil saturation, water movement, ambient temperature and humidity, concentration of sulfate, and type of sulfate or combination of sulfates involved. Depending on the aforementioned variables, solutions containing calcium sulfate are generally less aggressive than solutions of sodium sulfate, which is generally less aggressive than magnesium sulfate. Table 6.3 provides criteria that should maximize the service life of concrete subjected to the more aggressive exposure conditions.

Table 6.3—Requirements to protect against damage to concrete by sulfate attack from external sources of sulfate

Severity of potential exposure	Water-soluble sulfate (SO ₄) in soil, % by mass*	Sulfate (SO ₄) [†] in water, ppm	w/cm by mass, max. [‡]	Cementitious material requirements
Class 0 exposure	0.00 to 0.10	0 to 150	No special requirements for sulfate resistance	No special requirements for sulfate resistance
Class 1 exposure	> 0.10 and < 0.20	> 150 and < 1500	0.50 [‡]	C150 Type II or equivalent [§]
Class 2 exposure	0.20 to < 2.0	1500 to < 10,000	0.45 [‡]	C150 Type V or equivalent [§]
Class 3 exposure	2.0 or greater	10,000 or greater	0.40 [‡]	C150 Type V plus pozzolan or slag [§]
Seawater exposure	—	—	See Section 6.4	See Section 6.4

*Sulfate expressed as SO₄ is related to sulfate expressed as SO₃, as given in reports of chemical analysis of portland cements as follows: SO₃% × 1.2 = SO₄%.
[†]ACI 318, Chapter 4, includes requirements for special exposure conditions such as steel-reinforced concrete that may be exposed to chlorides. For concrete likely to be subjected to these exposure conditions, the maximum w/cm should be that specified in ACI 318, Chapter 4, if it is lower than that stated in Table 6.3 of 201.2R.
[‡]Values applicable to normalweight concrete. They are also applicable to structural lightweight concrete except that the maximum w/cm ratios 0.50, 0.45, and 0.40 should be replaced by specified 28-day compressive strengths of 26, 29, and 33 MPa (3750, 4250, and 4750 psi), respectively.
[§]For Class 1 exposure, equivalents are described in Sections 6.2.5, 6.2.6, and 6.2.9. For Class 2 exposure, equivalents are described in Sections 6.2.5, 6.2.7, and 6.2.9. For Class 3 exposure, pozzolan and slag recommendations are described in Sections 6.2.5, 6.2.8, and 6.2.9.

Portland-cement concrete can be also be attacked by acidic solutions, such as sulfuric acid. Information on acid attack is provided in Section 6.5.

6.2.4 Sampling and testing to determine potential sulfate exposure—To assess the severity of the potential exposure of concrete to detrimental amounts of sulfate, representative samples should be taken of water that might reach the concrete or of soil that might be leached by water moving to the concrete. A procedure for making a water extract of soil samples for sulfate analysis is given in Appendix A. The extract should be analyzed for sulfate by a method suitable to the concentration of sulfate in the extract solution, such as the photometer methods used in ASTM C1580. If the amount of sulfate determined in the first analysis is outside of the optimum concentration range for the analytical procedure used, the extract solution should be either concentrated or diluted to bring the sulfate content within the range appropriate to the analytical method, and the analysis should be repeated on the modified extract solution.

6.2.5 Material qualification of pozzolans and slag for sulfate-resistance enhancement—Tests 1 year in duration are necessary to establish the ability of pozzolans and slag to enhance sulfate resistance. Once this material property has been established for specific materials, proposed mixtures using them can be evaluated for Class 1 and 2 exposures using the 6-month criteria in Sections 6.2.6 and 6.2.7.

Fly ashes, natural pozzolans, silica fumes, and slags may be qualified for sulfate resistance by demonstrating an expansion ≤ 0.10% in 1 year when tested individually with portland cement by ASTM C1012 in the following mixtures.

For fly ash or natural pozzolan, the portland cement portion of the test mixture should consist of cement with Bogue-calculated C₃A of not less than 7%. The fly ash or natural pozzolan proportion should be between 25 and 35% by mass, calculated as percentage by mass of the total cementitious material.

For silica fume, the portland cement portion of the test mixture should consist of a cement with Bogue-calculated C₃A of not less than 7%. The silica fume proportion should be between 7 and 15% by mass, calculated as percentage by mass of the total cementitious material.

For slag, the portland cement portion of the test mixture should consist of a cement with Bogue-calculated C₃A of not

less than 7%. The C₃A should be calculated for the sum of the portland cement plus calcium sulfate in the cement. Some processing additions, if present in sufficient proportions, can distort the calculated Bogue values. Formulas for calculating Bogue compounds may be found in ASTM C150. The slag proportion should be between 40 and 70% by mass, calculated as a percentage by mass of the total cementitious material.

Material qualification tests should be based on passing results from two samples taken at times a few weeks apart. The qualifying test data should be no older than 1 year from the date of test completion.

The reported calcium-oxide content analyzed in accordance with ASTM C114 of the fly ash used in the project should be no more than 2.0 percentage points greater than that of the fly ash used in qualifying test mixtures. The reported aluminum-oxide content analyzed in accordance with ASTM C114 of the slag used in the project should be no more than 2.0 percentage points higher than that of the slag used in qualifying test mixtures.

6.2.6 Type II equivalent for Class 1 exposure

- ASTM C150 Type III cement with the optional limit of 8% maximum C₃A; ASTM C595 Type IS(MS), Type IP(MS), Type IS-A(MS), or Type IP-A(MS); ASTM C1157 Type MS; or
- Any blend of portland cement of any type meeting ASTM C150 or C1157 with fly ash or natural pozzolan meeting ASTM C618, silica fume meeting ASTM C1240, or slag meeting ASTM C989 that meets the following requirement when tested in accordance with ASTM C1012:

Expansion ≤ 0.10% at 6 months

Any fly ash, natural pozzolan, silica fume, or slag used should be previously qualified in accordance with Section 6.2.5.

6.2.7 Type V equivalent for Class 2 exposure

- ASTM C150 Type III cement with the optional limit of 5% maximum C₃A or ASTM C150 cement of any type having expansion at 14 days no greater than 0.040% when tested by ASTM C452 or ASTM C1157 Type HS; or
- Any blend of portland cement of any type meeting



**Exhibit 56: Structural and Thermal
Analysis Investigation**



Exhibit 56 [REDACTED] – Summary Final Report – Revision dated 24 Feb 2012

1.0 Duties and Responsibilities

This report summarizes the activity of [REDACTED] related to the structural and thermal analysis investigation work performed at the Davis-Besse nuclear power plant.

1.1 3D Nastran [REDACTED] FEM

Primary responsibility is the development of 3D Nastran [REDACTED] Finite Element Models (FEM's) for use in computing thermal transient temperature distributions due to various environmental conditions. These 3D [REDACTED] FEM's include pressure loading that result from wind loading due to Tornados and other Wind conditions during the winter and summer cases. [REDACTED]



The 3D Nastran [REDACTED] FEM is used in the thermal transient heat transfer analysis performed to compute solar heating/cooling for the following environmental conditions:

- ✓ Summer Solstice (Hot w/o Wind, Hot w/34 mph Wind & Ave w/o Wind)
- ✓ Autumn Equinox (“ “ “ “ “ “ “ “ “ “ “)
- ✓ Winter Solstice (Ave w/o Wind)
- ✓ 1978 Blizzard (w/105 mph Wind)
- ✓ Vernal Equinox (Ave w/o Wind, Ave w/36 mph Wind)

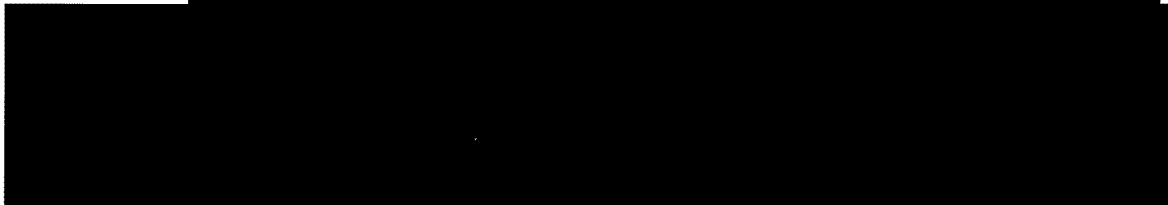
Note: The initial series of analysis showed Vernal Equinox conditions were not critical.

The 3D Nastran [REDACTED] FEM's were also used to provide approximations for stresses & deflections throughout the Davis-Besse Shield Building due to combined loading effects of wind, thermal transients and gravity. [REDACTED]



1.2 Nastran 2-D Plane-Strain [REDACTED] Idealizations

During the course of these investigations, several hundred individual time slices were processed and evaluated. [REDACTED]





2.0 Nastran Finite Element Model Definitions

The analysis code used for the transient thermal and structural analysis is MD/Nastran 2010 v1.3. MD Nastran is a general purpose finite element program for performing linear, nonlinear structural analysis, vibration, dynamics and thermal analysis.

2.1 3D [REDACTED] Finite Element Model

Figure 2.1.1 shows an isometric view of the 3D Nastran [REDACTED] idealization. Key point details of the development and definition for the 3D Nastran Thermal Transient and Structural FEM are the following:

- ✓ The 3D Nastran [REDACTED] models idealize the entire Shield Building [REDACTED]. The Nastran 360° 3D [REDACTED] idealization was developed primarily for efficient use in the thermal transient temperature analysis. [REDACTED]
- ✓ Element size through the 30" concrete wall [REDACTED]. The total number of elements and node comprising the Nastran 3D [REDACTED] model are [REDACTED] elements and [REDACTED] nodes. The total number of degrees of freedom [REDACTED] DOF's.
- ✓ The reference drawings used to develop the Nastran 3D [REDACTED] FEM are Dwg. No. C-100, C-104 & C-109
- ✓ The overall region idealized is from EL 567' 6" [base truncation level] to the top of the Dome EL 824' 3 1/2". The inside radius RIF = 69'6" and outside radius ROF = 72' [vertical wall thickness = 2' 6"]. The Dome wall thickness = 2'.
- ✓ Concrete Reinforcement [REDACTED].
- ✓ The steel reinforcement is [REDACTED]. Figure 2.1.3 illustrates the steel reinforcement [REDACTED] at a typical section cut.
- ✓ [REDACTED] Nastran [REDACTED] models idealize hoop and vertical reinforcement [REDACTED].
- ✓ For the Dome region, OF and IF rebar is idealized [REDACTED].

The 3D Nastran [REDACTED] FEM secondary use is also used to provide a cross check validation of results from other analysis models. [REDACTED] 3D Nastran [REDACTED] FEM is configured for use [REDACTED].

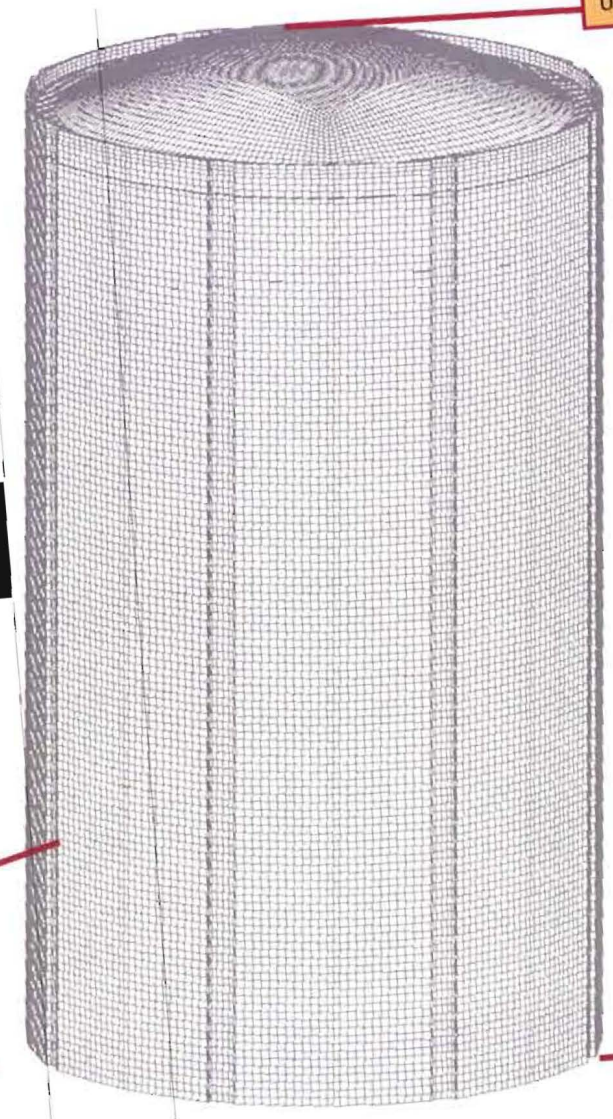
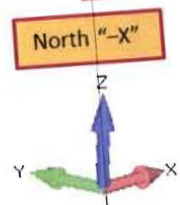
The 3D Nastran thermal transient & structural model is [REDACTED].



- ✓ The 3D Nastran [Redacted] models idealize the entire containment concrete building [Redacted]
- ✓ The overall region idealized is from EL 567' 6" [base truncation level] to the top of the Dome EL 824' 3 1/2".
- ✓ The inside radius $R_{IF} = 69' 6"$ and outside radius $R_{OF} = 72'$ [vertical wall thickness = 2' 6"]. The Dome wall thickness = 2'.
- ✓ Concrete Reinforcement [Redacted]

3D [Redacted] Idealization : Key Envelope Dimensions

- a.) Net height of the Vertical Walls = 242' (EL 567' 6" to EL 809' 6")
- b.) Net height to the top of Dome = 256' 9-1/2" (EL 567' 6" to EL 834' 3-1/2")
- c.) Inside Diameter of Vertical Walls = 139' ($R_i = 69' 6"$)
- d.) Vertical Wall Thickness = 2' 6" [o.d. = 144' or $R_o = 72'$]



Upper EL 824' 3 1/2"

Base EL 567' 6" Truncation Level

Figure 2.1.1
3D Nastran [Redacted] Model Idealization



✓ The 3D Nastran models

✓ For the Dome region OF and IF

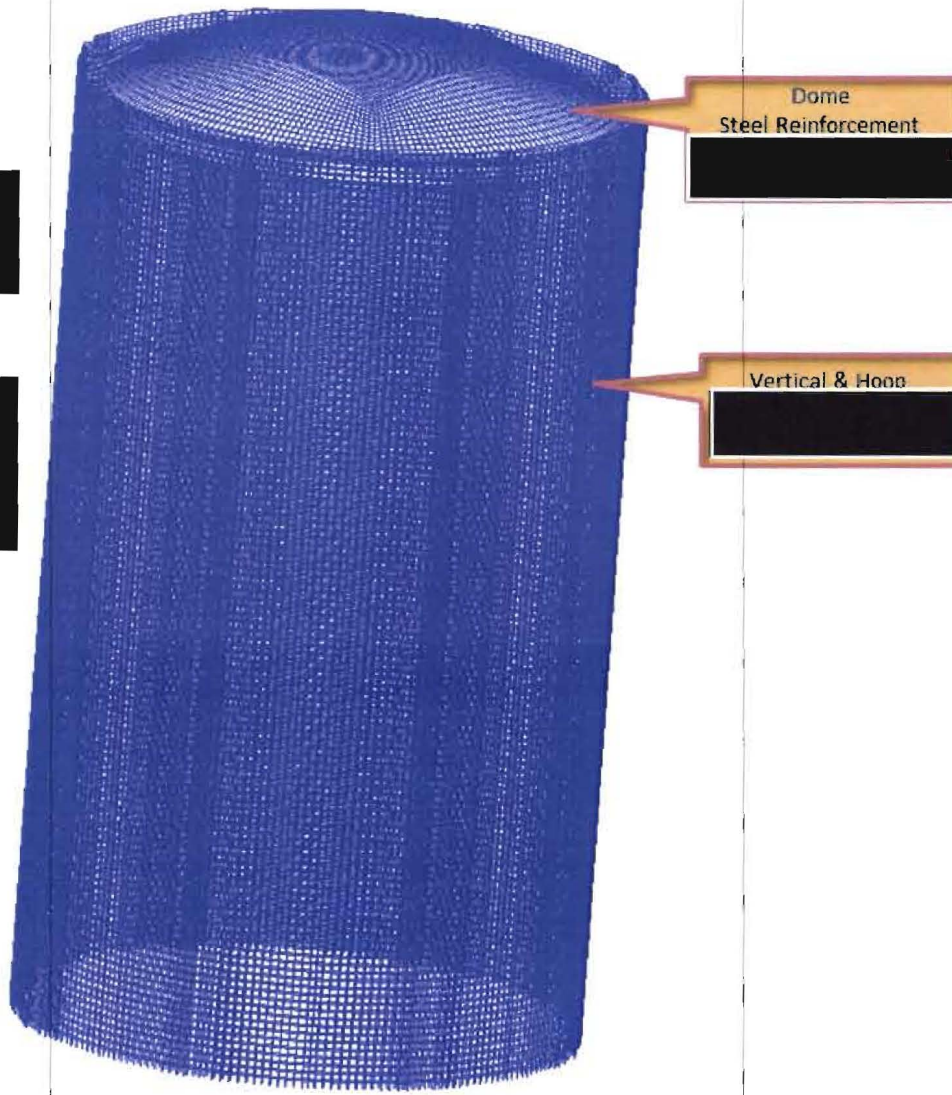


Figure 2.1.2
3D Nastran Model: Steel Reinforcement

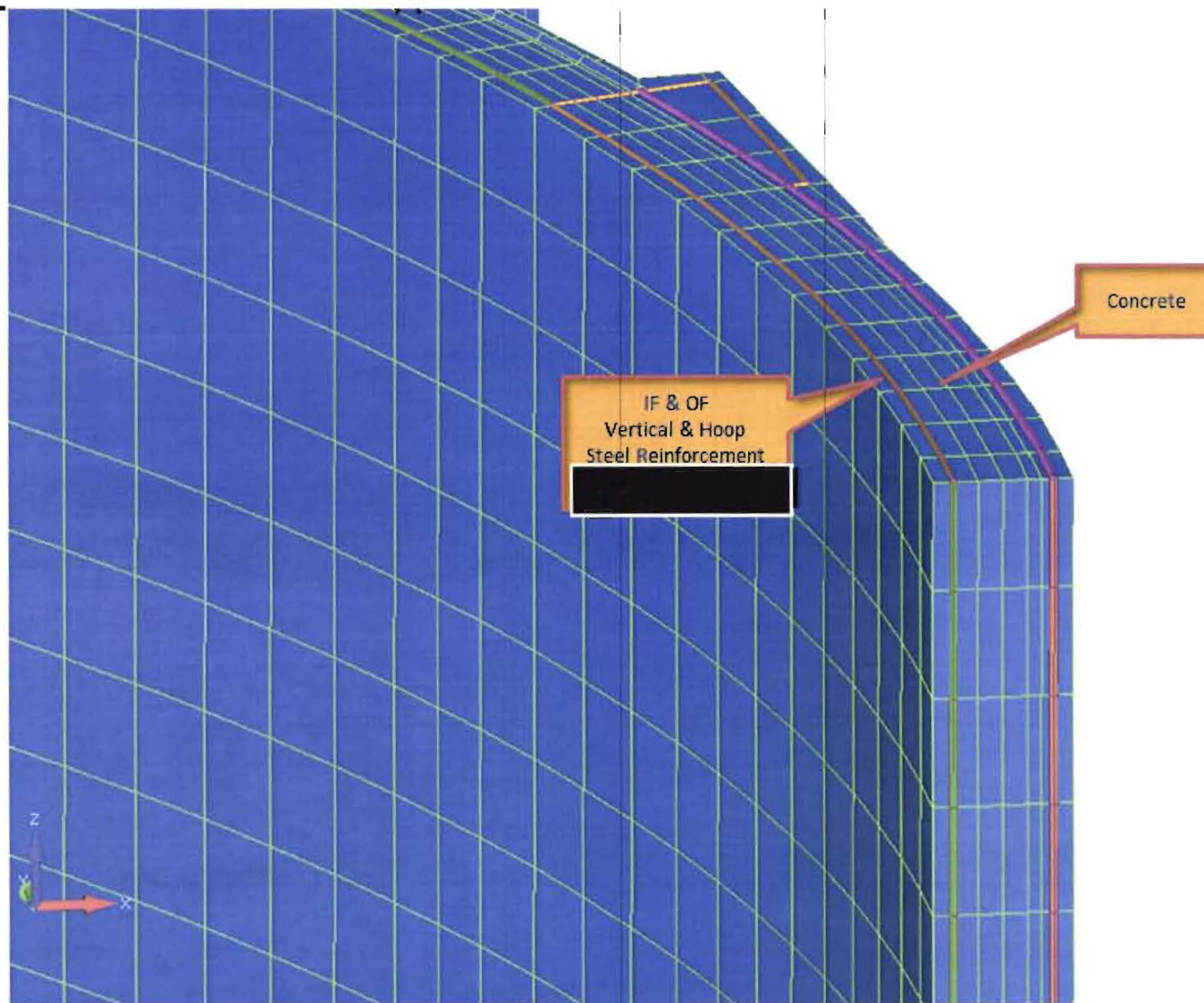


Figure 2.1.3
3D Nastran [REDACTED] Model: Typical Section Cut



Material Properties for Davis-Besse Overall ██████████ Finite Element Model [FEM] Idealizations

Revised 17 Jan 2012

USBR Test Values per e-mail memorandum 11 January 2012

Temperature (°F)	Thermal Properties					Mechanical Properties			Failure Criteria	
	29-Nov-11 Density, w (lb/in ³)	11-Jan-12 Conductivity, k (Btu/hr-in ² -°F)	11-Jan-12 Diffusivity, α (in ² /hr)	11-Jan-12 Specific Heat, c_p (Btu/lb-°F ²⁴)	(1) Emissivity, ϵ	11-Jan-12 Thermal Expansion, γ (in/in/°F (x10 ⁻⁶))	9-Dec-11 Young's Modulus, E_s (lbs/in ² (x10 ⁶))	29-Nov-11 Poisson's Ratio, ν ⁽³⁾	12-Jan-12 Failure Stress, f_t (lbs/in ²)	12-Jan-12 Fracture Energy, G_f (lbs/in)
≤ 50	0.0868	0.308	7.632	0.478	0.93	5.20	4.94	0.20	600	0.54
100	"	0.243	6.624	0.428	"	"	"	"	"	"
≥ 150	"	0.185	5.760	0.378	"	"	"	"	"	"



Generic Steel - Rebar & Inner Steel Containment

Eckert & Drake, "Heat & Mass Transfer"

Temperature (°F)	Thermal Properties					Mechanical Properties		
	Density, w (lb/in ³)	Conductivity, k (Btu/hr-in ² -°F)	Diffusivity, α (in ² /hr)	Specific Heat, c_p (Btu/lb-°F ²⁴)	(1) Emissivity, ϵ	(1) Thermal Expansion (in/in/°F (x10 ⁻⁶))	Young's Modulus, E (lbs/in ² (x10 ⁶))	Poisson's Ratio, ν
80	0.282	2.670	86.074	0.110	0.25	6.80	29.00	0.30

$\alpha = k/(w \cdot c_p)$

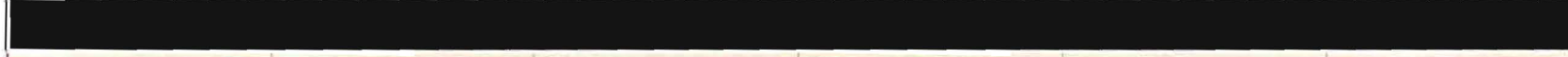
(2) Assumed LCS

(3) Legacy CR3

Table 1. Concrete & Steel



Notes on Radiation used on Transient Thermal Analysis



Note: Material property values for submodels representative of specific regions may reflect localized measurements.

Figure 2.1.4
Material Properties for Davis-Besse 3D Nastran ██████████ Model



2.2 Nastran 2D Plane-Strain Utility Idealization



Figure 2.2.1 shows an overall isometric view of the complete 2D Nastran plane-strain [REDACTED] idealization and a close-up view of the rebar and concrete mesh details. Key point details of the development and definition for the 2D Nastran plane-strain FEM are the following:

- ✓ The 2D Nastran plane-strain models idealize a section cut through the Shield Building at EL 683' 6".
- ✓ The total number of elements and node comprising the Nastran 2D plane-strain model are [REDACTED] elements and [REDACTED] nodes.
- ✓ The total number of degrees of freedom [REDACTED] DOFs.
- ✓ The reference drawings used to develop the Nastran 2D plane-strain [REDACTED] Dwg. No. C-110
- ✓ The overall region idealized is at EL 683' 6" This elevation is defined as a reference elevations [REDACTED]. EL 683' 6" is along the vertical walls approximately half-way between EL 567' 6" [base truncation level] to just under the ring girder EL 801' 6-1/2".
- ✓ The steel reinforcement [REDACTED]

The 2D Nastran plane-strain structural model is also used [REDACTED]

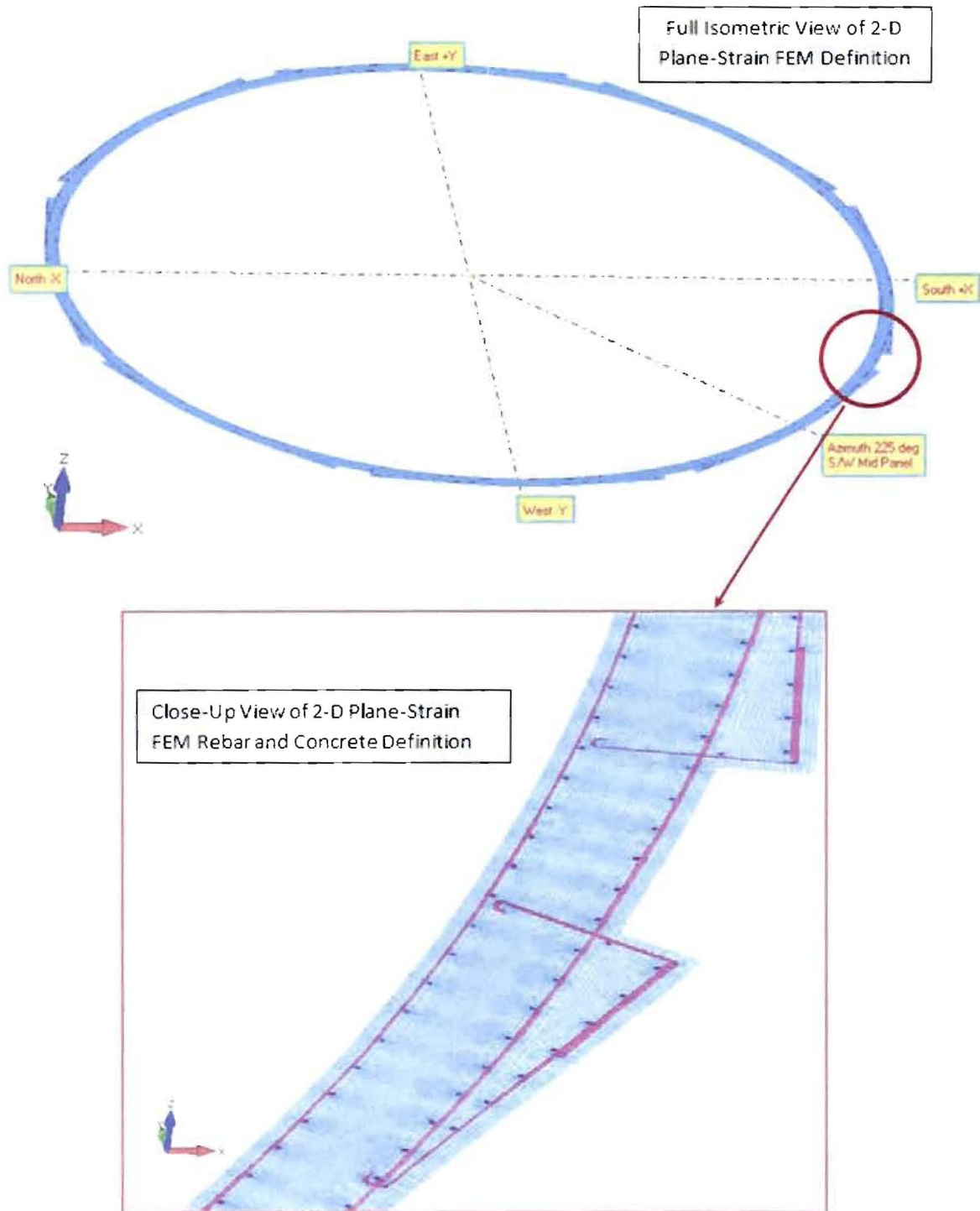


Figure 2.2.1
2D Nastran Plane-Strain [REDACTED]



3.0 Step-by-Step Analysis Process

[REDACTED]

[REDACTED]

[REDACTED]

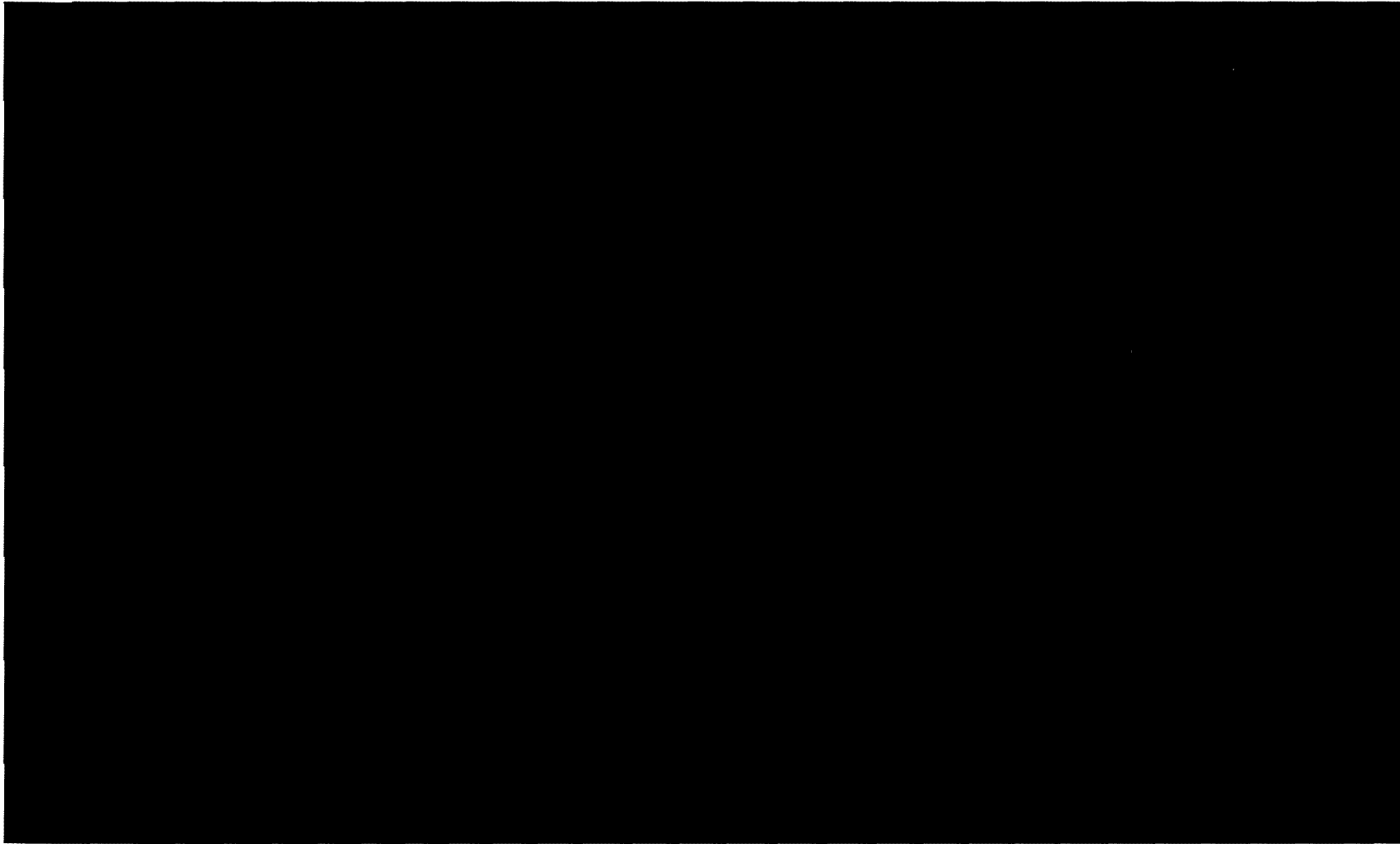


Figure 3.0.1
Schematic Flow Chart Representation of “*Step-by-Step*” Analysis



3.1 Typical Output Results 2D Plane-Strain Utility Model

The plane-strain idealization for the full 360° Shield Building wall was [REDACTED]. Transient thermal temperatures due to the environmental conditions: Summer Solstice, Autumn Equinox, Winter Solstice and 1978 Blizzard conditions [REDACTED].

Figures 3.1.1 and 3.1.2 show examples of output results [REDACTED]. These summary plots show the distribution of maximum principal and radial stresses for the peak summer solstice condition at 7:30 pm; respectively.

In these figures the S-W facing Flutes are showing the highest magnitude of maximum principal and radial stresses. The peak stress results occur at the outer rebar regions due to SCF effects where the overlapping rebar ends in the thick portion of the Flute.

Radial stresses are plotted for each of the selected time slices as the sun traverses the sky during the 24 hour period beginning.

One of the key aspects of this 2D plane-strain [REDACTED] is that all of the action is in the thick portion of the Flutes with peripheral, secondary action along the rebar at the OF.

The magnitude of radial stresses reach peak values at the outer rebar regions [REDACTED].

One of the key aspects of this study is that all of the action is in the thick portion of the Flutes with peripheral, secondary action along the rebar at the OF

Figure 3.1.3 shows summary peak radial stresses during the 24 hour period for the environmental conditions listed above. From Figure 3.1.3 the time slices producing the highest radial stresses [REDACTED].

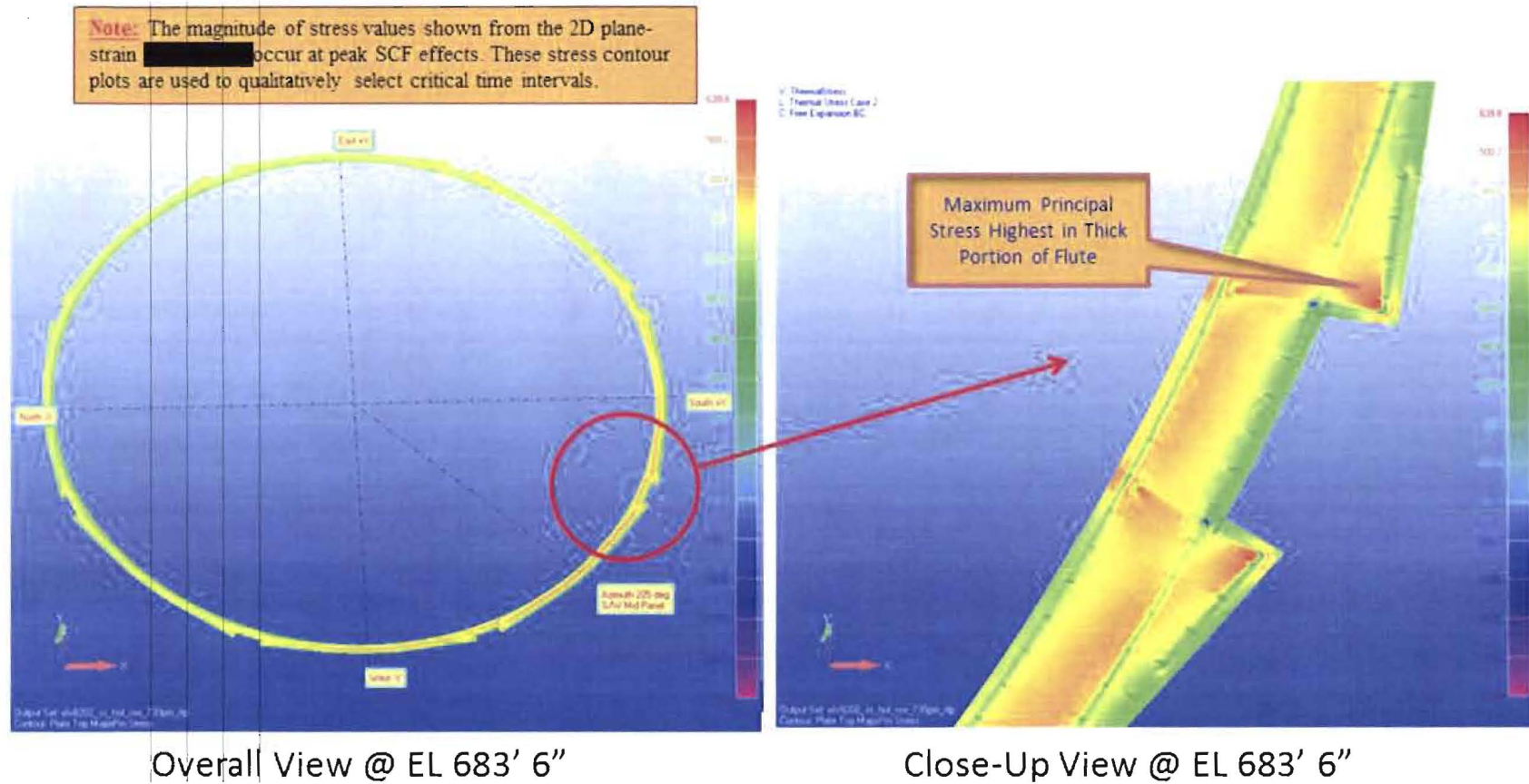


Figure 3.1.1

Summer Solstice Hot No Wind 7:30 pm, *Constant* Concrete CTE = 5.20×10^{-6} in/in/°F
2D Plane-Strain Maximum Principal Stress Distribution

Note: The thick regions of the West and Southwest facing architectural flutes indicate the highest magnitude of maximum principal stress values resulting from the summer solstice conditions.

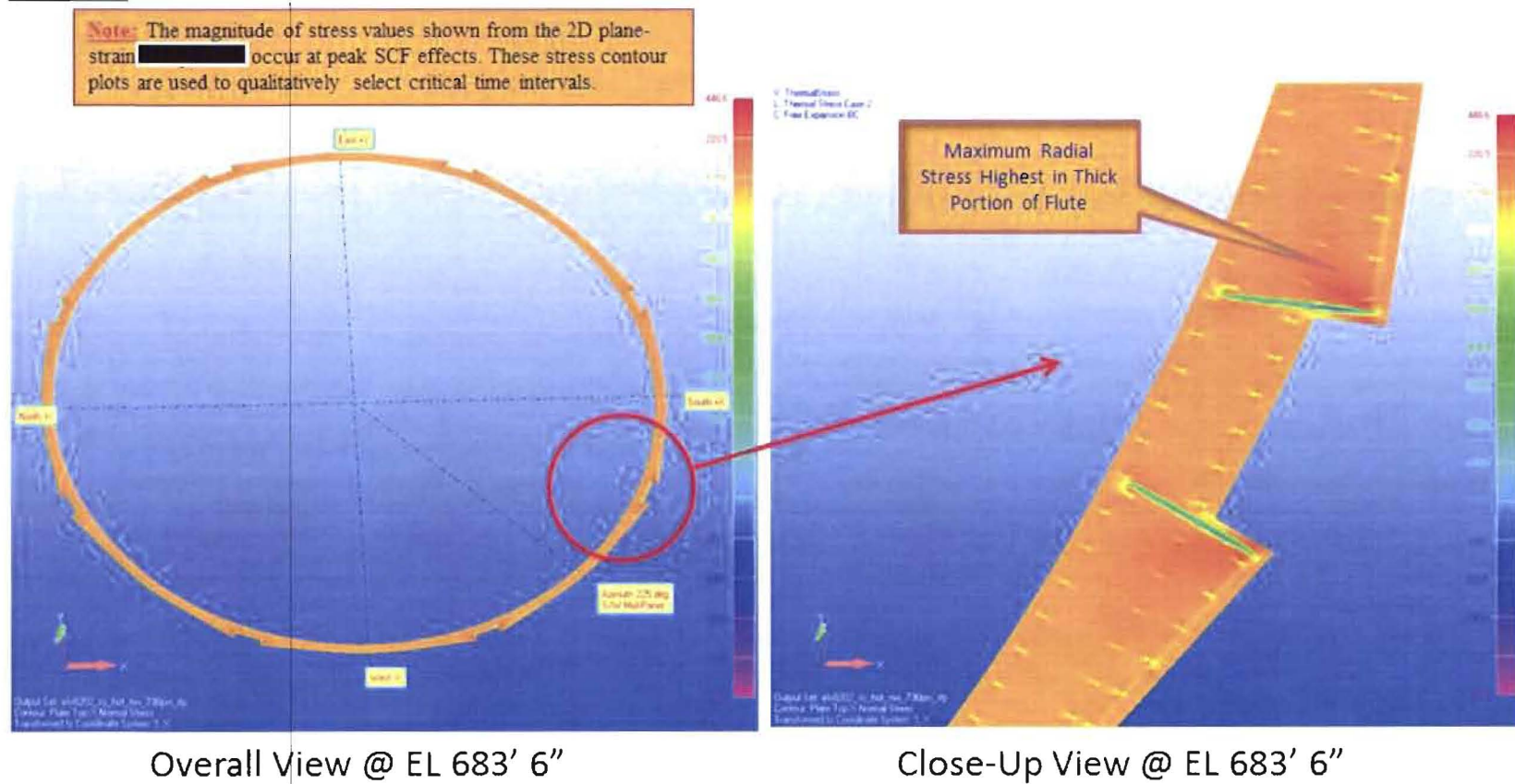


Figure 3.1.2
Summer Solstice Hot No Wind 7:30 pm, *Constant* Concrete CTE = 5.20×10^{-6} in/in/ $^{\circ}$ F
2D Plane-Strain Radial Stress Distribution

Note: The thick regions of the West and Southwest facing architectural flutes indicate the highest magnitude of maximum principal stress values resulting from the summer solstice conditions.

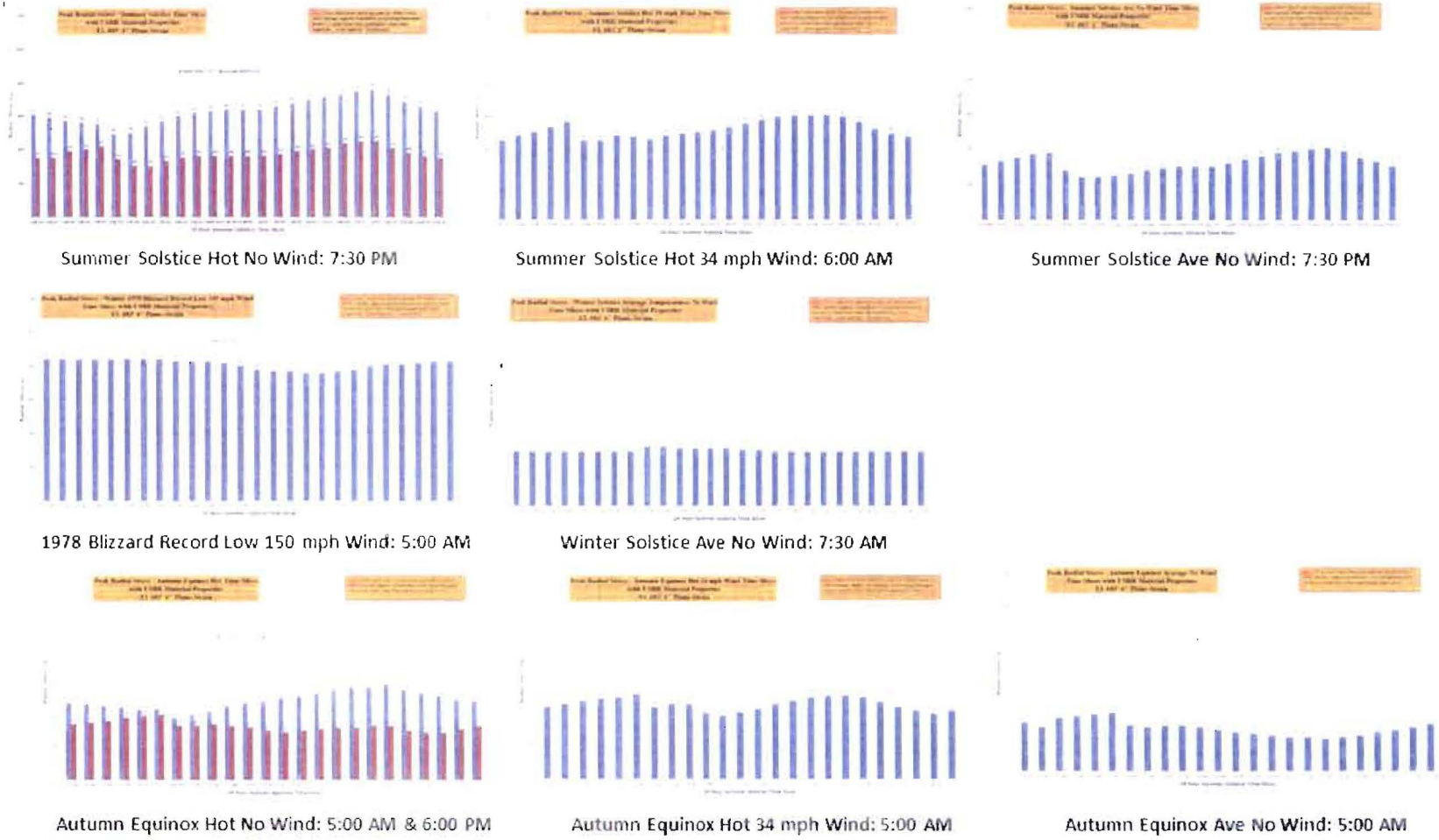


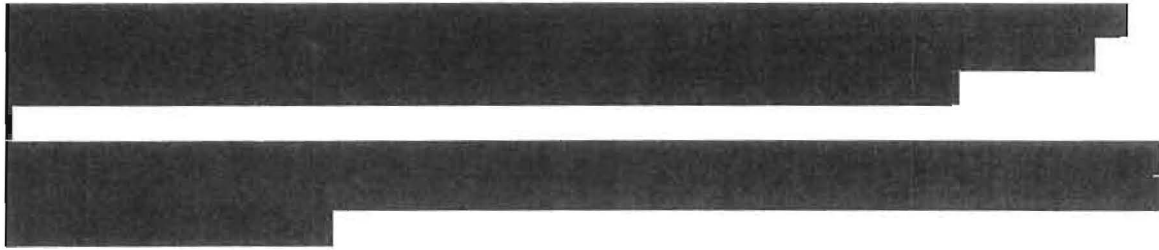
Figure 3.1.3

Survey Radial Stress Results; Nastran 2D Plane-Strain FEM; Heat Transfer Analysis; 24/1 Hour Time [192 - 1 hour Time Slices]

Note: [Redacted]



3.2 Typical Output Results 3D [REDACTED] FEM



Figures 3.2.1 and 3.2.2 show examples of output results from the mapped thermal transient thermal stress analyses. These summary plots show the distribution of maximum principal and radial stresses for the peak summer solstice condition at 7:30 pm; respectively.

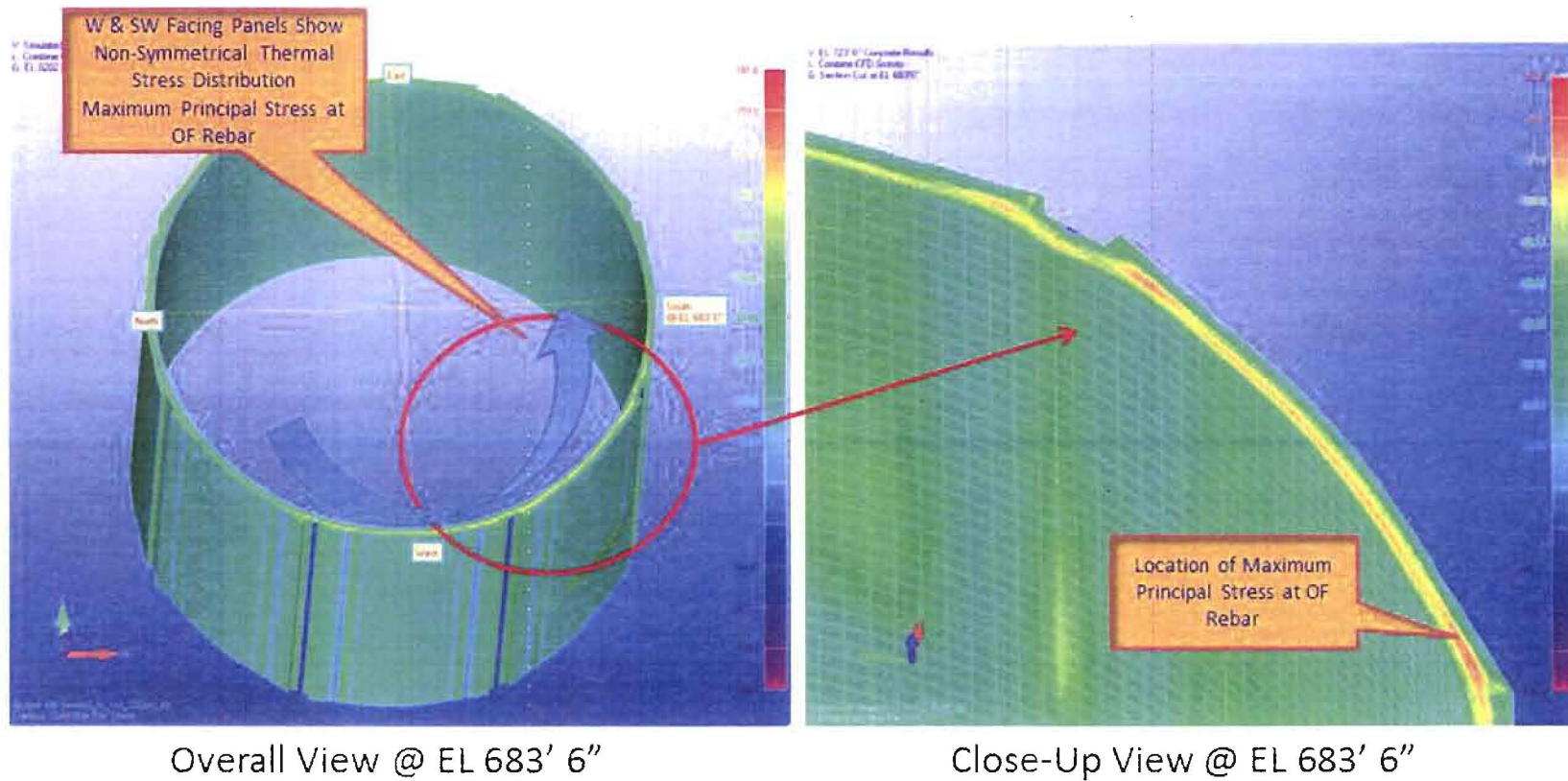
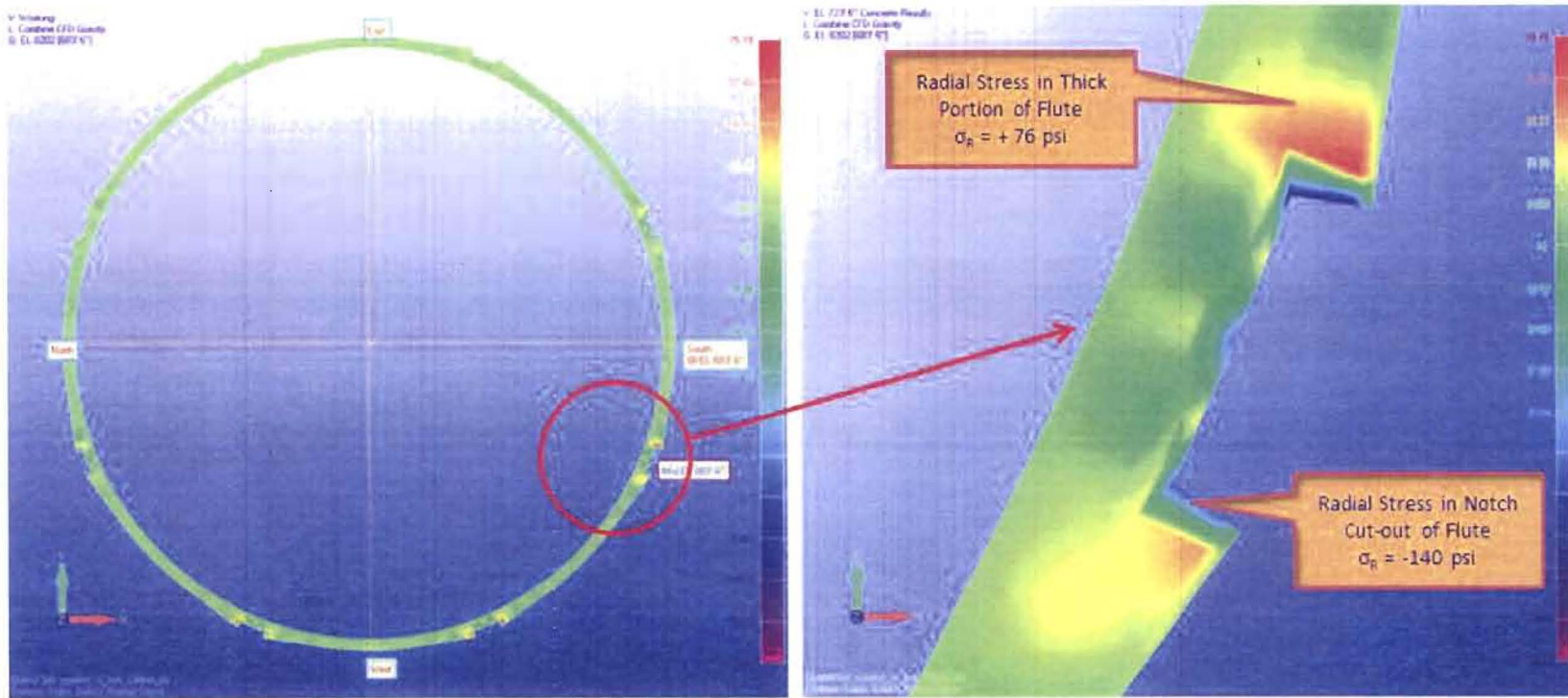


Figure 3.2.1
Summer Solstice Hot No Wind 7:30 pm, Constant Concrete CTE = 5.20×10^{-6} in/in/°F
3D [REDACTED] FEM Maximum Principal Stress Distribution

Note: Non-Symmetric Thermal Stresses Due to Uneven/Higher Heating Gradients on South Facing Panels.



Overall View @ EL 683' 6"

Close-Up View @ EL 683' 6"

Figure 3.2.2
Summer Solstice Hot No Wind 7:30 pm, Constant Concrete CTE = 5.20×10^{-6} in/in/°F
3D [REDACTED] FEM Radial Stress Distribution

Note: Non-Symmetric Thermal Stresses Due to Uneven/Higher Heating Gradients on South Facing Panels.



4.0 Summary Results and Comments

The following paragraphs list results of peak radial stresses [REDACTED]. These results are from using the 3D Nastran 3D [REDACTED] FEA model for constant coefficient of thermal expansion (CTE) thermal stress analysis.

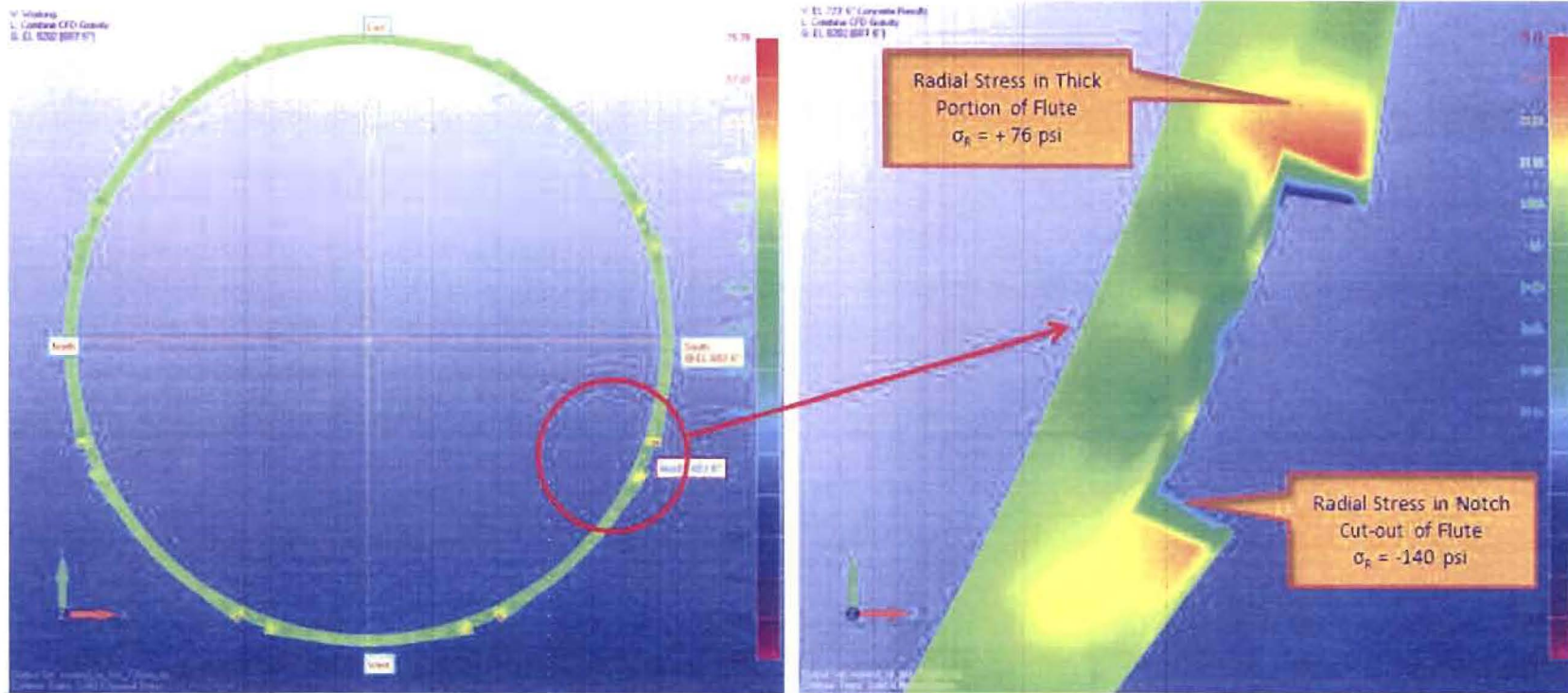
4.1 Summer Solstice Conditions

Table 4.1 summarizes results from the Summer Solstice conditions. These results correlate with the hot daytime peak temperatures that occurred during the period from 1959 to 2004 in the Toledo, OH area. The “No Wind” condition removes heat by convection. The hot condition uses the high temperatures measured for June of 104°F during the day 84°F at night. The average conditions used the average day temperature of 83°F and 63°F at night. For all cases gravity is also include. The contribution due to pressure loading from wind has been demonstrated to have a negligible impact on overall stress results.

ID	Case Description	2D Nastran Plane-Strain	3D Nastran [REDACTED]	FEM Peak Radial Stress	
		Time Slice Peak Stress	Thick Flute Portion	Architectural Notch	
1	Summer Solstice Hot No Wind	7:30 PM	+ 76 psi	- 140 psi	
2	Summer Solstice Hot 34 mph Wind	6:00 PM	+ 46 psi	- 68 psi	
3	Summer Solstice Ave No Wind	7:30 PM	+ 69 psi	- 126 psi	

Table 4.1
Summer Solstice - Summary Results for Radial Stress @ EL 683' 6"

Figure 4.1.1 through **Figure 4.1.3** show summary results listed in **Table 4.1** for radial stress due to thermal transients.



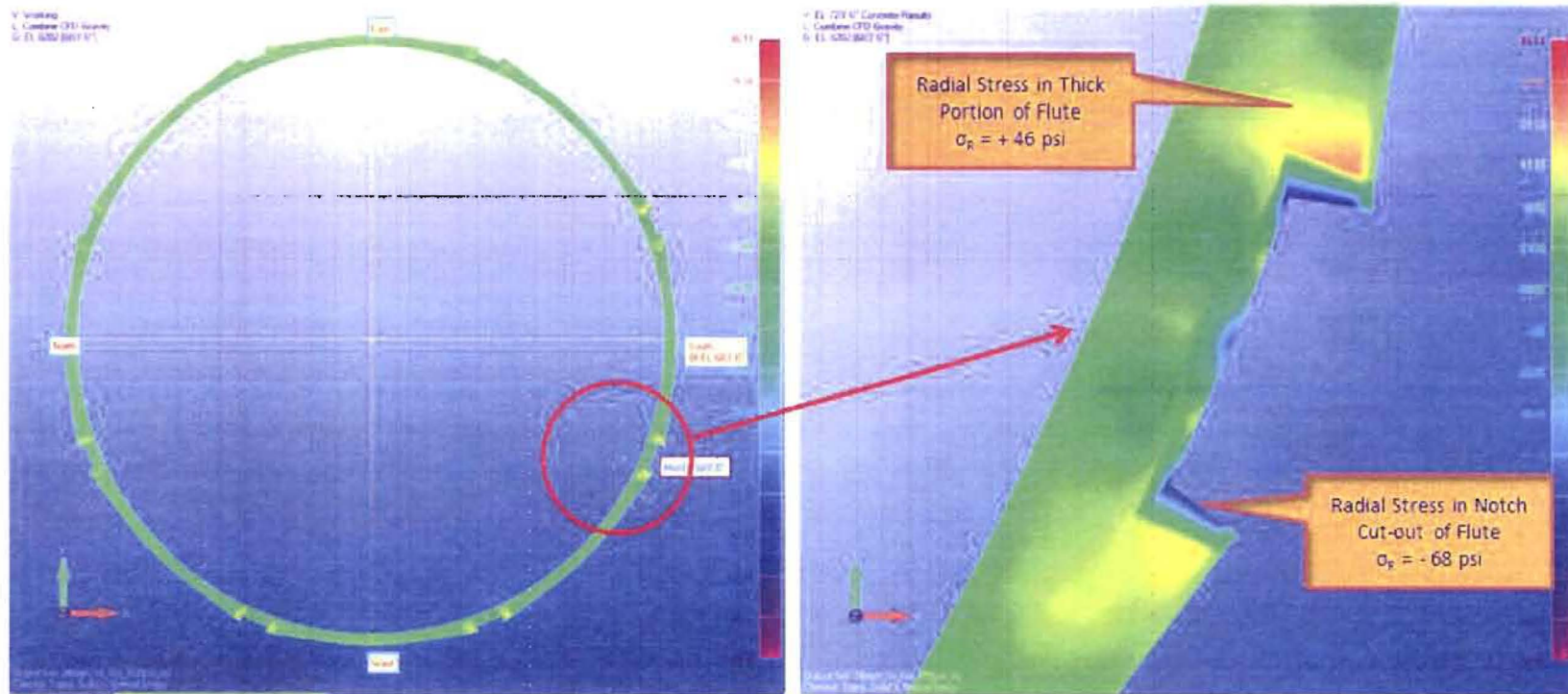
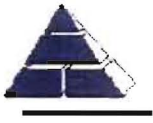
Overall View @ EL 683' 6"

Close-Up View @ EL 683' 6"

Figure 4.1.1

Summer Solstice Hot No Wind 7:30 pm, Constant Concrete CTE = 5.20×10^{-6} in/in/°F
- 3D [REDACTED] FEM Radial Stress Distribution

Note: Non-Symmetric Thermal Stresses Due to Uneven/Higher Heating Gradients on South Facing Panels.



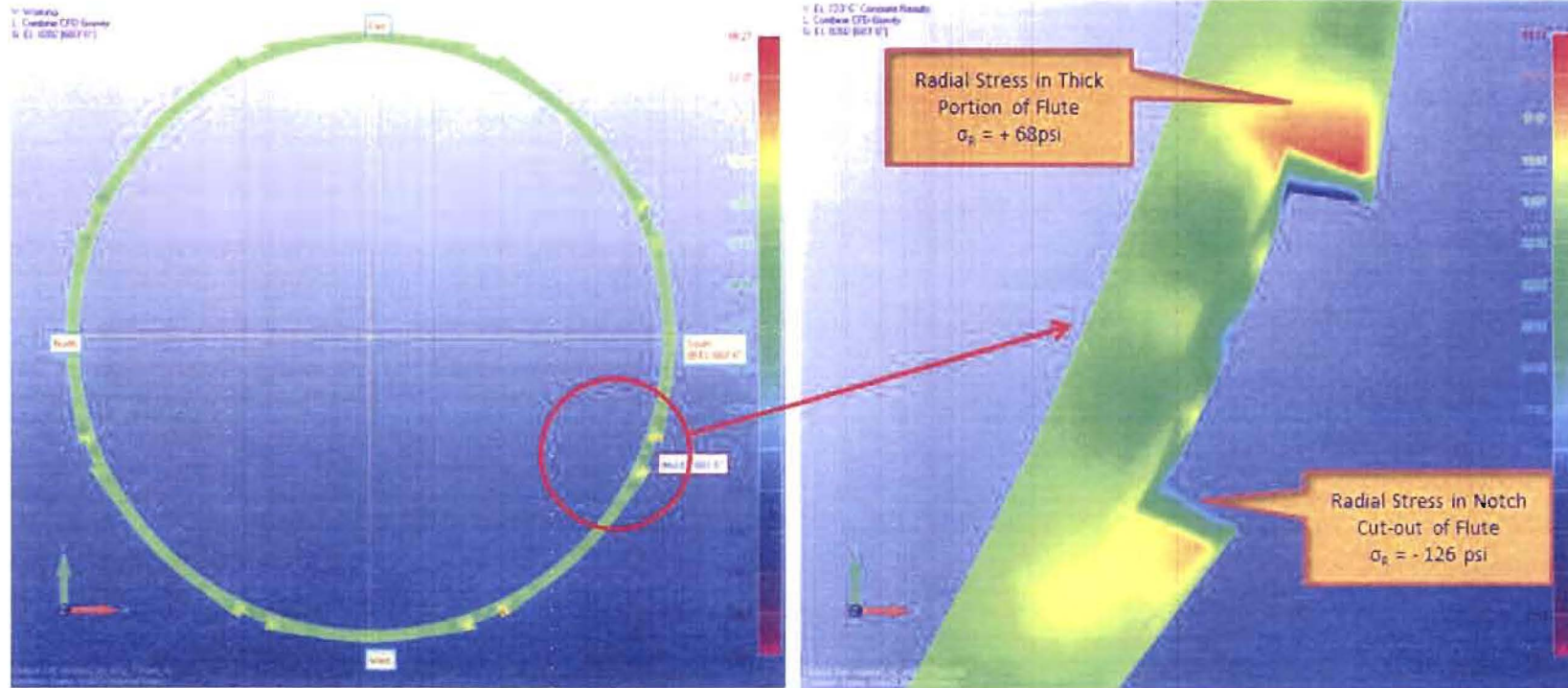
Overall View @ EL 683' 6"

Close-Up View @ EL 683' 6"

Figure 4.1.2

Summer Solstice Hot 34 mph Wind 7:30 pm, Constant Concrete CTE = 5.20×10^{-6} in/in/°F
3D [REDACTED] FEM Radial Stress Distribution

Note: Non-Symmetric Thermal Stresses Due to Uneven/Higher Heating Gradients on South Facing Panels.



Overall View @ EL 683' 6"

Close-Up View @ EL 683' 6"

Figure 4.1.3

Summer Solstice Ave No Wind 7:30 pm, *Constant* Concrete CTE = 5.20×10^{-6} in/in/°F
3D [REDACTED] FEM Radial Stress Distribution

Note: Non-Symmetric Thermal Stresses Due to Uneven/Higher Heating Gradients on South Facing Panels.



4.2 Winter Solstice & 1978 Blizzard Conditions

Table 4.2 summarizes results from the Winter Solstice and 1978 Blizzard conditions. The 1978 Blizzard computed cold temperatures correlate with the coldest daytime peak temperature of -24°F that occurred during the 1978 blizzard, 105 mph southwest wind using low ambient temperatures, 105 mph wind present, 120°F steel secondary containment wall with gravity included. [Reference Exhibit 65]

ID	Case Description	2D Nastran Plane-Strain	3D Nastran [REDACTED]	FEM Peak Radial Stress
		Time Slice Peak Stress	Thick Flute Portion	Architectural Notch
4	Winter 1978 Blizzard Record Low	5:00 AM	- 79 psi	+ 190 psi
5	Winter Solstice Ave No Wind	7:30 AM	- 20 psi	+ 53 psi

Table 4.2

Winter Solstice & 1978 Blizzard- Summary Results for Radial Stress @ EL 683' 6"

Figure 4.2.1 through **Figure 4.2.2** show summary results listed in **Table 4.2** for radial stress due to thermal transients.

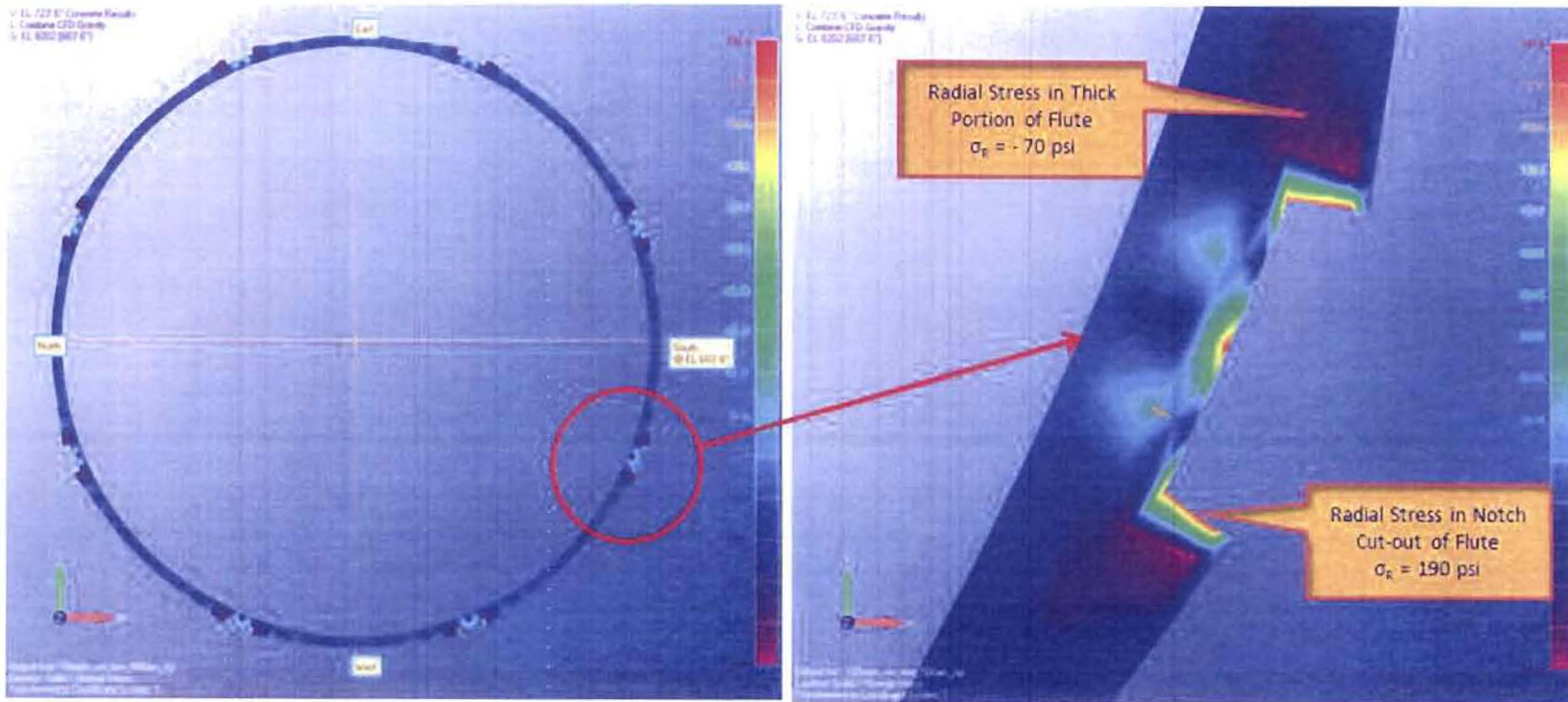
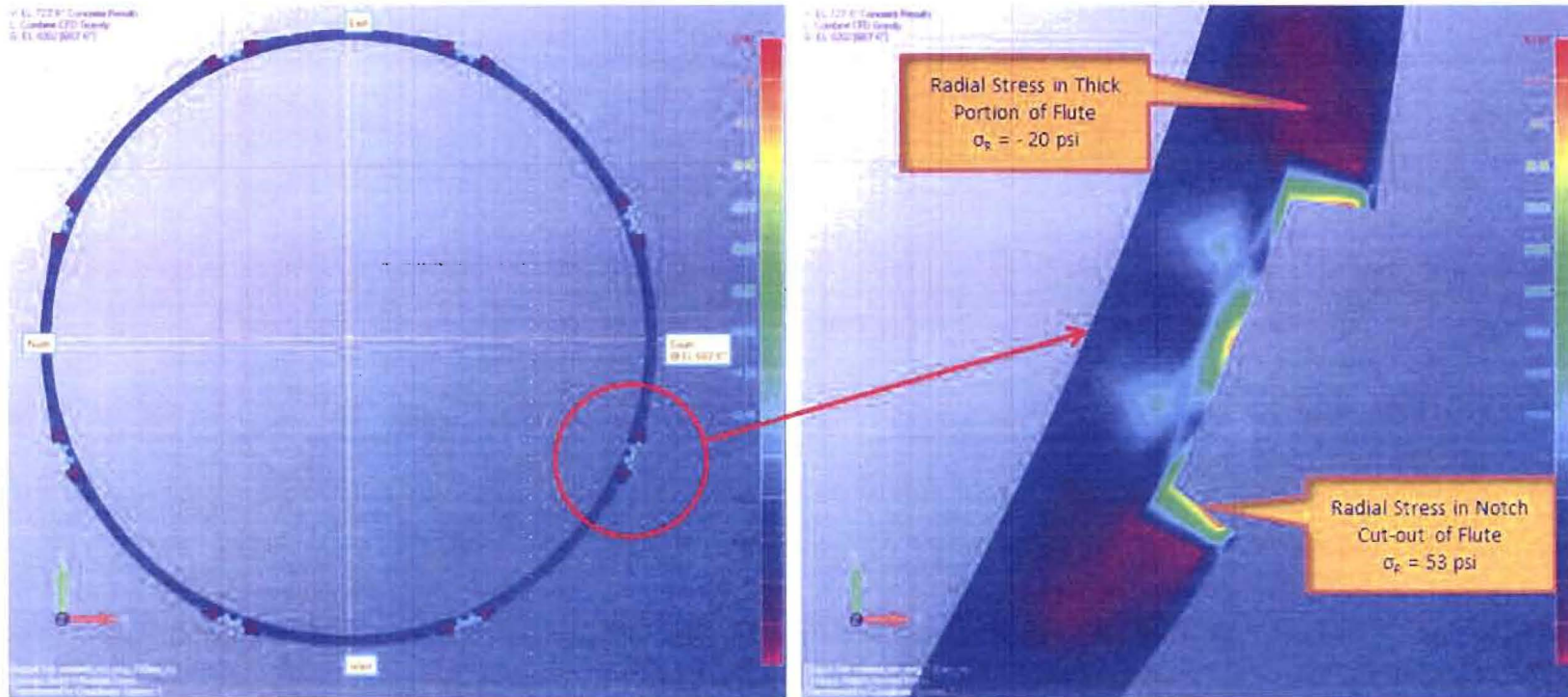
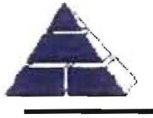


Figure 4.2.1
1978 Blizzard Condition 5:00 am, *Constant* Concrete CTE = 5.20×10^{-6} in/in/ $^{\circ}$ F
Radial Stress Distribution



Overall View @ EL 683' 6"

Close-Up View @ EL 683' 6"

Figure 4.2.2

Winter Solstice Ave Temperatures 7:30 am, Constant Concrete CTE = 5.20×10^{-6} in/in/°F
Radial Stress Distribution



4.3 Autumn Equinox Conditions

Table 4.3 summarizes results from the Autumn Equinox conditions.

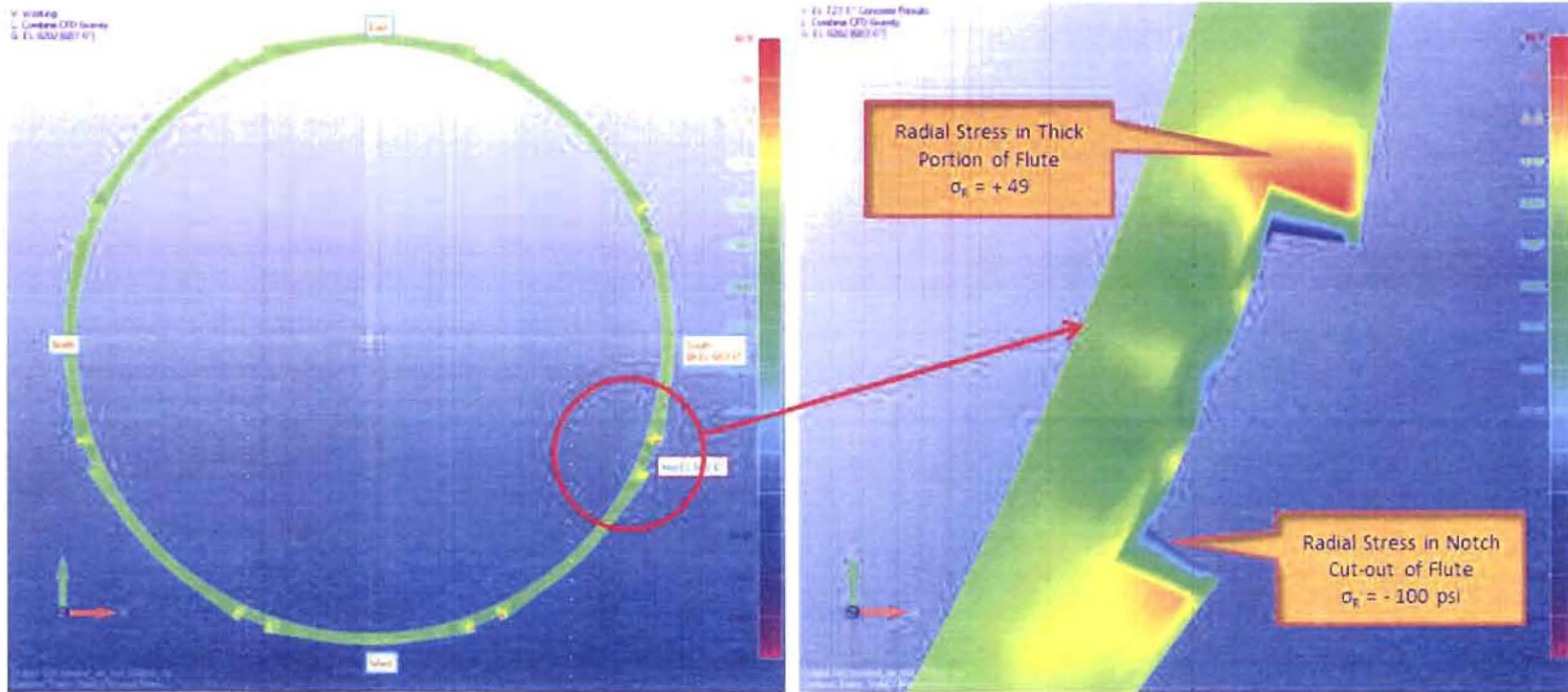
The Autumn Equinox conditions listed below correlate with the high September conditions during the 24 hour period when temperatures are at their lowest and at 3:30 pm when the temperatures on the Southwest facing panels are highest. The average and high September temperatures are computed with and without 34 mph wind condition present.

ID	Case Description	2D Nastran Plane-Strain	3D Nastran [REDACTED]	FEM Peak Radial Stress
		Time Slice Peak Stress	Thick Flute Portion	Architectural Notch
6	Autumn Equinox Hot No Wind	6:00 PM	+ 49 psi	- 100 psi
7	Autumn Equinox Hot 34mph Wind	5:00 AM	- 30 psi	+ 79 psi
8	Autumn Equinox Ave No Wind	5:00 AM	- 20 psi	+ 58 psi

Table 4.3

Autumn Equinox - Summary Results for Radial Stress @ EL 683' 6"

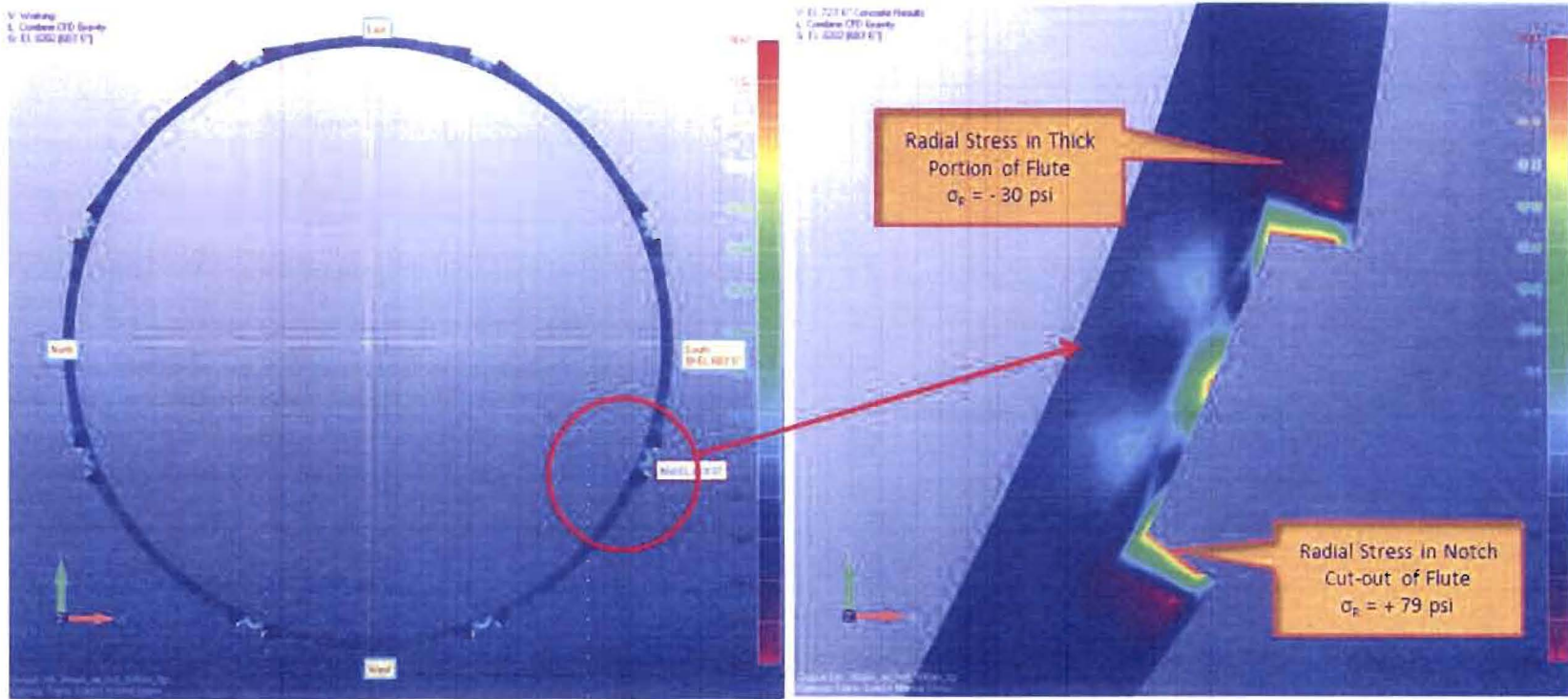
Figure 4.3.1 through **Figure 4.3.3** show summary results listed in **Table 4.3** for radial stress due to thermal transients.



Overall View @ EL 683' 6"

Close-Up View @ EL 683' 6"

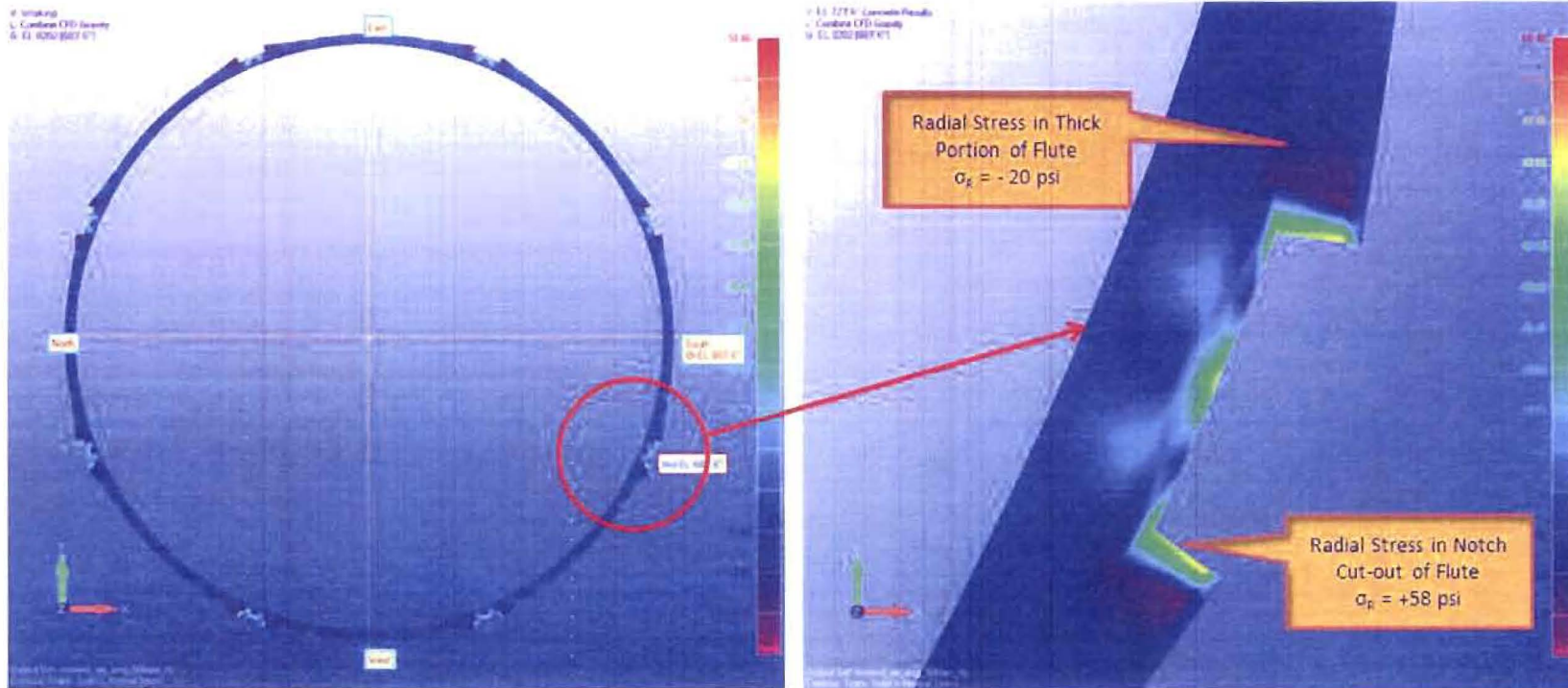
Figure 4.3.1
Autumn Equinox Hot No Wind 6:00 pm, *Constant* Concrete CTE = 5.20×10^{-6} in/in/°F
Radial Stress Distribution



Overall View @ EL 683' 6"

Close-Up View @ EL 683' 6"

Figure 4.3.2
Autumn Equinox Hot 34 mph Wind 6:00 pm, *Constant* Concrete CTE = 5.20×10^{-6} in/in/°F
Radial Stress Distribution



Overall View @ EL 683' 6''

Close-Up View @ EL 683' 6''

Figure 4.3.3
Autumn Equinox Ave No Wind 5:00 am, *Constant* Concrete CTE = 5.20×10^{-6} in/in/ $^{\circ}$ F
Radial Stress Distribution



4.4 Summary Results & Comment from 3D Nastran [REDACTED] Idealization

The 3D [REDACTED] models show that the region of highest maximum principal stress is at the outer most layers of concrete OF and inboard to the 1st rebar layer. From the OF layer of rebar inboard, maximum principal stress levels drop off dramatically due to the high stress gradients. *These results should indicate the regions of concern at the outer 2-3" of concrete*

4.4.1 Summer Solstice Cases

- The S/W facing panels and architectural flutes indicate the highest magnitudes of maximum principal and radial stress.
- It is not believed the magnitude of radial stresses is sufficient to either initiate delamination cracks or propagate any cracks that may be present.

4.4.2 Winter Solstice Cases

- For the normally occurring winter cold temperatures radial stresses in the thick portion of the architectural flutes are low or compressive.
- For the low temperatures during the 1978 Blizzard event the magnitude of radial stresses in the "notch" cut-out of the architectural flutes is approximately 190 psi.
- It is not believed the magnitude of radial stresses is sufficient to either initiate delamination cracks or propagate any cracks that may be present.

4.4.3 Autumn Equinox Cases

- The S/W facing panels and architectural flutes indicate the highest radial stress.
- It is not believed the magnitude of radial stresses is sufficient to either initiate delamination cracks or propagate any cracks that may be present.



4.5 Summary Results: 3D Nastran [REDACTED] Idealization with Simulated 30'x30' "Crack"

To investigate potential for extended crack growth in a pre-existing crack region, the 3D Nastran [REDACTED] idealization was modified to simulate a 30' x 30' "Crack"



The 30 ft x 30 ft "failed" region [REDACTED]

It is desired to evaluate [REDACTED] S/W facing flutes with and without the simulated "Crack"

As shown in **Table 4.5** the magnitude of maximum principal stresses increased a slight amount from $\sigma_{MP} = 162$ psi (No crack) to $\sigma_{MP} = 184$ psi (w/crack). there is only a marginal increase in the magnitude of radial stress, from $\sigma_R = 76$ psi (No crack) to $\sigma_R = 92$ psi (w/crack).

It is not believed that the increase magnitudes in either the radial or maximum principal stresses are sufficient to propagate cracks that may have formed.

ID	Case Description	2D Nastran Plane-Strain	3D Nastran [REDACTED]	FEM Peak Stress Values at "Crack"	
		Time Slice Peak Stress	Radial Stress	Max. Princ. Stress	
9	Summer Solstice Hot No Wind;	7:30 PM	+ 76 psi	+ 162 psi	
10	Summer Solstice Hot No Wind; Crack	7:30 PM	+ 92 psi	+ 184 psi	

Table 4.5
Summer Solstice with Simulated 30'x30' "Crack"
Summary Results for Radial Stress @ EL 785' 10"

Figure 4.5.1 through **Figure 4.5.2** show views of the 3D Nastran [REDACTED] FEM with the simulated "Crack" region.

Figure 4.5.3 shows summary stress results listed in **Table 4.5** for maximum principal stress due to summer solstice thermal transients.



- V Crack/Delamination
- L Nz 1G Gravity Load Test
- C Translations Tz Base Rotations & Corners
- G: 30x30 Crack Region, Delamination Gap Region All

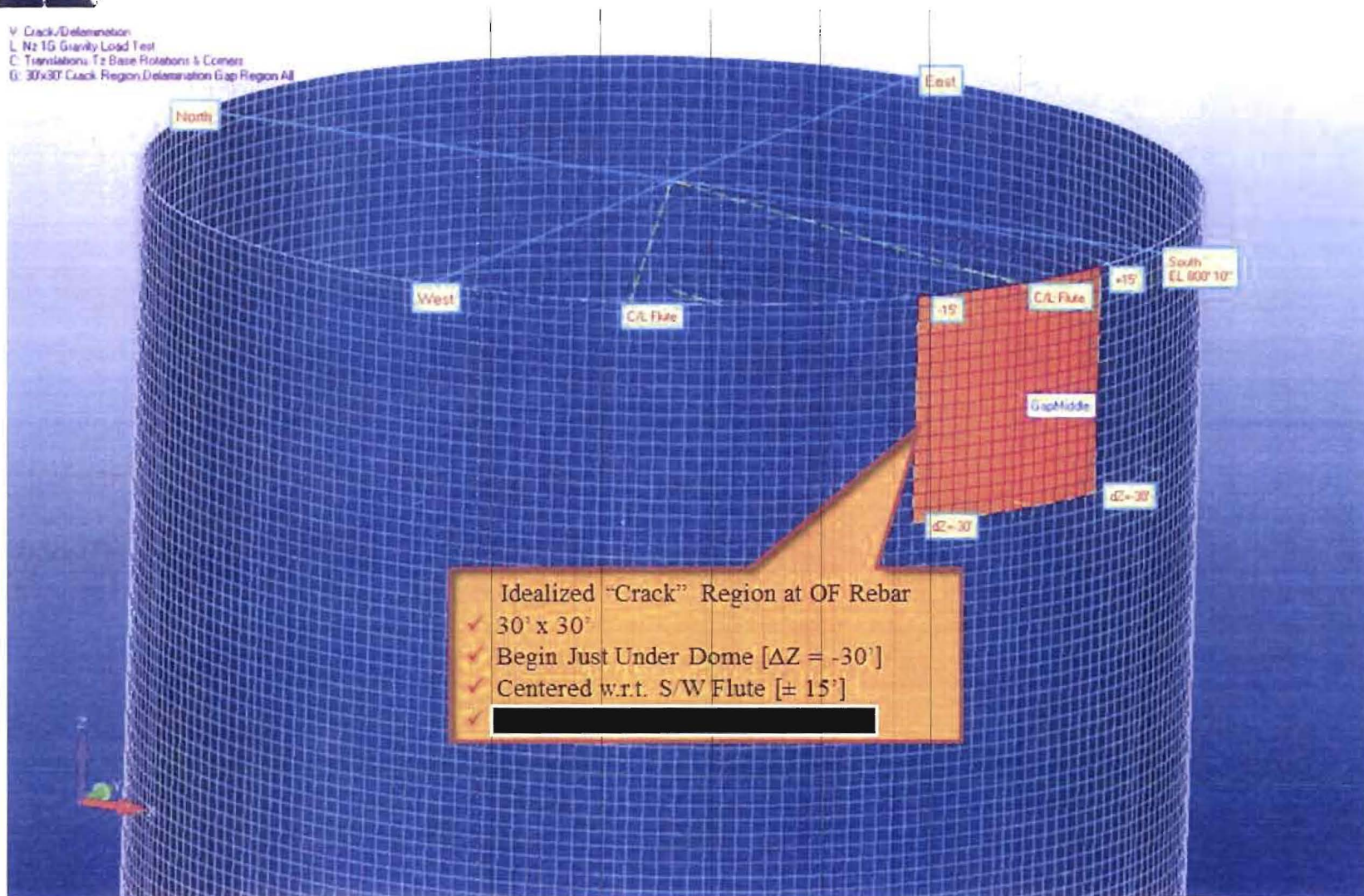


Figure 4.5.1
"Thin-Crack" region introduced as idealized the "Cracked" boundary at the OF Rebar

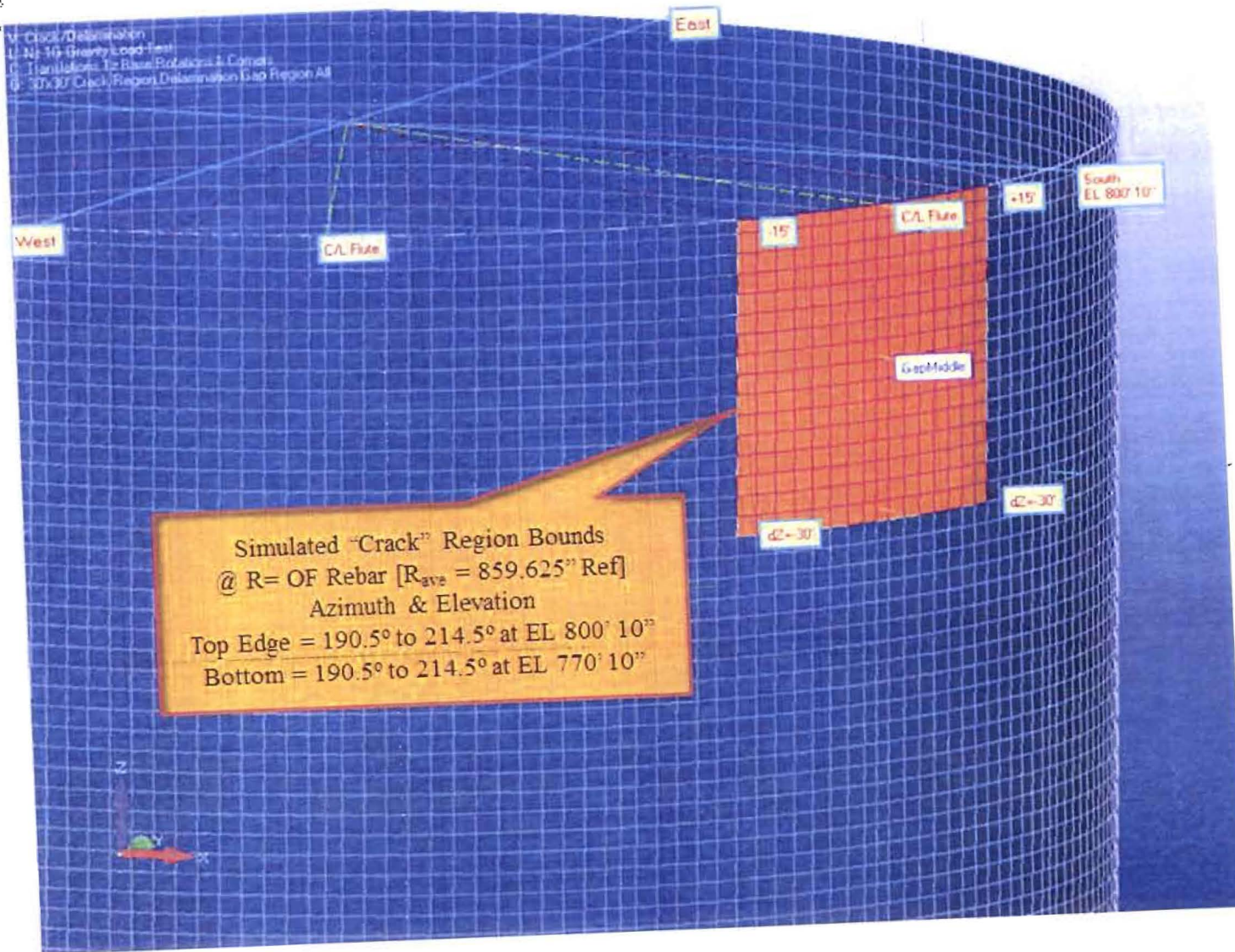


Figure 4.5.2
"Thin-Crack" region introduced as idealized the "Cracked" boundary at the OF Rebar

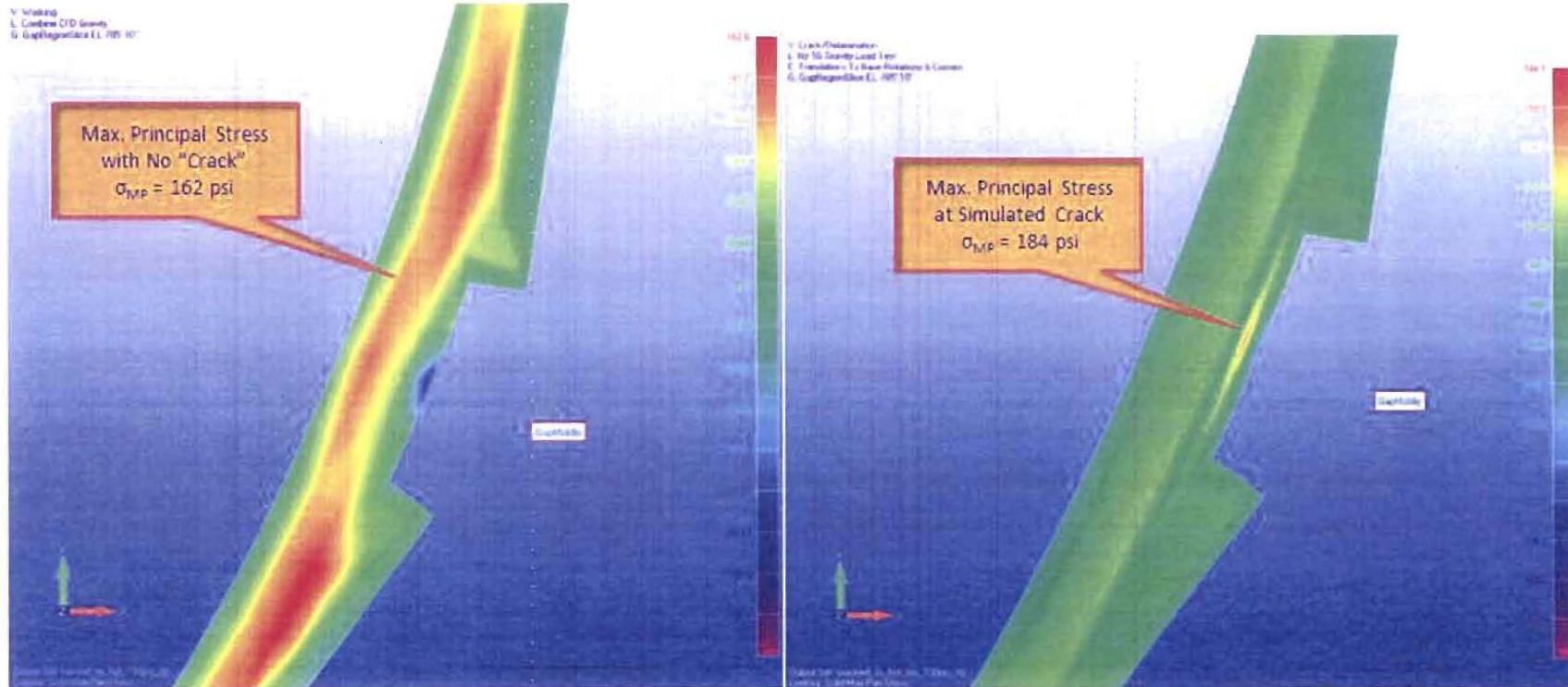


Figure 4.5.3
Summer Solstice Hot No Wind 7:30 pm, *Constant* Concrete CTE = 5.20×10^{-6} in/in/°F
Maximum Principal Stress Distribution

1



4.6 Miscellaneous Plane-Strain Results – Overlapping Reinforcement

Both the plane-strain and 3D [REDACTED] models show regions of positive radial stress in the thick portion of the flutes. The average magnitudes of stress are about +350 psi. See Figure 4.6.1 The magnitude of these positive radial stresses are not believed high enough to cause cracks but the thick portion of the flutes is the only large region where radial stresses are positive.

It is known that there are regions where reinforcement overlaps in regions where the rebar either transitions to a different size or rebar of the same size is continued and the overlap acts as a splice. The plane-strain models with overlapping rebar indicate that the effects of the localized stress concentration factor (SCF) around can be linked together to form a line of cracks. The overlapping rebar also makes it difficult to fill voids due to large aggregate blocking distribution of concrete paste.

Figure 4.6.1 shows results of a parametric analysis to qualitatively view of the effects when rebar is closely spaced or overlaps.

Localized cracks that may develop at the overlapping rebar (vertical & hoop) could link to the adjacent SCF point since the distance to next pair of overlapping rebar isn't very far. The OF layer is more susceptible to this crack propagation because it is the OF layer where maximum principal stress are highest. Overlapping rebar along the IF face doesn't have maximum principal stress available to propagate cracks.

In addition, it should be noted that with the exception of the localized SCF peak tension radial stresses, regions immediately adjacent to the high tension stresses show significantly lower stress... even negative (compression) values. It is believed any localized cracks around the rebar would not propagate due to these thermal stresses and the surrounding compressive stresses would arrest any localized cracks initiating due to the localized SCF points.

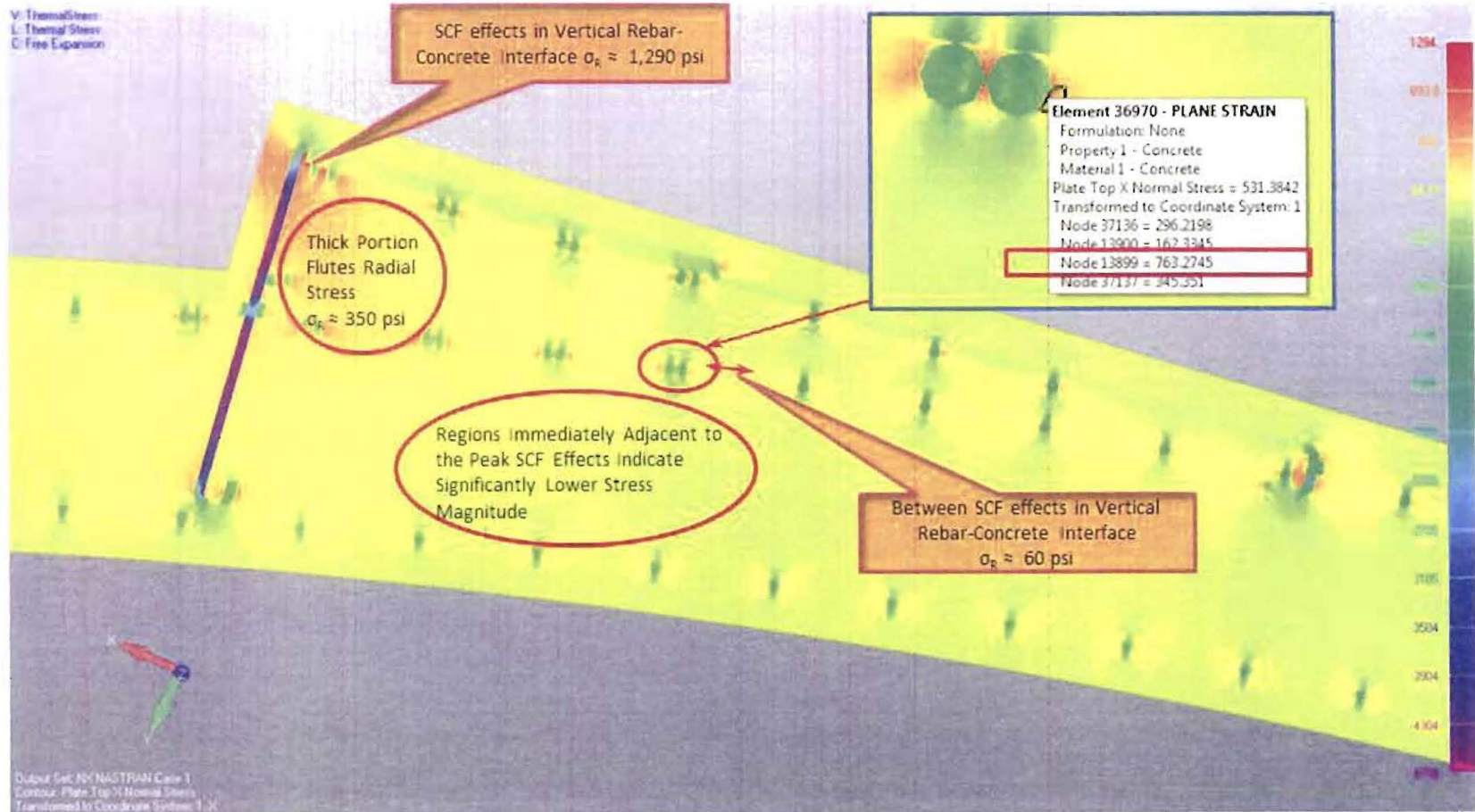


Figure 4.6.1
Typical Radial Stress Contour from 2D Plane-Strain Nastran ██████████
With SCF Effects due to Overlap of Vertical Rebar



4.7 Effects of Variable $CTE=f\{T\}$

Two (2) of the concrete core samples from Davis-Besse Shield Building were sent to the United States Bureau of Reclamation (USBR) for mechanical and thermal properties testing. The coefficient of thermal expansion (CTE) was tested in accordance with the USBR test procedure 4910-92. The average value for CTE over the temperature range of approximately 33°F to 150°F given is $CTE = 5.20 \times 10^{-6}$ in/in/°F... constant value. [Reference Figure 2.1.4]



The temperature range for Winter Solstice Average is indicated on **Figure 4.7.1** (+27°F to +63°F) and shows that $CTE=f\{T\}$ remains within the linear range of USBR data. Therefore during average winter conditions a variable $CTE = f\{T\}$ will produce the same results as constant CTE.

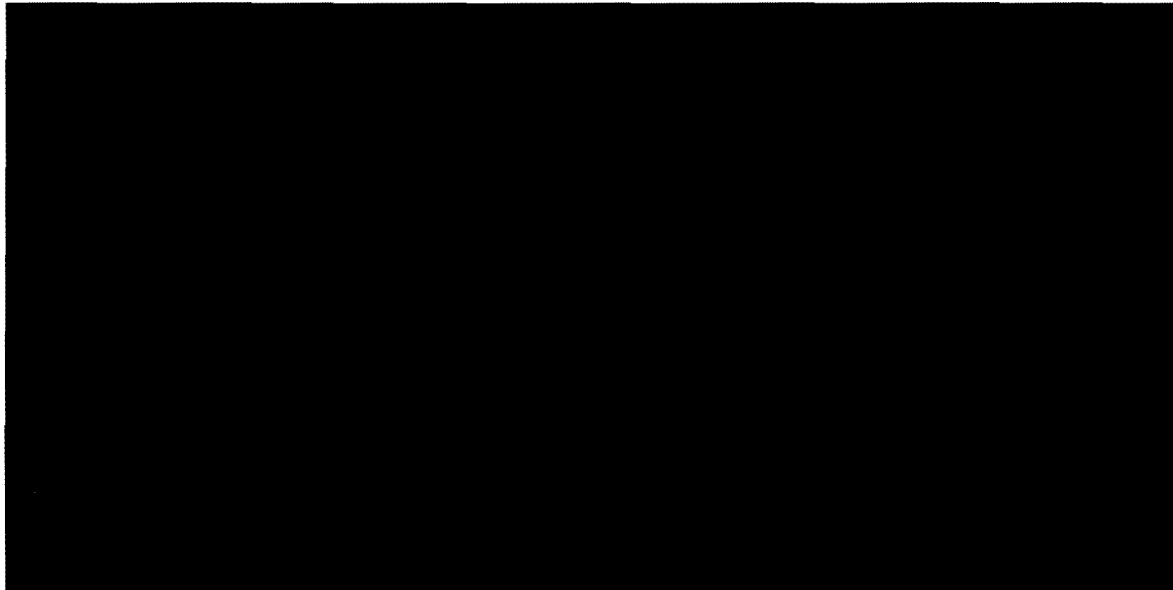


Figure 4.7.1
Qualitative Characteristics for nonlinear $CTE=f\{T\}$
Average Winter Temperature Range Shown

Figure 4.7.12 shows the assumed $CTE=f\{T\}$ with the computed temperature range from 1978 Blizzard cold temperatures. As shown on **Figure 4.7.1** the temperature range from the 1978 Blizzard extends into the nonlinear range of the $CTE = f\{T\}$ data suggested by Prof. Xi.

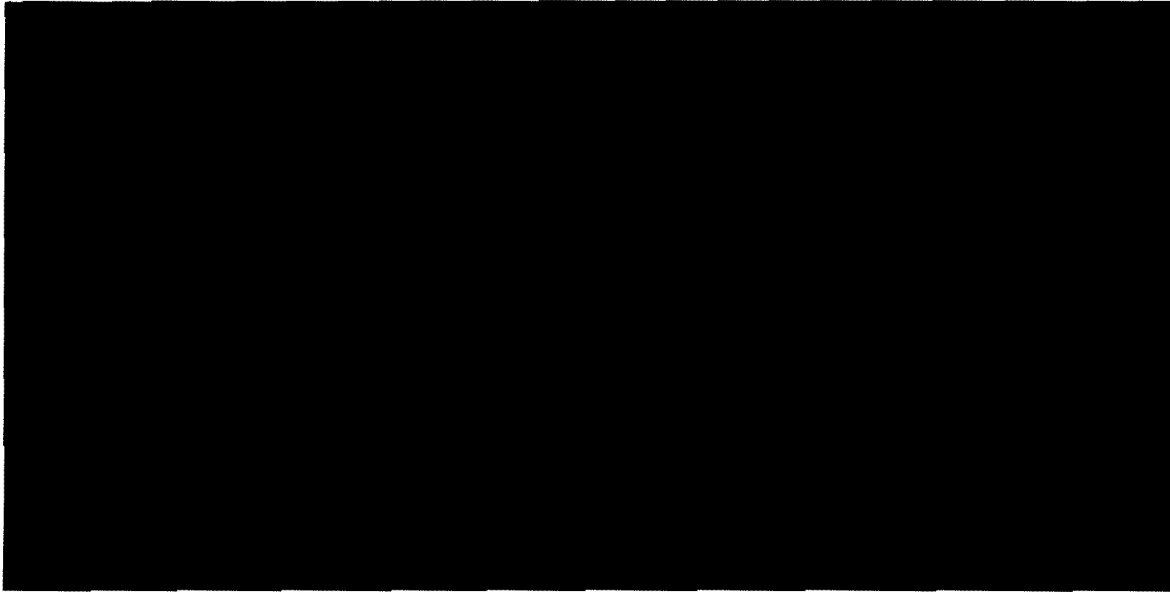


Figure 4.7.2
Qualitative Characteristics for nonlinear $CTE=f\{T\}$
Average Winter Temperature Range Shown

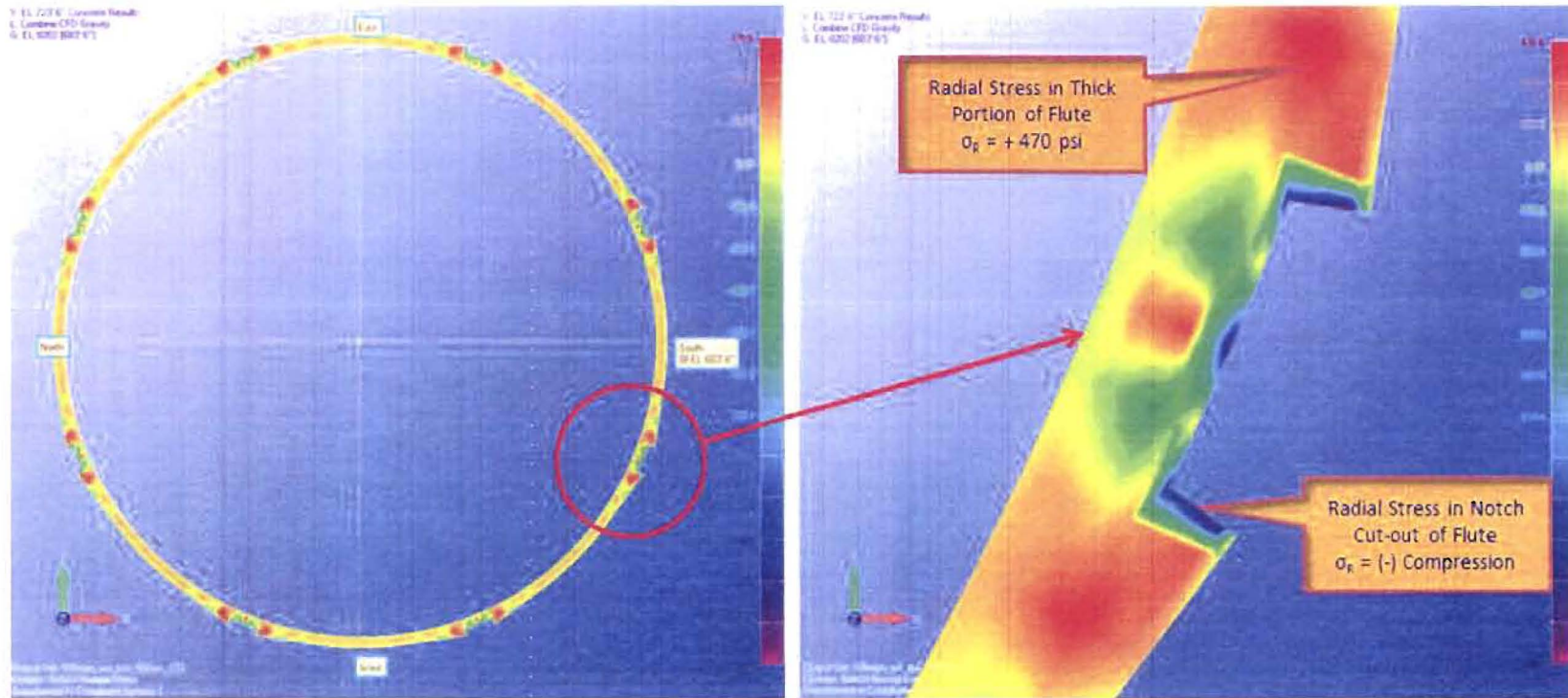
For reference, recall **Figure 4.2.1**, “1978 Blizzard Condition 5:00 am, *Constant* Concrete $CTE = 5.20 \times 10^{-6}$ in/in/ $^{\circ}$ F - Radial Stress Distribution”, peak radial stress in the thick portion of the flutes are computed at $\sigma_R = -70$ psi.

Figure 4.7.3 shows radial stress contour from the 3D Nastran [REDACTED] FEM for the 1978 Blizzard condition assuming a variable/temperature dependent concrete $CTE=f\{T\}$ similar to **Figure 4.7.2**. Results for radial stress in the thick portion of the flutes are $\sigma_R = +470$ psi for the 1978 Blizzard condition compared to $\sigma_R = -70$ psi when CTE is constant.

The temperature range shown during the 1978 Blizzard cold conditions (-27° F to $+32.4^{\circ}$ F) does fall into the non-linear region when a variable $CTE=f\{T\}$ is considered. Therefore, if one views the 1978 Blizzard event as a catastrophic “once-in-a-lifetime” event then the concrete may have cracked way back then and the likelihood of another 1978 Blizzard is remote.

The simulated “crack” model described in paragraph 5.0 was addressed using the variable $CTE=f\{T\}$. Analysis results did not show and significant change in the state of stress surrounding the simulated “crack” region when variable $CTE=f\{T\}$ is used in place of the constant CTE.

It should be noted the variable $CTE=f\{T\}$ is based on “academic” predictions scaled to match the USBR test results and then extrapolated beyond the known test range. These results remain qualitative until conclusive data; precise material properties that is, are available. These qualitative results do suggest strong evidence to support the hypothesis that the 1978 Blizzard event could be one of the primary contributors to the cracks. Exhibit 61: explores variations on the variable CTE concept.



Overall View @ EL 683' 6"

Close-Up View @ EL 683' 6"

Figure 4.7.3
Radial Stress Contour from 3D Nastran [REDACTED] FEM
1978 Blizzard Condition, *Variable* Concrete CTE = $\{T\}$ @ 93% Saturation



5.0 Summary Review and Comments

- ✓ The 3D Nastran [REDACTED] models indicate the regions of interest for highest radial stresses are in the thick portions of the Flutes. The magnitudes of radial stresses from any of the thermal transient stress analysis are not sufficient to initiate or propagate cracks that may have formed without another mechanism for crack initiation & crack growth present. [Reference pages 19, 20, 21, 35 & 38]
- ✓ The plane-strain and other sub-models show localized peaks in the radial stresses resulting from stress concentration factors (SCF) around discontinuities. These SCF effects can result from (a.) overlap of adjacent reinforcing bar, (b.) abrupt change in stiffness [Steel-Concrete] and (c.) thermal gradients with abrupt change in coefficient of thermal expansion (CTE). [Reference page 35]
- ✓ It is not unusual to have peak stresses at points where SCF's are known to exist and some localized dis-bonding of the concrete to the rebar may result. With the exception of these localized peak tension radial stresses, regions immediately adjacent to the high tension stresses show significantly lower stress... even negative (compression). Localized cracks that may develop around the rebar due to these SCF would not propagate due to thermal stresses alone and the surrounding compressive stresses would arrest any localized cracks initiating due to the localized SCF points.
- ✓ The 3D Nastran [REDACTED] models indicate stress gradients exist due to thermal transient conditions. The maximum principal stresses are largest at the outer most 2" - 3" of concrete at the outer rebar layer. Thermal stress gradients lead to significantly lower stress as one move inboard the radial direction from the OF toward the IF of the Shield Building wall. At approximately 6" - 8" inboard of the outer most layers, radial stresses drop off to levels that would clearly not initiate cracks. [Reference Figures 4.1.1, 4.1.2 & 4.1.3]
- ✓ Some qualitative results suggest strong evidence to support the hypothesis that the 1978 Blizzard event could be one of the primary contributors to the cracks. These qualitative results indicate the low temperatures during the 1978 Blizzard may be a catastrophic "once-in-a-lifetime" that may have cracked concrete. At date of release of this report these results remain qualitative and academic until conclusive data in the form of precise material properties are available, i.e. $CTE=f\{T\}$, allowing for a quantitative re-assessment of the 1978 Blizzard condition. [Reference Figure 4.7.3]



Exhibit 57: Temperature Dependent CTE



Temperature dependent coefficient of thermal expansion (CTE)

Under low temperatures, concrete may expand (instead of contract) during a cooling period. This possible expansion is due to ice formation in the concrete. During a severe cooling process, the temperature of concrete in outer layer of the cylindrical wall is lower than that of inner layer. So, ice may form in the outer layer of the wall resulting in an expansion and ice may not form in the inner layer of the wall leading to continuous contraction. This special outer-expansion-and-inner-contraction deformation pattern can result in a tensile stress in the radial direction of the wall. Delamination cracking may occur in the case of excessively high radial tensile strength. The key issue here is the coefficient of thermal expansion (CTE) of concrete under low temperatures. Did the Davis Besse concrete in outer layer of the wall expand during the blizzard? If yes, how much did it expand? Was the expansion high enough to cause the cracking? These questions will be discussed in the following sections.

The effect of temperature on CTE of concrete

CTE of concrete depends on temperature. The reason is that the state of moisture inside of concrete depends on temperature. Under elevated temperatures (e.g. fire), liquid water turns into vapor which generate high vapor pressure. This case is not within the scope of this project, and thus will not be discussed further. Under low temperatures, liquid water or vapor turns into ice which is associated with a 9% volume expansion. After all moisture freezes, the effective CTE of concrete is a mixture of CTE of concrete and CTE of ice. The CTE of ice is about 5 times of the CTE of concrete without ice. Therefore, at a very low temperature, the CTE of concrete is not the same as the CTE of concrete at room temperature. Accurately speaking, the effective CTE of concrete depends both on temperature and on ice content, and thus on moisture content. The effect of temperature will be discussed first, and the effect of moisture will be discussed later.

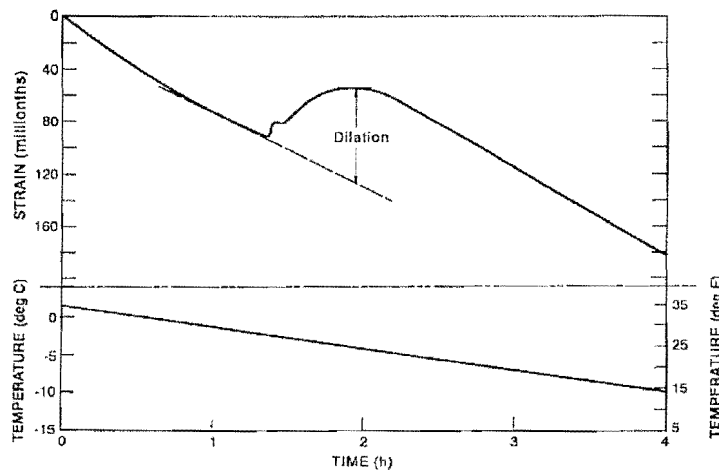


Fig. 1 A typical strain and temperature chart (ASTM C671)

Literature review showed that the ice formation starts at 0°C and completes at about -15°C or lower depending on the microstructure of concrete. This freezing process is due to the fact that the freezing point of water depends on pore size in concrete. The freezing point of water in large air voids is close to 0°C, and thus the water in large air voids freezes first; and the freezing point in small pores could be well



below 0°C, and the water in small pores freezes after the water in large voids. For a continuous cooling process, the strain of a concrete specimen is shown in Fig. 1, contracting first, expanding due to ice formation, and then contracting again after the completion of ice formation. In Fig. 1, the slope of the strain vs. temperature curve is CTE. It is very clear that the slope of the curve, the CTE is not a constant.

Depending on concrete mix design and cooling condition (temperature range and freeze-thaw cycles), the curve could be significantly different, as shown in Fig. 2. The shape of the curve, i.e. the temperature dependency of CTE is closely related to the internal structure of concrete.

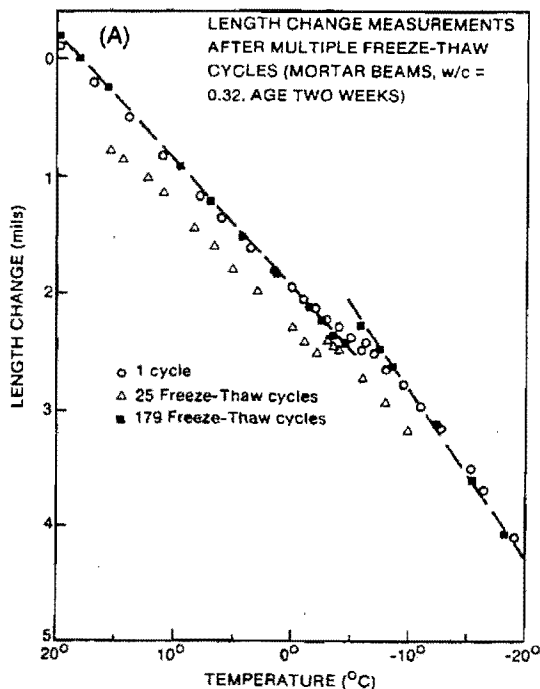


Fig. 2 Test data of concrete length changes under low temperatures (Bazant et al. 1988; see Refs. 18 and 19 for test results from T.C. Powers and R.A. Helmuth)

Experimental studies showed that properly air-entrained mortars contract upon freezing, while non-air-entrained mortars or improperly air-entrained mortars expand. The expansion of the latter is attributed primarily to hydraulic pressure, owing to the rapid growth of ice, which nucleates at low temperatures in laboratory samples (Sun and Scherer 2010).

Moisture in concrete

Because of very small pores in concrete, water in the pores exists as a mixture of liquid and vapor in above ground concrete structures. Internal relative humidity (or pore relative humidity), RH of concrete are often used to represent internal moisture state of concrete. The internal RH can be correlated to the moisture content in concrete (the weight of moisture in concrete) by adsorption isotherms. Adsorption isotherm is a relationship among weight of internal moisture, temperature, and RH. Fig. 3 shows experimental results of adsorption isotherms in the literature in comparison with the predictions of a theoretical model developed by Xi et al. (1994). In the figure, the horizontal axis represents RH (where p is water vapor pressure and p_s is the saturation pressure at a given temperature); and the vertical axis stands for moisture content in gram of moisture in gram of concrete. So, with a given concrete mix



design, temperature, and RH, the moisture content in the concrete can be obtained from the adsorption isotherms.

It is important to note that RH = 100% does not mean all pores are filled up by water, it means the vapor pressure in the pore reaches the saturation pressure of vapor at the given temperature. At this stage, the concrete reaches its adsorption capacity, which is different from absorption capacity. There may be only limited layers of water molecular covering the surface of pore walls at RH = 100%. When all pores are filled up by water, the concrete reaches its absorption capacity.

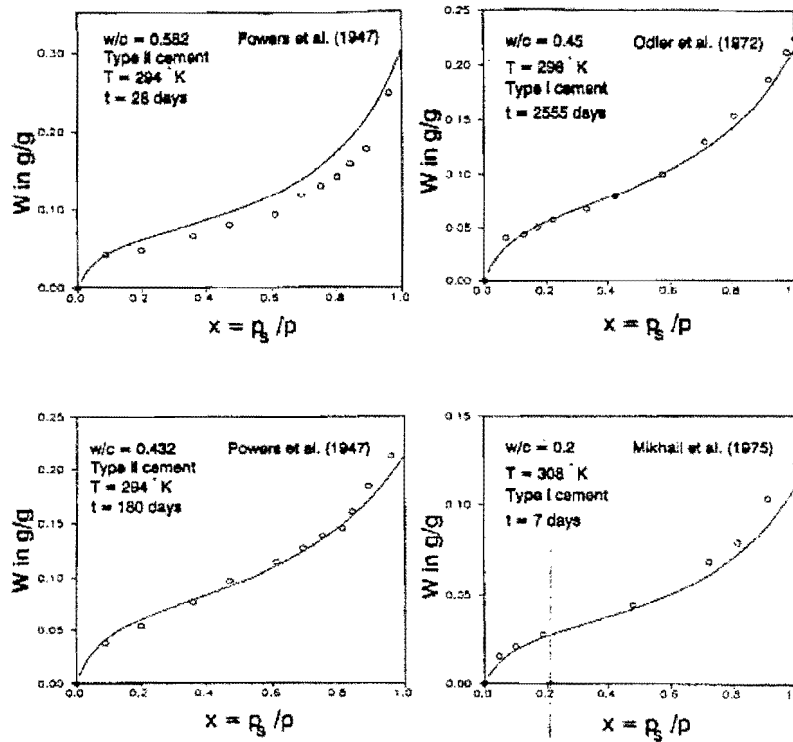


Fig. 3 Adsorption test data and comparisons with predictions of a theoretical model (Xi et al. 1994)

For above ground structures such as Davis Besse containment structure, it is more suitable to use RH and adsorption isotherms for estimating the internal moisture content. For under water structures, the absorption capacity is a better indicator.

The effect of moisture on CTE

The general trend is that the higher the initial moisture content before ice formation, the larger amount of ice formed in the concrete, and possibly the larger dilation of concrete during the ice formation process. The following figures show available test data in the literature.

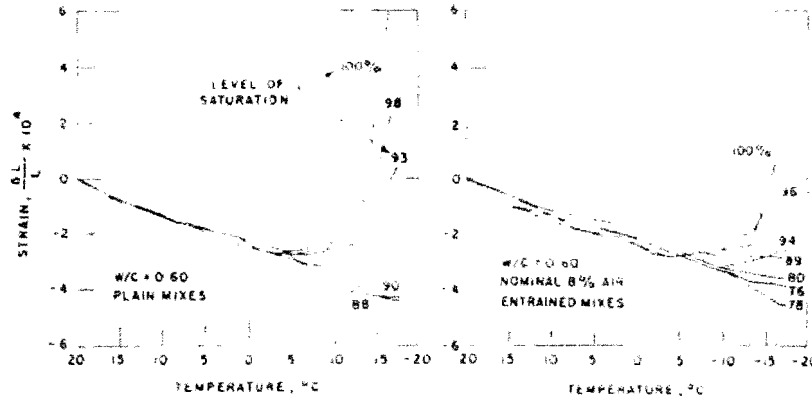


Fig. 4 Temperature vs. dilation of concretes at various levels of saturations (Grieve et al. 1987)

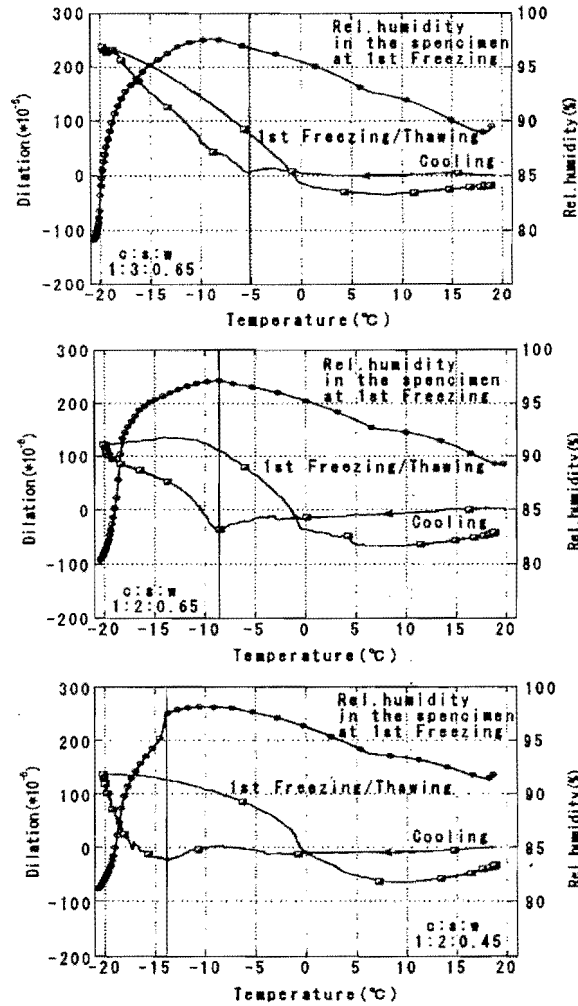
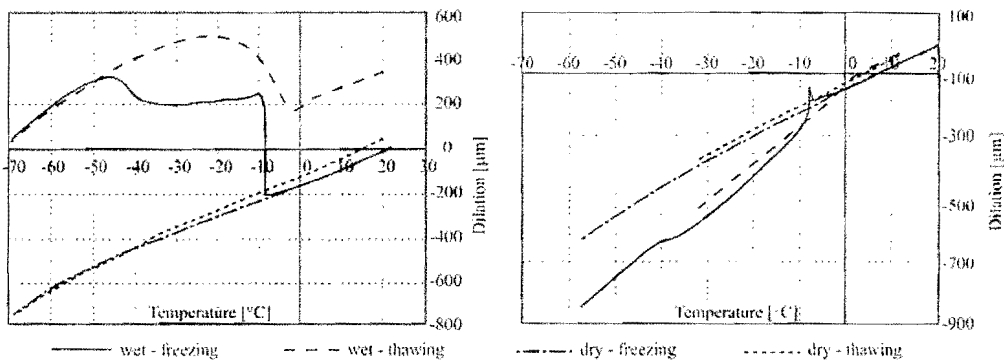


Fig. 5 Dilatation of concrete and internal relative humidity (Zhou and Mihashi 2008)



In Fig. 4, there is almost no expansion when the saturation level in the concretes is below 90%. However, in Fig. 5, there are significant expansions at low temperatures even the initial RHs in the concrete samples are below 90% (see the first and the second figures, the RHs are about 88%). Fig. 6 shows the dilations of concrete under dry and wet conditions. One can see from Fig. 6(a) that the concrete at wet-freezing condition expands significantly (near 8 degree C), while the concrete at dry-freezing condition does not expand at all. Therefore, the moisture content has a major effect on the expansion of concrete during ice formation process, and the extent of moisture effect depends on internal structure of the concrete. The internal structure of concrete depends on mix design, curing conditions, and age of the concrete. In Fig. 6(b), even if at wet-freezing condition, the concrete with proper air-entrainment only expands slightly near 8 degree C).



(a) w/c = 0.5 non-air-entrained concrete

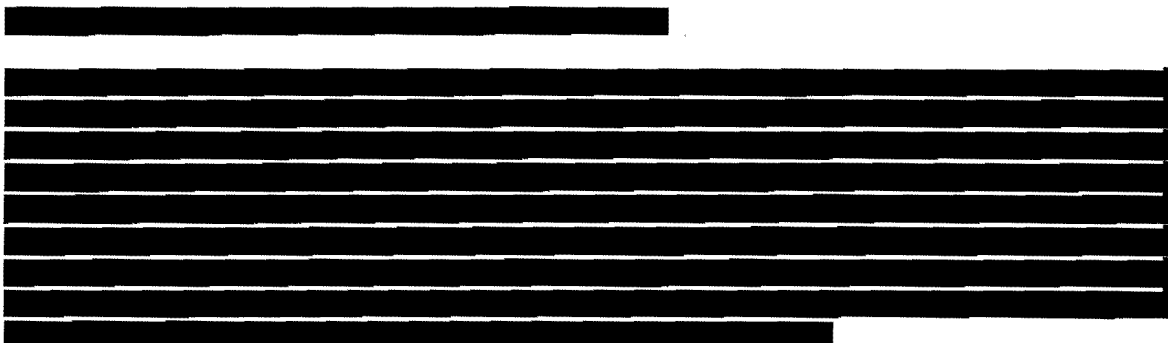
(b) w/c = 0.35 air-entrained concrete.

Fig. 6 Influence of saturation on dilation of concrete (Zuber and Marchand 2004)

In summary, at a sufficiently high RH level and under a continuous cooling process, there are three possible types of temperature-dependent thermal strains for concrete:

- Type 1 – Contraction, significant expansion, and contraction, as shown in Fig. 1 and Fig. 6(a).
- Type 2 – Contraction, slight expansion, and contraction, as shown by solid squares in Fig. 2 and Fig. 6(b).
- Type 3 – Contraction, as shown by hollow circles in Fig. 2.

From Exhibit 52 Univ. of Colorado lab test report, the relation of thermal strain and temperature of Davis Besse concrete follows Type 3 when the sample is dry, and Type 1 when the sample is wet. So, Davis Besse concrete does expand under low temperatures.





[Redacted text]

[Redacted text]

[Redacted text]

[Redacted text]

[Redacted text]

[Redacted text]

[Redacted text]

[Redacted text]

[Redacted text]

[Redacted text]

[Redacted text]

The resulting temperature dependent CTE at the temperature ranges are:

$T > 23^{\circ}\text{F} (-5^{\circ}\text{C})$, $\text{CTE} = 5.2 \times 10^{-6}/^{\circ}\text{F}$ (The same as USBR test data),

$8.6^{\circ}\text{F} (-13^{\circ}\text{C}) < T < 23^{\circ}\text{F} (-5^{\circ}\text{C})$, $\text{CTE} = -4.94 \times 10^{-6}/^{\circ}\text{F}$,

$1.4^{\circ}\text{F} (-17^{\circ}\text{C}) < T < 8.6^{\circ}\text{F} (-13^{\circ}\text{C})$, $\text{CTE} = -43.1 \times 10^{-6}/^{\circ}\text{F}$,

Below $1.4^{\circ}\text{F} (-17^{\circ}\text{C})$, $\text{CTE} = 5.2 \times 10^{-6}/^{\circ}\text{F}$ (The same as the CTE under room temperature).

Conclusions

CTE of concrete depends on temperature, internal moisture, and internal structure of concrete. Some concretes may expand during the ice formation process if their internal moisture content is sufficiently high.

Davis Besse concrete showed expansive strains under low temperatures (Exhibit 52). Therefore, a temperature dependent CTE was developed [Redacted text]

[Redacted text]



References

- Bazant, Z.P., Chern, J.C., Rosenberg, A.M., and Gaidis, J.M. (1988) "Mathematical Model for Freeze-Thaw Durability of Concrete", *Journal of American Ceramic Society*, 71(9), 776-783.
- Grieve, R., Slater, W.M., and Rothenburg, L. (1987) "Deterioration and Repair of Above Ground Concrete Water Tanks in Ontario, Canada", *Research Report to Ontario Ministry of the Environment*, Golder Associates and W.M. Slater & Associates, Inc.
- Sun, Z., and Scherer, G.W. (2010) "Effect of Air Voids on Salt Scaling and Internal Freezing", *Cement and Concrete Research*, 40, 260-270.
- Xi, Y., Bazant, Z.P., and Jennings, H.M. (1994) "Moisture Diffusion in Cementitious Materials: Adsorption Isotherm", *Journal of Advanced Cement-Based Materials*, 1, 248-257.
- Zhou, Z.Y., and Mihashi, H. (2008) "Micromechanics Model to Describe Strain Behavior of Concrete in Freezing Process", *Journal of Materials in Civil Engineering*, ASCE, 20(1), 46-53.
- Zuber, B., and Marchand, J. (2004) "Predicting the Volume Instability of Hydrated Cement Systems upon Freezing using Poromechanics and Local Phase Equilibria", *Materials and Structures*, 37, 257-270.



Exhibit 58: Carbonation Lab Testing



Performance Improvement International

Providing a competitive advantage through research and applications

To: [REDACTED]

From: [REDACTED]

Date: 02/27/2012

Subject: Laminar Cracking of Davis-Besse Shield Building – Concrete Sample Testing for Carbonation

[REDACTED]

Based on my observation and examination of concrete-core samples received from the Davis-Besse Shield Building, my findings for Carbonation are detailed in what follows.

[REDACTED]



Carbonation in Concrete

Carbonation in Concrete

Laboratory tests and examinations were conducted on several concrete core samples to determine the extent of carbonation within the samples.

The cracked concrete samples, which are vulnerable to carbonation, were isolated and fractured in a plane perpendicular to the original cracked surface.

Figures A1 and A2 show examples of the carbonation depth as measured from the exterior surface. The exterior surface is the portion of the shield building that is exposed to the elements; it is the outer diameter surface.

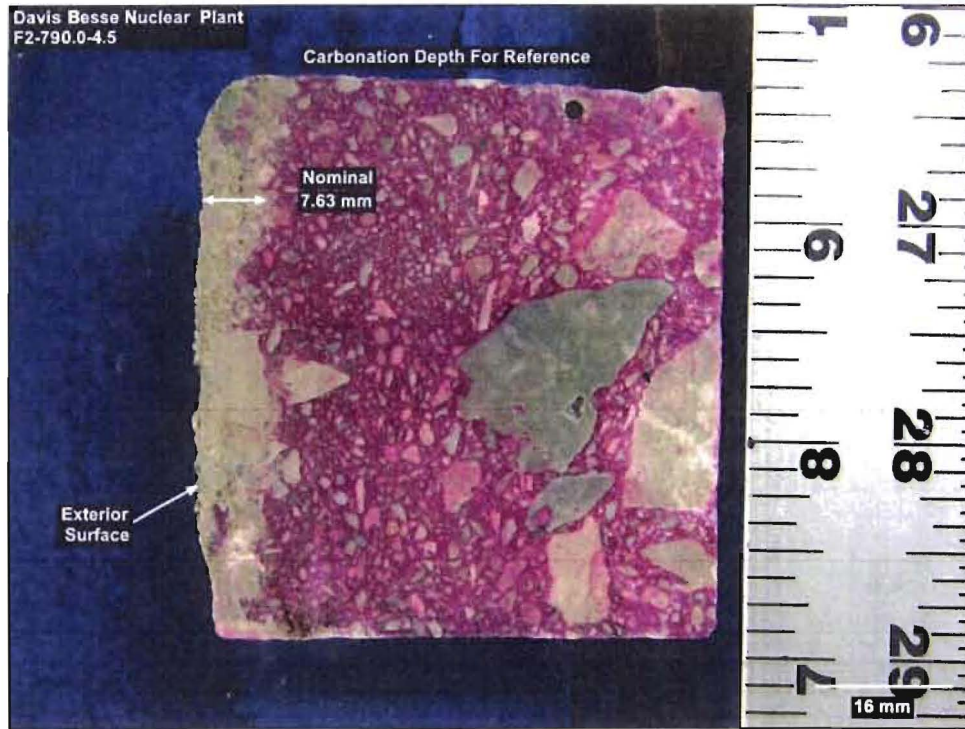


Figure A 1: Fracture Sample with Carbonation Layer (Core F2-790.0-4.5)

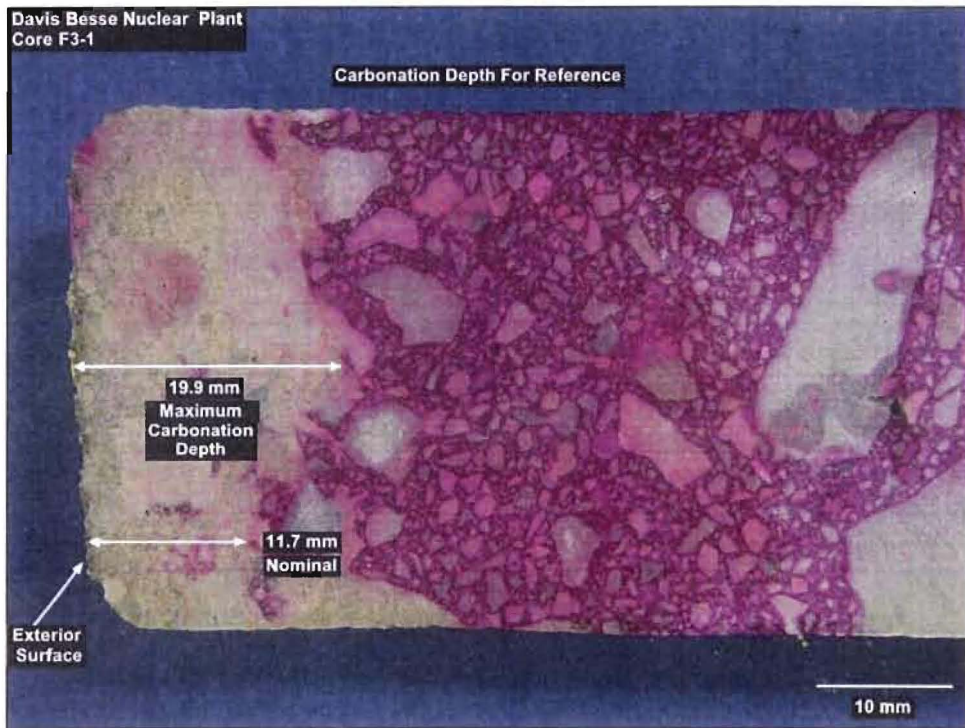


Figure A 2: Fracture Sample with Carbonation Layer (Core F3-1)



The following table shows the nominal carbonation depth as measured from the exterior surface. The table lists the 16 samples used in determining the average nominal carbonation depth which, as previously stated, is 8.57 mm.

Table A 1: Nominal Carbonation-Layer Depth from Exterior Surface (Carbonation Rate Determination)

Core Sample	Nominal Carbonation Depth From Exterior Surface (reference), mm
F3-1	11.7
S11-1	9.33
S11-2	10.00
S12-1	8.59
S12-2	8.33
S16-3	7.73
S5-1	7.90
S5-2	7.87
S7-1	7.75
S7-2	9.07
S7-3	7.56
S9-1	10.05
S9-2	7.65
S-7-656.5-6.5	8.84
S-9-653-1	8.65
S-9-785-22.5	6.06
AVERAGE	8.57

Longitudinal Fracture

Carbonation analysis was conducted for both longitudinal and transverse cracks. Figure A3 shows a longitudinal crack for reference. As can be seen, the longitudinal cross-section is defined as the plane that is parallel to the longer dimension of the core sample.

Several longitudinal cracks with no evidence of carbonation were evidenced. For example, Figure A4, Core F2-790.0-4.5, shows that a distance of 7 inches from the surface, no carbonation is detected.

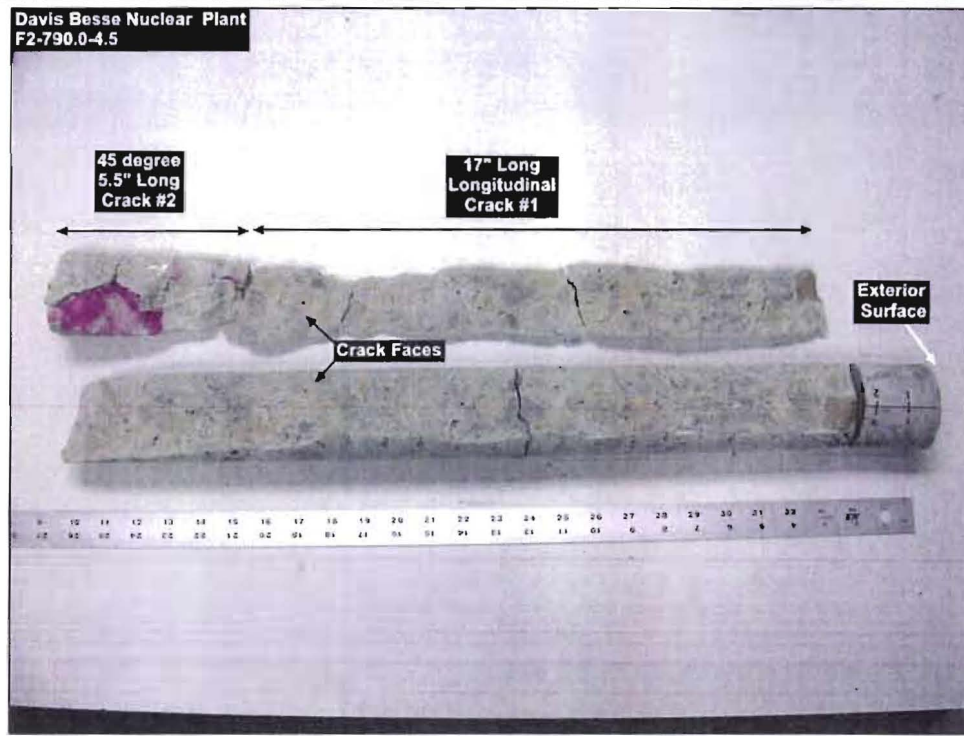


Figure A 3: Longitudinal Crack (Reference)

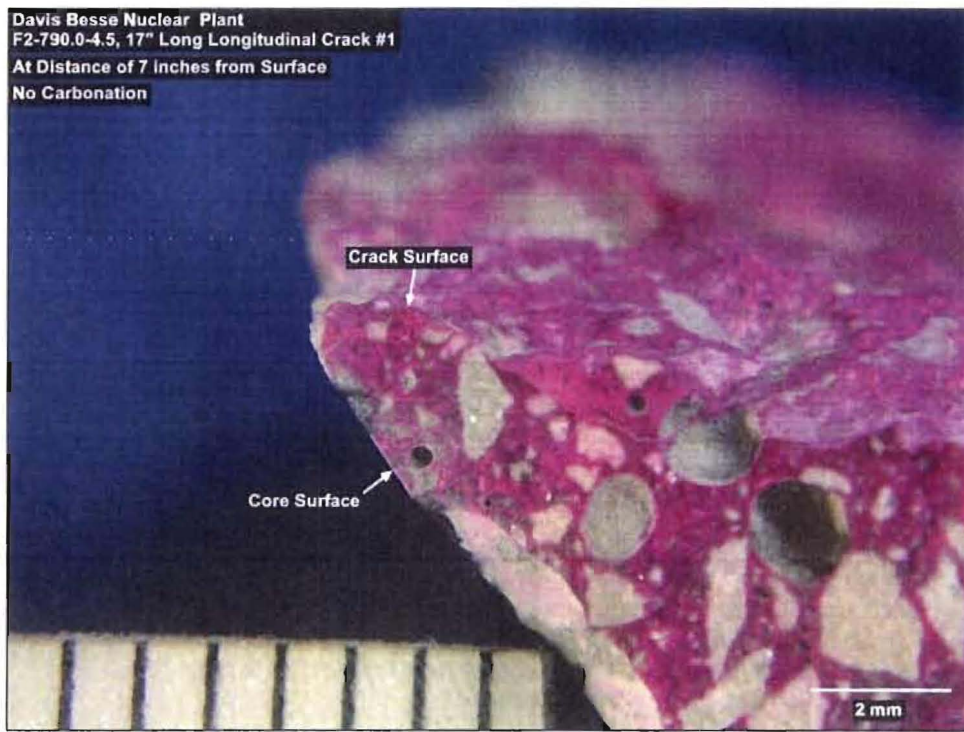


Figure A 4: Longitudinal Crack with no Evidence of Carbonation



The Following table shows several samples with longitudinal cracks at various distances from the exterior surface. For the samples in the table listed below, there is no carbonation layers formed at any of the various distances within each respective sample.

Table A 2: Carbonation Results from several Samples with Longitudinal Cracks (No Carbonation)

Core Sample	Crack	Distance From Exterior Surface	Maximum Carbonation Depth, mm
F2-790.0-4.5 17" Long Crack	Longitudinal Crack #1	7"	0
F2-790.0-4.5 17" Long Crack	Longitudinal Crack #1	10.5"	0
F2-790.0-4.5 17" Long Crack	Longitudinal Crack #1	13"	0
F2-790.0-4.5 17" Long Crack	Longitudinal Crack #1	16"	0
F2-790.0-4.5 17" Long Crack	Longitudinal Crack #1	20"	0
F2-790.0-4.5 5.5" Long Crack	45 Degree Crack #2	21" to 22"	0
F2-790.0-4.5 5.5" Long Crack	45 Degree Crack #2	23" to 26"	0
F4-794.0-3.5 19" Long Crack	Longitudinal Crack #1	9"	0
F4-794.0-3.5 19" Long Crack	Longitudinal Crack #1	13"	0
F4-794.0-3.5 19" Long Crack	Longitudinal Crack #1	17.5"	0
F4-794.0-3.5 19" Long Crack	Longitudinal Crack #1	20"	0
F4-794.0-3.5 19" Long Crack	Longitudinal Crack #1	23"	0
F4-794.0-3.5 19" Long Crack	Longitudinal Crack #1	26"	0
F5-791.0-4 9" Long Crack	Longitudinal Crack #1	7.5"	0
F5-791.0-4 9" Long Crack	Longitudinal Crack #1	9"	0
F5-791.0-4 9" Long Crack	Longitudinal Crack #1	11"	0
F5-791.0-4 9" Long Crack	Longitudinal Crack #1	14.5"	0
S2-798.5-4.5 5" Long Crack	Longitudinal Crack #1	1"	0
S2-798.5-4.5 5" Long Crack	Longitudinal Crack #1	2.5"	0
S2-798.5-4.5 5" Long Crack	Longitudinal Crack #1	4"	0



The following table shows the results from carbonation analysis on several core samples with longitudinal cracks.

Table A 3: Carbonation Analysis on Longitudinal Cracks

Core Sample	Crack	Longitudinal Crack Length	Maximum Carbonation Depth, mm
F3-1	#1	7"	5.4
S11-1	N/A	N/A	N/A
S11-2	#1	6 ¾"	0
S11-2	#2	6 ¾"	2.09
S12-1	#1	5 ½"	0
S12-1	#2	1 ½"	2.70
S12-2	#1 ^b	1 ½"	2.99
S16-3	N/A	N/A	N/A
S5-1	N/A	N/A	N/A
S5-2	N/A	N/A	N/A
S7-1	#1	2 ⅝"	0
S7-2	N/A	N/A	N/A
S7-3	N/A	N/A	N/A
S9-1	N/A	N/A	N/A
S9-2	N/A	N/A	N/A

*N/A = No Longitudinal Crack

*Crack Found Upon Sectioning

Transverse Fracture

Figure A6 shows an example of a transverse fracture sample, Core S5-2, which was determined to have a measured carbonation layer of 0.455 mm.

For comparison with Figure A6, Figure A7 shows an example of a transverse fracture sample, Core S7-656.5-6.5, which was determined to have no carbonation layer.

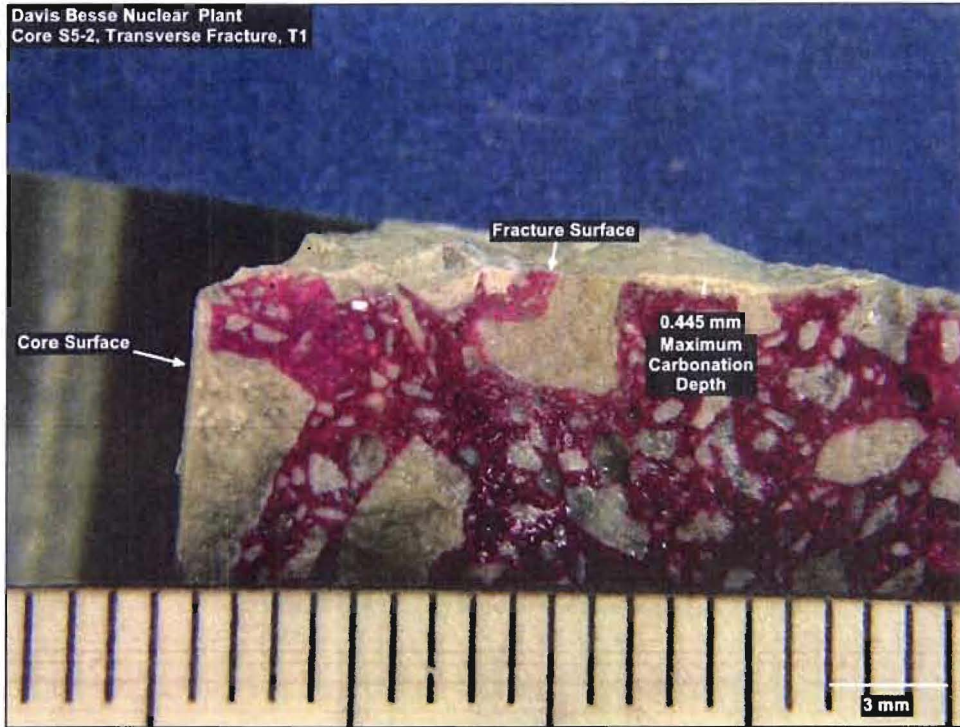


Figure A 5: Carbonation Detected on a Transverse Fracture Sample (Core S5-2), 1.8 yrs.

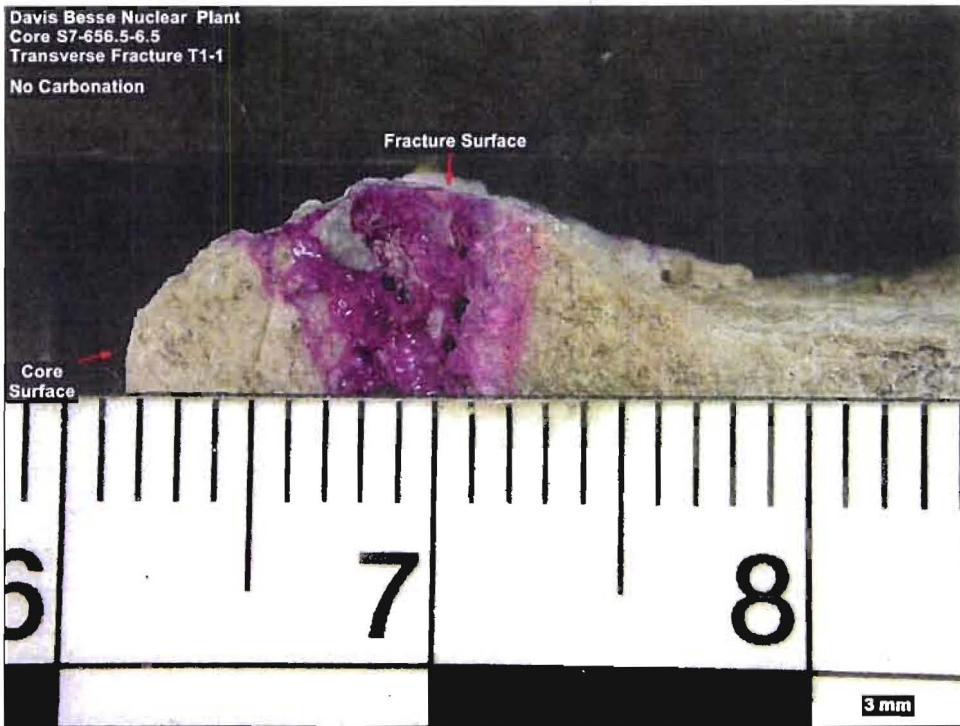


Figure A 6: Transverse Fracture Sample with No Carbonation (Core S7-656.5-6.5)



The following table is a list of transverse fracture core samples along with their associated carbonation depth. Core samples with an asterisk in their identification number are those with transverse cracks as identified by the plant IR Inspection.

Table A 4: Transverse Fracture Carbonation Analysis

Core Sample	Fracture (Crack)	Distance From Surface, inches	Maximum Carbonation Depth, mm
F3-1	#T1	7	0.582
S11-1*	#T1	8	0
S11-1*	#T2	5 ½	0
S11-2	#T1	8	0
S12-1	#T1	21	0
S12-2*	#T1	5 ½	0.264
S12-2*	#T2	16 ½	0.686
S16-3*	#T1	14 ½	0.343
S16-3*	#T2	15 ½	0
S16-3*	#T3	21 ½	0
S5-1*	#T1	9	0.500
S5-1*	#T2	9 ½	0.897
S5-1*	#T3	14 ½	0.604
S5-1*	#T4	16 ¼	0.893
S5-2	#T1	12 ⁵ / ₈	0.445
S7-1*	#T1	4 ¼	0
S7-1*	#T2	10	0
S7-1*	#T3	16 ³ / ₄	0
S7-2	#T1	15 ³ / ₈	1.42
S7-3*	#T1	6 ½	0.710
S9-1*	#T1	4 ½	0.329
S9-1*	#T2	12 ¼	0
S9-2	#T1	10 ¼	0.388

*Core samples with transverse cracks as identified by the plant IR inspection



**Exhibit 59: Test Report from the United States
Bureau of Reclamation (USBR)**



United States Department of the Interior

BUREAU OF RECLAMATION
P.O. Box 25007
Denver, Colorado 80225-0007


IN REPLY REFER TO:

86-68180
RES-3.40

JAN 19 2012

MEMORANDUM

To: Performance Improvement International
2111 S El Camino Real
Suite 200
Oceanside, CA 92054
Attention: Dr. Chong Chiu

From: Katie Bartojay, P.E., Civil Engineer, Materials Engineering and Research
Laboratory Group (MERL) 

Subject: Thermal Properties Testing Results on Submitted Concrete Core
Specimens

Materials Engineering and Laboratory Report No. MERL-2012-02

INTRODUCTION

Six concrete core samples were delivered to the Bureau of Reclamation's Materials Engineering and Research Laboratory (MERL) on December 19, 2011. The specimens were identified as F4-791-2.5 #1 through #4 and S7-782.0-8.5 #5 and #6. All six specimens were approximately 2.5-inches in diameter and 4-inches long.

The submitted samples were tested for thermal diffusivity, specific heat, and thermal coefficient of linear expansion testing on concrete cores. Conductivity was calculated using the specific heat and diffusivity results.

CONCLUSIONS AND DISCUSSION

Thermal Diffusivity

Thermal diffusivity measures the rate at which temperature changes take place in concrete and is defined as an index of the facility with which a material will undergo temperature change [i]. Thermal diffusivity was tested in accordance with Reclamation's test procedure USBR 4909-92, "*Thermal Diffusivity of Concrete*" (with modifications to account for upgraded equipment). Two concrete core specimens marked S7-782.0-8.5 #5 and S7-782.0-8.5 #6 were tested over three temperature ranges: 35°F to 75°F; 75°F to 115°F; and 115°F to 155°F. A small diameter hole was drilled from one end to accept a

thermocouple to be located at the approximate center of the specimen. The hole was filled with epoxy before testing.

Specific Heat

Specific heat is the amount of heat required to raise the temperature of a unit mass of material one degree [i]. Specific heat was tested in accordance with Reclamation’s test procedure USBR 4907-92, “*Specific Heat of Aggregates, Concrete, and Other Materials*” (with modifications to account for upgraded equipment). Two concrete core specimens marked F4-791-2.5 #1 and F4-791-2.5 # 2 were tested over a temperature range of approximately 35°F to 150°F.

Thermal Conductivity

Conductivity is the rate at which heat is transmitted through a unit thickness of material. The coefficient of thermal conductivity (*K*) represents the uniform flow of heat through a thickness of material when subjected to a unit temperature difference between two faces [i]. Thermal conductivity was calculated from the specific heat (*c*), diffusivity (δ), and concrete density (ρ). The hardened density determined from this study was used in this calculation.

$$K = c \rho \delta \quad [ii]$$

Thermal diffusivity, specific heat and conductivity tests results are summarized in Table 1 and reported graphically in the Attachment.

Table 1 – Summary of thermal properties of select cores

Temperature (°F)	Specific Heat (<i>c</i>) Btu/(lbm·°F) F4-791-2.5 #1	Diffusivity (<i>d</i>) ft ² /hr S7-782.0-8.5 #5	Conductivity (<i>K</i>) Btu/(ft ² ·hr·°F/ft) Calculated
50	0.478	0.054	3.79
100	0.428	0.049	3.08
150	0.378	0.044	2.44

Typical ranges of these thermal properties for normal concrete[ii] are approximately:

- 0.02 to 0.06 ft²/hr for Diffusivity
- 0.20 to 0.28 Btu/lb per °F for Specific Heat
- 0.8 to 2.1 Btu/ft²/hr °F/ft for Conductivity

The specific heat values measured for the submitted specimens were not in the typical range for normal concrete. The calculated conductivity was also outside the range for normal concrete.

Coefficient of Linear Thermal Expansion

Thermal coefficient of linear expansion is the change in a unit length per degree of temperature change of the concrete [iii]. Thermal Coefficient of Expansion was tested in accordance with Reclamation’s test procedure USBR 4910-92, “*Coefficient of Linear Thermal Expansion*” (with modifications to account for upgraded equipment). Two

concrete core specimens marked F4-791-2.5 #3 and F4-791-2.5 #4 were tested over a temperature range of approximately 33°F to 150°F. Coefficient of linear thermal expansion tests results are summarized in Table 2 and reported in the Attachment.

Table 2 --Summary of coefficient of linear thermal expansion

Specimen ID	Average Coefficient of Linear Thermal Expansion
	(Inch/Inch/°F)
F4-791-2.5 #3	5.2×10^{-6}
F4-791-2.5 #4	5.1×10^{-6}
Average	5.2×10^{-6}

The coefficient of linear thermal expansion of concrete varies greatly with aggregate mineralogy and can be as low as 4×10^{-6} per degree F to as high as 13×10^{-6} per degree F^[ii]. The values determined by this testing are in the range for normal concrete.

The test results derived from this work shall not be used to imply endorsement by the Bureau of Reclamation or the U.S. Government and cannot be used for advertising or commercial purposes.

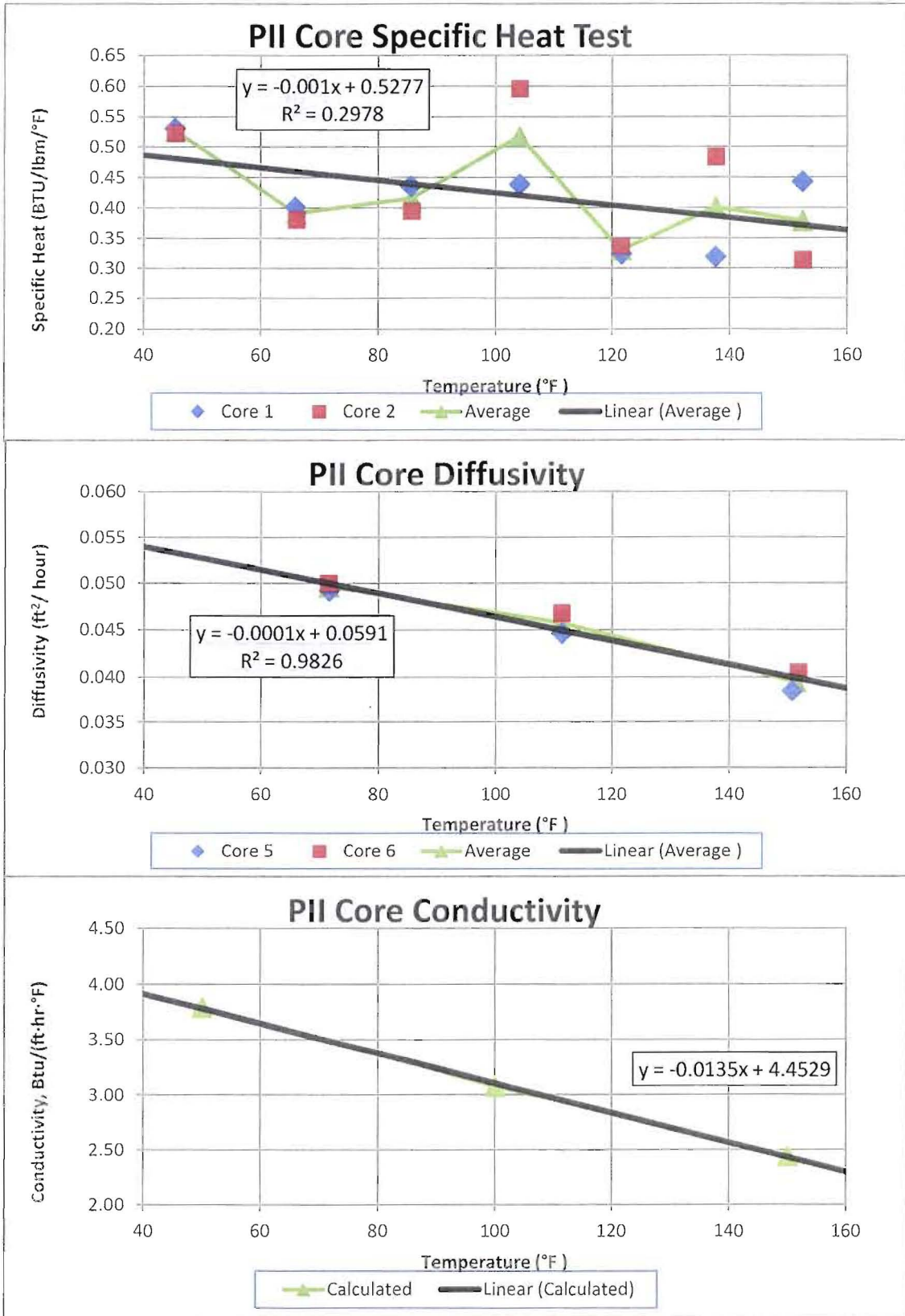
Attachments

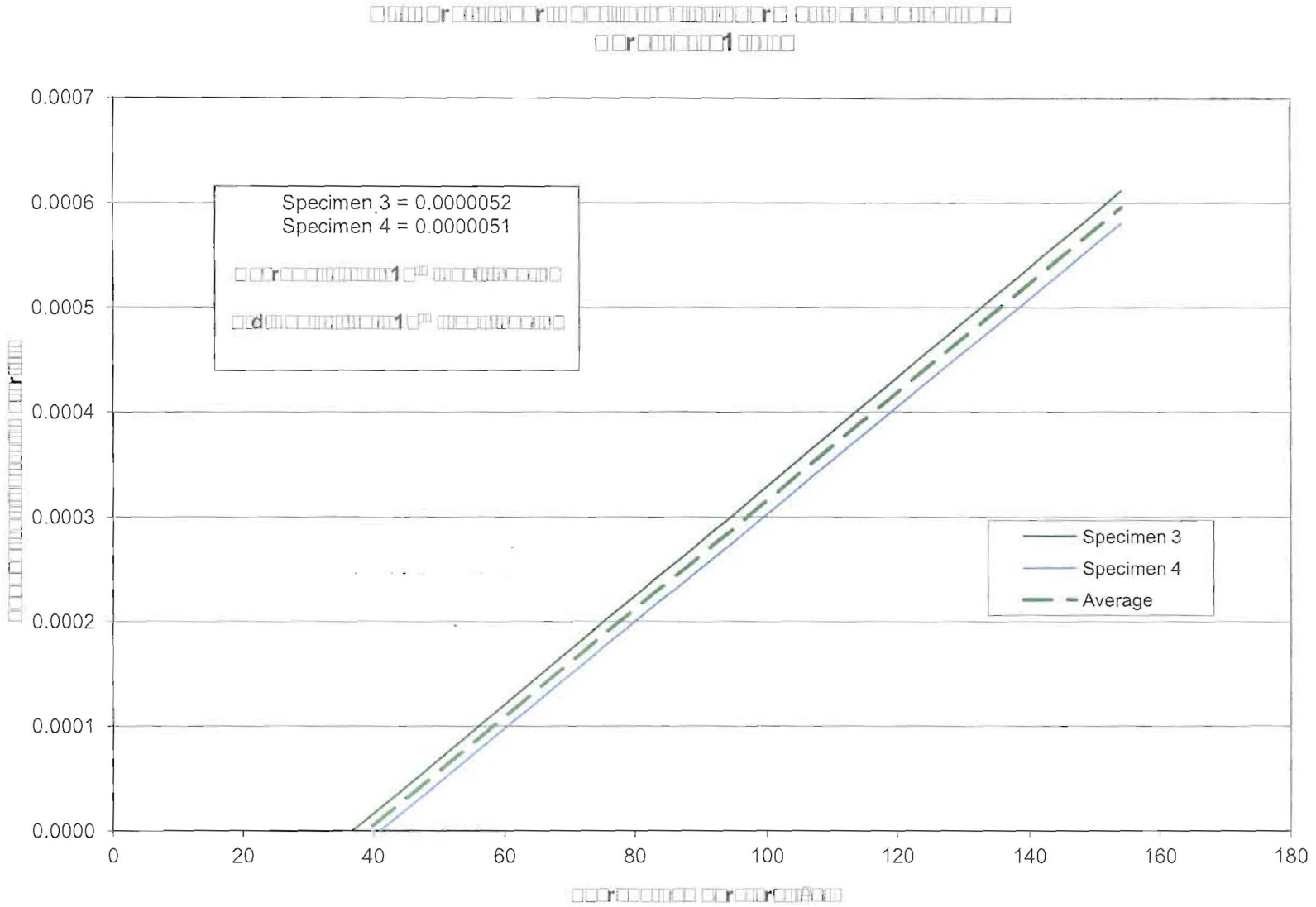
cc: Dr. Yungpin Xi, University of Colorado, yungpin.xi@colorado.edu (electronic copy)

[i] Concrete, Mindess and Young, Prentice-Hall, Inc., 1981

[ii] "Properties of Concrete, Fourth Edition" A.M. Neville, Pearson Education Limited, 2009.

[iii] "Concrete Manual, Part I, Eighth Edition", A Water Resources Technical Publication, U.S. Department of Interior, Bureau of Reclamation, Denver, CO, 1988 Reprint.





Project: PII Cores
Test Date: 12/21/2011
Test Age: not known

Bureau of Reclamation
Materials Engineering and Research Laboratory



Coefficient of Thermal Expansion of High Moisture Concrete

The coefficient of thermal expansion (CTE) of high moisture concrete is a highly nonlinear function of temperature. This is associated with the 9% volume expansion of the freezing of entrapped water. The freezing of water in small concrete pores does takes place at a lower temperature than 32°F due to surface tension which prevents the rearrangement to form ice. The end effect is that water in concrete freezes at varying temperatures depending on the pore size. This nonlinear dependence of the CTE with temperature is shown in Exhibit 57 and used as an input to the finite element analysis presented here.



Tests of moisture penetration were also performed at the University of Colorado at Boulder, which showed that a 1-D depth of water penetration up to 3 or 4 inches is possible when there are winds in excess of 90mph (such as during the 1978 blizzard).

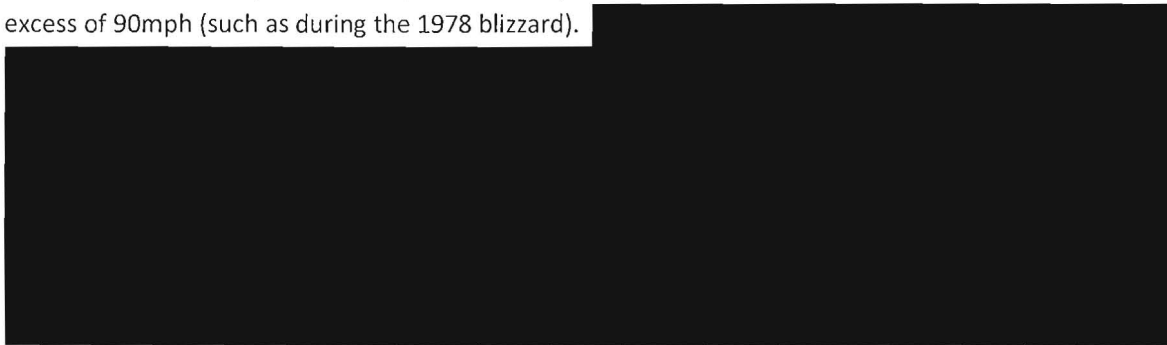




Figure 1 below shows the location of [REDACTED]

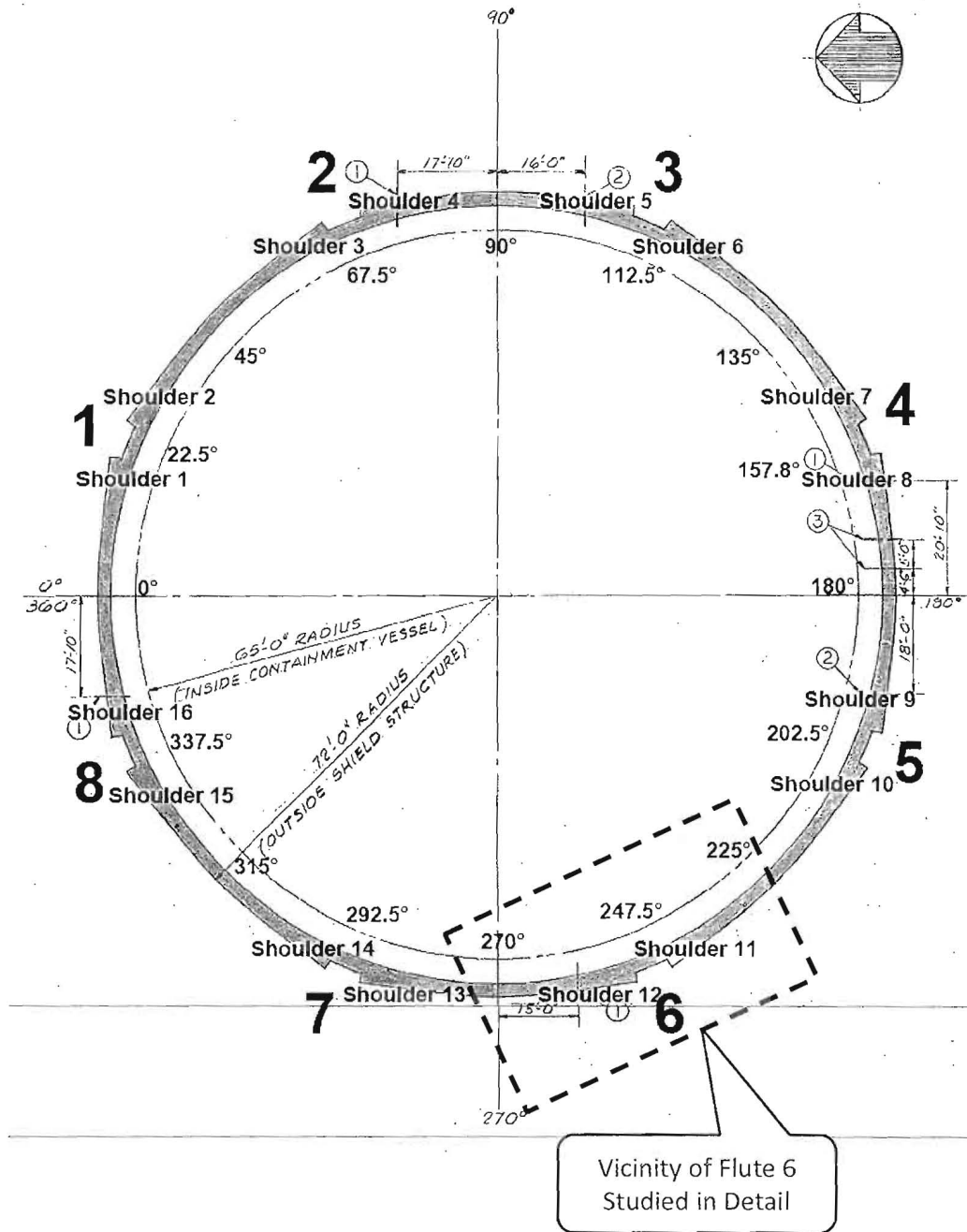


Figure 1 – Shield Building with Flute Numbers and Azimuth Locations [REDACTED]



Exhibit 60: Test Report from the University of Colorado

**OBSOLETE EXHIBIT
CONTENT UPDATED ELSEWHERE**



**Exhibit 61: Stress State during the
1977 and 1978 Blizzards**



Stress State during the 1978 and 1977 Blizzards

Table of Contents

Summary of Results.....	2
Modeling Summary	2
Overall Approach.....	2
Finite Element Software	3
Temperature Conditions.....	3
██████████	3
Modeled Geometry	3
Material Properties.....	3
Coefficient of Thermal Expansion of High Moisture Concrete.....	4
██████████	5
Circumferential Temperature Distribution at O.F. Horizontal Rebar	6
████████████████████	7
██████████	9
1978 Blizzard Condition	10
1977 Blizzard Condition	14



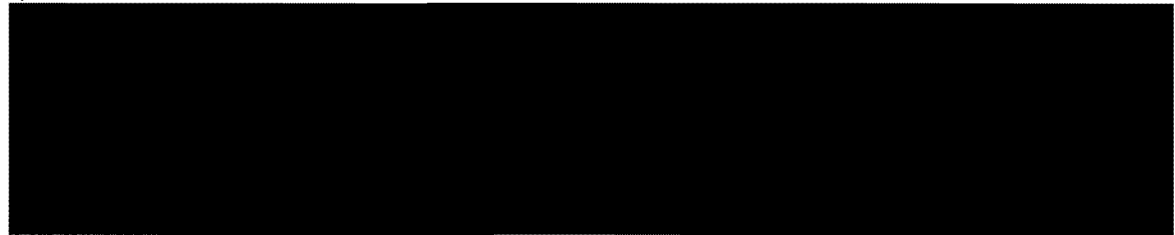
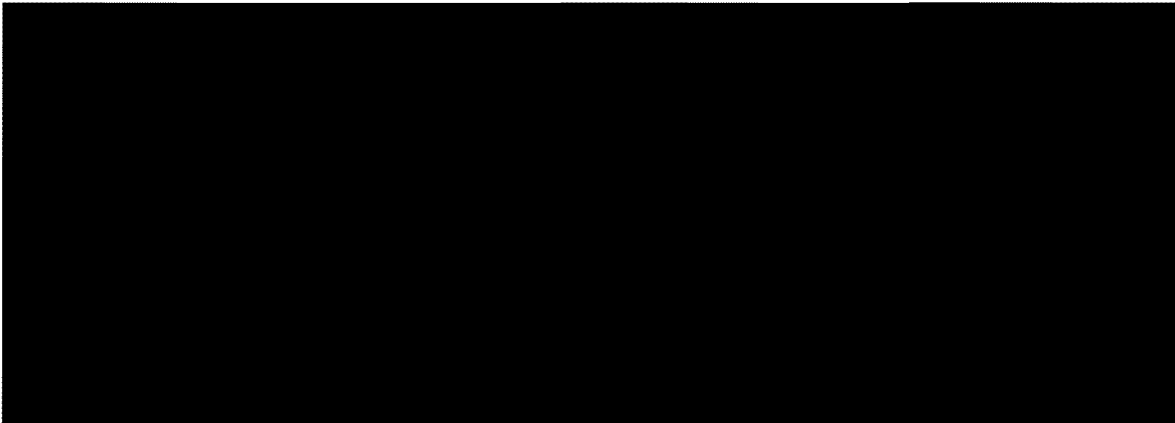
Summary of Results

The results of the analysis presented in this report can be summarized as follows:

- The blizzard of 1978 produced stresses above the tensile strength in the hoop direction, likely resulting in damage. The area exceeding the tensile strength is confined to a circumferential plane at the depth of the outer face main cylindrical wall under the raised shoulders.
- The 1977 blizzard shows significantly lower stress compared to the blizzard of 1978. The hoop stress approached the tensile strength of the concrete and it is limited to a small area. For these reasons only minor damage, if any, is predicted.

Modeling Summary

Overall Approach





Finite Element Software

[REDACTED] was used exclusively in the finite element analysis presented here.

Temperature Conditions

The following two temperature conditions are presented in this report. The details of the temperature conditions and the selection of the time of day are summarized separately in the Root Cause Analysis Report:

- 1) Low temperature during the 1978 blizzard (105 mph wind, winter solstice, 5:00 AM)
- 2) Low temperature during the 1977 blizzard (76 mph wind, winter solstice, 5:00 AM)

[REDACTED]
Expansion of concrete due to freezing of entrapped moisture was studied in the [REDACTED]. This model is utilized to determine the stress state in a subsection of the structure spanning from the middle of one panel to the middle of the adjacent panel. The raised shoulders and the flute geometry are included in the model. Nominal steel reinforcement is included using a technique called [REDACTED]. The detailed stress concentration at the steel and concrete interface is not included in the model.

Modeled Geometry

The drawings used as geometry input for this model are:

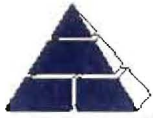
- Drawing No: C-100 Rev. 5 "Shield Building Foundation Plan & Details SH. 1"
- Drawing No: C-110 Rev. 6 "Shield Building Roof Plan Wall Section & Details"

All vertical reinforcing bars in the containment shell section are modeled as rebar #10 (diameter 1.270") at 12" center to center spacing. The inner face horizontal rebars are #8 (diameter 1.000") at 12" spacing. The outer face horizontal rebars are # 11 (diameter 1.410") at 12" spacing. The vertical and horizontal rebars in the shoulder sections are #8 at 12" spacing.

Material Properties

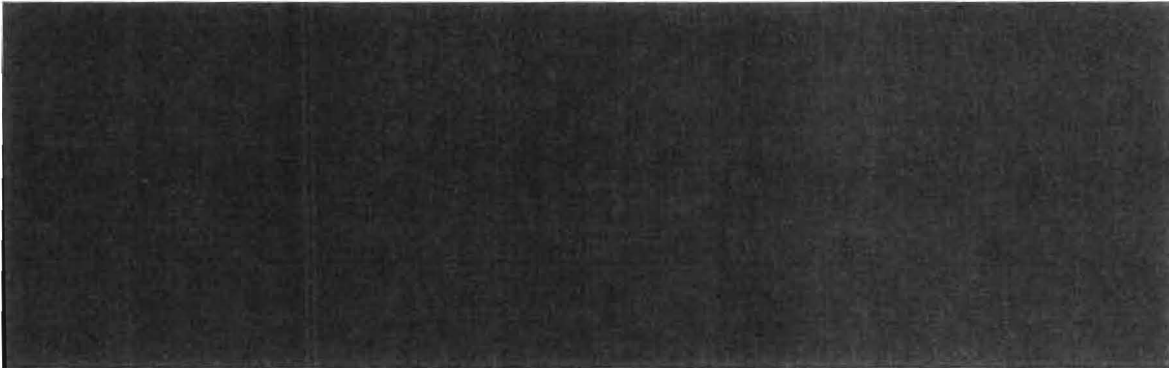
The material properties used as input to the finite element analysis in this report are summarized in the following documents attached to the Root Cause Analysis Report:

- Exhibit 56, Figure 2.1.4: Material Properties for Davis-Besse 3D [REDACTED] Model
- Exhibit 56, Section 4.7: Effects of Variable CTE
- Exhibit 57: Temperature dependent coefficient of thermal expansion (CTE)



Circumferential Temperature Distribution at O.F. Horizontal Rebar

(See Exhibit 65) The temperature profiles around the Shield Building at the outer face horizontal rebars are shown in Figure 2.



The figure shows 8 sets of double peaks for each temperature profile. The double peaks represent the warmer temperature under the shoulders. The temperature is warmer under the shoulders because there is a thicker layer of concrete at those locations which reduces the heat loss to the exterior during the blizzards.

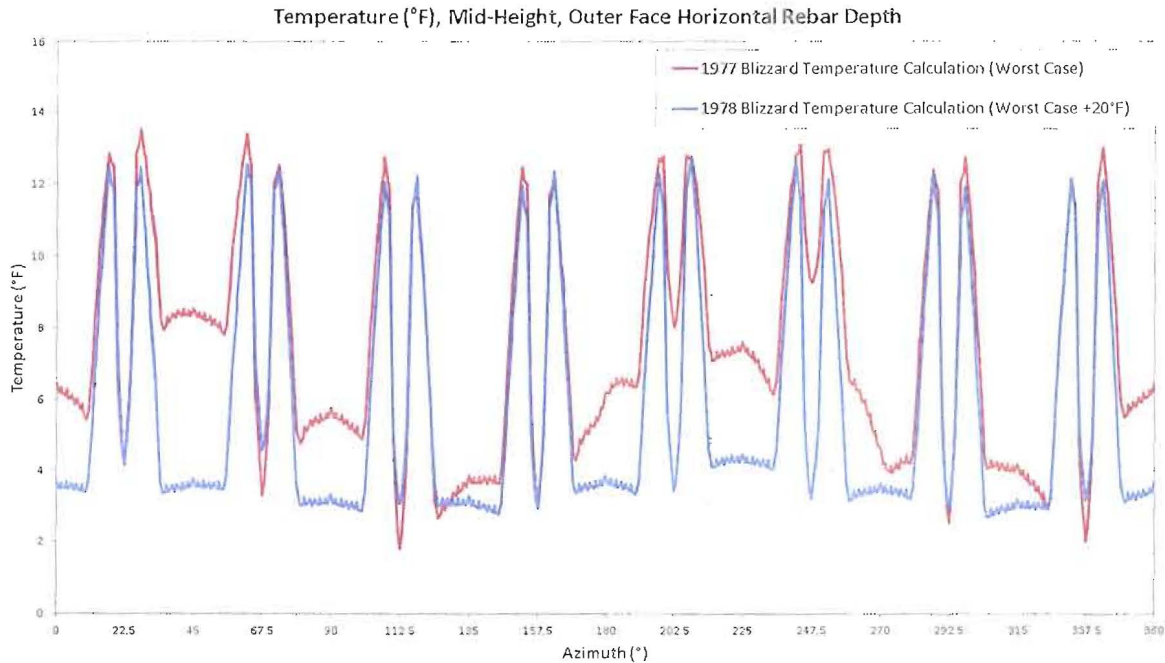
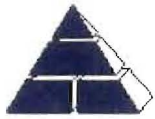


Figure 2 – Circumferential Temperature Distribution at the O.F. Horizontal Rebar Depth



[REDACTED]

includes concrete and steel rebars at nominal (as designed) spacing.

[REDACTED]

[REDACTED]

Figures 3 through 5 below depict the geometry and finite element mesh of the [REDACTED]

[REDACTED]

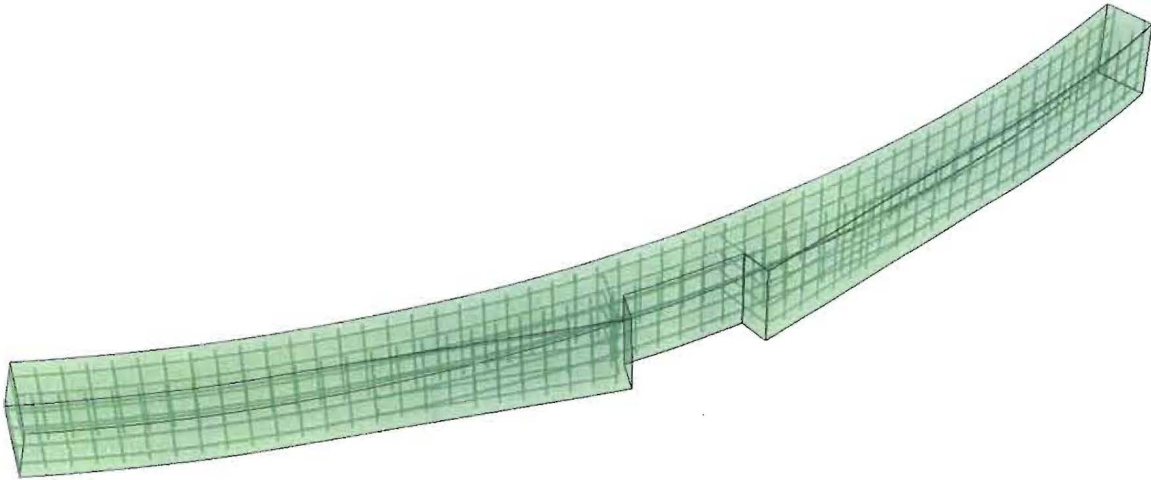


Figure 3 -- [REDACTED] Geometry and Rebars

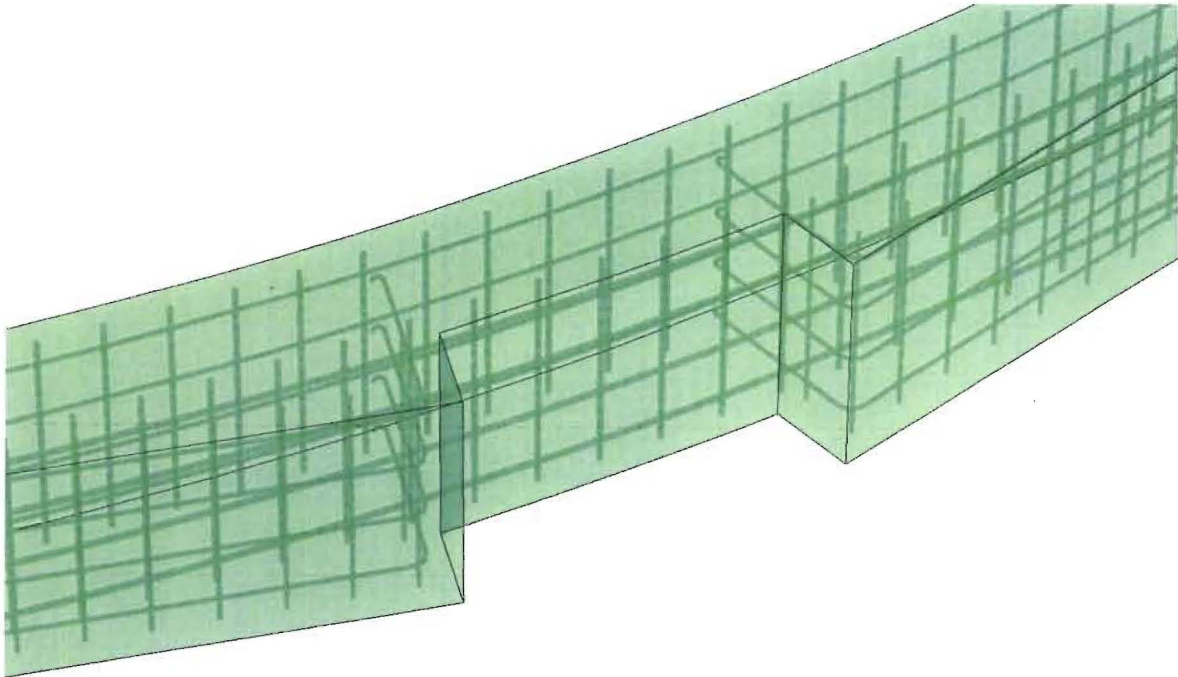
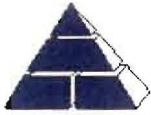


Figure 4 – [REDACTED] Detail of Flute Region

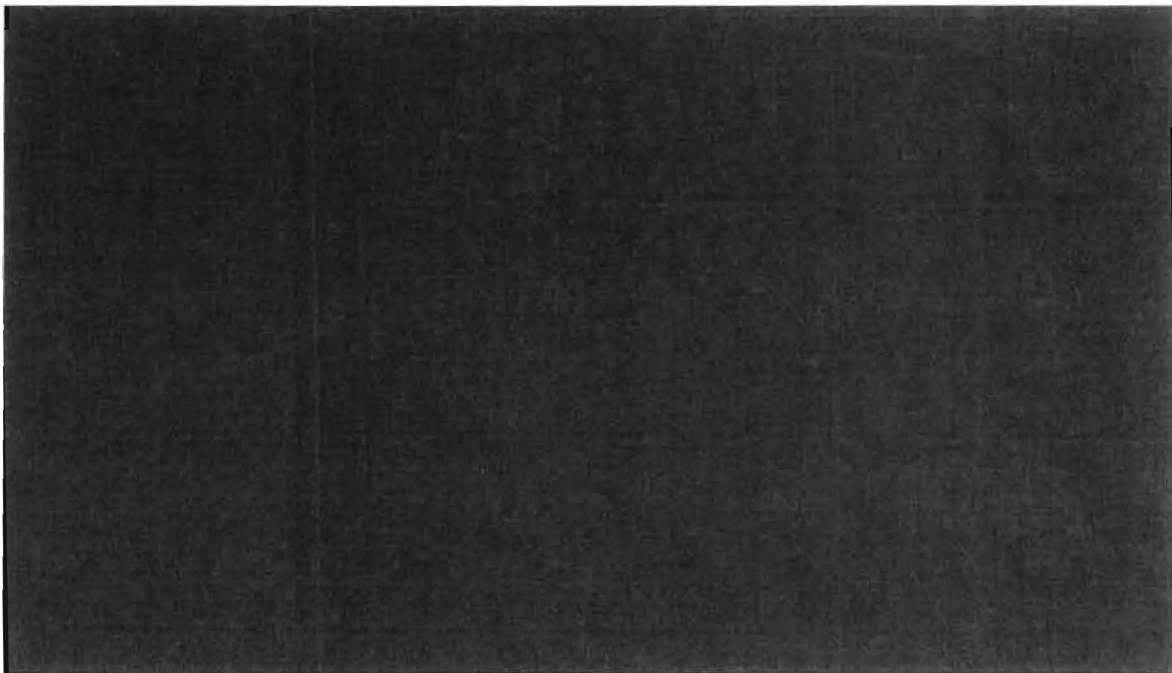


Figure 5 – [REDACTED]; Detail of Flute Region with Mesh



This section summarizes the results [REDACTED] is used to make predictions about the delamination propensity due to the two blizzard conditions. This model does not attempt to make predictions of stress concentration effects around the included reinforcing bars due to lack of detail at the concrete/steel interface.

The tensile strength of the Davis-Besse concrete is in the range of 836 to 962 psi. The contours in the stress figures in this section are assigned an upper limit of 900 psi. A tensile stress exceeding 900 psi is indicated by light grey contours in the stress figures. The interpretation of any light grey area in the contour plots below is that damage may occur in that area. The damage that results from any tensile stress above the strength of the concrete depends on 3D stress state as well as the strain energy available to open the crack. Low strain energy results in microcracks and high strain energy results in more microcracking and eventually a structural crack.

The stress contour results shown in this section can be summarized as follows:

- Higher tensile stress and larger stressed areas is predicted in the 1978 blizzard compared to the 1977 blizzard
- Blizzard of 1978:
 - Tensile stresses high enough to damage the concrete is predicted
 - The high stresses are distributed over large areas in the observed crack locations under the thick sections of the shoulders and not in the thinner sections in the flute and panels
- Blizzard of 1977:
 - Tensile stresses are lower or equal to the strength of the concrete
 - The highest tensile strength are confined to small areas under the thick sections of the shoulders



1978 Blizzard Condition

The result [REDACTED] due to the 1978 blizzard condition is shown in this section. The temperature contours can be seen in Figure 6 and the stress results is shown in Figures 7 through 12.

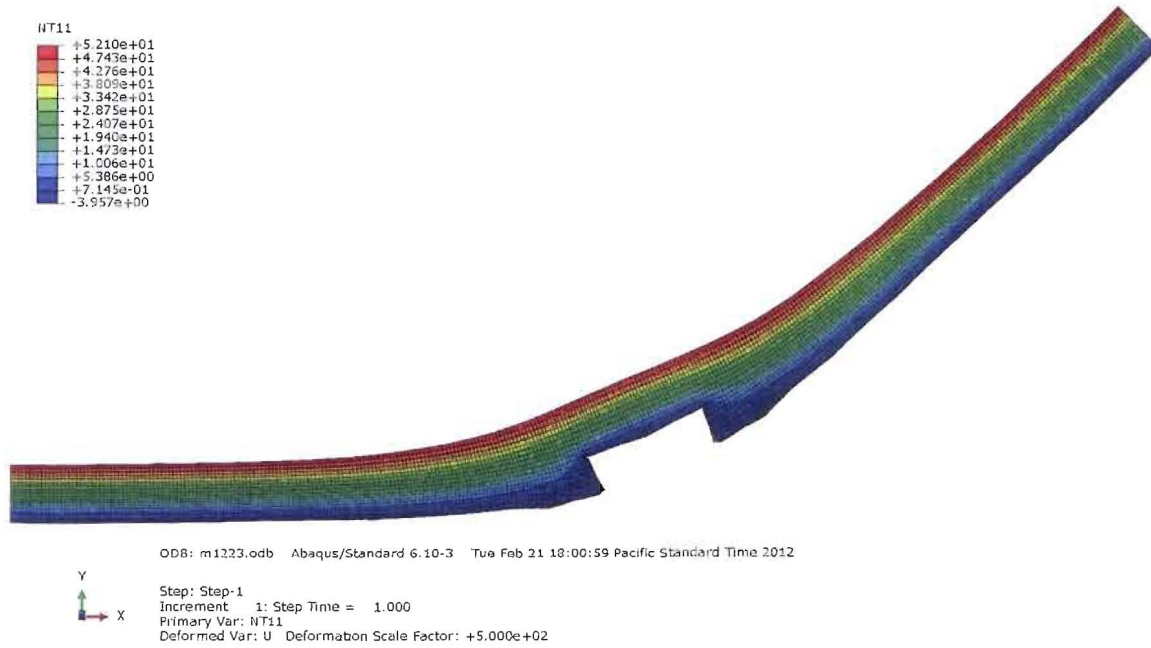


Figure 6 – Temperature (°F) during the Blizzard of 1978; Deformation Scale Factor 500X

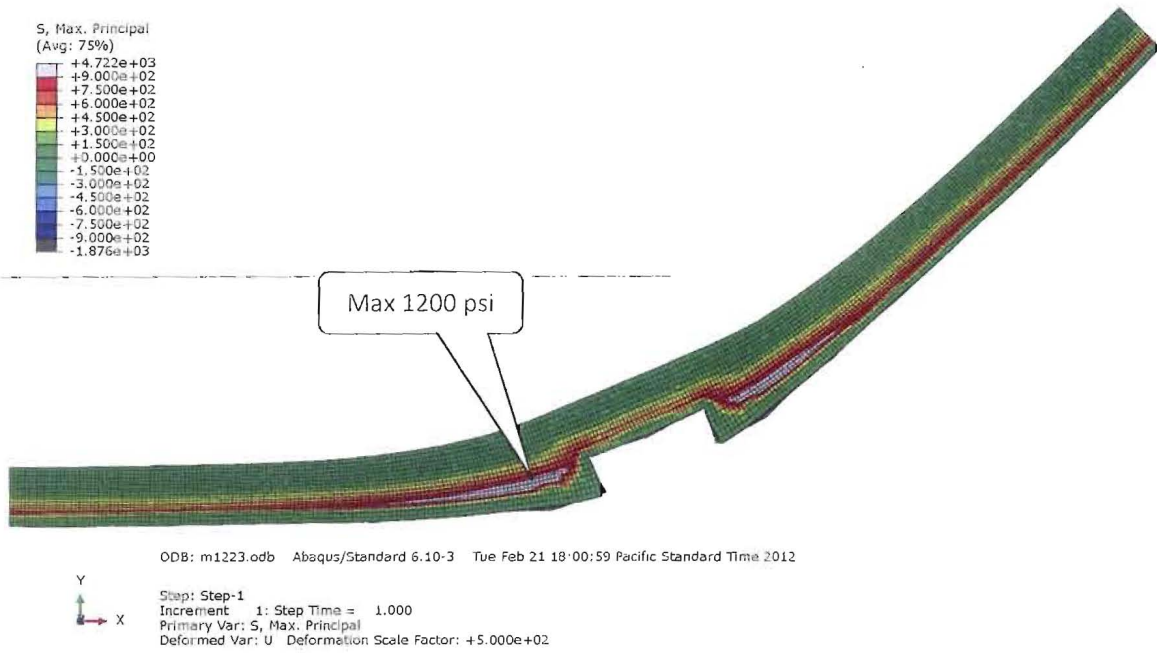


Figure 7 – Max Principal Stress (psi) during the 1978 Blizzard; Deformation Scale Factor 500X

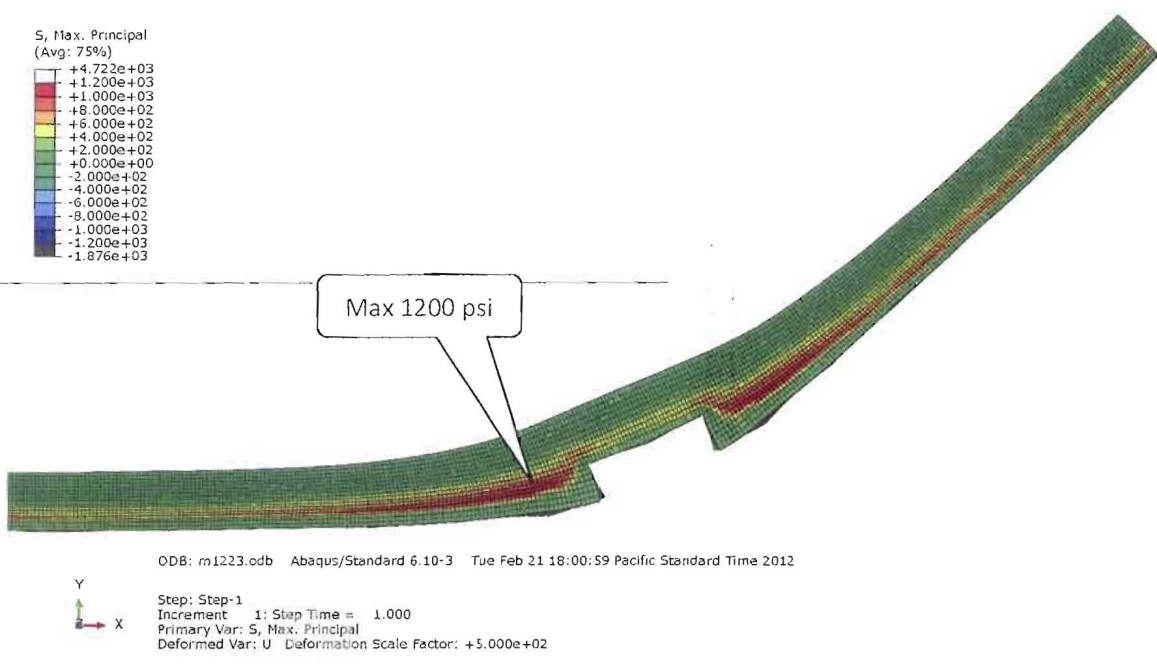


Figure 8 – Max Principal Stress (psi) during the 1978 Blizzard; Deformation Scale Factor 500X; Wider Contour Range (+/- 1200 psi)

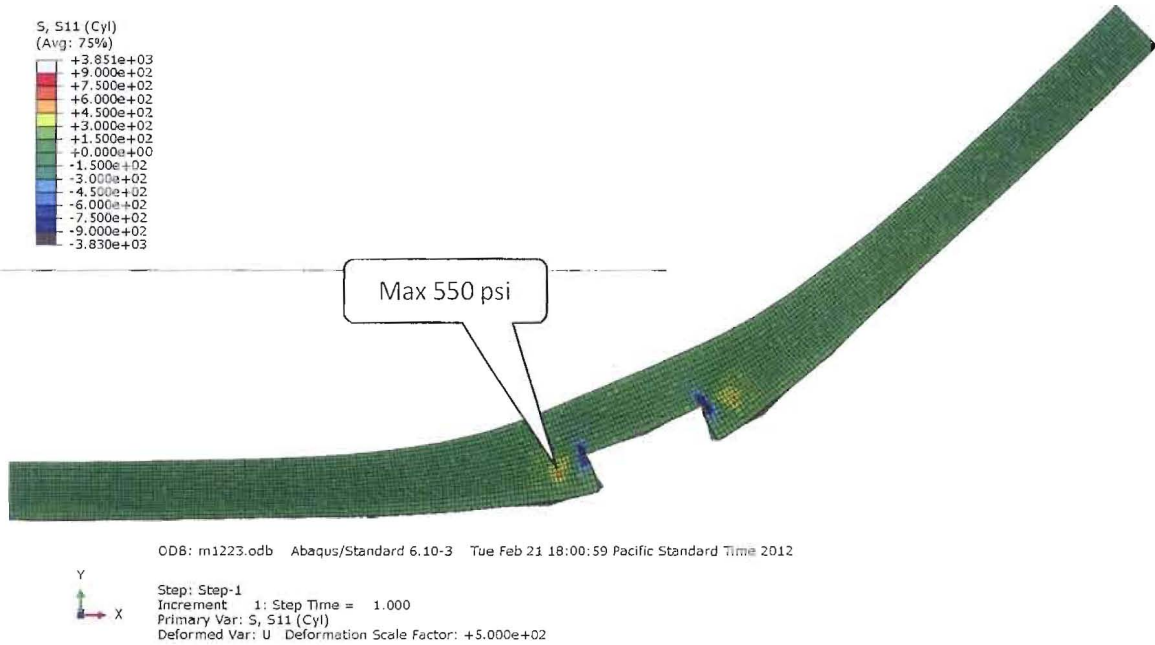
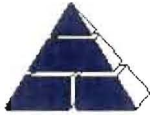


Figure 9 – Radial Stress (psi) during the Blizzard of 1978; Deformation Scale Factor 500X

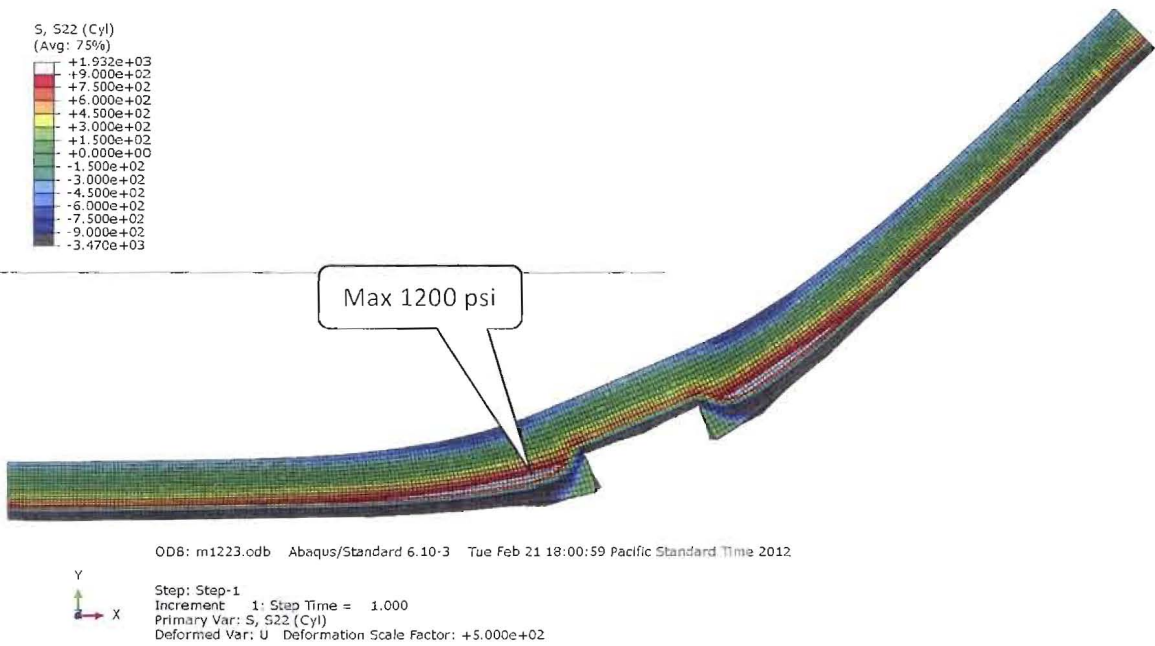


Figure 10 – Hoop Stress (psi) during the Blizzard of 1978; Deformation Scale Factor 500X

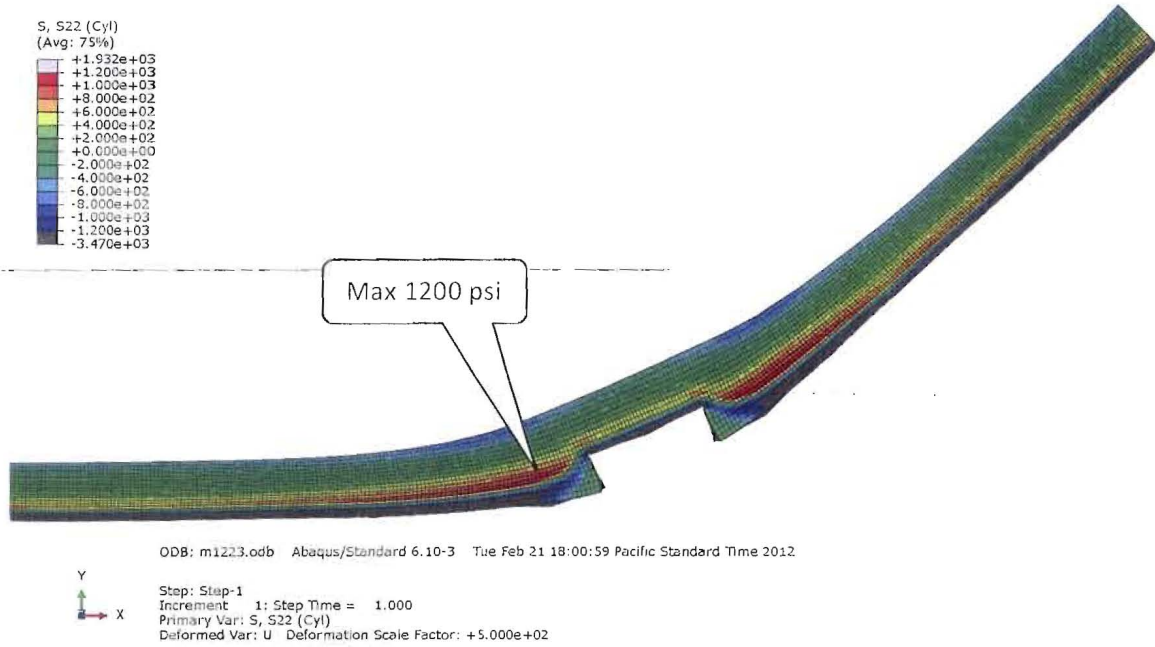


Figure 11 – Hoop Stress (psi) during the Blizzard of 1978; Deformation Scale Factor 500X; Wider Contour Range (+/- 1200 psi)

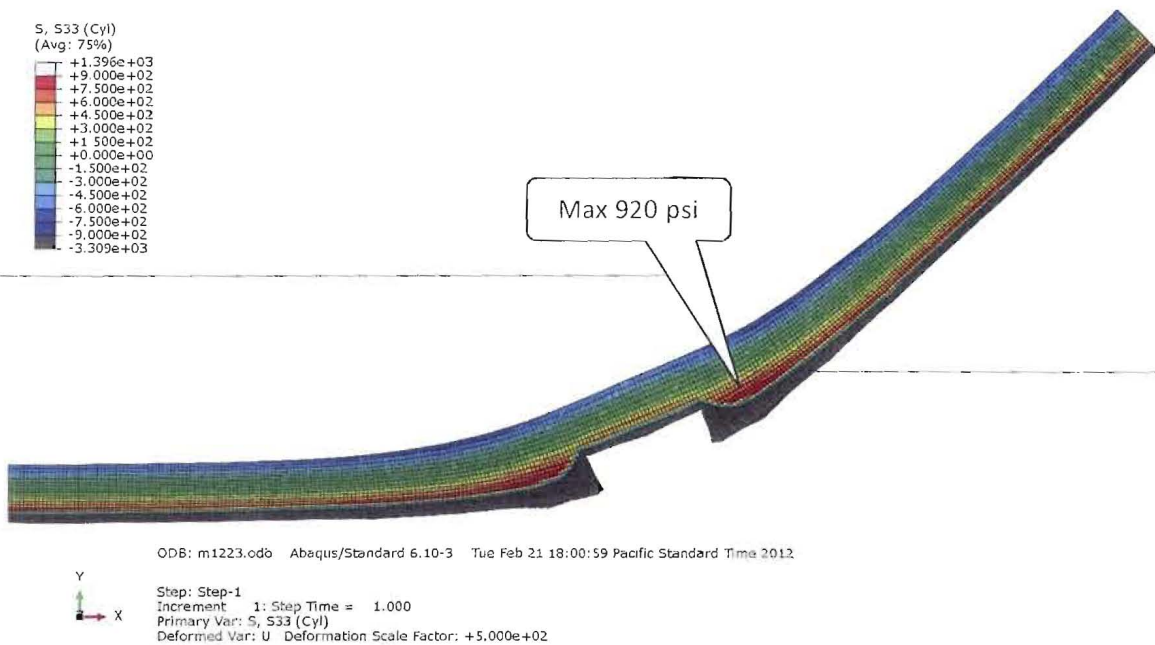


Figure 12 – Vertical Stress (psi) during the Blizzard of 1978; Deformation Scale Factor 500X



1977 Blizzard Condition

The result [REDACTED] due to the 1977 blizzard condition is shown in this section. Figure 13 depicts the temperature distribution in the model. Figures 14 through 17 show the stress state in the max principal, radial, hoop, and vertical directions, respectively.

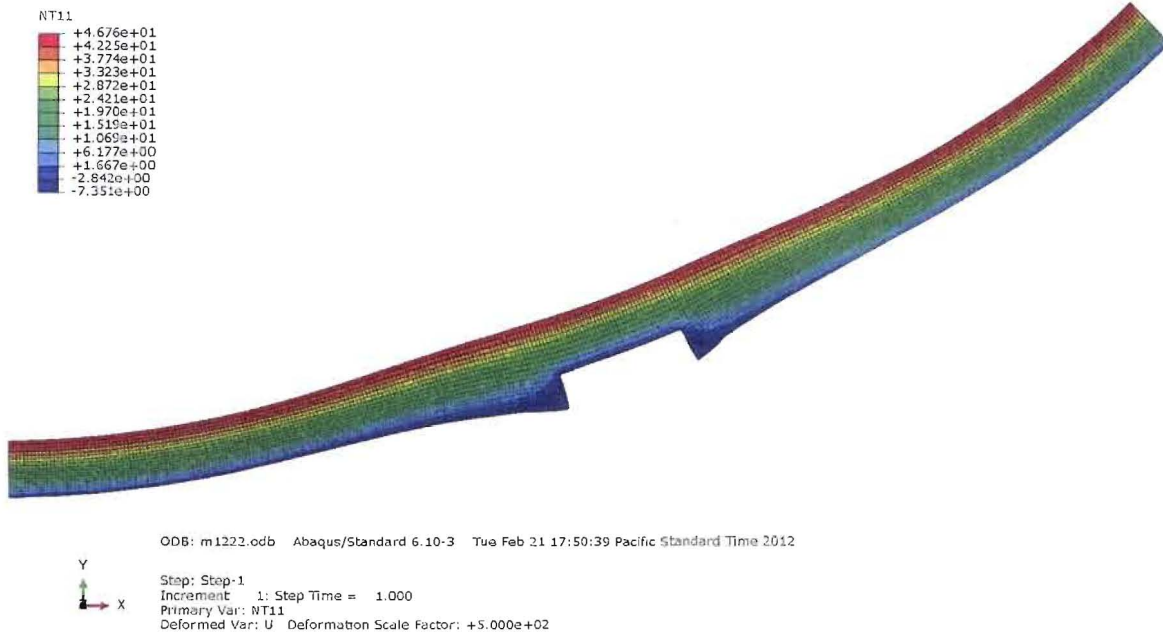


Figure 13 – Temperature (°F) during the Blizzard of 1977; Deformation Scale Factor 500X

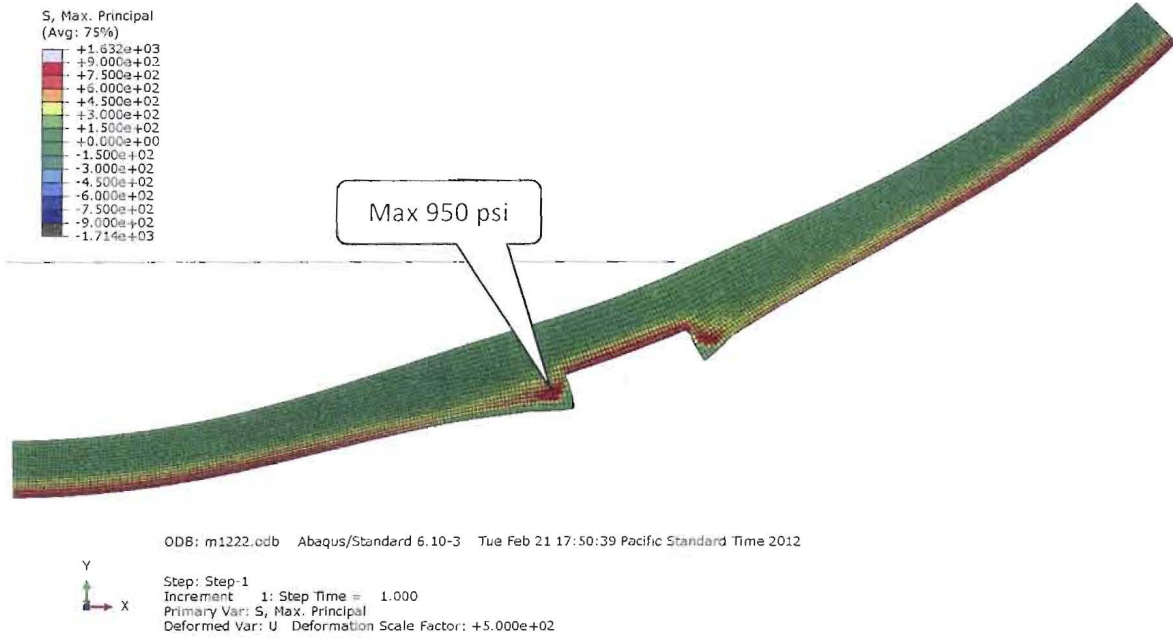


Figure 14 – Max Principal Stress (psi) during the Blizzard of 1977; Deformation Scale Factor 500X



Figure 15 – Radial Stress (psi) during the Blizzard of 1977; Deformation Scale Factor 500X

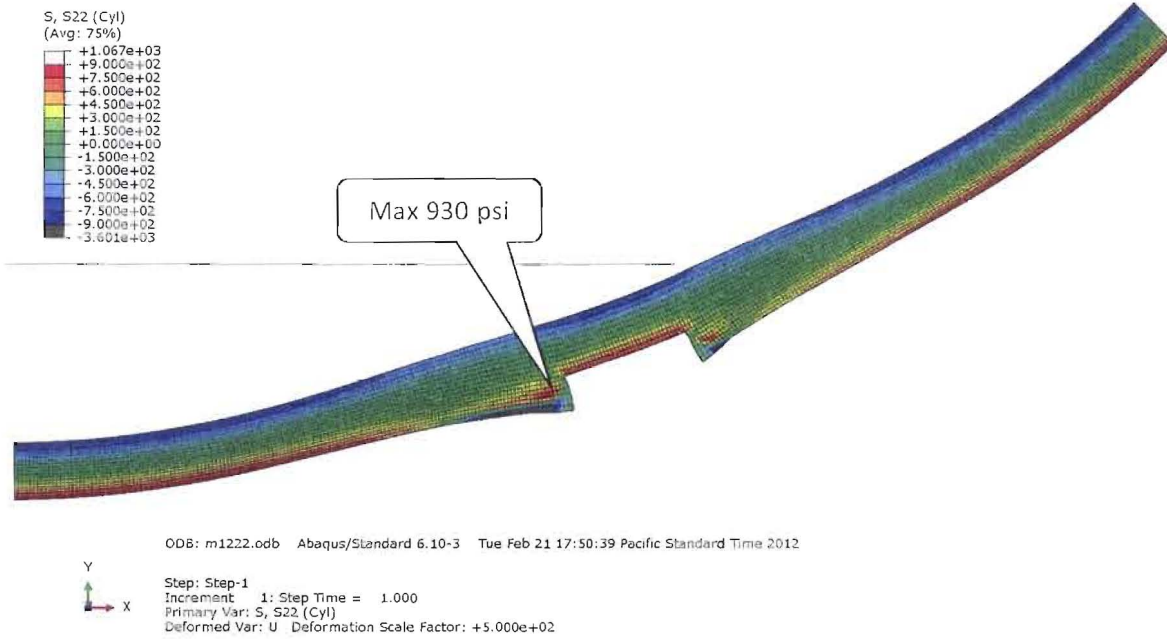


Figure 16 – Hoop Stress (psi) during the Blizzard of 1977; Deformation Scale Factor 500X

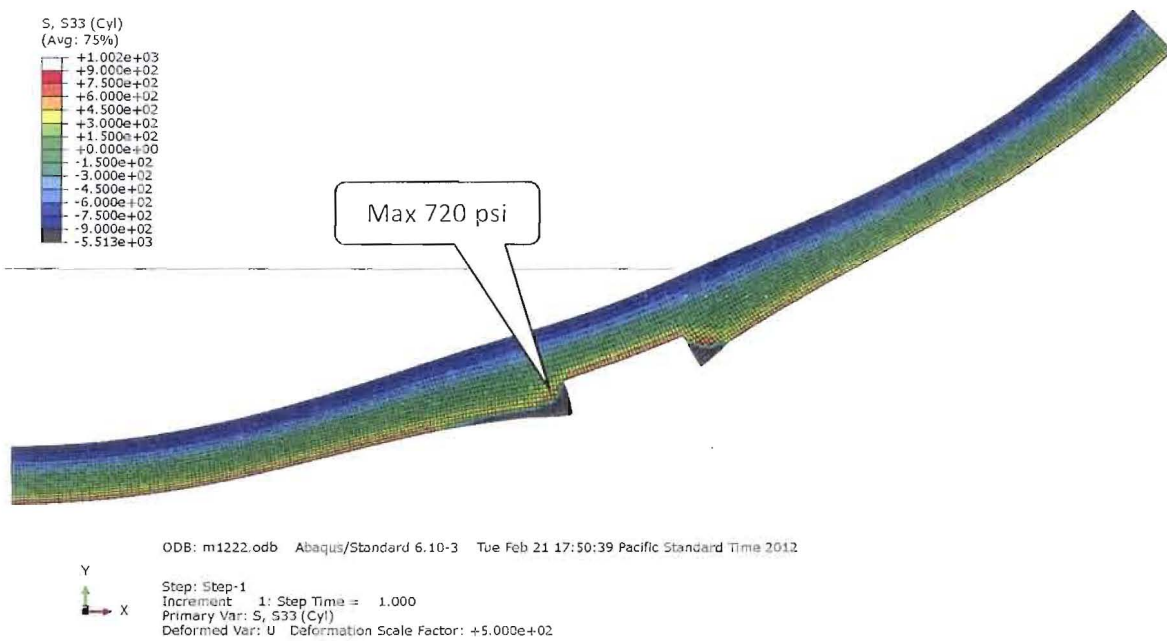


Figure 17 – Vertical Stress (psi) during the Blizzard of 1977; Deformation Scale Factor 500X



Exhibit 62: Stress Analysis due to 105 MPH Wind Load

Stress Analysis due to 105 mph Wind Load

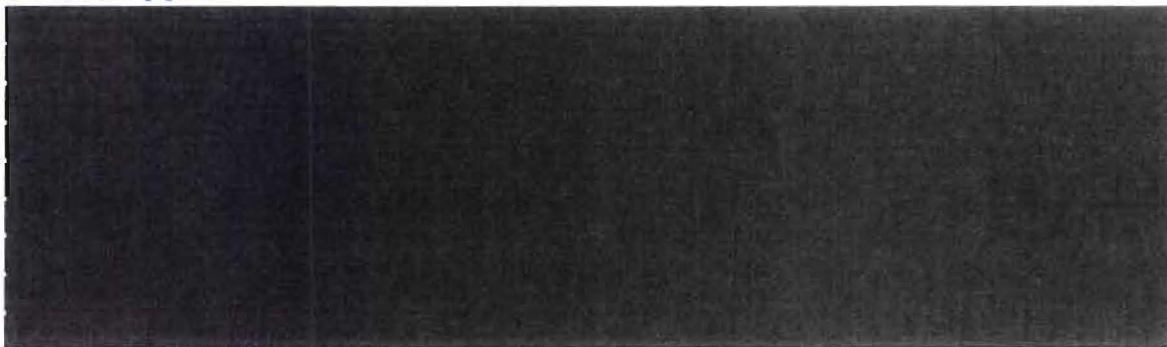
Summary of Results

The results of the analysis presented in this report can be summarized as follows:

- The wind pressure does not produce stresses capable of delaminating the structure.
- The 105 wind pressure load results in a max principal stress of about 55 psi
- The 105 wind pressure load results in a radial stress of less than 1 psi

Modeling Summary

Overall Approach



Finite Element Software

[REDACTED] was used exclusively in the finite element analysis presented here.

Modeled Geometry

The drawings used as geometry input for this model are:

- Drawing No: C-100 Rev. 5 "Shield Building Foundation Plan & Details SH. 1"
- Drawing No: C-110 Rev. 6 "Shield Building Roof Plan Wall Section & Details"

All vertical reinforcing bars in the containment shell section are modeled as rebar #10 (diameter 1.270") at 12" spacing. The inner face horizontal rebars are #8 (diameter 1.000") at 12" spacing. The outer face horizontal rebars are # 11 (diameter 1.410") at 12" spacing. The vertical and horizontal rebars in the shoulder sections are #8 at 12" spacing.

Material Properties

The material properties used for this analysis are summarized in Exhibit 56, Figure 2.1.4: Material Properties [REDACTED].

[REDACTED]

Figure 1 shows the radial displacement due to gravity and the 105 mph wind load. The maximum radial deflection is about 0.07 inch inward on the side of the structure facing the wind and about 0.07 inch outward on the sides of the structure that are parallel to the wind direction.

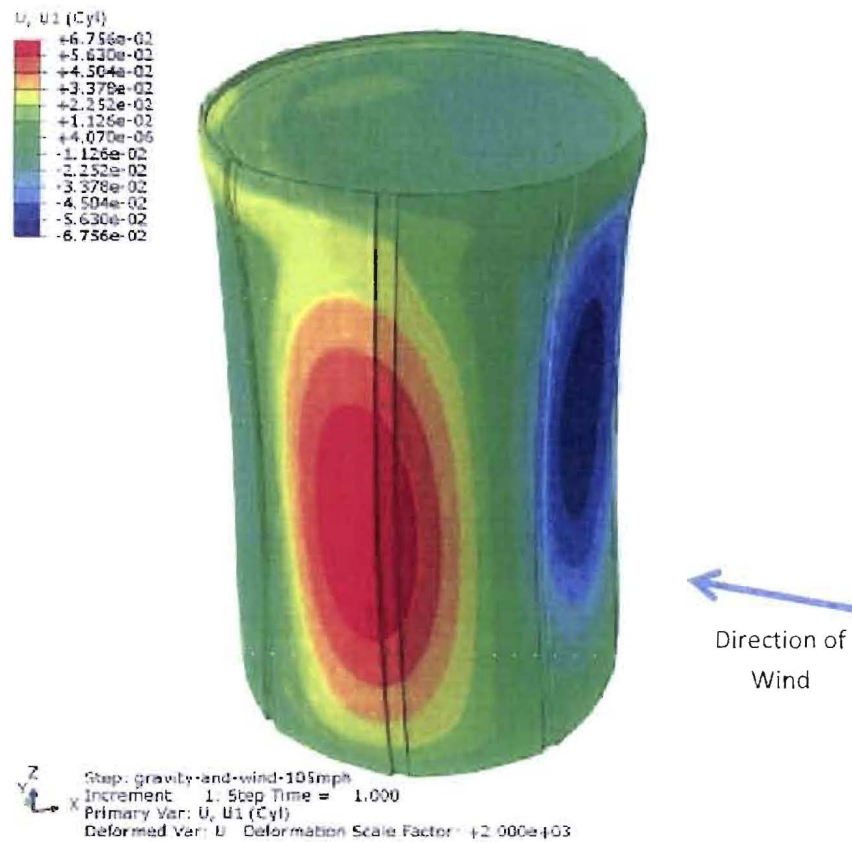


Figure 1 – Radial Displacement (inches) due to Gravity and 105 mph Wind Load; Deformation Scale Factor = 2000X

Figure 2 depicts the max principal stress [redacted] due to gravity and the 105 mph wind pressure load. The maximum stress due to the wind load is 55 psi although some larger stresses can be seen in the ring girder area. The stresses in the ring girder are a result of the dome weight and not due to the wind load.

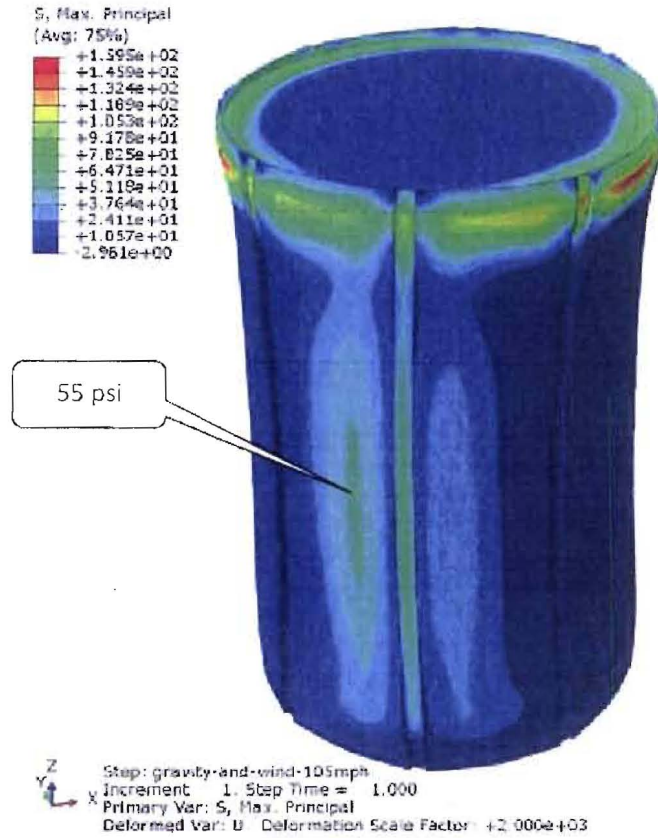


Figure 2 – Max Principal Stress (psi) due to Gravity and 105 mph Wind Load; Deformation Scale Factor = 2000X



Figure 3 – Location [redacted]

[REDACTED]

Figures 4 and 5 below depict the max principal and radial stress [REDACTED]. The max principal stress shown in Figure 4 correlates well with [REDACTED] shown in Figure 2. Both the location and magnitude of the max principal stress are in agreement. Figure 5 indicates that the radial stress is very low due to the combined gravity and wind load. The only location that experiences any significant radial stress is the corner of the flute. However, the corner of the flute location is a singularity due to the sharp angle between two elements in the finite element mesh. In the region of interest the radial stress is below 1 psi.

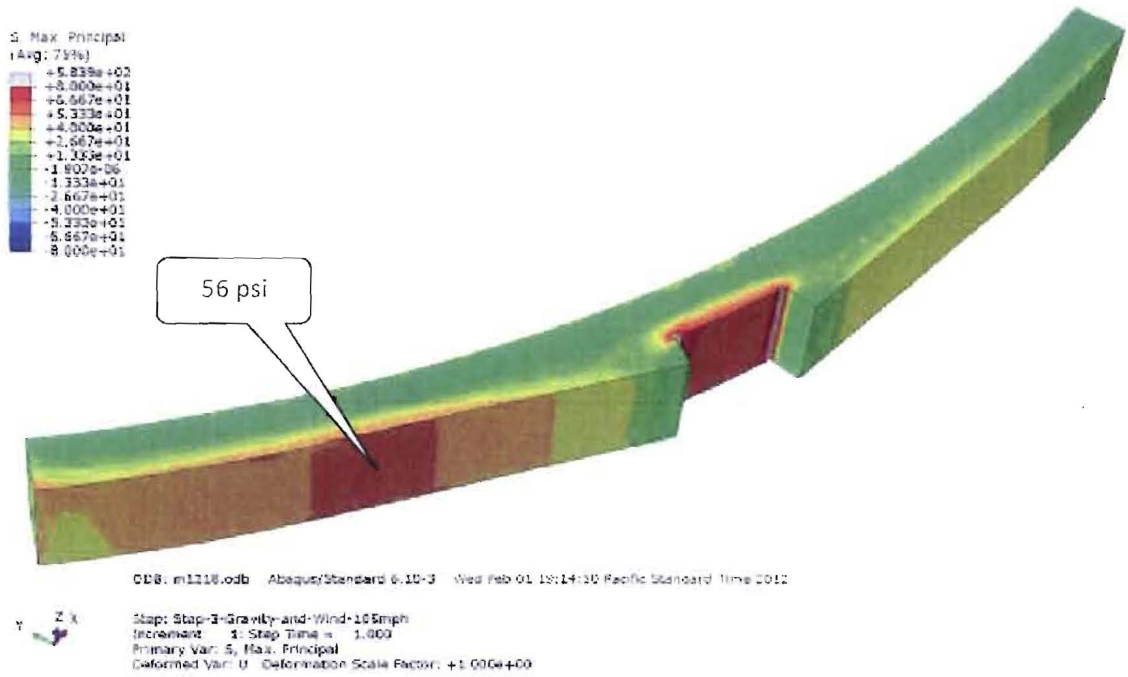


Figure 4 – Max Principal Stress (psi) due to Gravity and 105 mph Wind

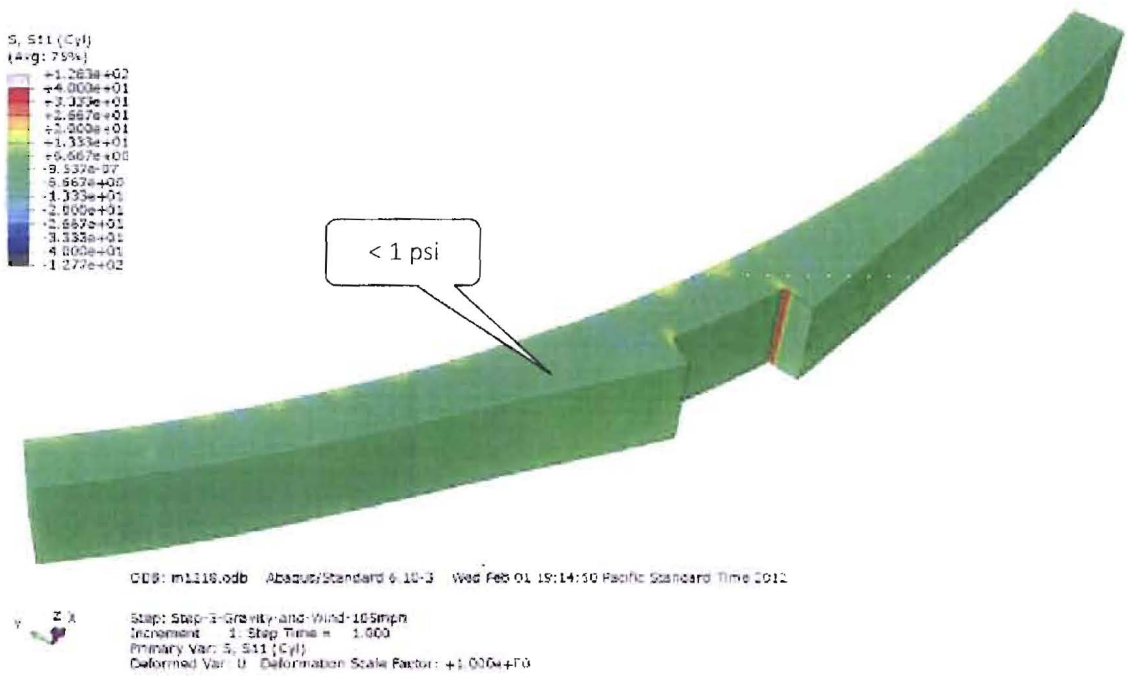
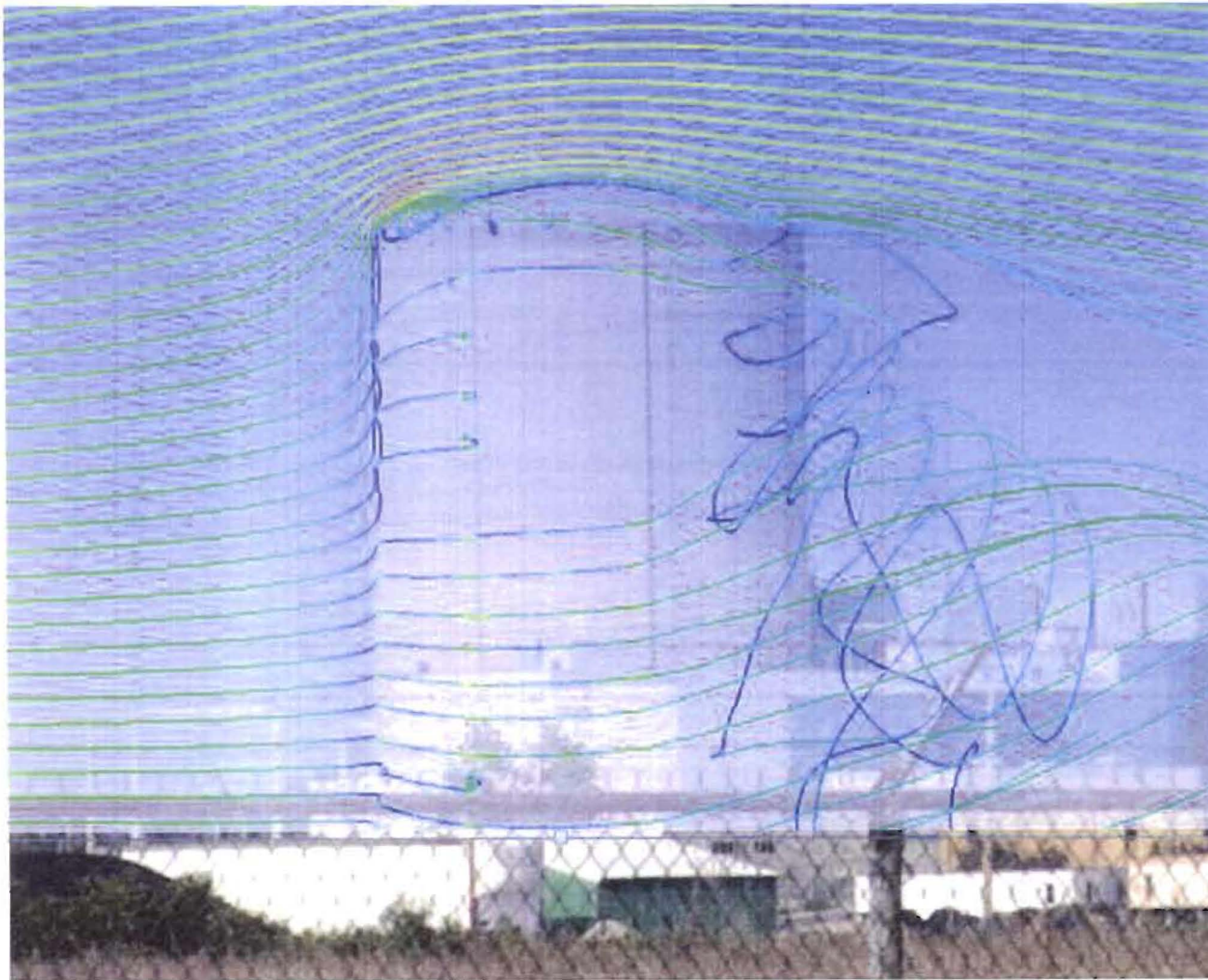


Figure 5 – Radial Stress (psi) due to Gravity and 105 mph Wind



Exhibit 63: CFD Analysis of Shield Building



CFD ANALYSIS OF DAVIS-BESSE CONTAINMENT TOWER

ANALYSIS PERFORMED BY: [REDACTED]

JANUARY 1, 2012

[REDACTED] information. Performance Improvement international, LLC. [REDACTED]



Davis-Besse Containment Tower Requirements

The CFD analysis performed for this report includes:

	Pages
• No surrounding buildings	
• 34mph from the Northwest (summer)	5-9
• 34mph from the Southwest (winter)	10-14
• 72mph from the Southwest (winter)	15-22
• With surrounding buildings	
• 34mph from the Northwest (summer)	24-28
• 72mph from the Southwest (winter)	29-34
• 105mph from the Southwest (winter)	35-40
• Tornado	41-44
• Category F2	
• Traveled from the Northwest to Southeast	

Boundary Conditions for the problem consisted of:

- Winter
 - Ambient temperature of -13°F.
 - Temperature of the containment tower remained at a constant 7°F.
- Summer
 - Ambient temperature of 104°F.
 - Temperature of the containment tower remained at a constant 130°F.

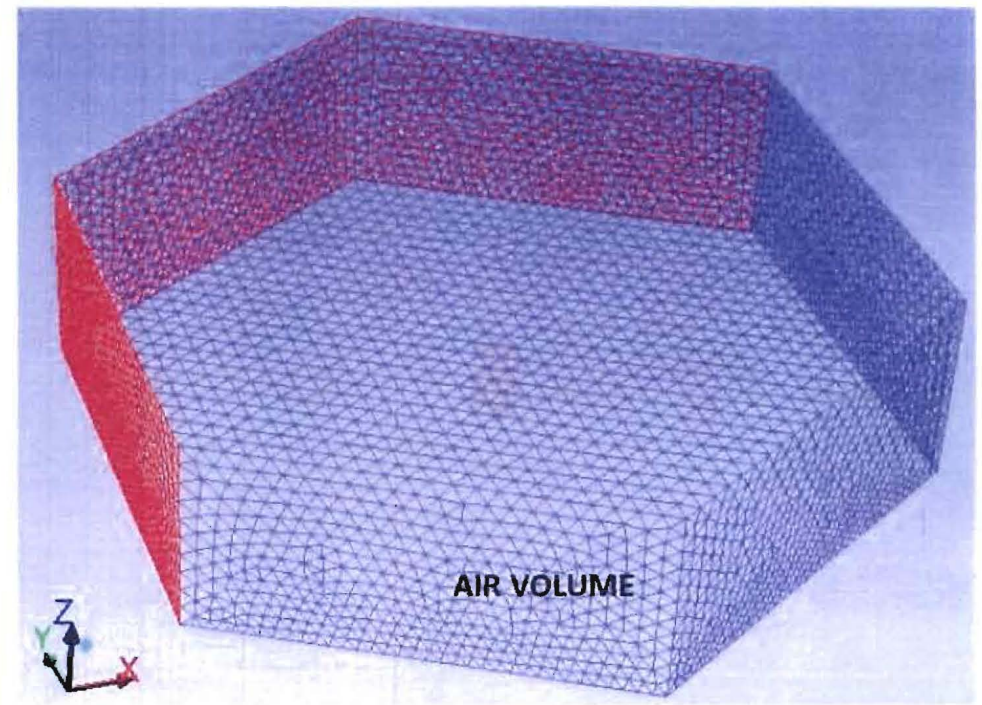
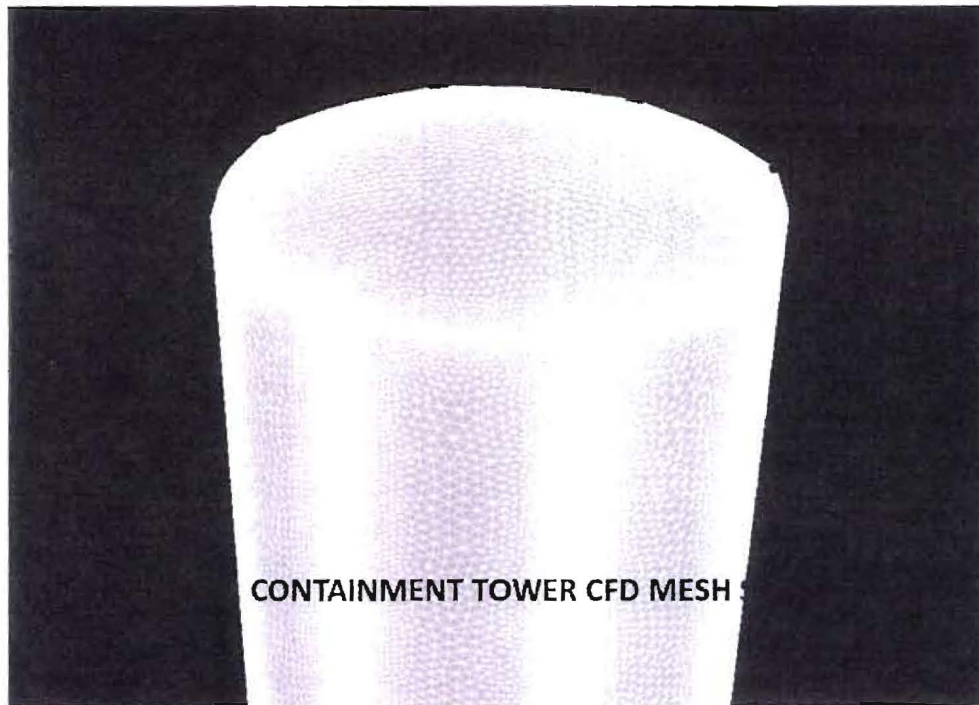
Results extracted from the CFD:

- Pressure distributions on the surface.
- Heat transfer coefficients.
- Vorticity shedding calculated on the 72mph case.

Model Creation

- The CFD mesh consisted of 3.6 million cells to create the air volume.
- Total size of the air volume was a 2,500 ft. diameter and a height of 670 ft.
- Using a large air volume eliminates any wall effects.

Using a small mesh size allows the vorticity shedding to be captured more accurately.





Solution Method

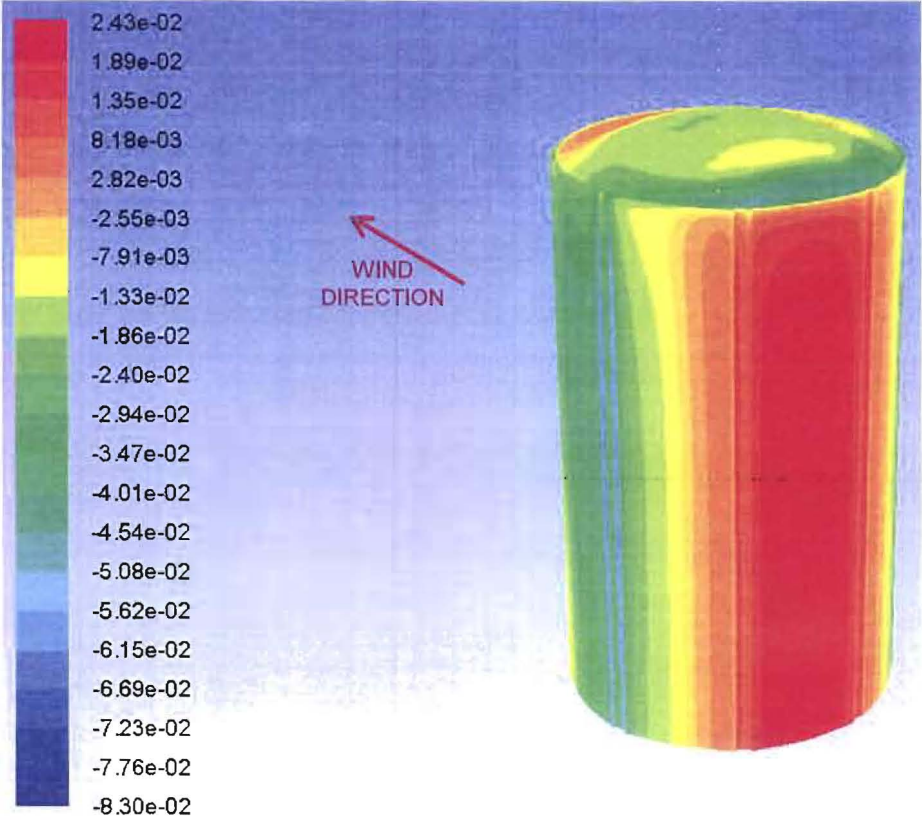
- The CFD program used for this analysis was Fluent version 13, an industry standard and proven analytical code.
- Incompressible ideal gas law was used, because the wind speeds are below Mach 0.55.
- The containment tower analysis without the buildings was done using a steady state solution.
- The containment tower analysis with the building was done using a transient analysis solution.



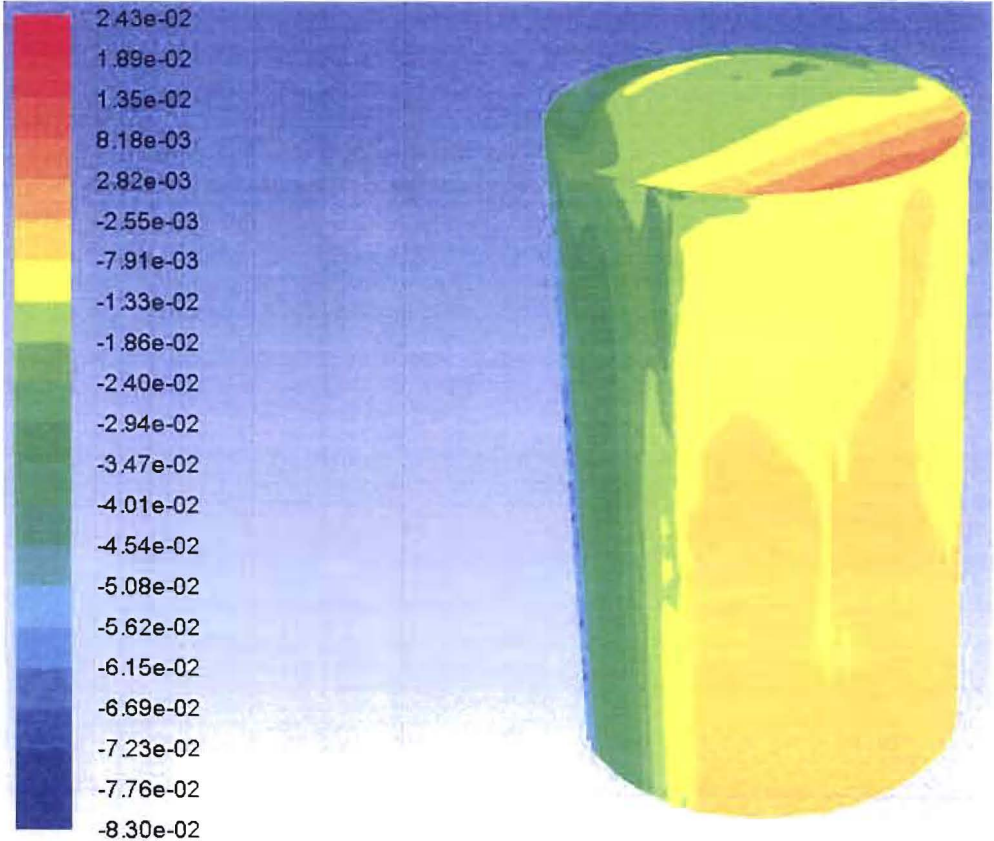
34mph FROM THE NORTHWEST (SUMMER)

Davis-Besse Containment Tower CFD Results

34mph Northwest Summer Conditions



FRONT



BACK

PRESSURE CONTOURS (psi)



HEAT TRANSFER COEFFICIENT HAND CALCULATIONS FOR ANALYTICAL COMPARISON

TOWER = 130°F (54.4°C)

AIR TEMP = 104°F (40°C)

TEMP AVERAGE = 117°F (42.22°C)

$\nu = 0.1693 \text{ cm}^2/\text{s}$

$k = 0.027 \text{ w/m}^*\text{k}$

$Pr = 0.71$

$U = 15.20 \text{ m/s (34mph)}$

$D = 44.73\text{m}$

$Re = U*D / \nu$

$Re = 40,159,244$

$Nu = h*D/k$

$Nu = 0.3 + (0.62*Re^{0.5}*Pr^{0.33})/([1+(0.4/Pr)^{0.67}]^{0.25}) * [1+(Re/282,000)^{0.625}]^{0.8}$

$Nu = 38,092$

$h = (38,092*0.027 \text{ w/m}^*\text{k}) / 44.73\text{m}$

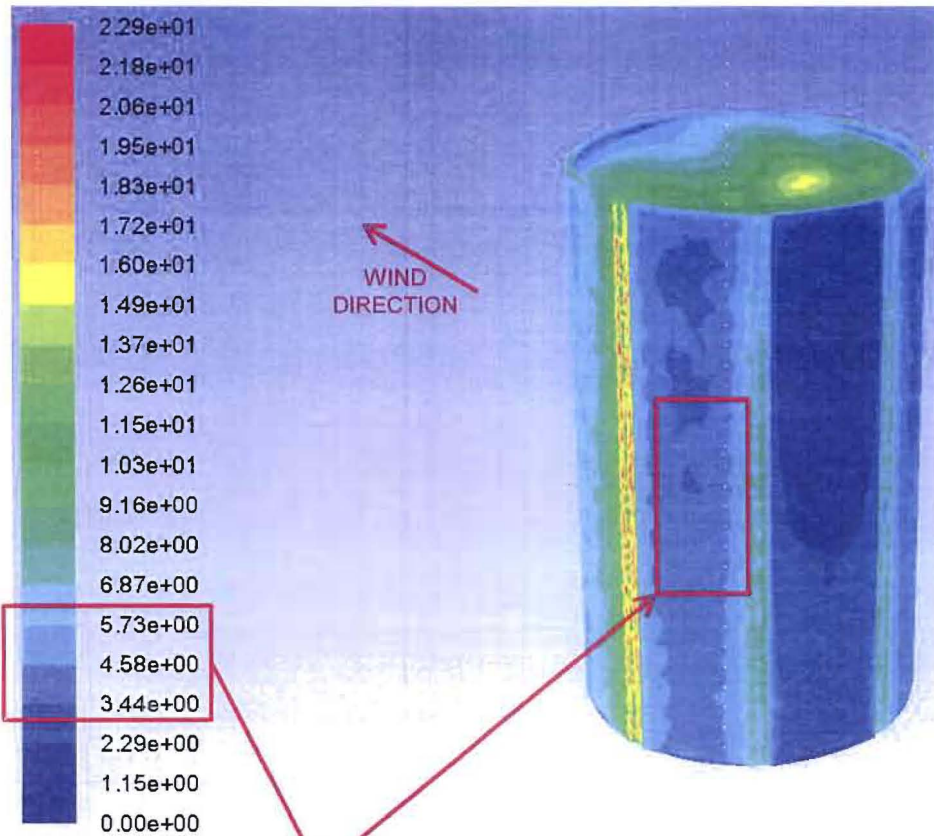
$h = 22.99 \text{ w/m}^2*\text{k} * 0.1761 \text{ BTU} / \text{hr}^*\text{ft}^2* \text{ }^\circ\text{F}$

$h = 4.05 \text{ BTU} / \text{hr}^*\text{ft}^2* \text{ }^\circ\text{F}$ (This number compares to the front surface of the tower (slide 8). Region of comparison is the light blue and cyan)

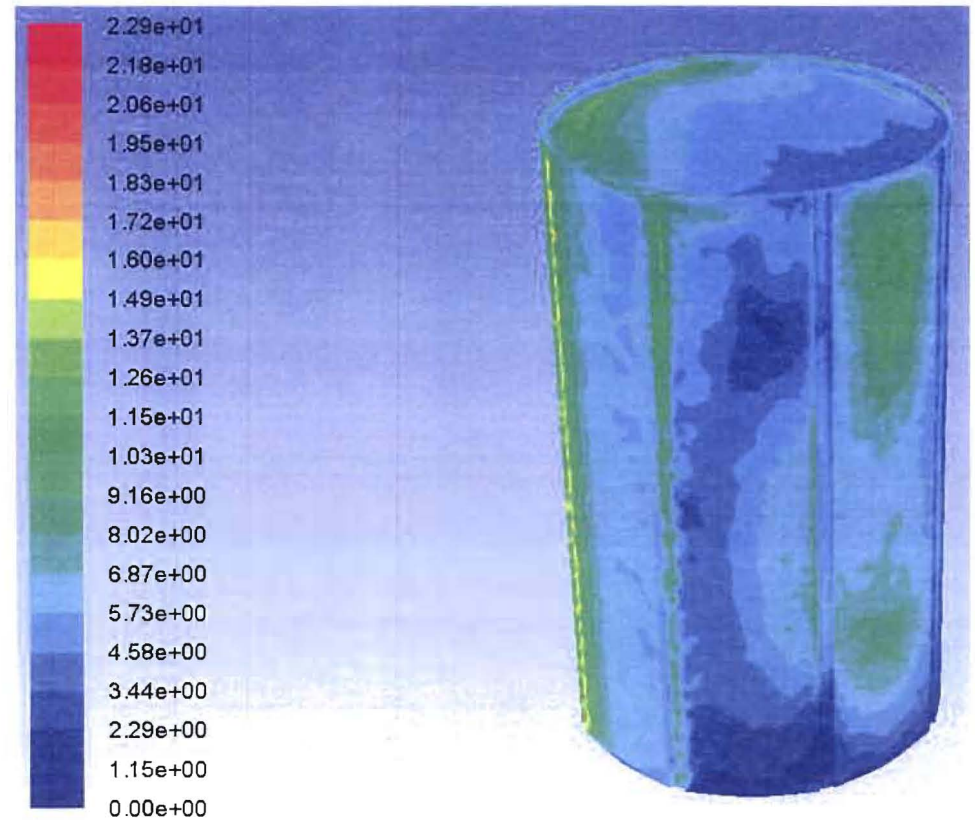
This indicates the CFD model has predicted the correct surface heat transfer coefficients

Davis-Besse Containment Tower CFD Results

34mph Northwest Summer Conditions



Hx AREA OF COMPARISON

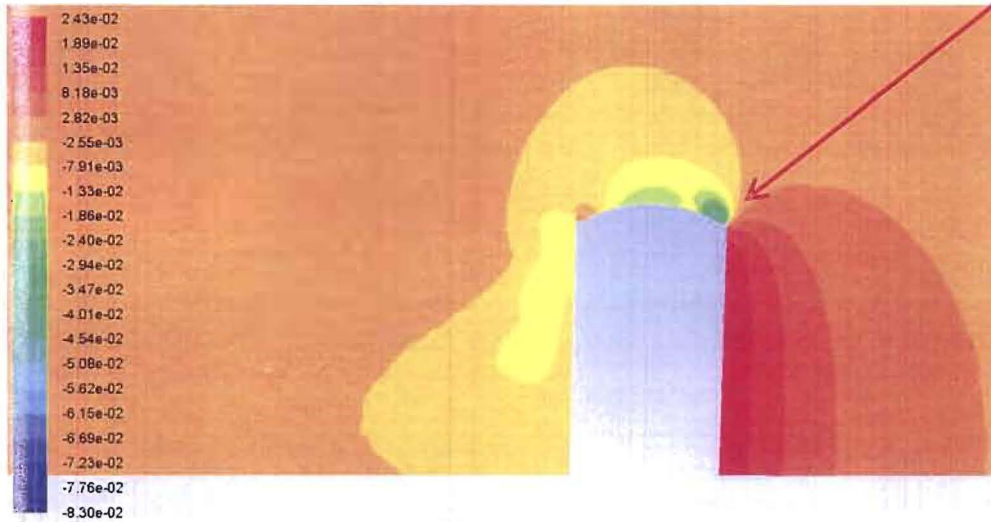


Heat Transfer Wall Coefficients (Btu/hr-ft²-°F)

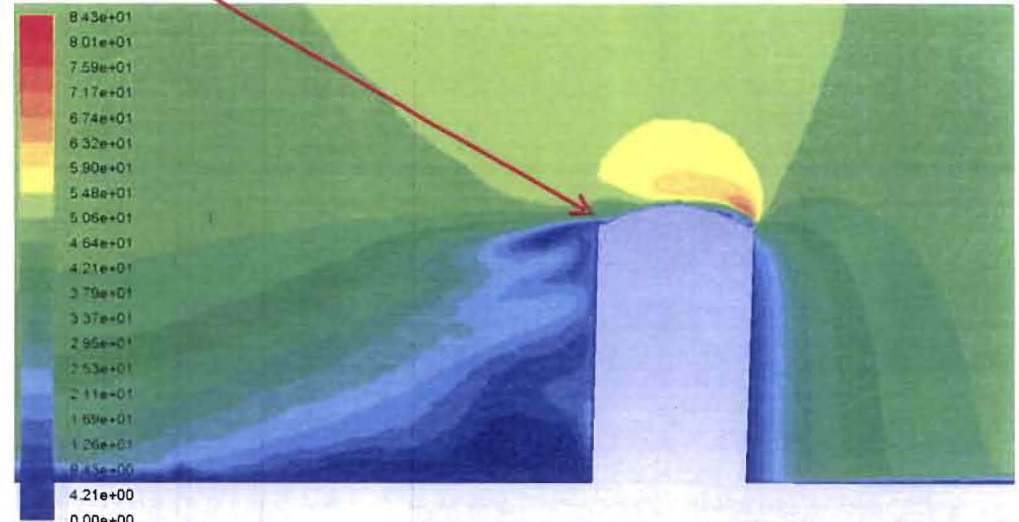
Davis-Besse Containment Tower CFD Results

34mph Northwest Summer Conditions

Flow separation



CROSS SECTION PRESSURE CONTOURS (psi)



CROSS SECTION VELOCITY CONTOURS (ft/s)

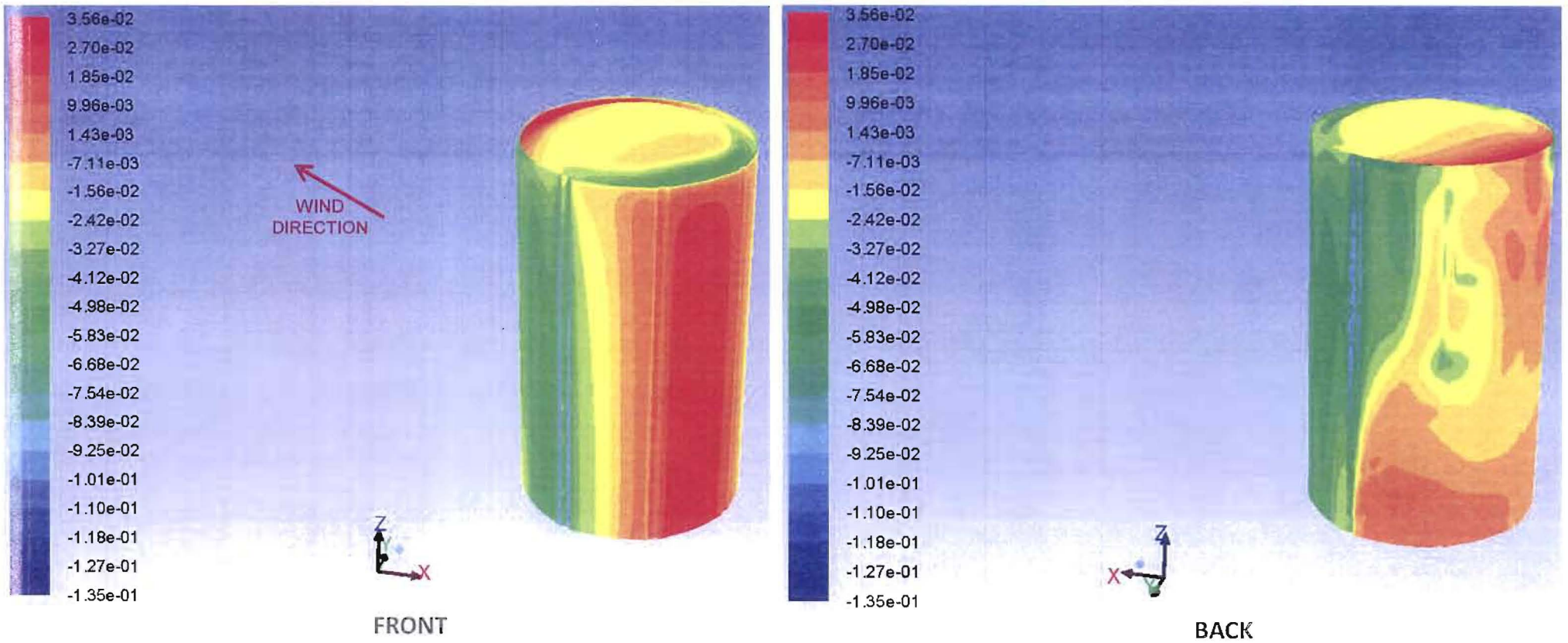
- The cross section picture of the pressure contour shows a steady gradient pressure buildup in front of the tower.
- At slow wind speeds the flow mainly stays attached except along the top front and aft edge.
- The flow tries to stay attached, but flow separation happens at the bottom half due to the low pressure region.
- The top dome has a profound effect on the flow separation.
- Another contributor of flow separation is the architectural flutes located on the side of the building.



34mph FROM THE SOUTHWEST (WINTER)

Davis-Besse Containment Tower CFD Results

34mph Southwest Winter Conditions



PRESSURE CONTOURS (psi)



HEAT TRANSFER COEFFICIENT HAND CALCULATIONS FOR ANALYTICAL COMPARISON

TOWER = -13°F (-25°C)

AIR TEMP = 7°F (-13.9°C)

TEMP AVERAGE = -3°F (-19.4°C)

$v = 0.1168 \text{ cm}^2/\text{s}$

$k = 0.02248 \text{ w/m}^*\text{k}$

$Pr = 0.72$

$U = 15.20 \text{ m/s (34mph)}$

$D = 44.73\text{m}$

$Re = U * D / v$

$Re = 58,210,273$

$Nu = h * D / k$

$Nu = 0.3 + (0.62 * Re^{0.5} * Pr^{0.33}) / ([1 + (0.4 / Pr)^{0.67}]^{0.25}) * [1 + (Re / 282,000)^{0.625}]^{0.8}$

$Nu = 55,111$

$h = (55,111 * 0.02248 \text{ w/m}^*\text{k}) / 44.73\text{m}$

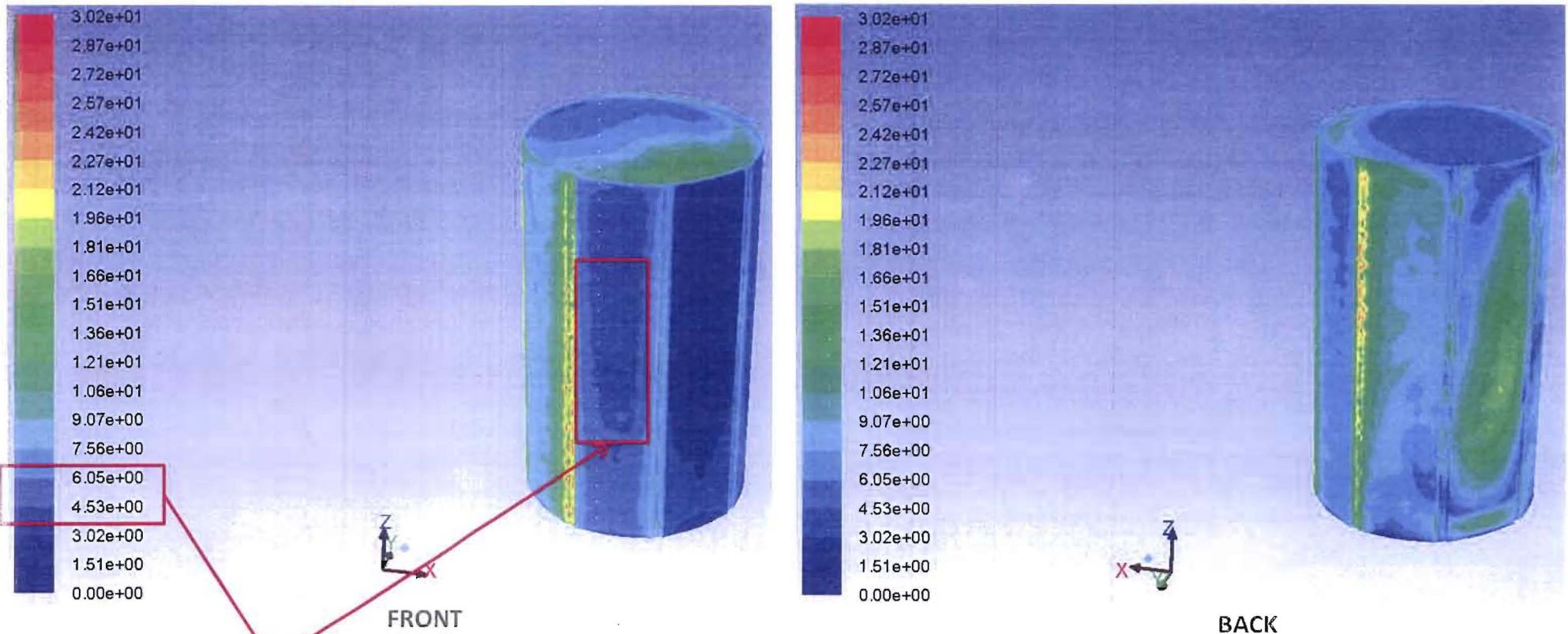
$h = 27.7 \text{ w/m}^2*\text{k} * 0.1761 \text{ BTU} / \text{hr}^*\text{ft}^2* \text{°F}$

$h = 4.87 \text{ BTU} / \text{hr}^*\text{ft}^2* \text{°F}$ (This number compares to the front surface of the tower (slide 13). Region of comparison is the light blue and cyan)

This indicates the CFD model has predicted the correct surface heat transfer coefficients.

Davis-Besse Containment Tower CFD Results

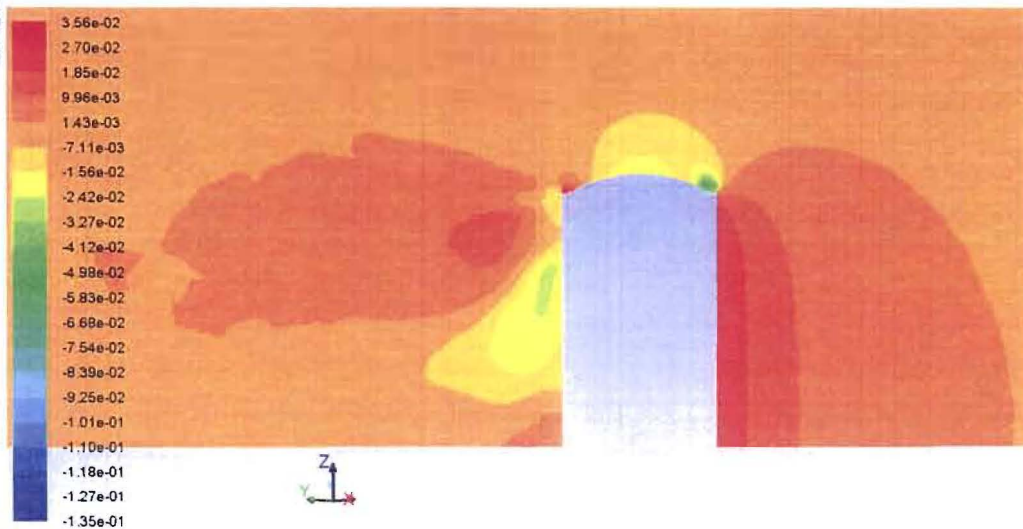
34mph Southwest Winter Conditions



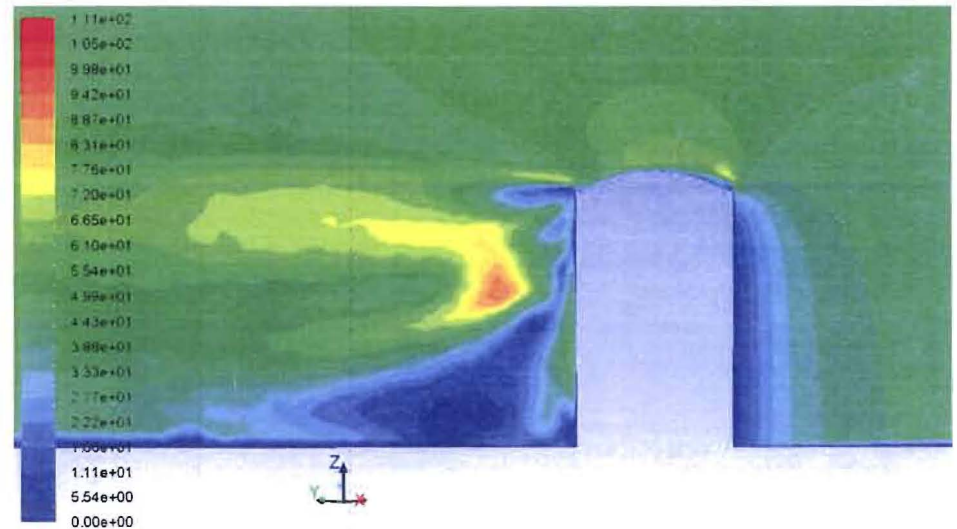
Heat Transfer Wall Coefficients (Btu/hr-ft²-°F)

Davis-Besse Containment Tower CFD Results

34mph Southwest Winter Conditions



CROSS SECTION PRESSURE CONTOURS (psi)



CROSS SECTION VELOCITY CONTOURS (ft/s)

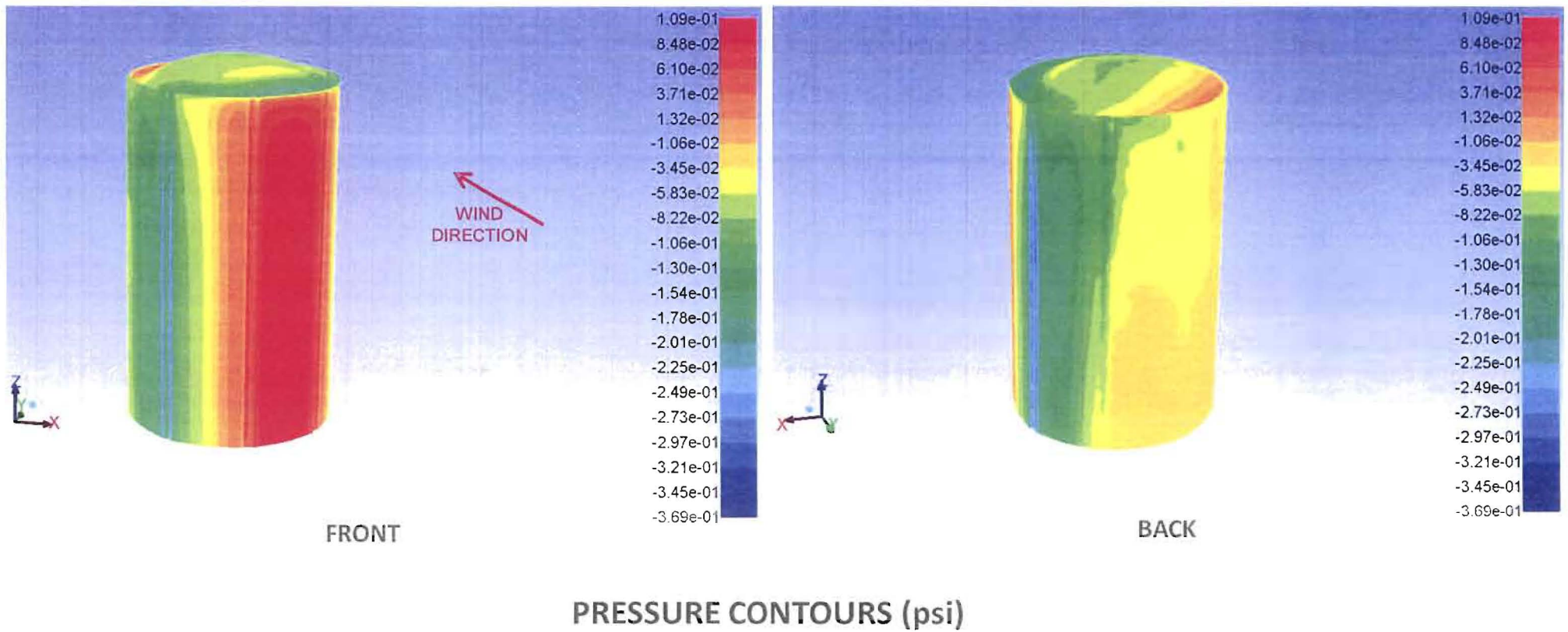
- The cross section picture of the pressure contour shows a smaller pressure buildup in front of the building.
- A cold dense air has a tendency to shed from structures more easily due to a higher Reynolds number.
- During winter conditions, the flow separates completely from the tower at 34mph. A result is vorticity shedding.
- An effect of the flow separation at lower speeds will cause a cyclic pressure loads on the containment tower.
- The top dome has increased the effect of flow separation.
- Another contributor of flow separation is the architectural flutes located on the side of the building.



72mph FROM THE SOUTHWEST (WINTER)

Davis-Besse Containment Tower CFD Results

72mph Southwest Winter Conditions





HEAT TRANSFER COEFFICIENT HAND CALCULATIONS FOR ANALYTICAL COMPARISON

TOWER = -13°F (-25°C)

AIR TEMP = 7°F (-13.9°C)

TEMP AVERAGE = -3°F (-19.4°C)

$v = 0.1168 \text{ cm}^2/\text{s}$

$k = 0.02248 \text{ w/m}^*\text{k}$

$Pr = 0.72$

$U = 32.63 \text{ m/s (72mph)}$

$D = 44.73\text{m}$

$Re = U*D / v$

$Re = 124,960,607$

$Nu = h*D/k$

$Nu = 0.3 + (0.62*Re^{0.5}*Pr^{0.33})/([1+(0.4/Pr)^{0.67}]^{0.25}) * [1+(Re/282,000)^{0.625}]^{0.8}$

$Nu = 97,032$

$h = (97,032 * 0.02248 \text{ w/m}^*\text{k}) / 44.73\text{m}$

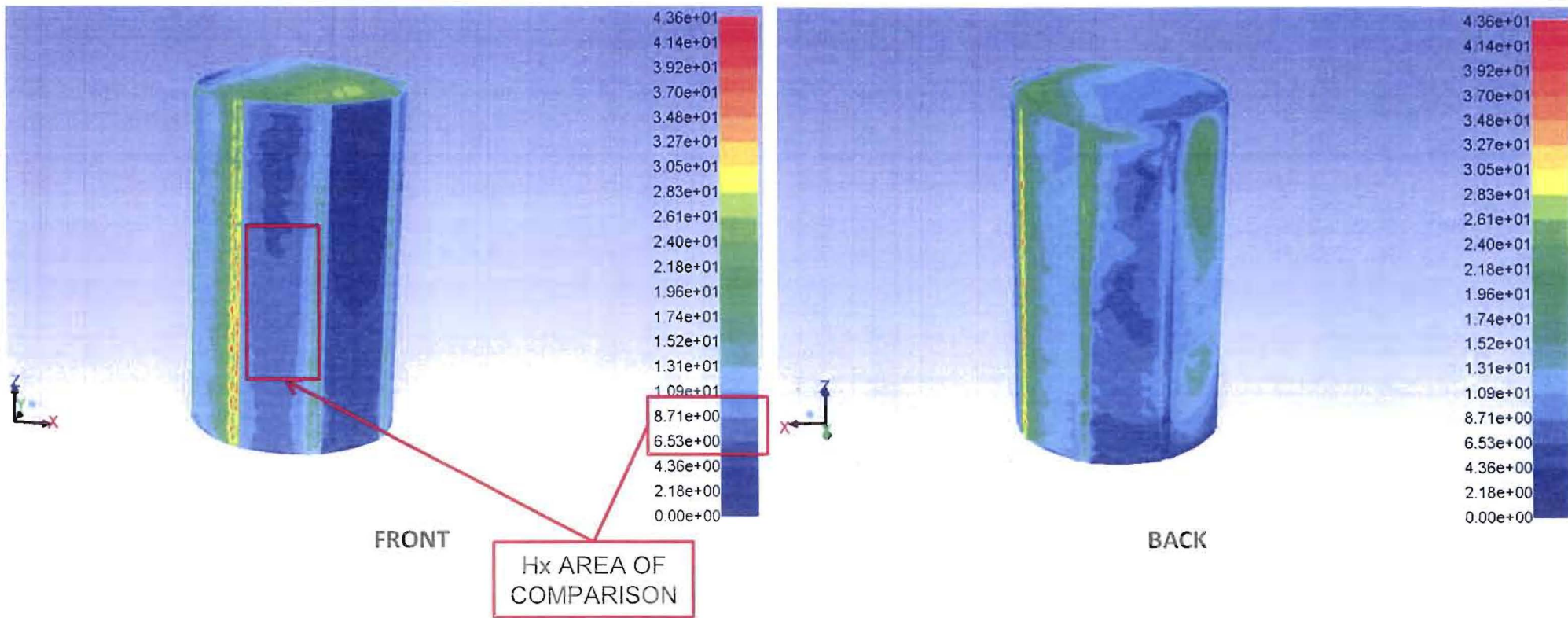
$h = 48.76 \text{ w/m}^2*\text{k} * 0.1761 \text{ BTU / hr}^*\text{ft}^2* \text{ }^\circ\text{F}$

$h = 8.587 \text{ BTU / hr}^*\text{ft}^2* \text{ }^\circ\text{F}$ (This number compares to the front surface of the tower (slide 18). Region of comparison is the light blue and cyan)

This indicates the CFD model has predicted the correct surface heat transfer coefficients.

Davis-Besse Containment Tower CFD Results

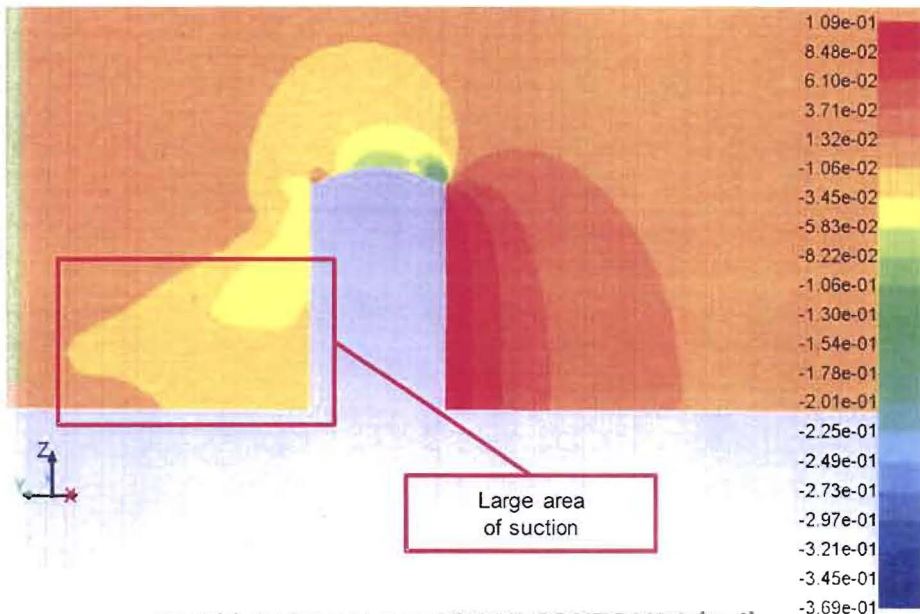
72mph Southwest Winter Conditions



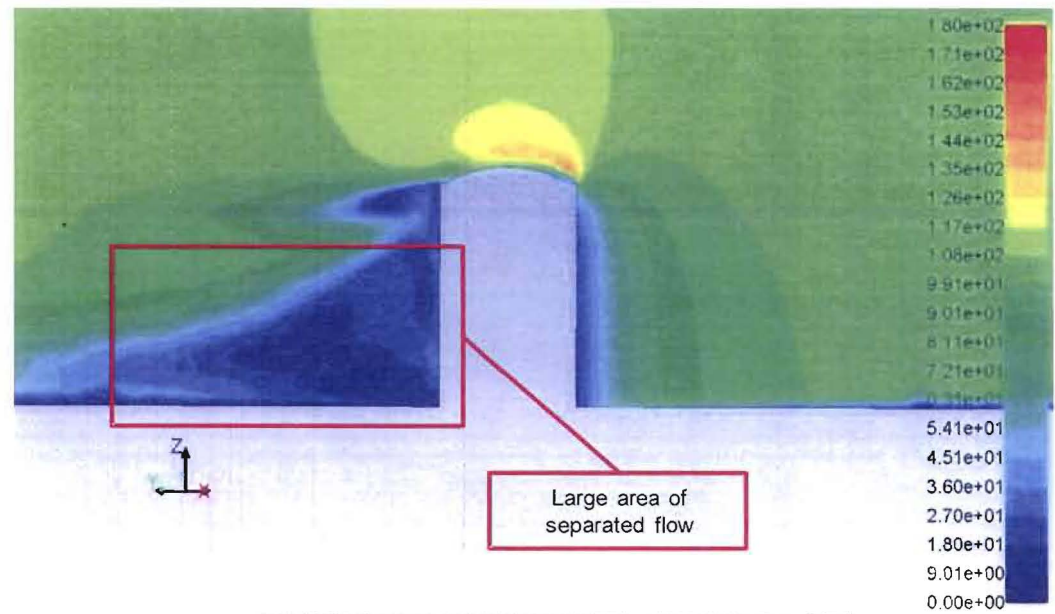
Heat Transfer Wall Coefficients (Btu/hr-ft²-°F)

Davis-Besse Containment Tower CFD Results

72mph Southwest Winter Conditions



CROSS SECTION PRESSURE CONTOURS (psi)



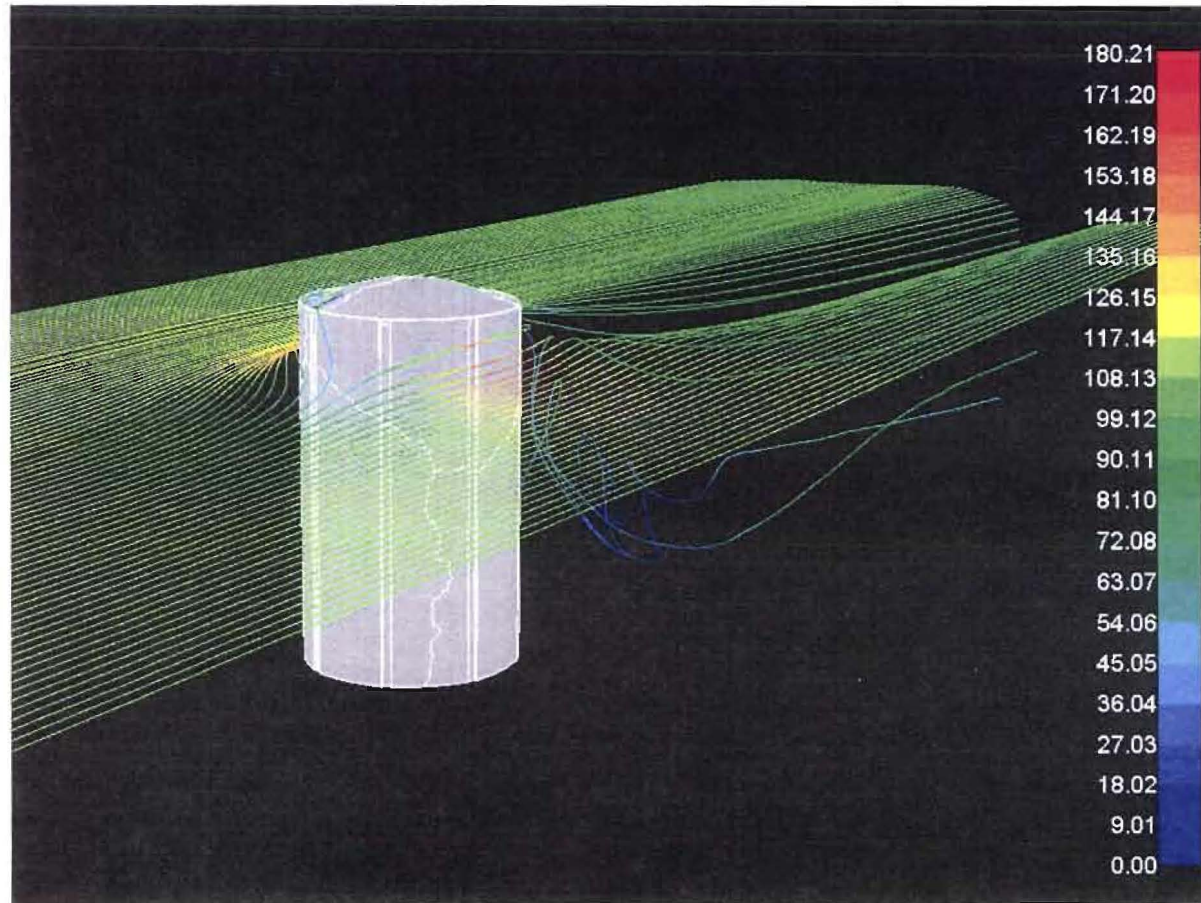
CROSS SECTION VELOCITY CONTOURS (ft/s)

- The pressure contour has stayed the same from the 34mph, but the pressure load and suction has increased.
- A cold dense air has a tendency to shed from structures more easily due to a higher Reynolds number.
- During winter conditions, the flow separates completely from the tower at 72mph.
- An effect of the flow separation at higher speeds will cause more cyclic pressure loads on the containment tower.
- The top dome has increased the effect of flow separation.
- Another contributor of flow separation is the architectural flutes located on the side of the building.



Davis-Besse Containment Tower CFD Results

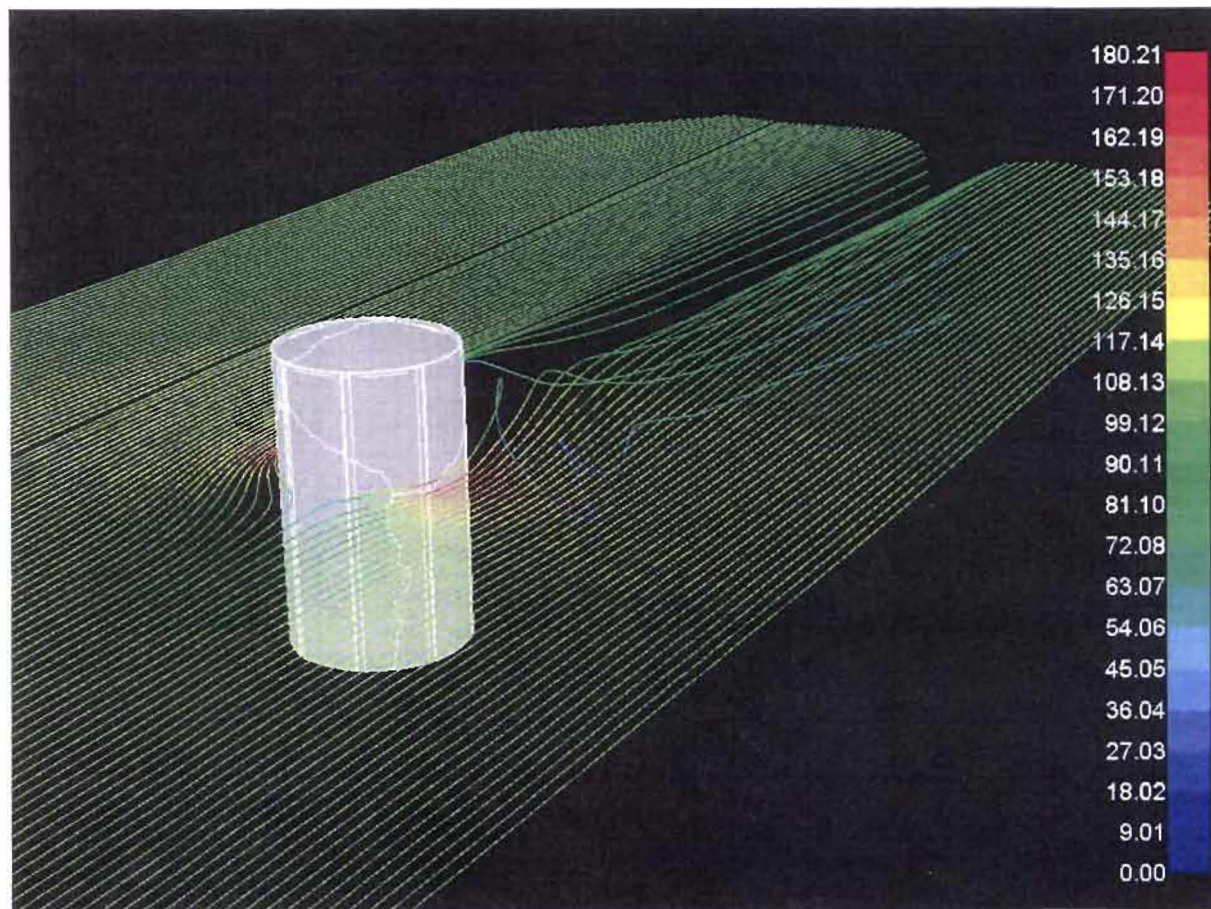
72mph Southwest Winter Conditions



Velocity path lines at 1/3 down from the top of the containment tower (ft/s)

Davis-Besse Containment Tower CFD Results

72mph Southwest Winter Conditions

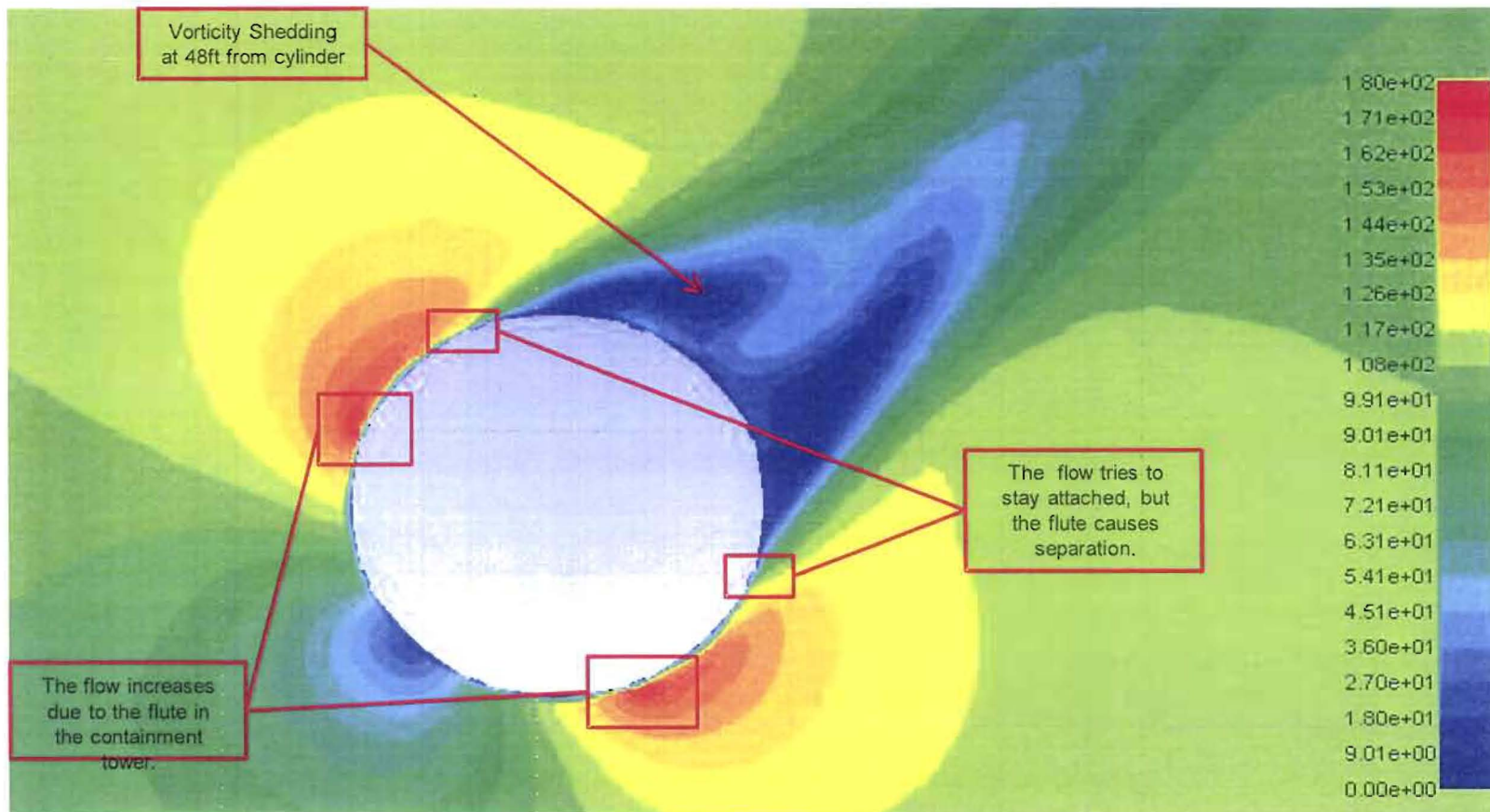


Velocity path lines halfway from the top of the containment tower (ft/s)



Davis-Besse Containment Tower CFD Results

72mph Southwest Winter Conditions

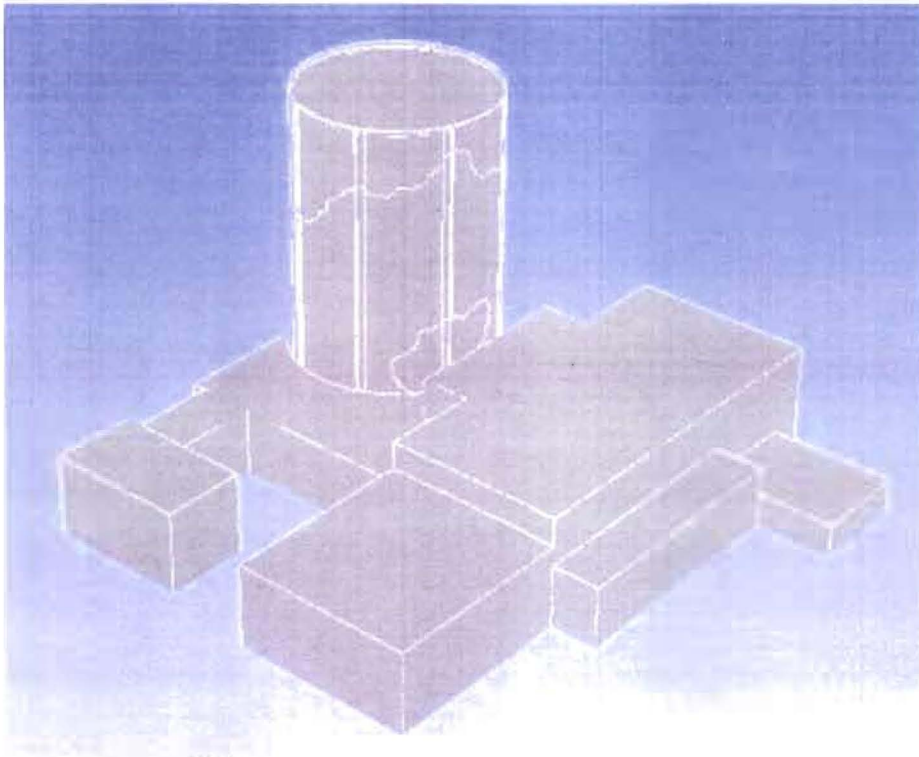


Velocity contours 1/3 down from the top at 72mph
Vorticity shedding frequency = $(108 \text{ ft/s}) / (48\text{ft}) = 2.25 \text{ hz}$

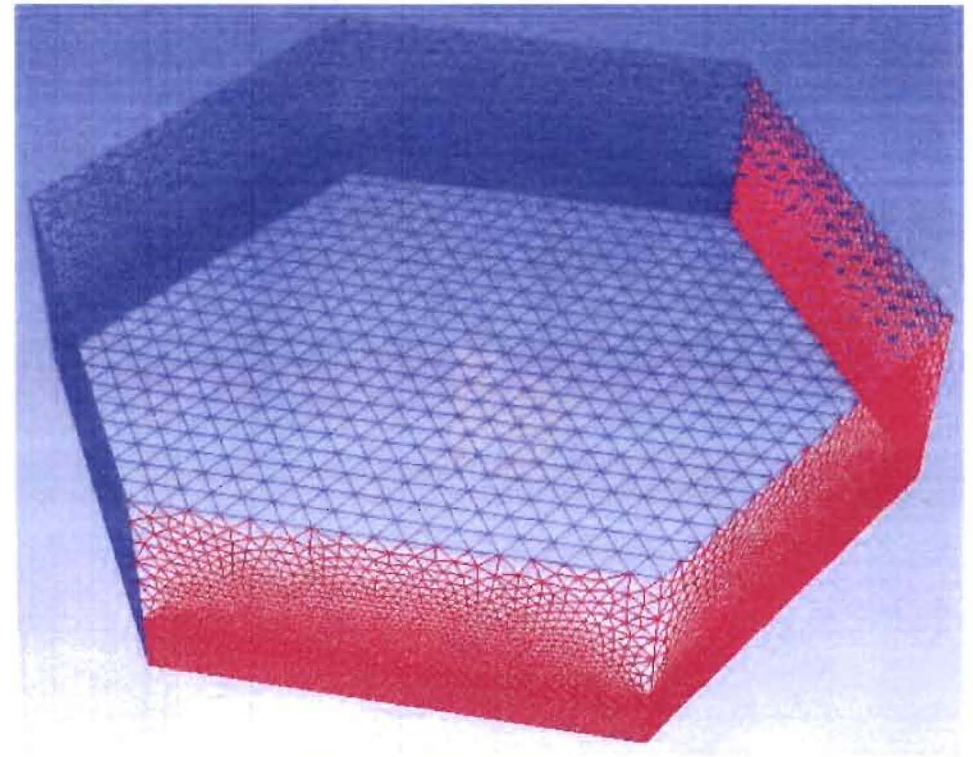
Model Creation of Containment Tower with Buildings

- The CFD mesh consisted of 3.26 million cells to create the air volume.
- Total size of the air volume was a 2,500 ft. diameter and a height of 670 ft.
- Using a large air volume eliminates any wall effects.

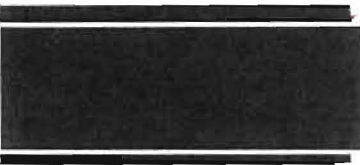
Using a small mesh size allows the vorticity shedding to be captured more accurately.



CONTAINMENT TOWER WITH BUILDINGS



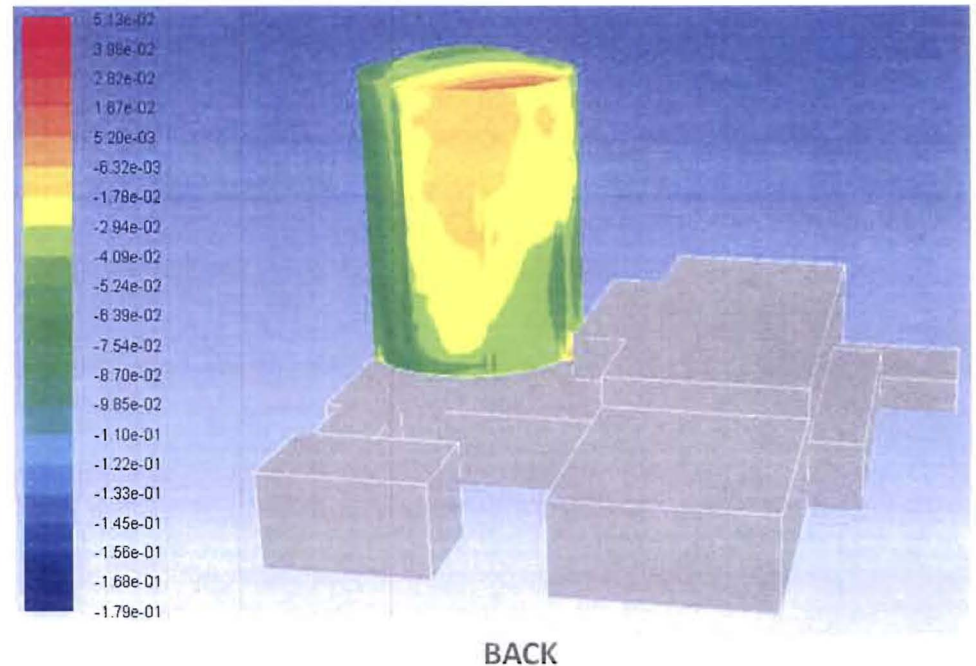
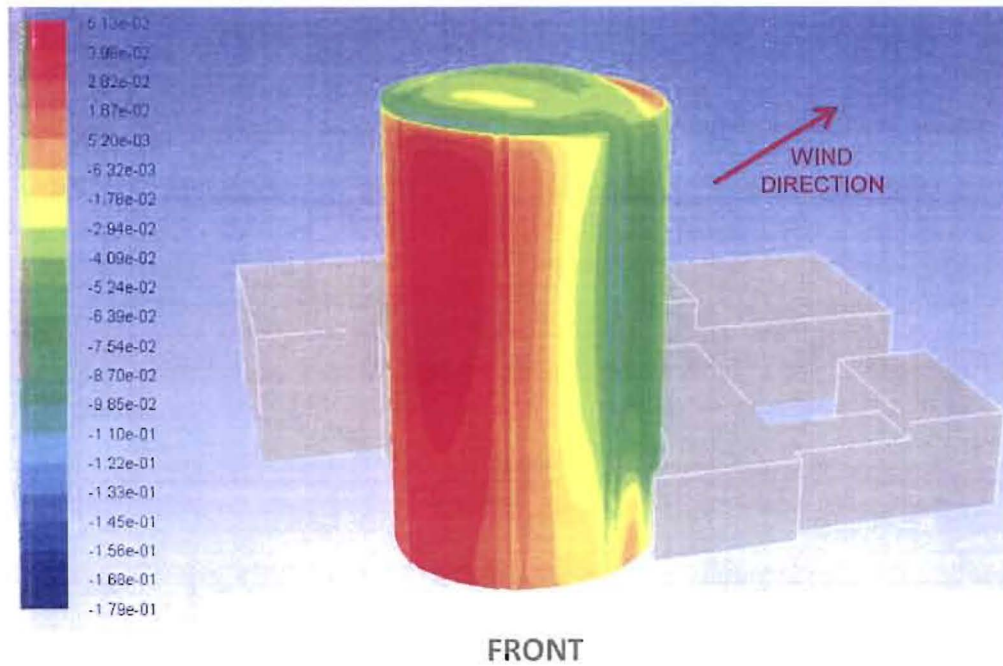
AIR VOLUME WITH BUILDINGS



34mph FROM THE NORTHWEST WITH BUILDINGS (SUMMER)

Davis-Besse Containment Tower CFD Results

34mph Northwest Summer Conditions

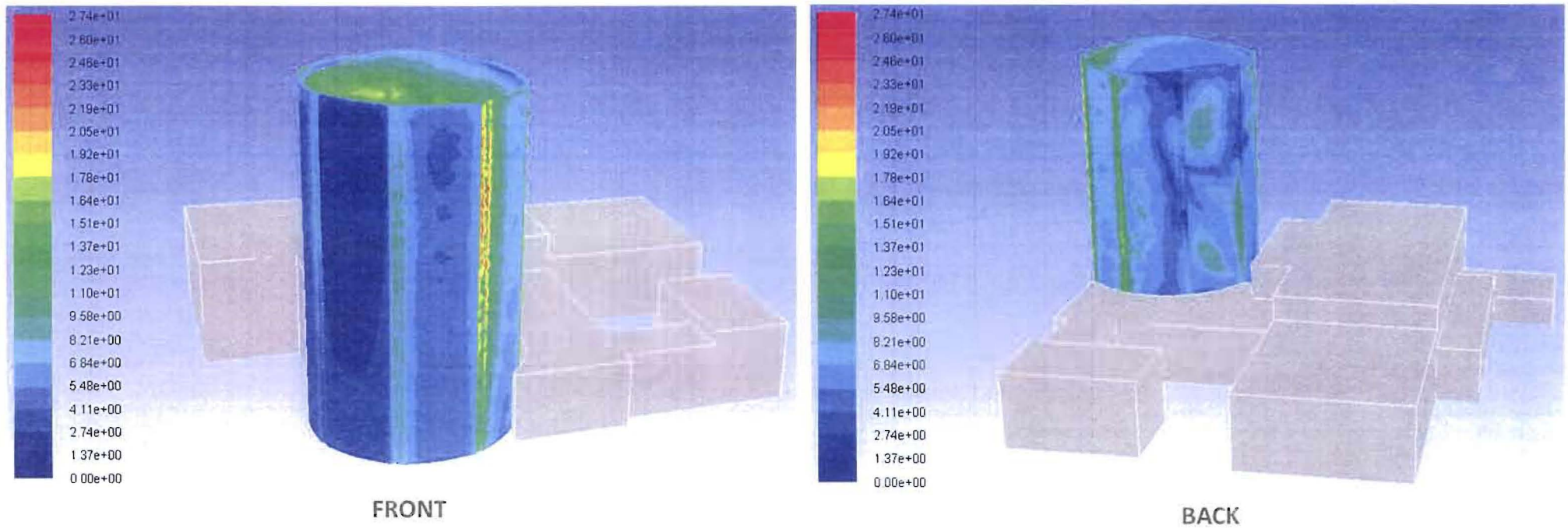


PRESSURE CONTOURS (psi)

- With the addition of the surrounding buildings, the pressure has increased by 0.027psi.

Davis-Besse Containment Tower CFD Results

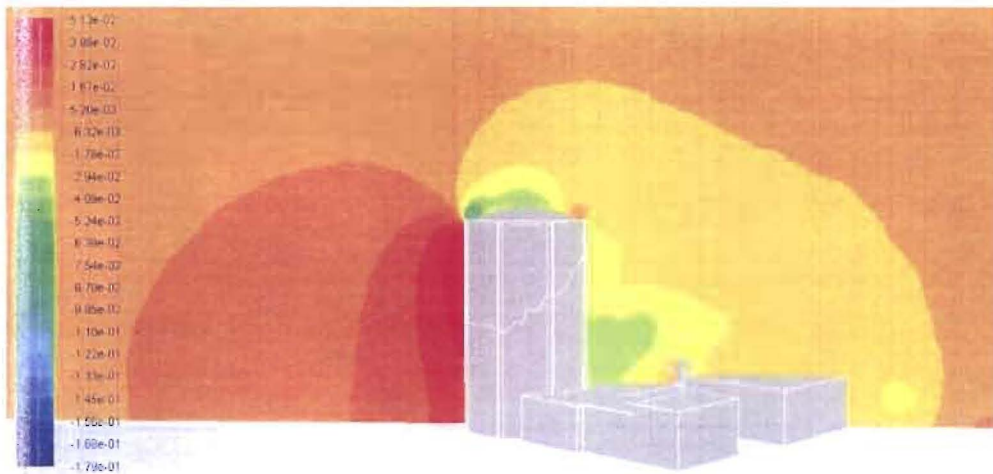
34mph Northwest Summer Conditions



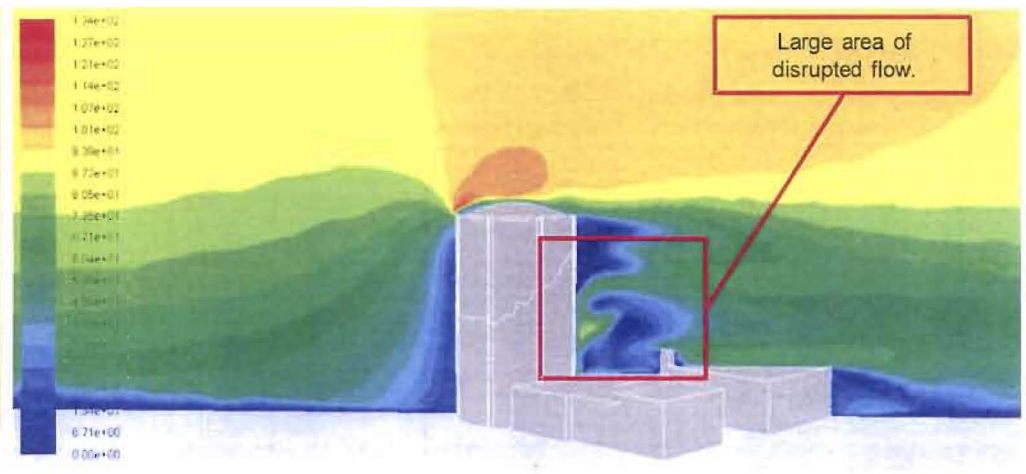
Heat Transfer Wall Coefficients (Btu/hr-ft²-°F)

Davis-Besse Containment Tower CFD Results

34mph Northwest Summer Conditions



CROSS SECTION PRESSURE CONTOURS (psi)

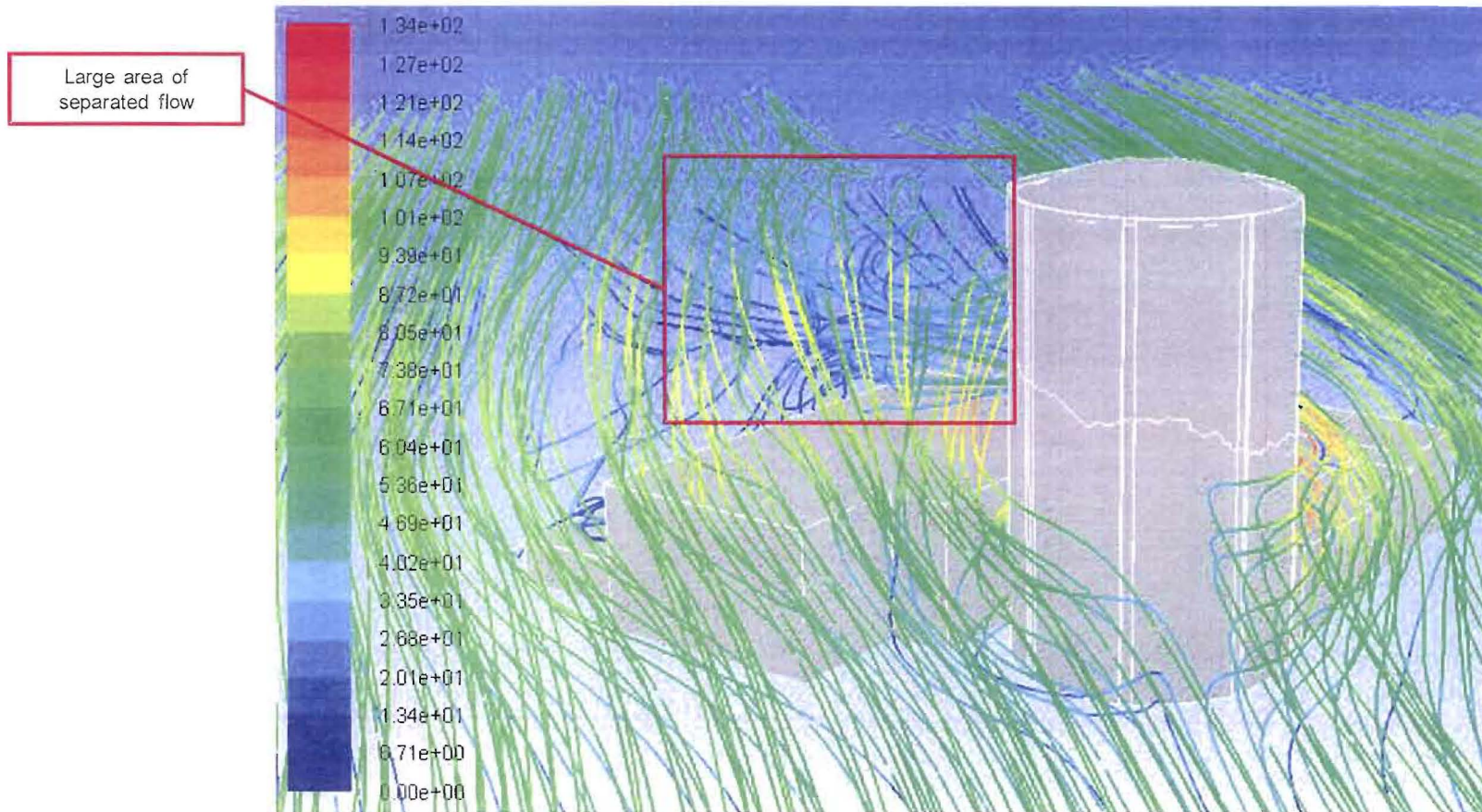


CROSS SECTION VELOCITY CONTOURS (ft/s)

- The pressure contours have dramatically changed with the addition of surrounding buildings.
- There is a large low pressure region located above the building on the aft side of the containment tower.
- The velocity vectors are disrupted from the buildings causing the flow to separate at lower wind speeds.

Davis-Besse Containment Tower CFD Results

34mph Northwest Summer Conditions



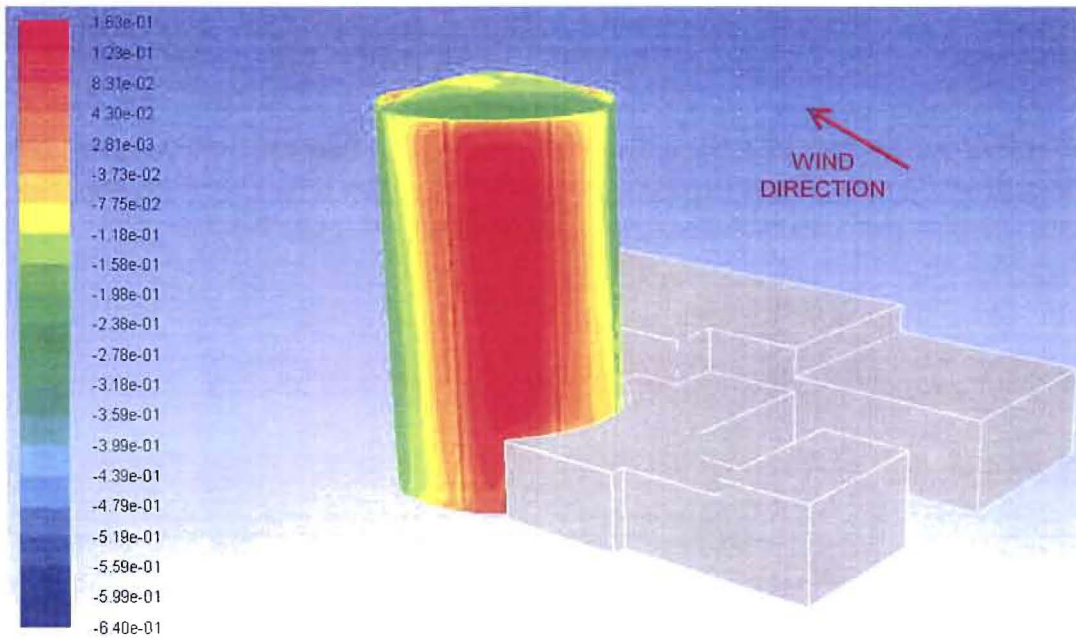
VELOCITY VECTORS (ft/s)



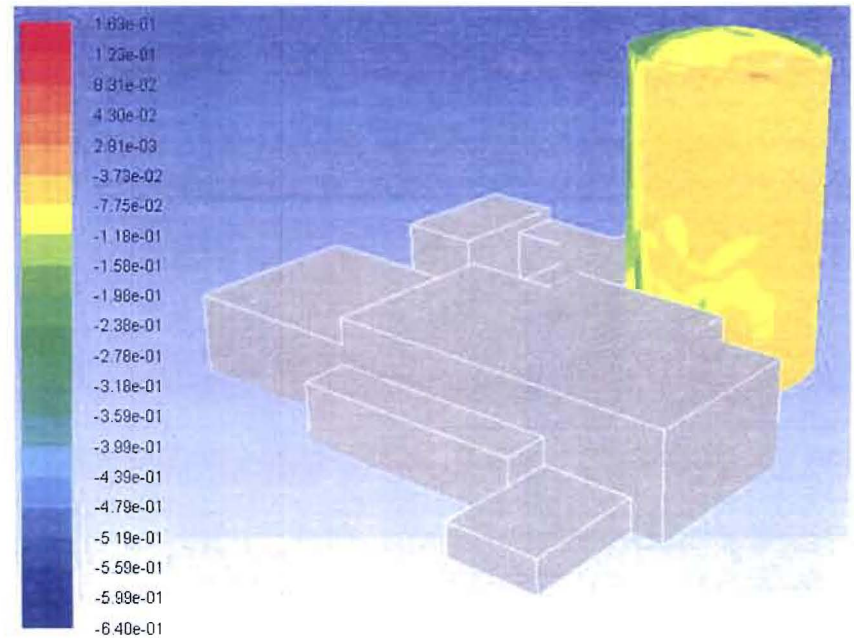
72mph FROM THE SOUTHWEST WITH BUILDINGS (WINTER)

Davis-Besse Containment Tower CFD Results

72mph Southwest Winter Conditions



FRONT



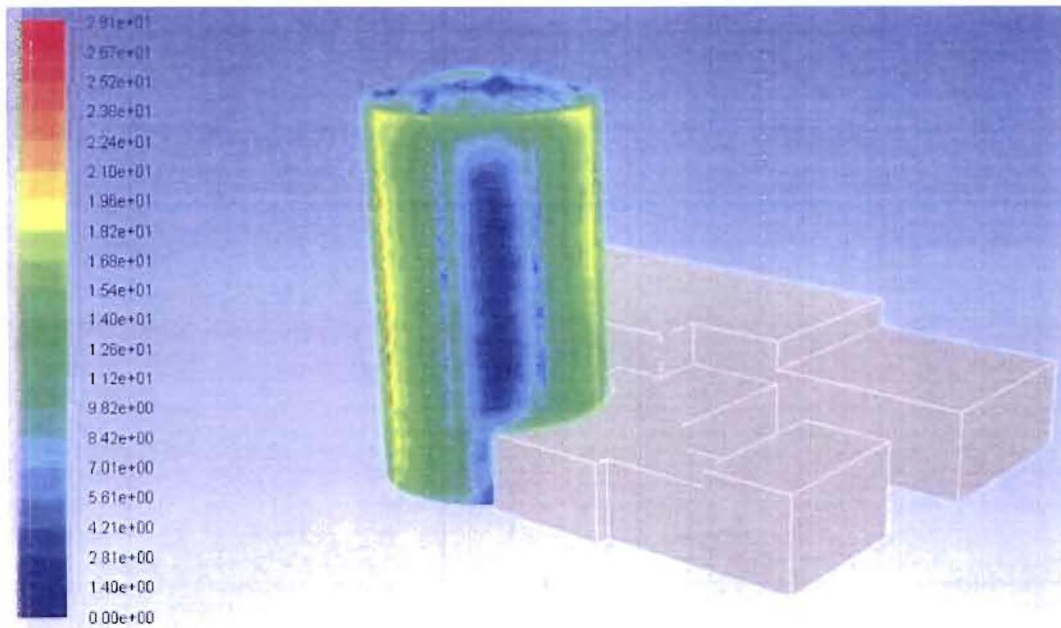
BACK

PRESSURE CONTOURS (psi)

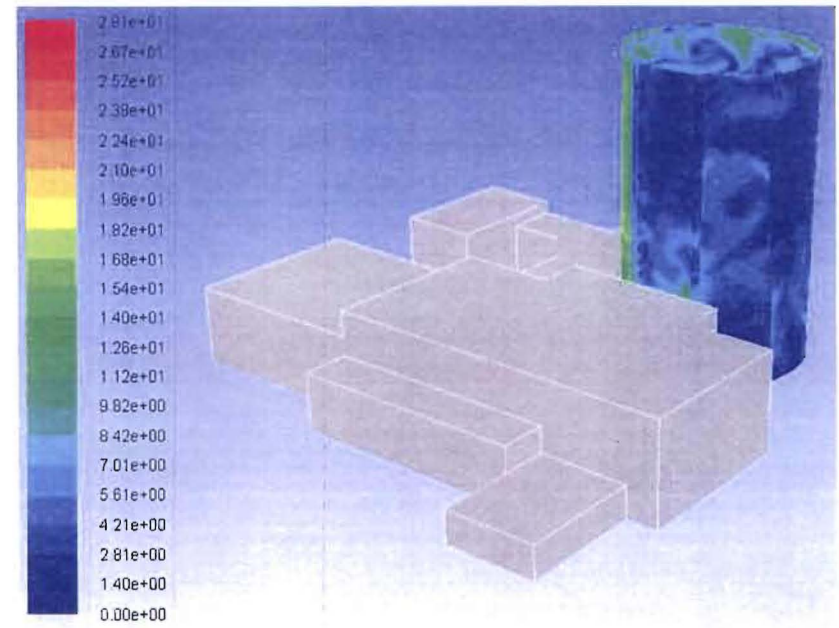
- With the addition of the surrounding buildings, the pressure has increased by 0.054psi.

Davis-Besse Containment Tower CFD Results

72mph Southwest Winter Conditions



FRONT

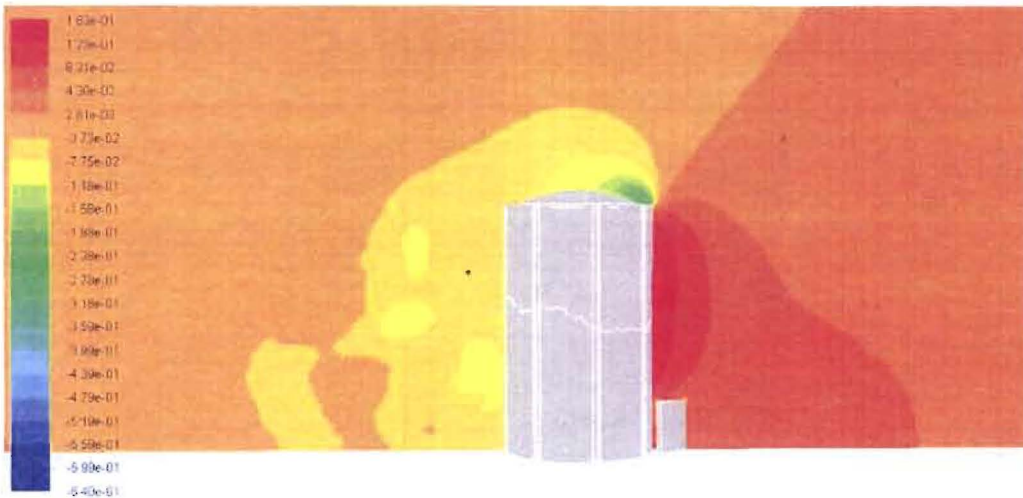


BACK

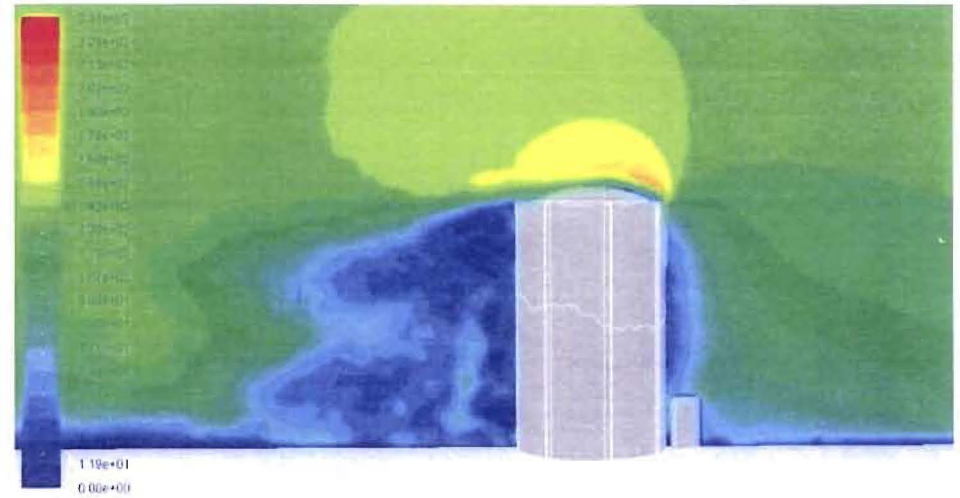
Heat Transfer Wall Coefficients (Btu/hr-ft²-°F)

Davis-Besse Containment Tower CFD Results

72mph Southwest Winter Conditions



CROSS SECTION PRESSURE CONTOURS (psi)

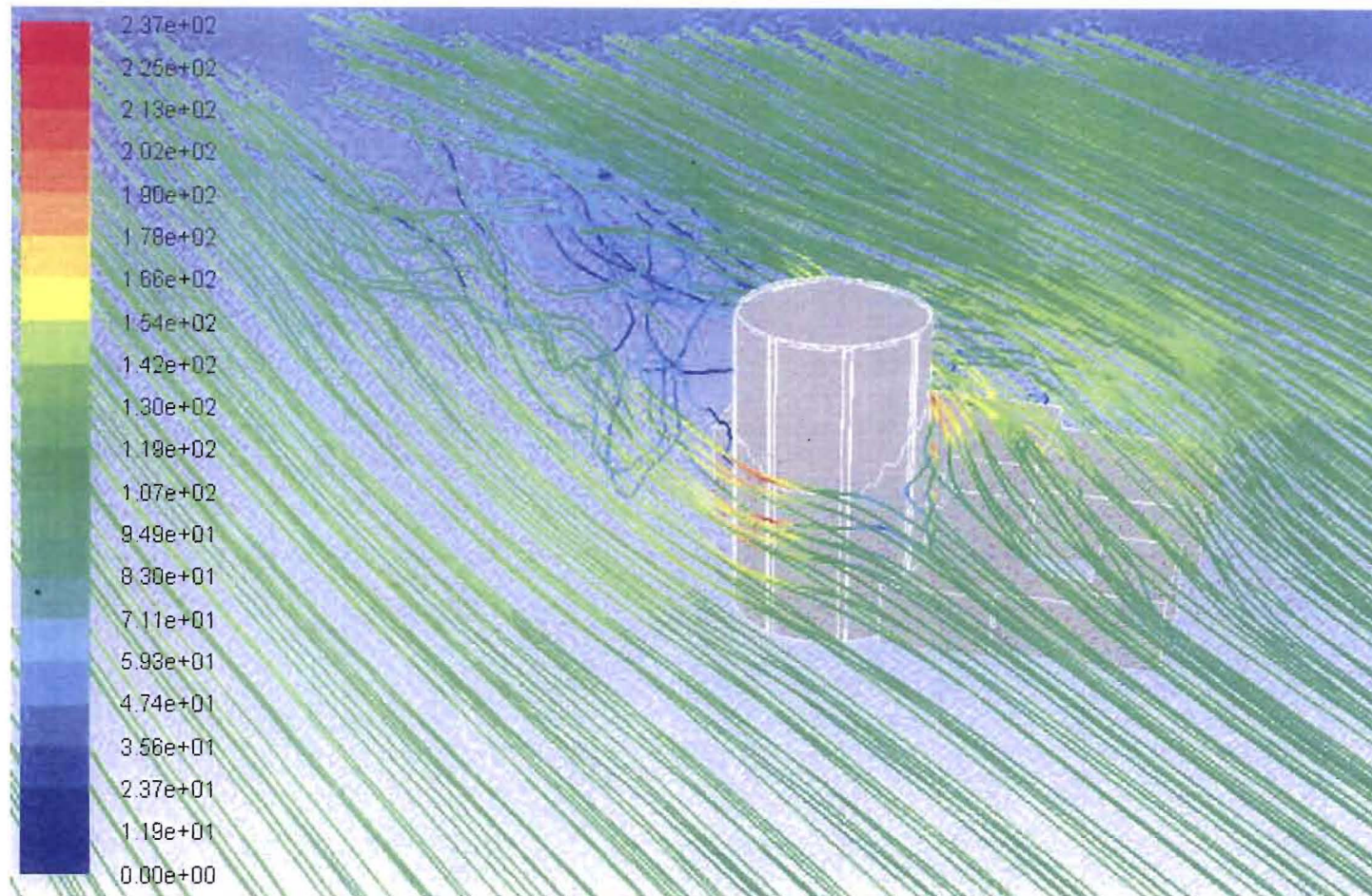


CROSS SECTION VELOCITY CONTOURS (ft/s)

- The stagnation pressure region has shifted up towards the top of the containment tower. This is a result of the buildings being in front of containment tower.
- The flow on the aft side of the tower is turbulent compared to the case with no buildings.

Davis-Besse Containment Tower CFD Results

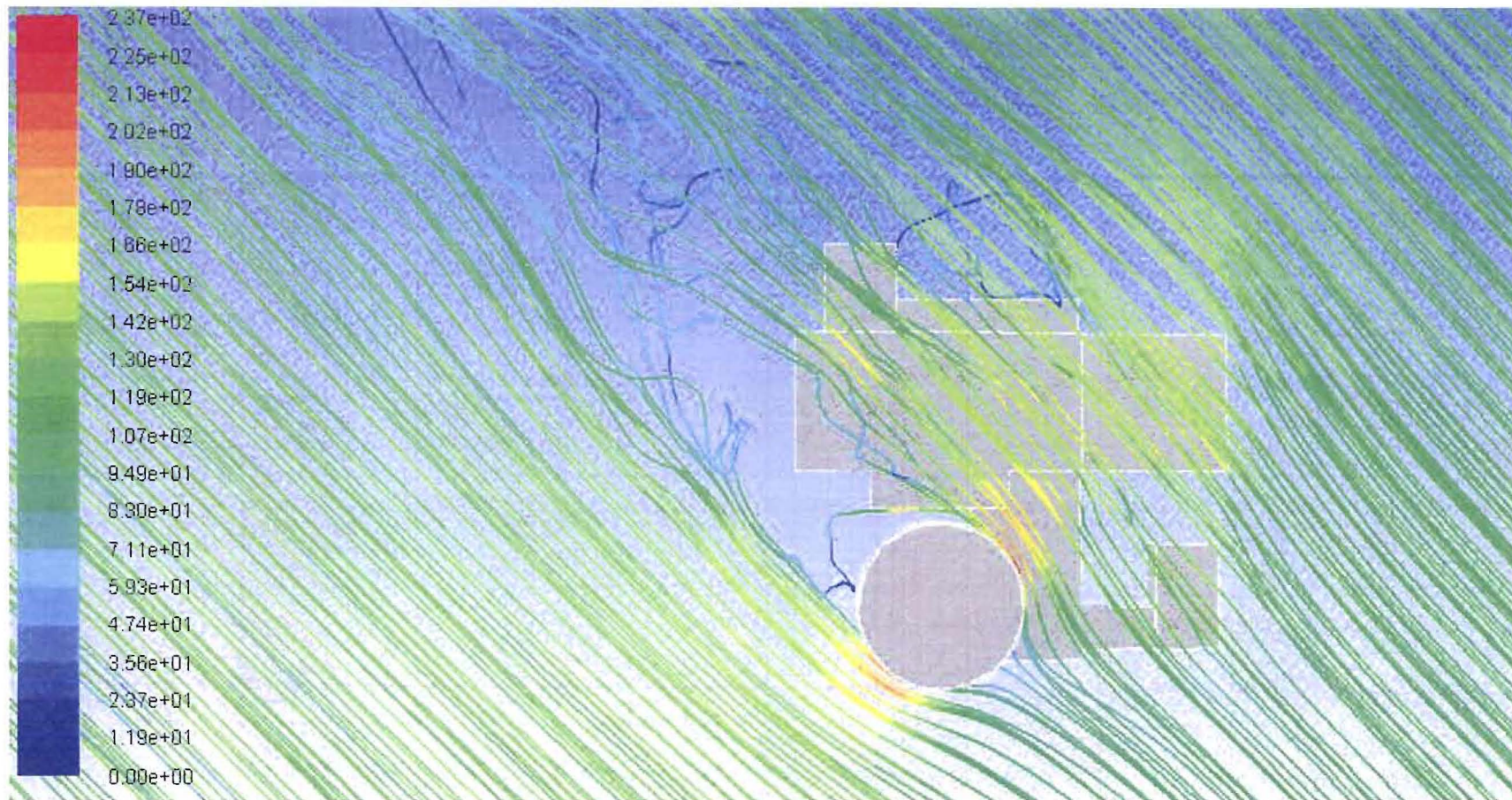
72mph Southwest Winter Conditions



VELOCITY VECTORS (ft/s)

Davis-Besse Containment Tower CFD Results

72mph Southwest Winter Conditions



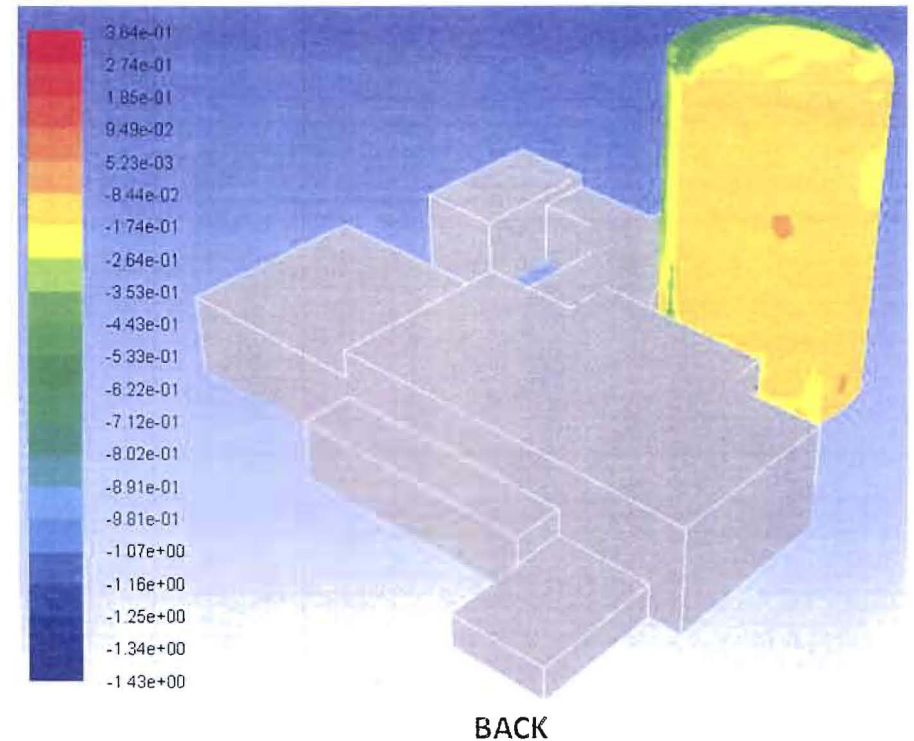
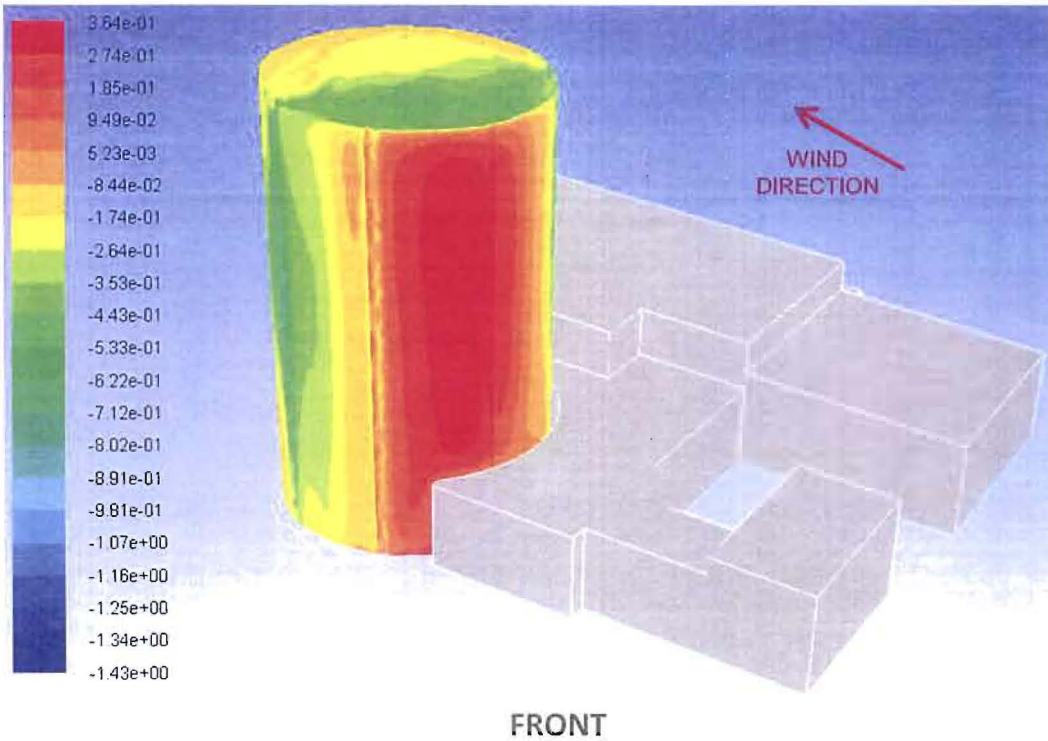
VELOCITY VECTORS (ft/s)



105mph FROM THE SOUTHWEST WITH BUILDINGS (WINTER)

Davis-Besse Containment Tower CFD Results

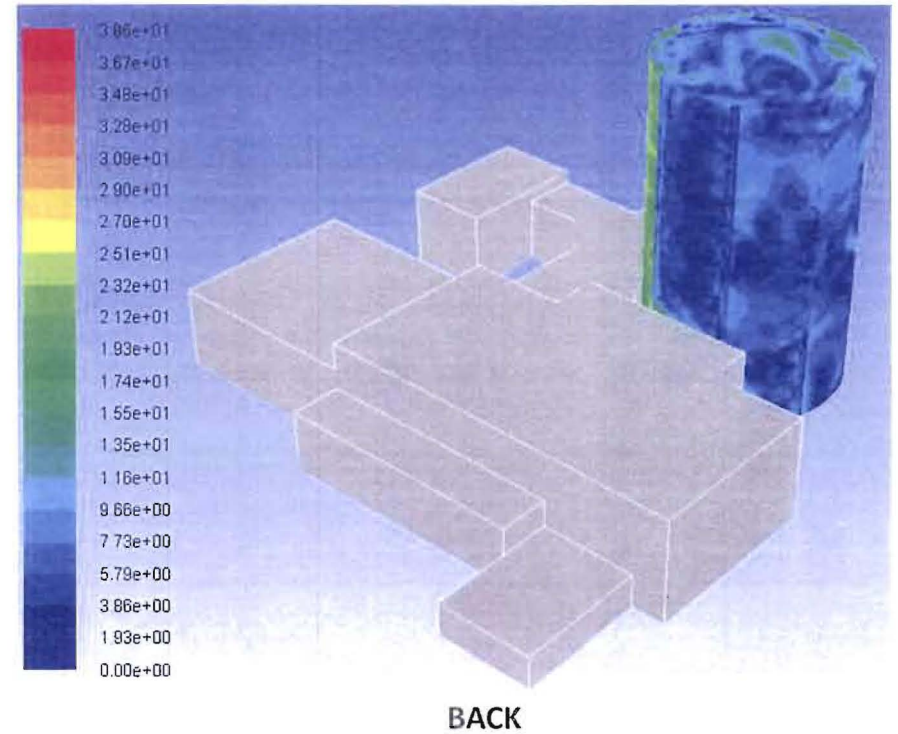
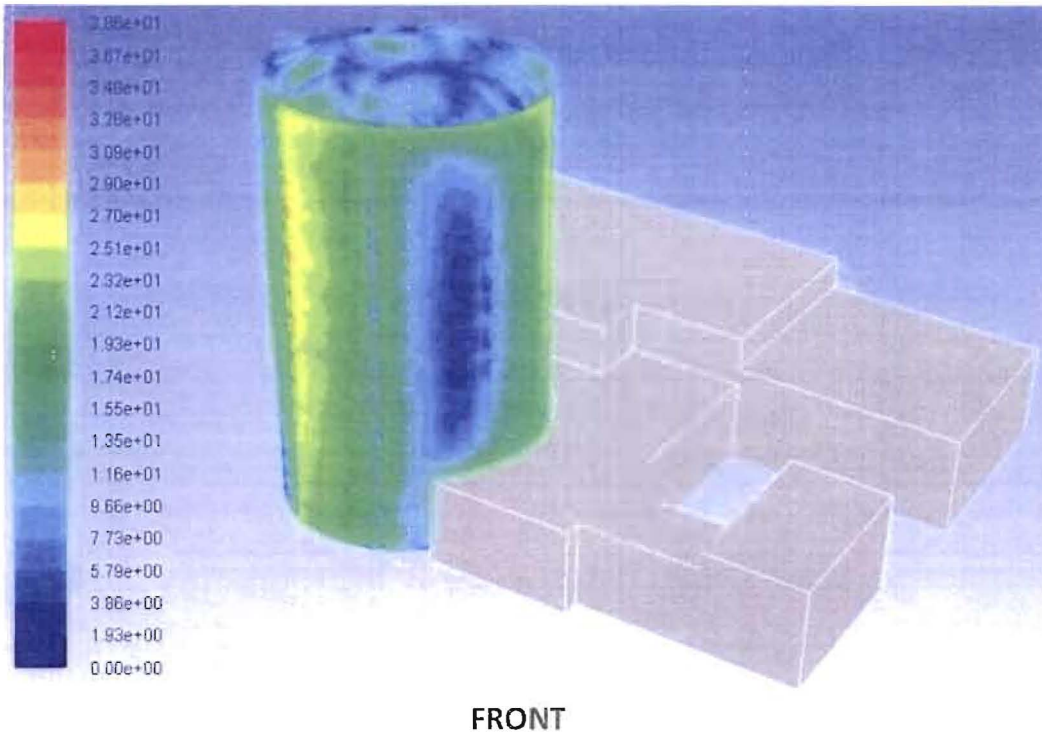
105mph Southwest Winter Conditions



PRESSURE CONTOURS (psi)

Davis-Besse Containment Tower CFD Results

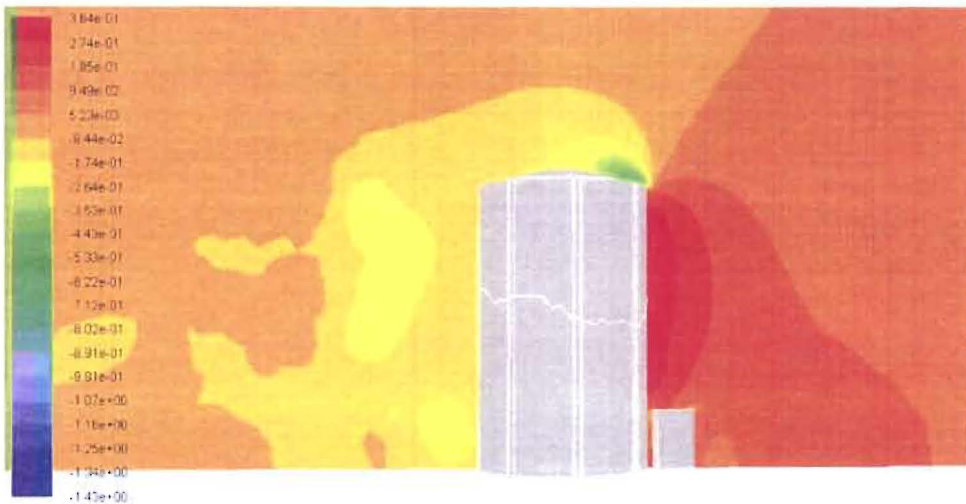
105mph Southwest Winter Conditions



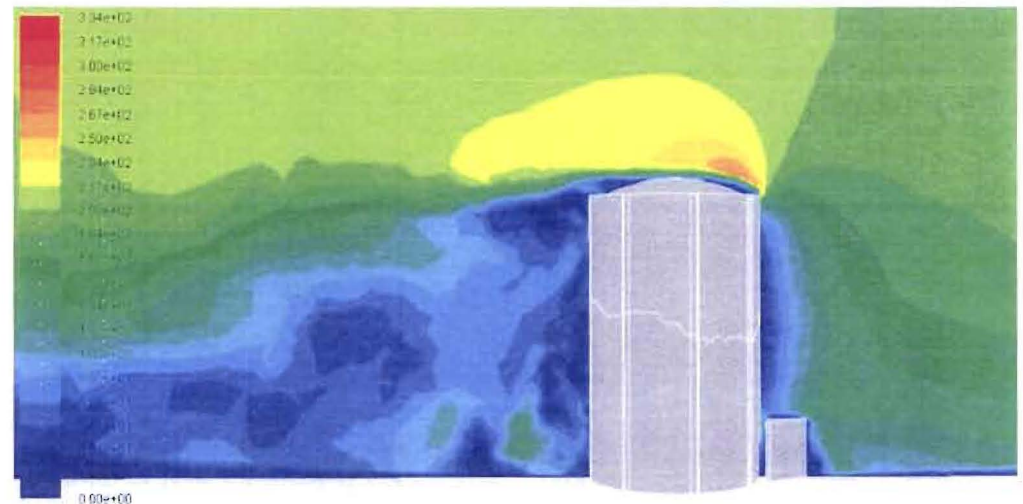
Heat Transfer Wall Coefficients (Btu/hr-ft²-°F)

Davis-Besse Containment Tower CFD Results

105mph Southwest Winter Conditions



CROSS SECTION PRESSURE CONTOURS (psi)

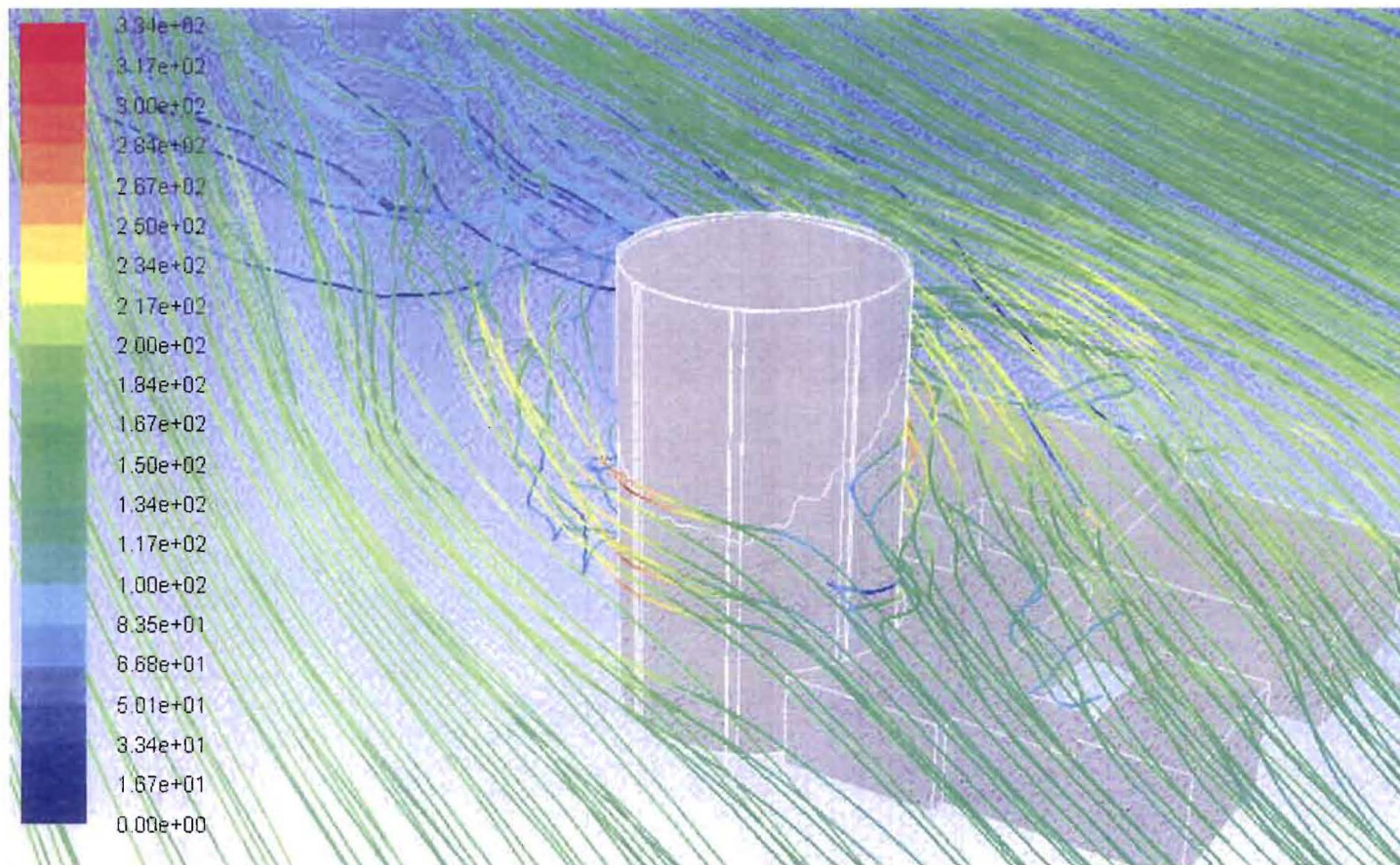


CROSS SECTION VELOCITY CONTOURS (ft/s)

- The stagnation pressure region has shifted up towards the top of the containment tower. This is a result of the buildings being in front of containment tower.
- The flow on the aft side of the tower is unsteady and turbulent.
- The addition of the buildings has caused the flow to rise do to the pressure increase just before reaching the building.
- This results in a higher pressure region at the midpoint causing a larger overturning moment.

Davis-Besse Containment Tower CFD Results

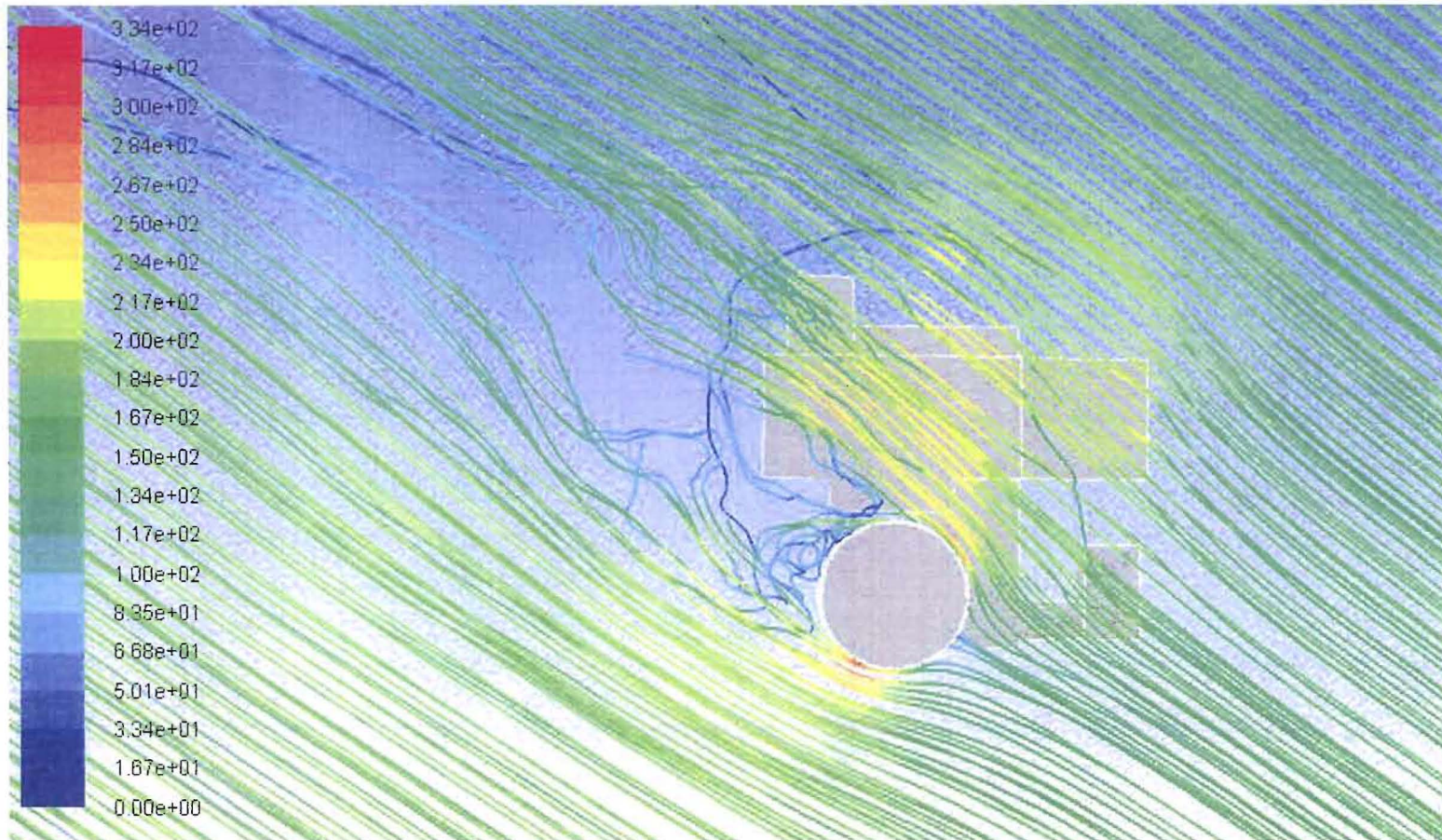
105mph Southwest Winter Conditions



VELOCITY VECTORS (ft/s)

Davis-Besse Containment Tower CFD Results

105mph Southwest Winter Conditions



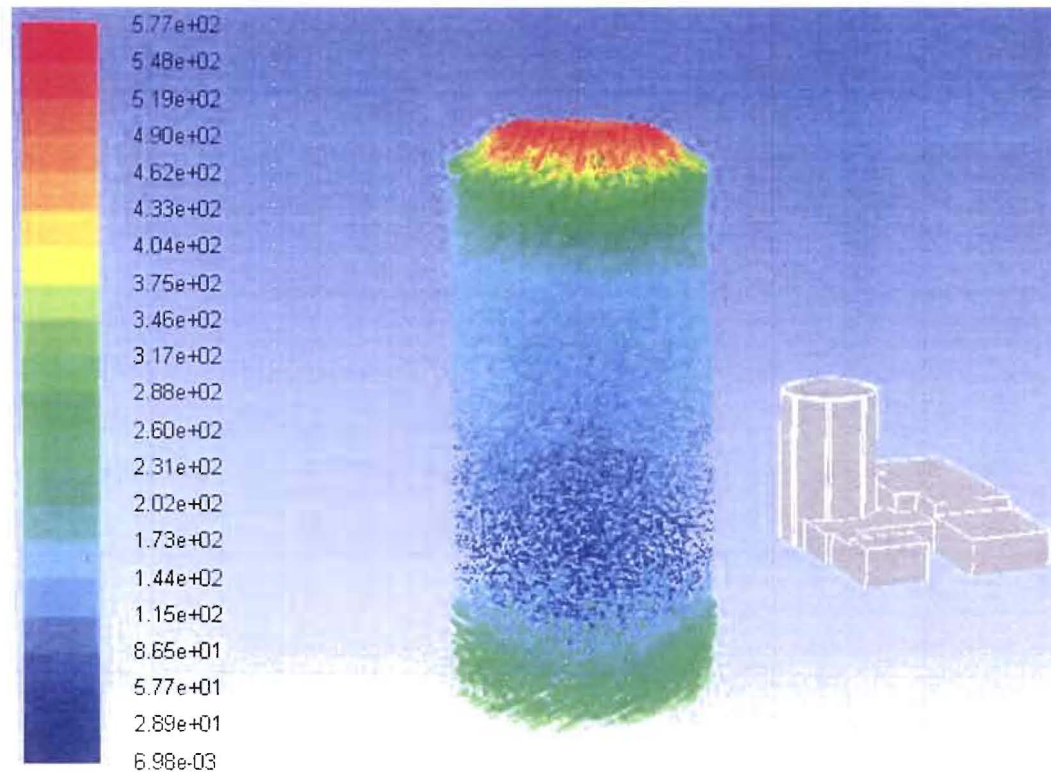
VELOCITY VECTORS (ft/s)



TORNADO CFD ANALYSIS

Tornado Conditions

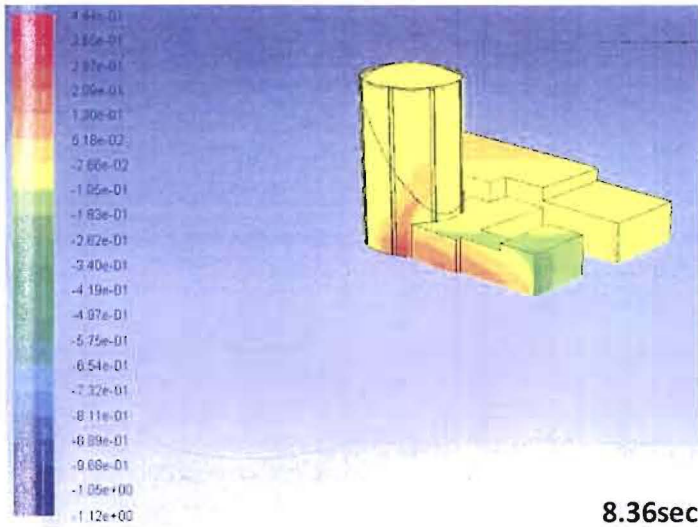
- F2 Tornado with winds between 113 and 157mph.
- Tornado touched down just west of the Davis-Bessie power plant between 845pm and 900pm on June 24, 1998.
- Tornado was 100 yards wide and traveled southeast for 3 ½ miles.
- Considerable damage was noted along this path with some barns totally destroyed.
- Slide 43 and 44 shows pressure contours on the buildings and containment tower as the tornado passes.



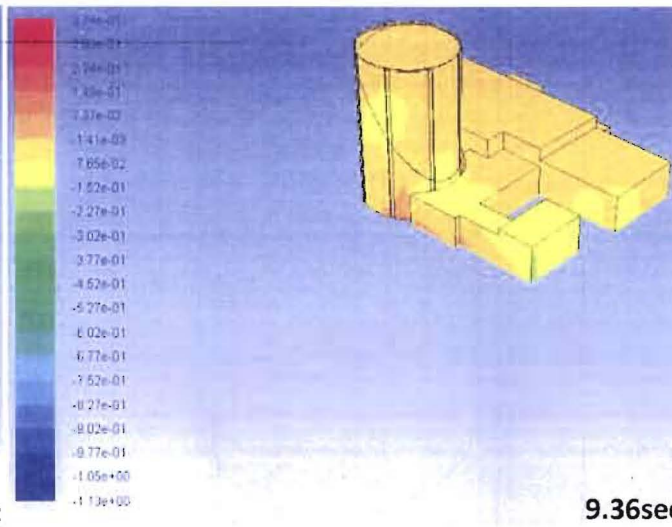
VELOCITY VECTORS SIMULATING A TORNADO (ft/s)

Davis-Besse Containment Tower CFD Results

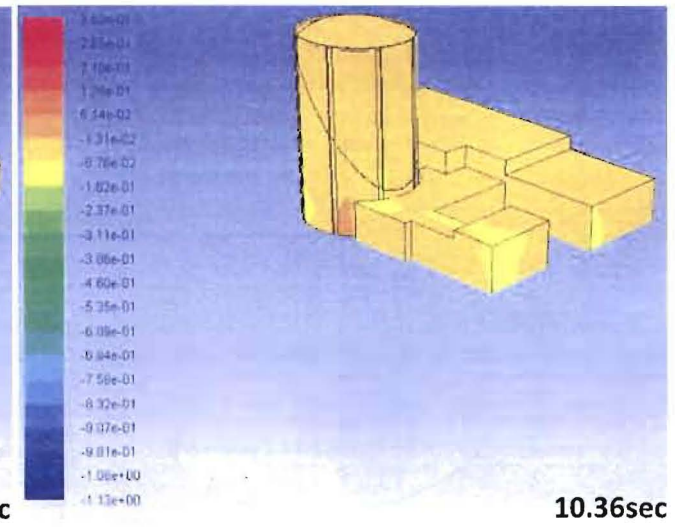
CFD Analysis of Tornado Passing by Containment Tower



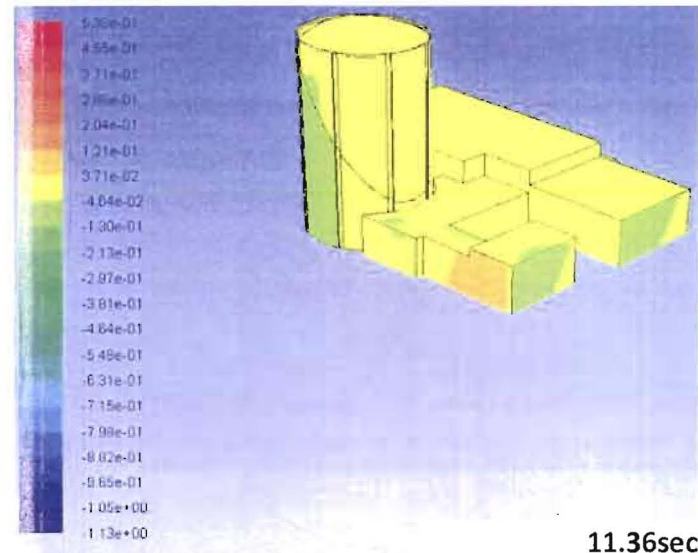
8.36sec



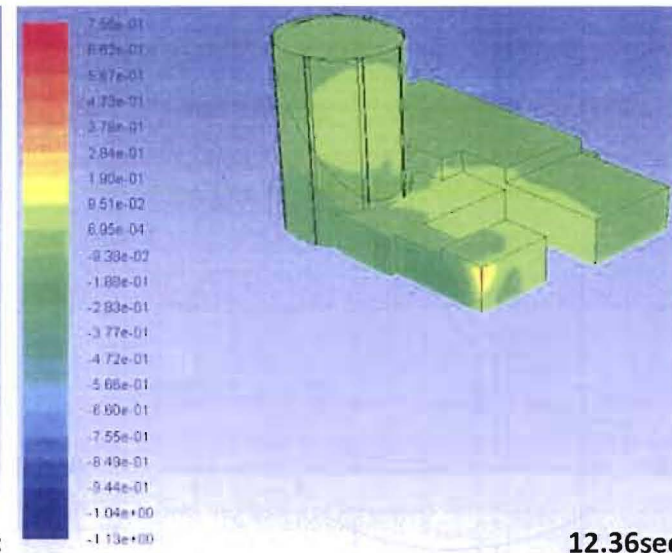
9.36sec



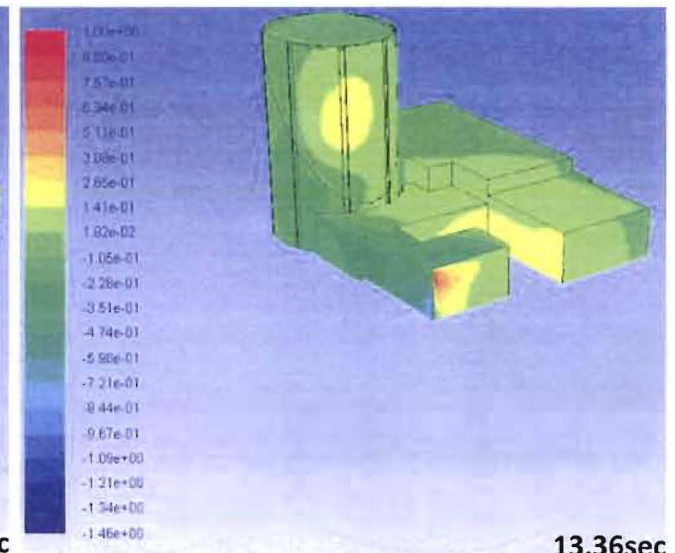
10.36sec



11.36sec



12.36sec



13.36sec

Davis-Besse Containment Tower CFD Results

CFD Analysis of Tornado Passing by Containment Tower

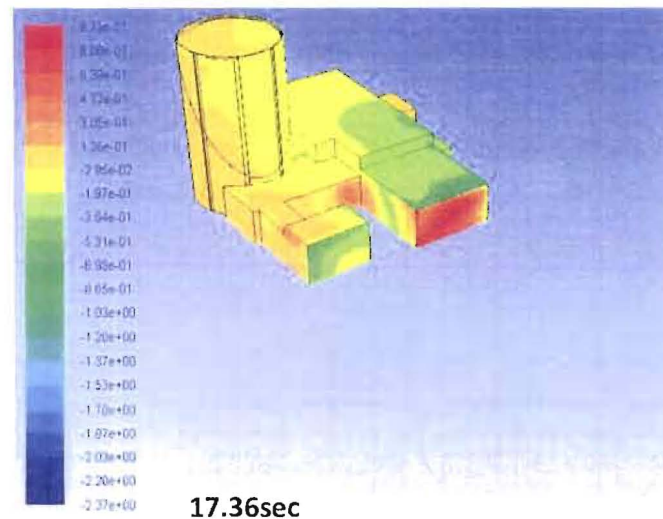
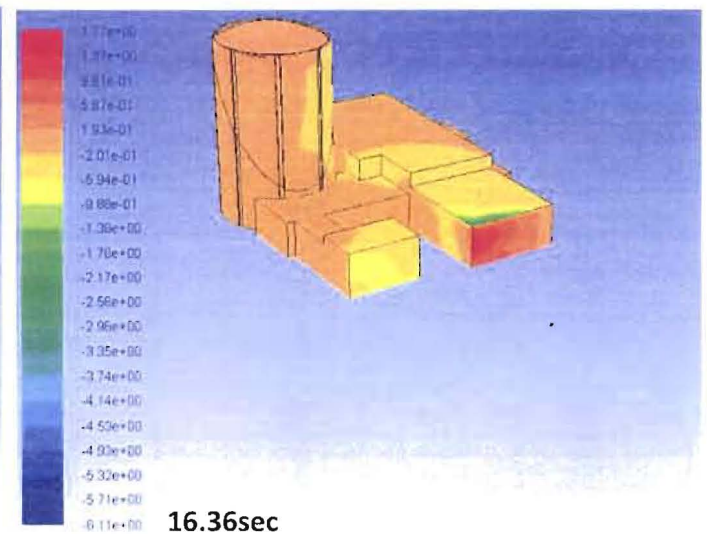
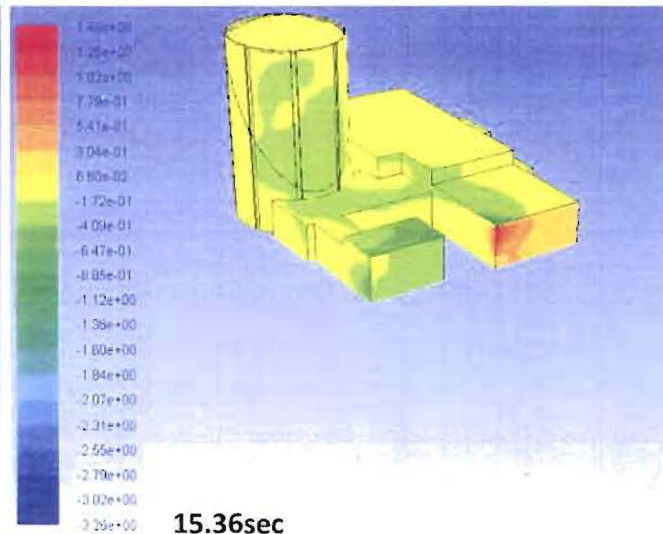
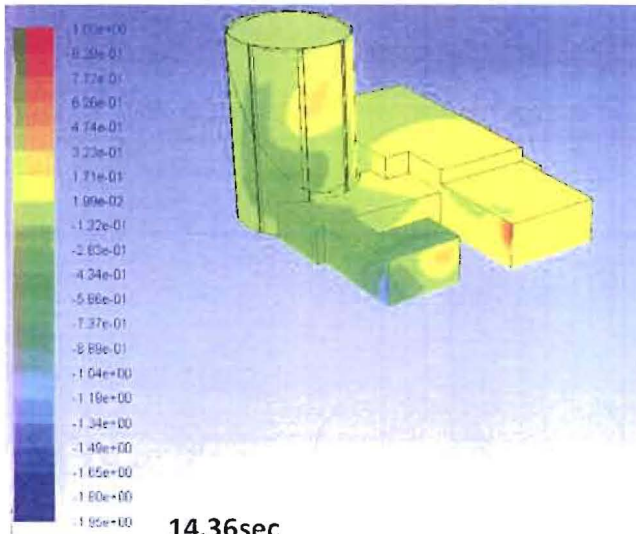




**Exhibit 64: Thermal Stress Analysis with
Gravity and Wind Load**

Thermal Stress Analysis with Gravity and Wind Load

Table of Contents

Summary of Results.....	2
Modeling Summary.....	2
Overall Approach.....	2
Finite Element Software.....	3
Modeled Geometry.....	3
Finite Element Models.....	3
[REDACTED] Descriptions.....	3
[REDACTED].....	4
[REDACTED].....	6
Thermal Stress Screening.....	7
Thermal Stress Screening Results.....	8
Combination Load Cases.....	9
Analysis Based on Measured Properties.....	10
Circumferential Temperature Distribution at O.F. Horizontal Rebar.....	11
[REDACTED].....	12
Stress State during Hot Summer Condition.....	13
Stress Analysis Results Summary.....	13
Shoulder 10 Location ([REDACTED]).....	14
Azimuth 225° Location ([REDACTED]).....	17

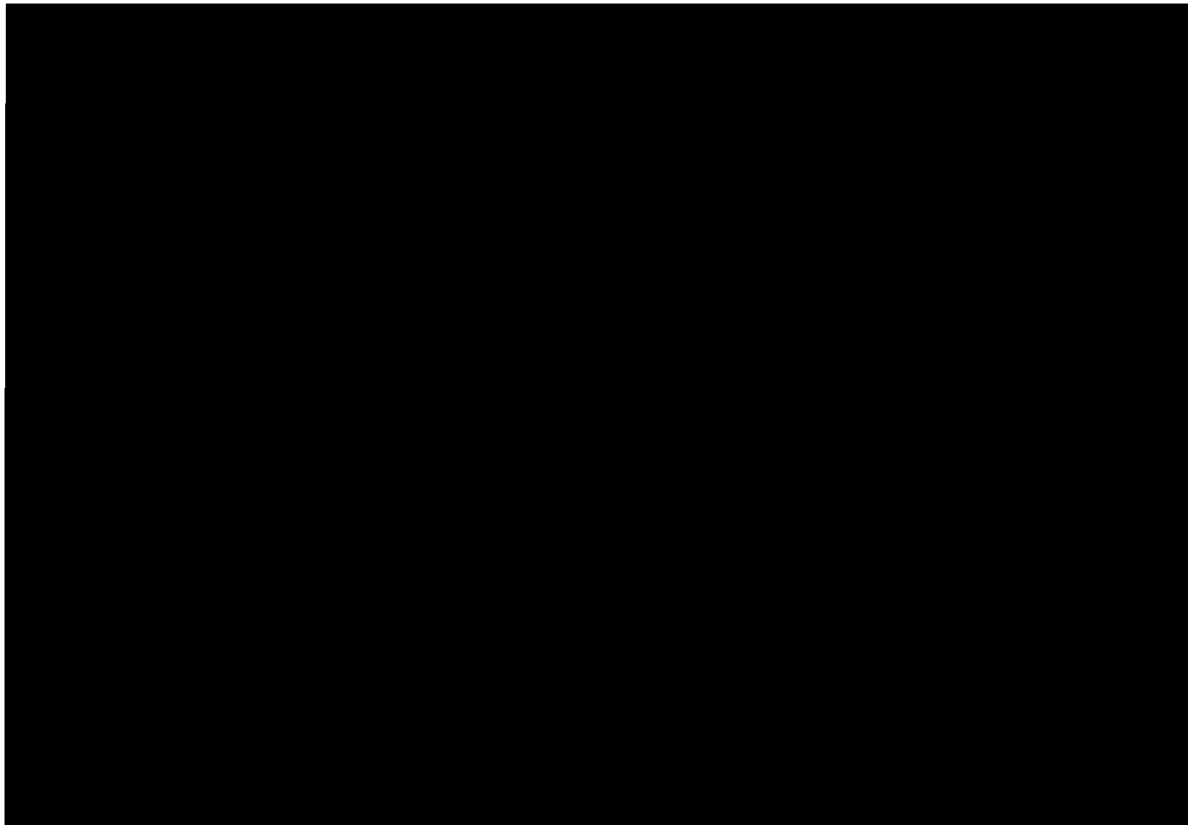
Summary of Results

The results of the analysis presented in this report can be summarized as follows:

- The temperature and wind conditions found to maximize the radial stress are not sufficient to delaminate the structure alone
- Thermally induced radial stresses is maximized at the hot summer temperatures
- At the location of the outer face horizontal rebar, the maximum radial stress due to temperature gradients, gravity, and wind is about 300 psi

Modeling Summary

Overall Approach



Finite Element Software

[REDACTED] was used exclusively in the finite element analysis presented here.

Modeled Geometry

The drawings used as geometry input for this model are:

- Drawing No: C-100 Rev. 5 "Shield Building Foundation Plan & Details SH. 1"
- Drawing No: C-110 Rev. 6 "Shield Building Roof Plan Wall Section & Details"

All vertical reinforcing bars in the containment shell section are modeled as rebar #10 (diameter 1.270") at 12" center to center spacing. The inner face horizontal rebars are #8 (diameter 1.000") at 12" spacing. The outer face horizontal rebars are # 11 (diameter 1.410") at 12" spacing. The vertical and horizontal rebars in the shoulder sections are #8 at 12" spacing.

Finite Element Models

[REDACTED] Descriptions

There are two versions of [REDACTED] focusing on two distinct different geometric features in the structure. [REDACTED]

[REDACTED]

[REDACTED] The rebar spacing is nominal at 12 inches. [REDACTED]

[REDACTED]

[REDACTED]

[REDACTED] The green elements have concrete properties and the grey elements are representing the reinforcing bars with steel properties. [REDACTED]

[REDACTED]

[Redacted]

The geometry and mesh [Redacted] Figures 1 through 3.

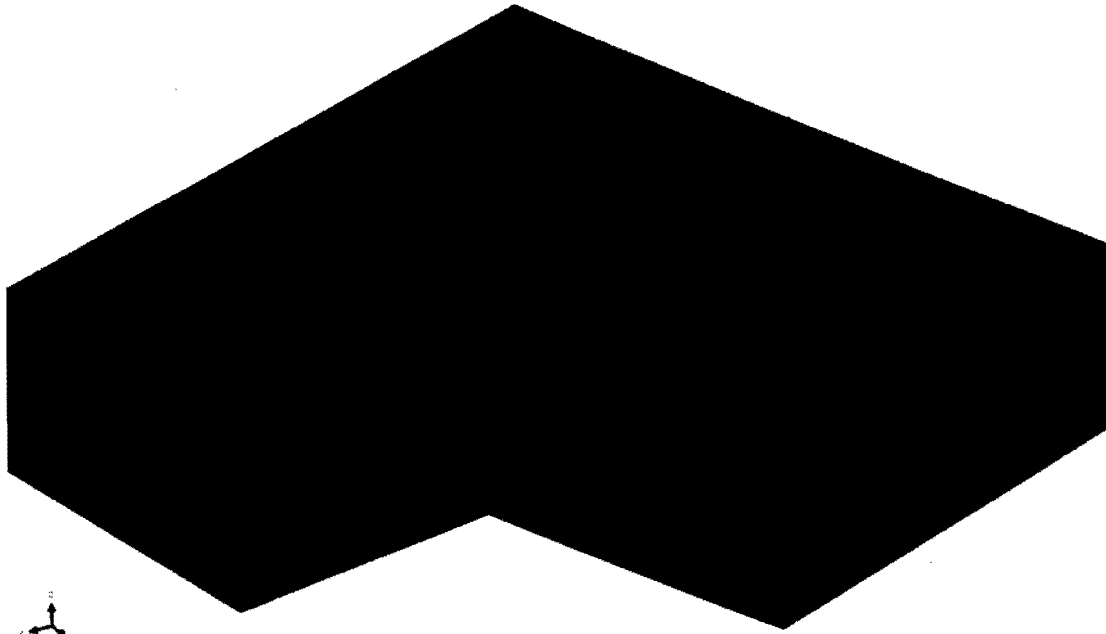


Figure 1 – [Redacted] – Shoulder/Flute; All Mesh Shown

[Redacted]

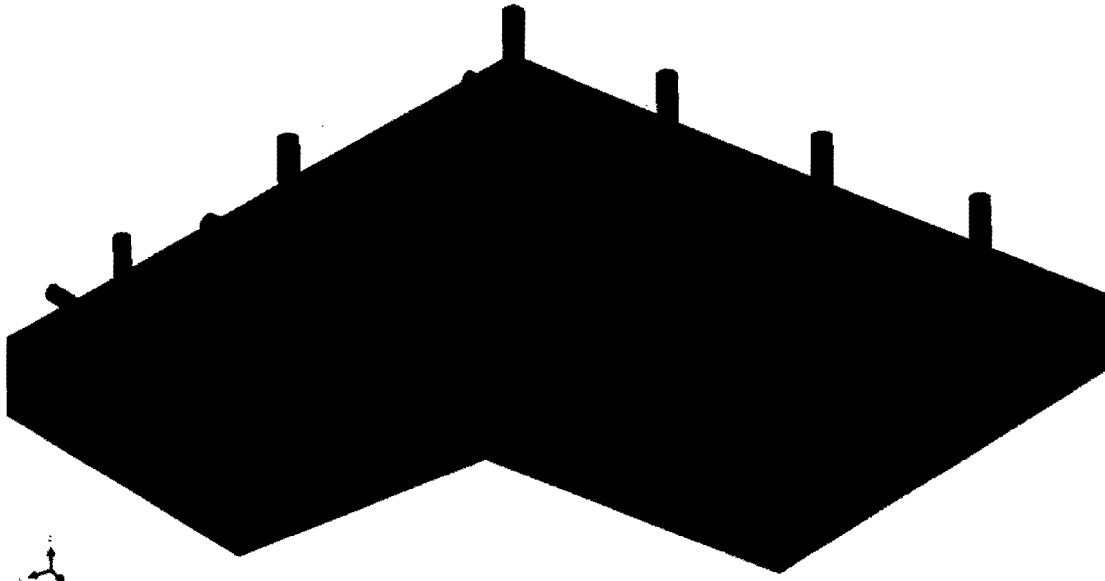


Figure 2 – [REDACTED] – Shoulder/Flute; Mesh with Rebars Exposed



Figure 3 – [REDACTED] – Shoulder/Flute; Rebar Mesh

[Redacted]

The geometry and mesh [Redacted] Figures 4 through 6.

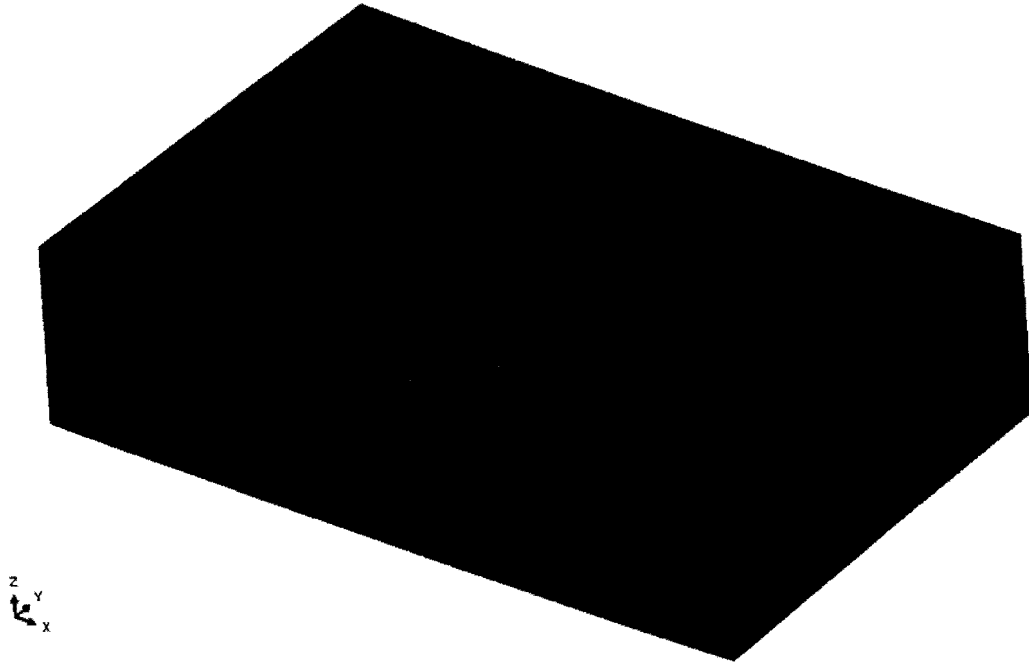


Figure 4 – [Redacted]; Shell Section; All Mesh

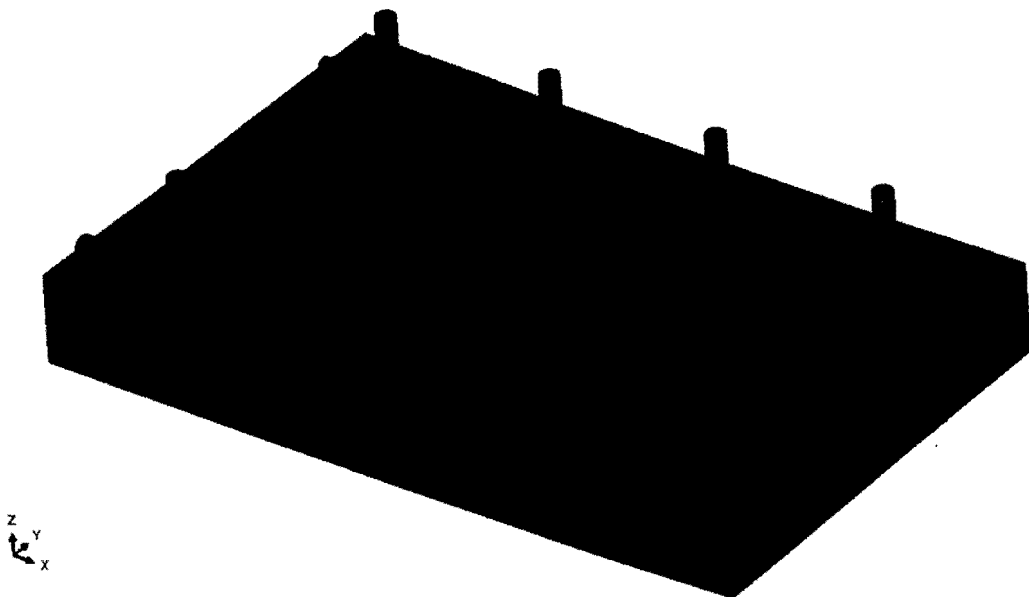


Figure 5 – [Redacted]; Shell Section; Mesh with Rebars Exposed

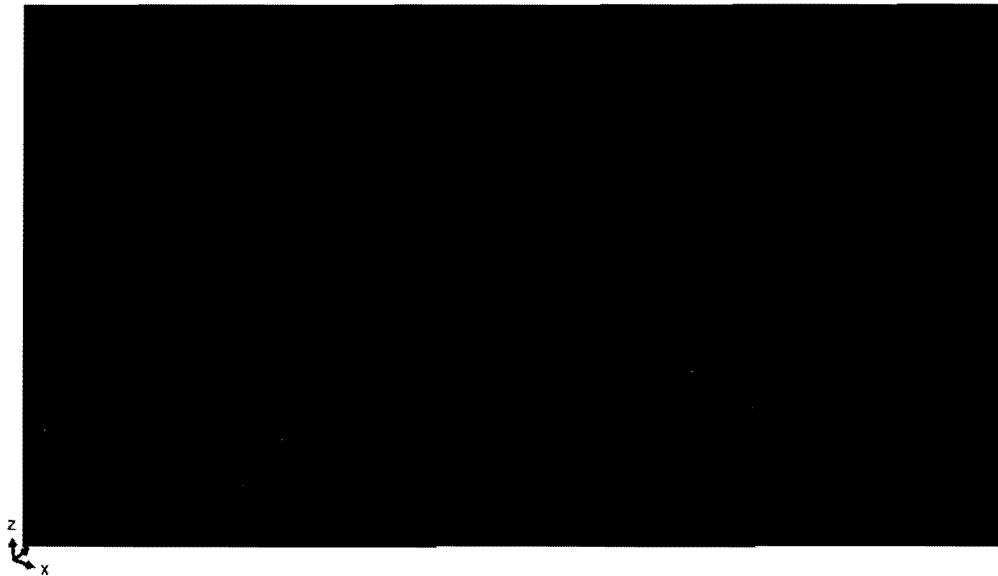
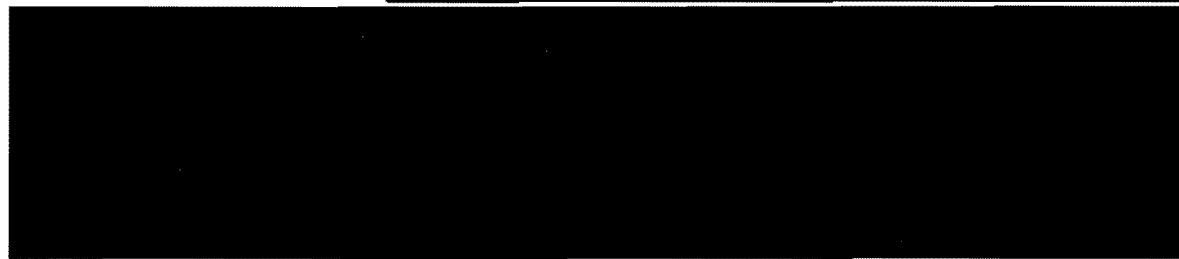


Figure 6 – [REDACTED]; Shell Section; Rebar Mesh

Thermal Stress Screening

In order to understand the effect of the various thermal conditions that the containment structure may be subjected to, a screening analysis was performed. The screening analysis was performed using preliminary material properties before the official material properties were obtained.

The screening analysis considered a total of 32 thermal conditions. They included the summer and winter solstice, the spring and autumn equinox, windy and calm condition, as well as average and hot/cold ambient temperatures. [REDACTED]

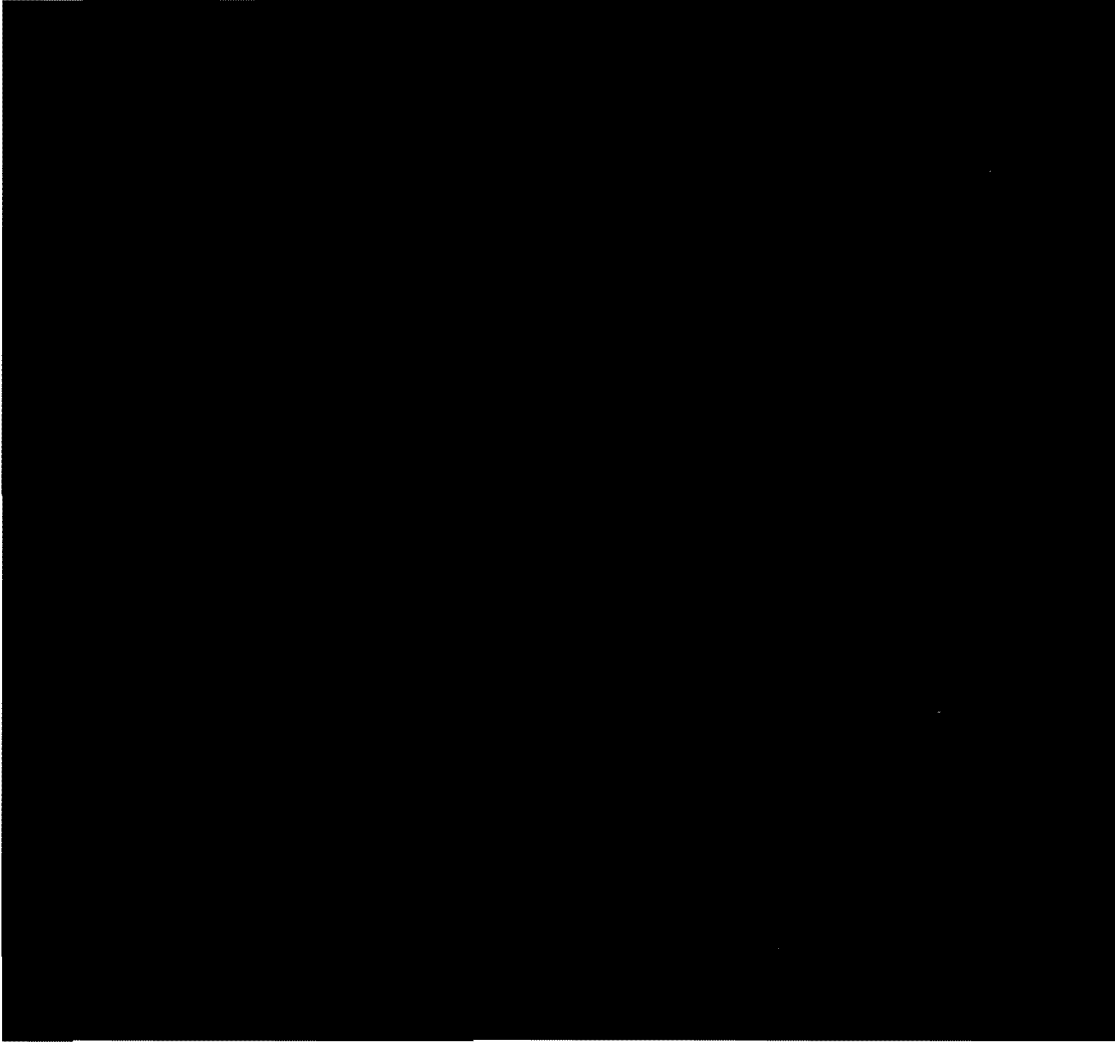


[REDACTED] The six thermal conditions resulting in the highest radial stress in the screening analysis is analyzed with gravity and wind pressure loads in the next section.



Thermal Stress Screening Results

Table 1 –

A large, solid black rectangular redaction box covers the entire content area of the table, obscuring all data and text within its boundaries.

A horizontal black redaction bar is located at the bottom left of the page, below the main redaction box.

Combination Load Cases

The result of the screening analysis identified the thermal conditions most likely resulting in the highest radial stress. [REDACTED]

[REDACTED] These combination load cases were again solved with the preliminary material properties since the official values had not yet been obtained.

[REDACTED]

Table 2 – [REDACTED]

[REDACTED]

[REDACTED]

Analysis Based on Measured Properties

The six cases predicted to result in the maximum radial stress is analyzed using measured material properties from samples taken from the Davis-Besse containment structure. The material properties used for the analysis are summarized in a separate section in the Root Cause Analysis Report (Exhibit 56, Figure 2.1.4: Material Properties [REDACTED]).

The conditions analyzed using the measured material properties are the same six conditions presented in Table 2. They are listed below along with the time of day determined to produce the highest radial stress. [REDACTED]

[REDACTED]

[REDACTED]

Circumferential Temperature Distribution at O.F. Horizontal Rebar

The temperature profiles for the six conditions resulting in the highest radial stress based on the screening analysis are shown in Figure 7. The temperature profiles are plotted in the circumferential direction around the shield building at the outer face horizontal rebar depth.

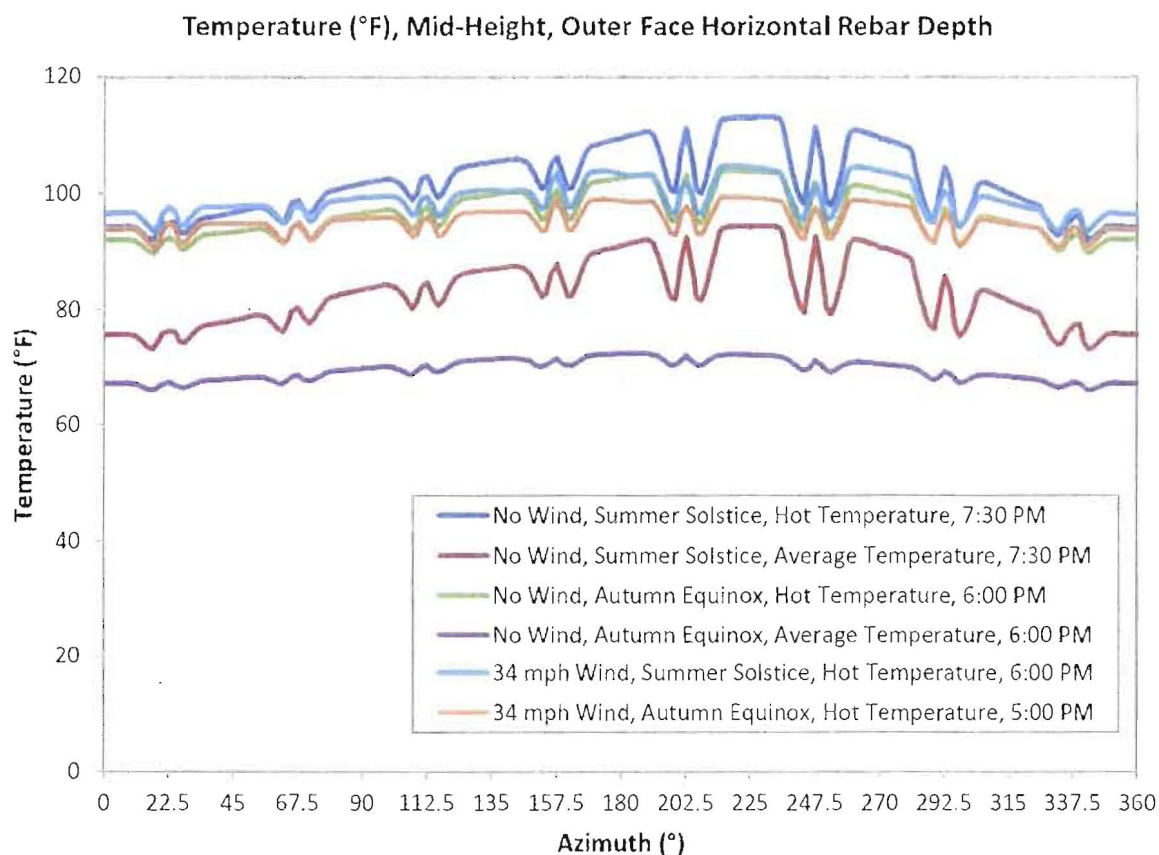


Figure 7 - Circumferential Temperature Distribution at O.F. Horizontal Rebar

For each of the six temperature profiles shown in Figure 7 eight set of double valleys can be seen. The valleys represent the lower temperature under the thick sections of the shoulders. These areas are covered by thicker layer of concrete so it takes longer for them to heat up due to the hot exterior conditions. Figure 7 also shows that the azimuth 225° location corresponds to the hottest location around the structure. The condition resulting in the hottest temperature at the outer face horizontal rebar depth is labeled "No Wind, Summer Solstice, Hot Temperature, 7:30 PM." This is the temperature condition studied [REDACTED] in the following sections.

The south to south-west side has the highest thermal gradient do to the solar heating during the day.

Figure 8 shows the location of the flutes, shoulders, and the azimuth convention for the Davis-Besse containment structure.

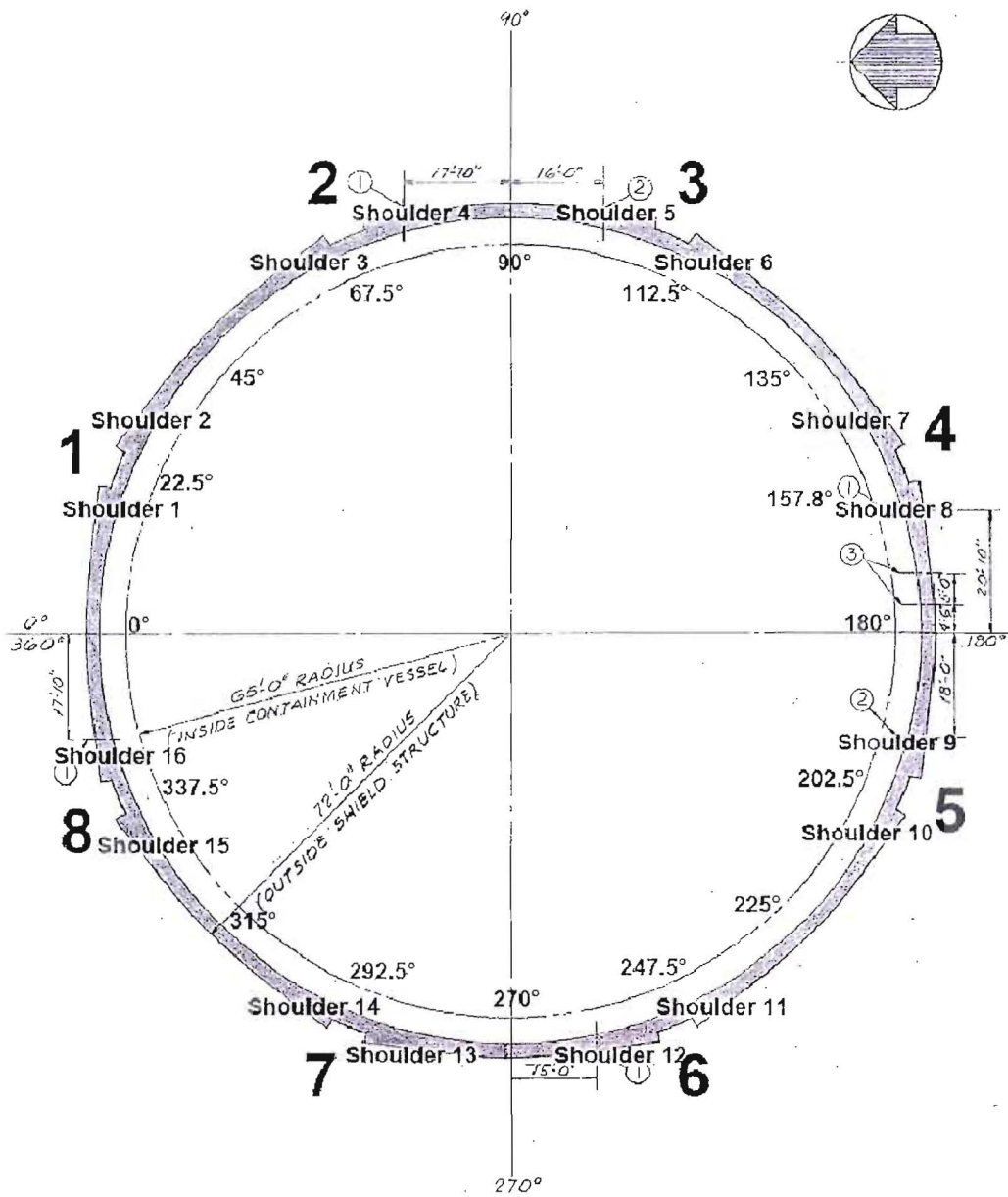


Figure 8 – Shield Building Flute Numbers and Azimuth Locations

Stress State during Hot Summer Condition

The results shown in this section describes the detailed stress state in the hottest location around the structure for the hot summer condition (No Wind, Summer Solstice, Hot Temperature, 7:30 PM)

Figures 9 through 13 show the results from the shoulder 10 location [REDACTED].
Figures 14 through 18 depict the same results from the azimuth 225° location [REDACTED].

For each of the two locations the result is presented in five figures. The first figure shows the temperature distribution and the following four figures depict the stress state:

1. Temperature Distribution
2. Max Principal Stress
3. Radial Stress
4. Circumferential (Hoop) Stress
5. Vertical Stress

The stress state is presented at the mid-height section [REDACTED]. The contour range is set to +/- 300 psi for all the stress figures so that they can be compared more easily.

Stress Analysis Results Summary

The maximum stress [REDACTED] is confined to the top and bottom of the outer face horizontal rebars. The maximum tensile stress is about 300 psi and not enough to crack the concrete.

Shoulder 10 Location ([REDACTED])

The temperature distribution, max principal stress, radial stress, hoop stress, and vertical stress in shoulder 10 are depicted in Figures 9 through 13, respectively. Figure 9 shows that the shoulder surface is hotter than the flute surface. This is the result of more solar exposure on the shoulder surface compare to the flute valley. Also, there is more surface area at the corner of the shoulder resulting in higher temperature during the hot ambient condition.

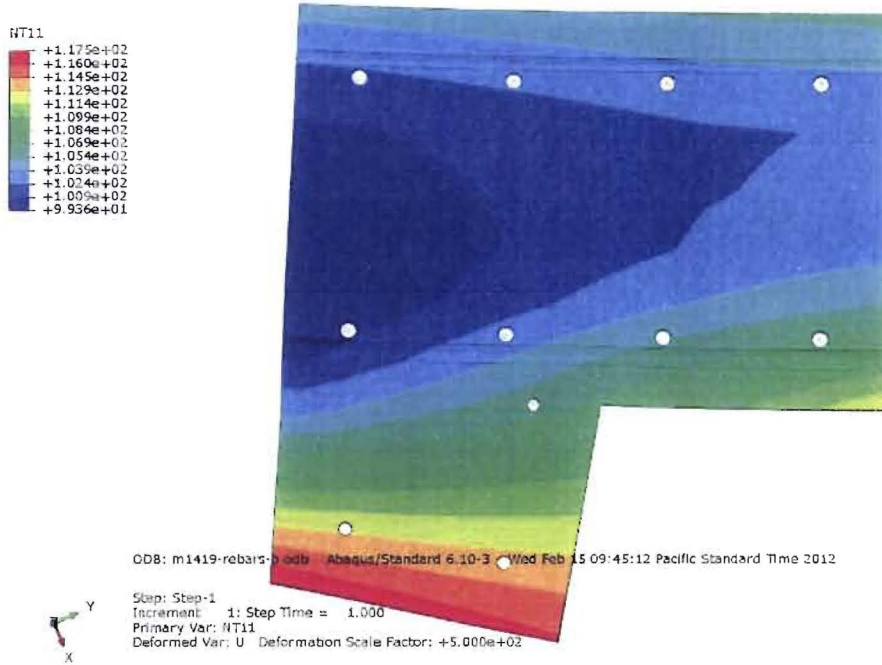


Figure 9 – Temperature Distribution (°F) [REDACTED] in the Shoulder 10 Location

Figures 10 through 13 depict the stress state using the max principal stress and the three stress components in a cylindrical coordinate system located at the containment structure center. The max principal and radial stresses are highest at the outer face horizontal rebar. The figures also indicate an area of high stress on the left edge of the model. This has been identified to be a singularity [REDACTED]

Comparing the stress in the three radial, hoop, and vertical directions (Figures 11 through 13 respectively) indicates that the radial component has the highest tensile stress. As shown in Figure 11, the radial tensile stress is below 300 psi which is less than the tensile strength of the concrete. It is concluded that the hot summer temperature condition is not capable of delaminating the structure in the flute/shoulder location.



Figure 10 – Max Principal Stress (psi) in the Flute/Shoulder

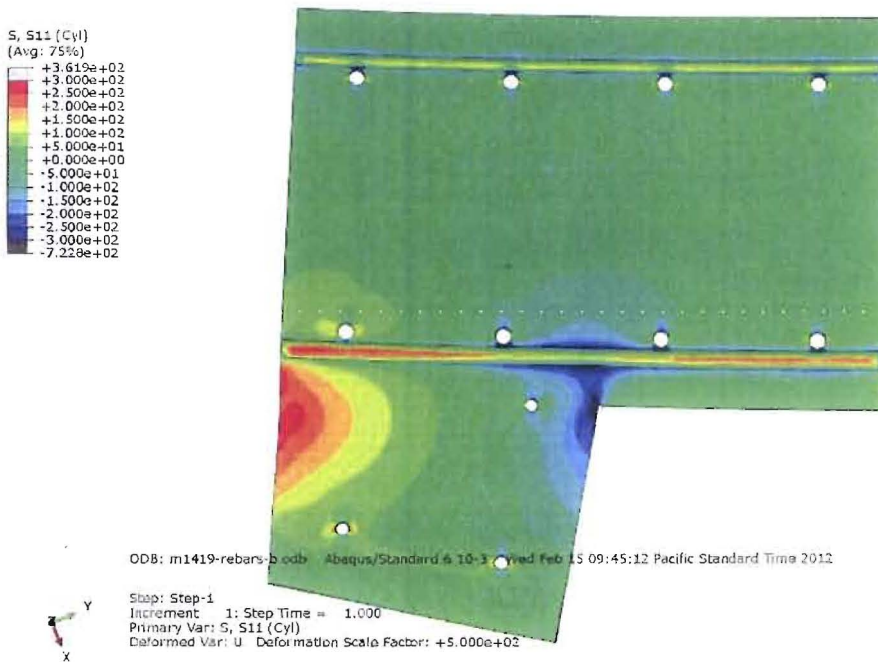


Figure 11 – Radial Stress (psi) in the Flute/Shoulder

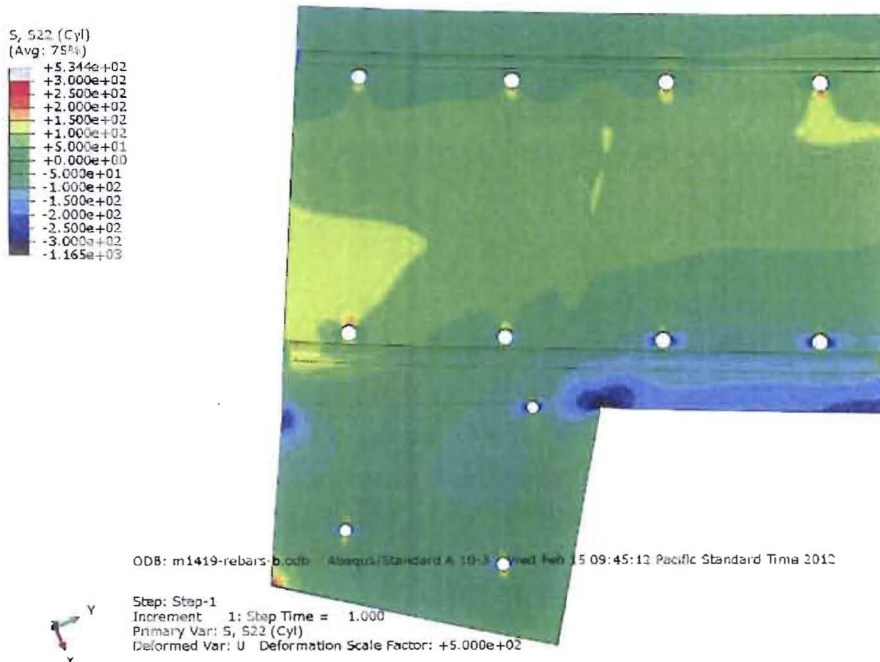


Figure 12 – Hoop Stress (psi) in the Flute/Shoulder

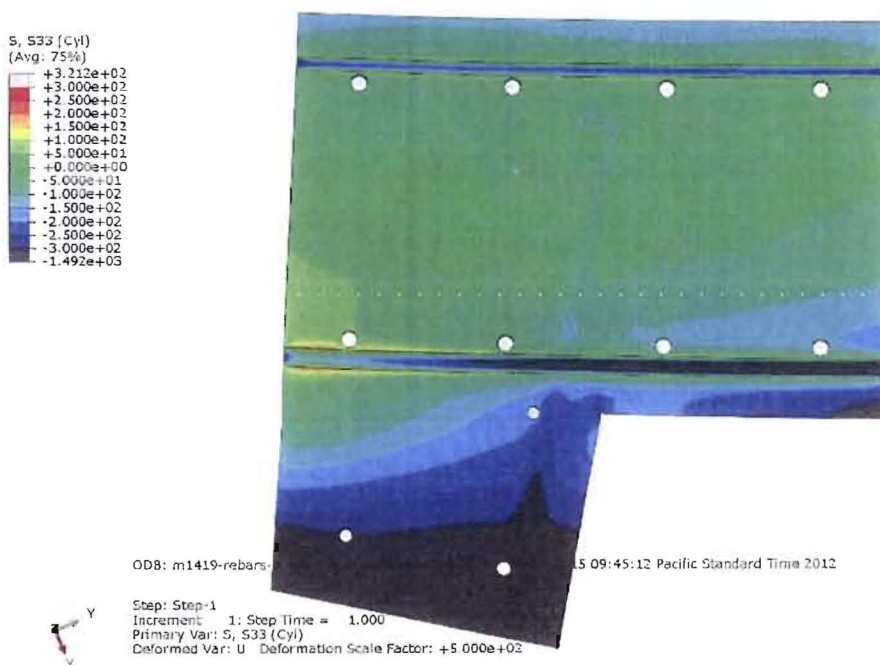


Figure 13 – Vertical Stress (psi) in the Flute/Shoulder

Azimuth 225° Location ([REDACTED])

The temperature distribution, max principal stress, radial stress, hoop stress, and vertical stress in the shell area at azimuth 225° are shown in Figures 14 through 18, respectively. Figure 14 shows that the exterior surface is hotter than the interior. This is the result of the hot ambient daytime condition and the colder nighttime condition.

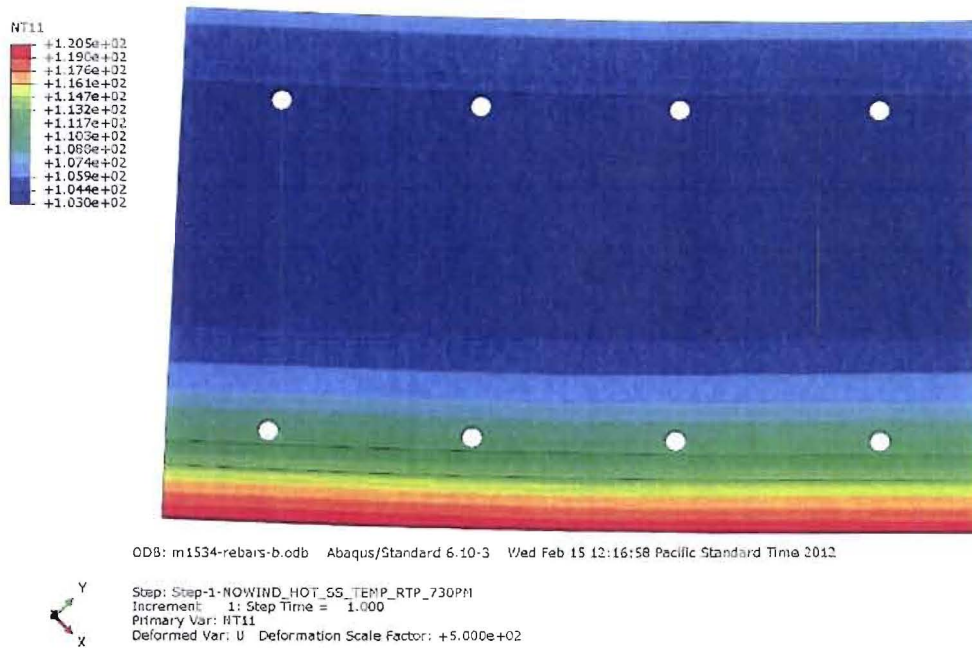


Figure 14 – Temperature Distribution (°F) [REDACTED] at the Azimuth 225° Location

Figures 15 through 18 depict the stress state using the max principal stress and the three stress components in a cylindrical coordinate system located at the containment structure center. The max principal and radial stresses are highest at the outer face horizontal rebar depth (see Figures 15 and 16). Comparing the stress in the radial, hoop, and vertical directions (Figures 16 through 18, respectively) indicates that the radial component has the highest tensile stress. As shown in Figure 16, the radial stress is below 300 psi which is less than the strength of the concrete. It is concluded that the hot summer temperature condition is not capable of delaminating the structure in the shell section location (middle of a panel).

Furthermore, Figures 17 and 18 show that the hotter exterior surface temperature results in compression stresses in both the hoop and vertical directions due to expansion of the outer layer.

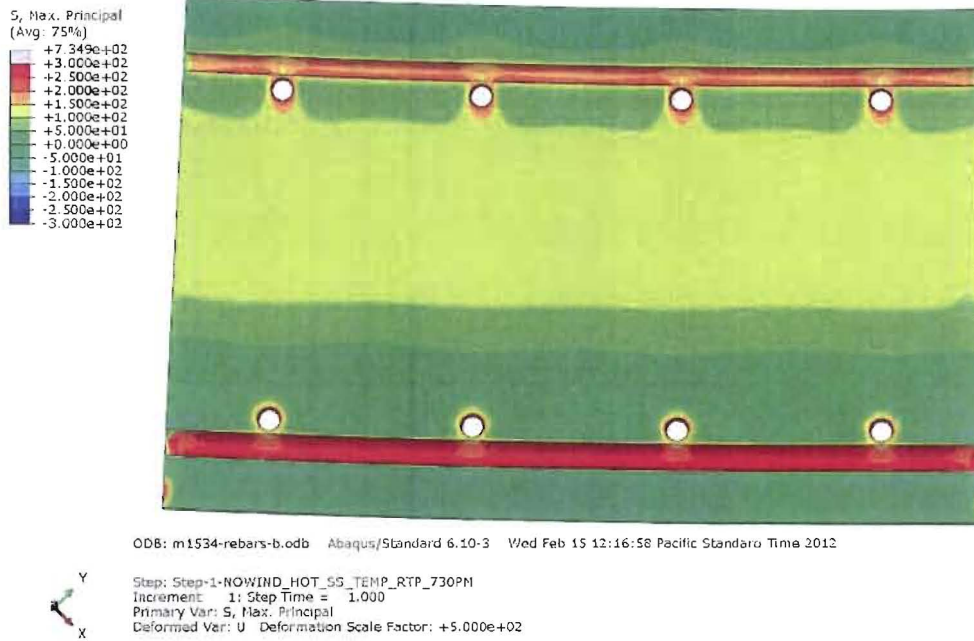


Figure 15 – Max Principal Stress (psi) [redacted] at the Azimuth 225° Location

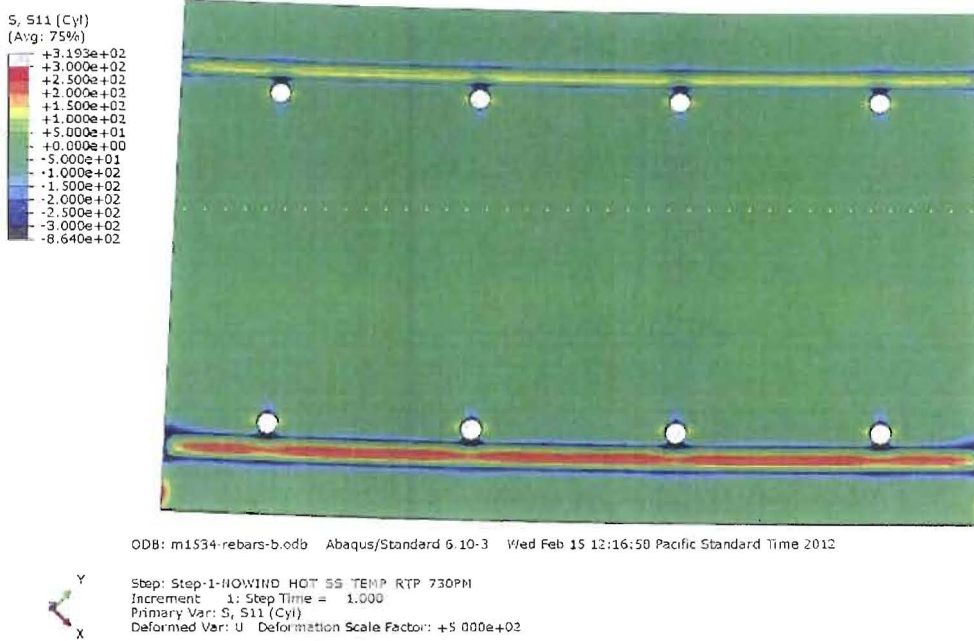


Figure 16 – Radial Stress (psi) [redacted] at the Azimuth 225° Location

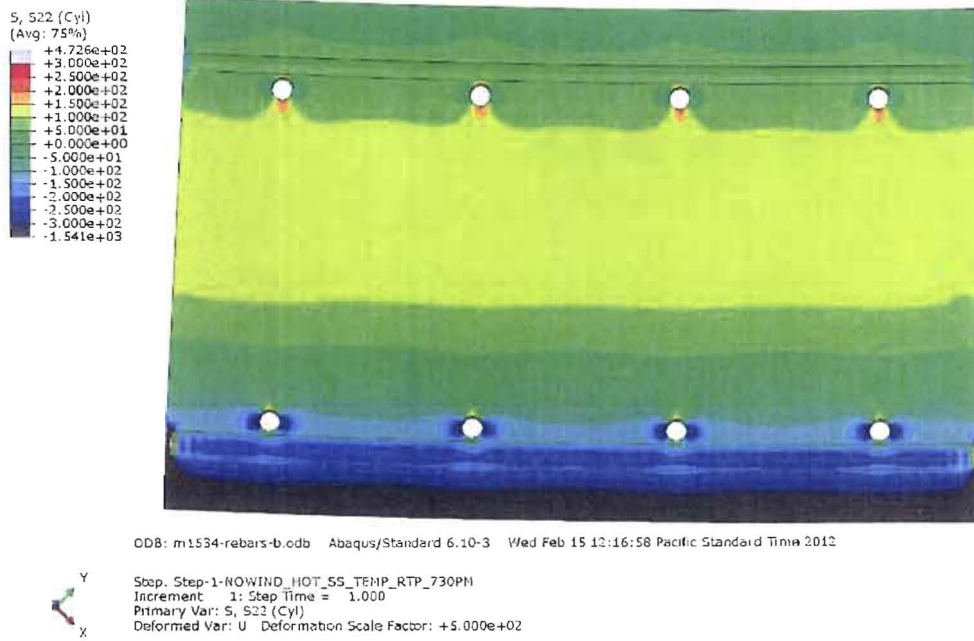


Figure 17 – Hoop Stress (psi) [redacted] at the Azimuth 225° Location

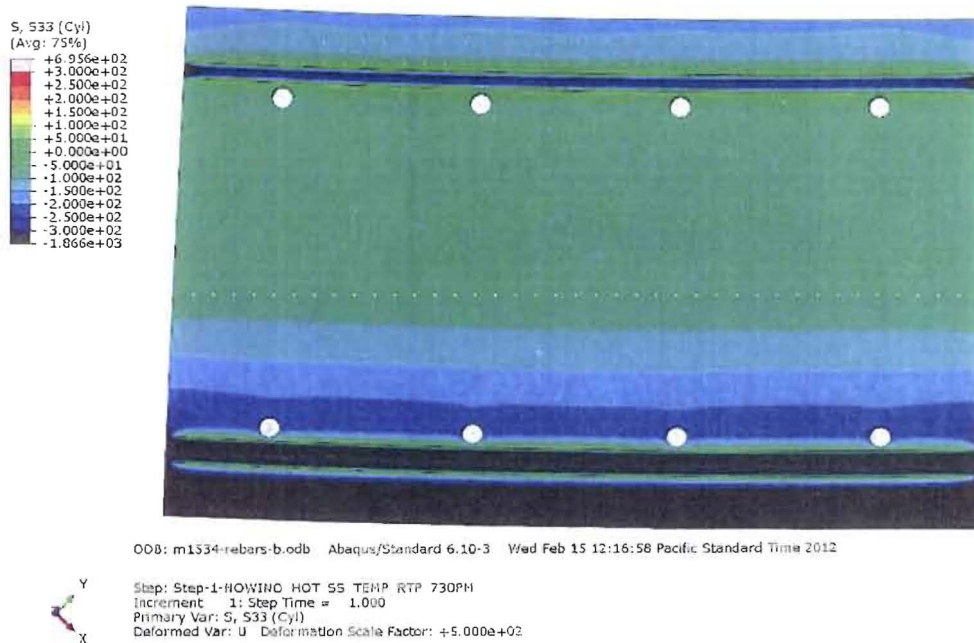


Figure 18 – Vertical Stress (psi) [redacted] at the Azimuth 225° Location



Exhibit 65: Thermal Analysis



DAVIS-BESSE THERMAL ANALYSIS

1.0 ANALYSIS MODEL

For the purposes of assessing the seasonal and daily variations in the temperature of the outer concrete shield building of the Davis-Besse reactor, a detailed 3D transient thermal analysis finite element based model was generated. This model was derived from the same 3D NASTRAN structural [REDACTED] model that was used for this effort and utilized the same node and element numbers. Additional surface flux thermal elements were added to the interior faces of the concrete in order to improve the capture of radiation heat transfer from the interior steel containment as well as convective heat transfer by the passage of the annular air. By preserving the same node numbers, this permitted directly mapping temperatures onto the NASTRAN structural model without having to interpolate temperatures between dissimilar meshes. This ensured that temperatures were accurately specified for all structural analyses performed with the NASTRAN [REDACTED] model. Similarly, preserving the element ID numbers ensured proper specification of thermal properties for all of the materials present.

The thermal analysis model that was used for this effort [REDACTED] and is shown in Figure 1. The majority of the concrete was modeled using linear 8 node brick elements. The steel rebar reinforcement was explicitly modeled using 1D bar elements that share the same nodes with the 3D solid elements used to represent the concrete.

[REDACTED] Only in the dome region OF and IF rebar were membrane elements used to approximate the smeared thermal properties of the rebar and concrete based upon a volumetric averaging of their properties.

All pre- and post processing of the thermal analysis model was performed using MSC MD.PATRAN version 10.2. MSC MD.PATRAN is an open ended pre- and post - processor that facilitates the creation and post-processing of results for a number of different CAE solvers. This includes MD.NASTRAN and ABAQUS, the two structural finite element analysis (FEA) solvers used for this effort. This enables models and results derived from one the analysis code to be converted into its equivalent in another code. In this way, the NASTRAN thermal models and results files could be converted into an equivalent ABAQUS version. [REDACTED]



. By doing so, this obviated the need to generate a separate ABAQUS based thermal analysis model.



FIGURE 1. NASTRAN TRANSIENT THERMAL ANALYSIS MODEL



2.0 THERMAL BOUNDARY CONDITIONS

2.1 RADIANT HEAT TRANSFER SOURCES

The primary intent of thermal analysis was to ascertain the variation in temperature that occurs daily as well as seasonally. To accomplish this, it is essential that the variation in the position of the sun as it transits across the sky be properly modeled. This entails specifying the zenith angle, Z , or the angle of the sun relative to a normal pointing directly overhead. The zenith angle is a function of both the latitude as well as the time of year. It is derived from the following relationship (see <http://edmall.gsfc.nasa.gov/inv99Project.Site/Pages/science-briefs/ed-stickler/ed-irradiance.html>):

Z = Zenith Angle = The angle from the zenith (a point directly overhead) to the Sun's position in the sky. The zenith angle is dependent upon the latitude, solar declination angle and time of day.

$$Z = \cos^{-1} (\sin \Phi \sin \delta + \cos \Phi \cos H)$$

Φ = Latitude

H = Hour Angle = $15^\circ \times (\text{Time} - 12)$ (Angle of radiation due to time of day where time is given as the hour of the day from midnight.)

δ = Solar Declination Angle

Solar Declination Angles for the Northern Hemisphere

Vernal Equinox March 21/22 $\delta = 0^\circ$

Summer Solstice June 21/22 $\delta = +23.5^\circ$

Autumn Equinox September 21/22 $\delta = 0^\circ$

Winter Solstice December 21/22 $\delta = -23.5^\circ$

The solar radiation that strikes the earth, also known as Insolation, is then simply given by

$$I = S \cos (Z)$$

I = Insolation or solar flux

S = solar flux $\sim 1000 \text{ Watts}/\text{m}^2 \sim 2.2 \text{ Btu}/\text{Hr} - \text{in}^2$ (Clear day insolation perpendicular to the incident solar radiation)

Z = Zenith angle



The solar insolation that strikes the earth is strongly affected by the angle of incidence with the surface being radiated by the sun. The more oblique the angle, the lower the flux. Consequently, in the latitudes farther from the equator, the solar insolation will be lower. In addition, seasonal variations will cause the solar declination to change by 47 degrees between the winter and summer solstices. Thus, the solar flux will be least during the winter and greatest during the summer in the northern hemisphere. The UV spectrum of sunlight is principally responsible for solar heating. It is strongly affected by the angle it passes through the atmosphere. This is shown in Figure 2

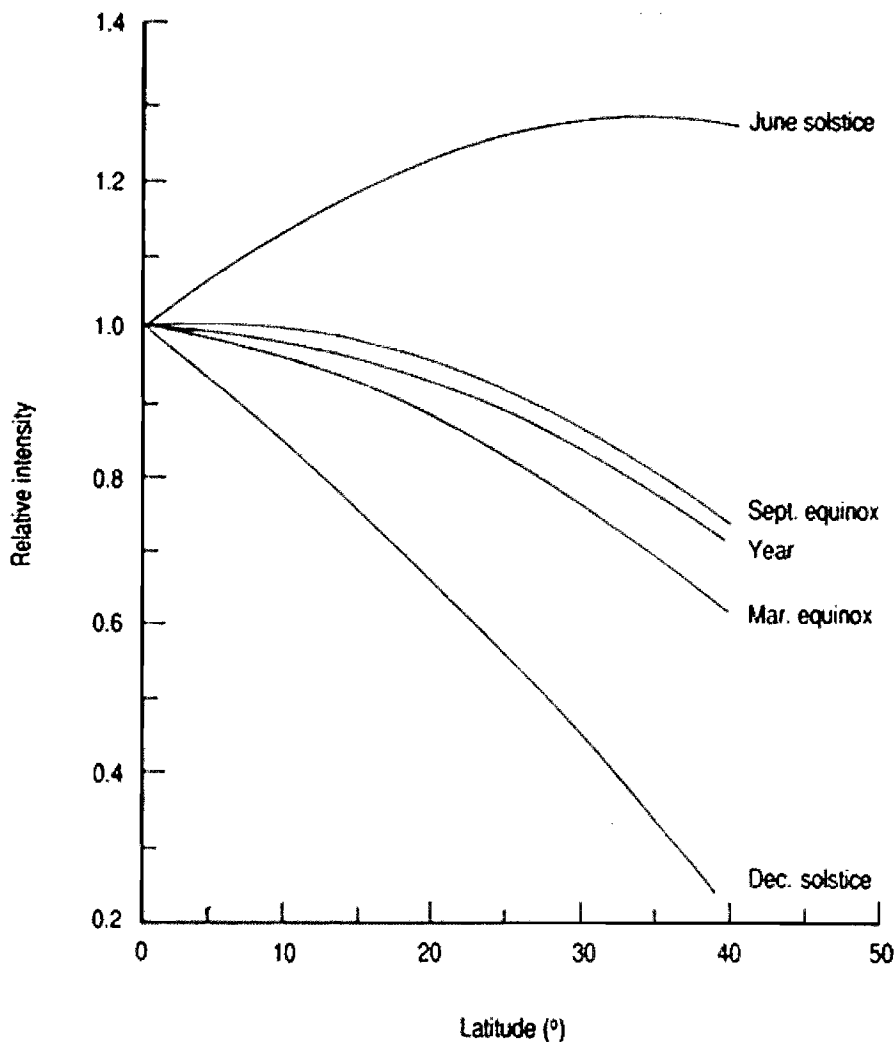


FIGURE 2. SEASONAL AND ANNUAL VARIATIONS IN RELATIVE SOLAR UV-A RADIATION (340 nm) FOR DIFFERENT LATITUDES (BASED ON JOHNSON ET AL 1976)